Evolution of Magnetic Activities in Late-Type Stars

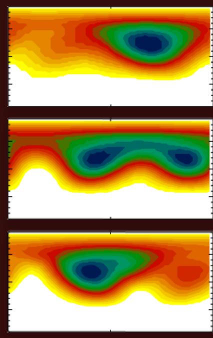

A Thesis submitted to

Pt. Ravishankar Shukla University, Raipur

For

The Degree of Doctor of Philosophy

in

PHYSICS

Under the Faculty of Science

2017

Supervisor:

Dr. Jeewan C. Pandey

Scientist E, ARIES, Manora Peak,

Nainital- 263 002, Uttarakhand, India

Investigator:

Subhajeet Karmakar

ARIES, Manora Peak,

Nainital- 263 002, Uttarakhand, India

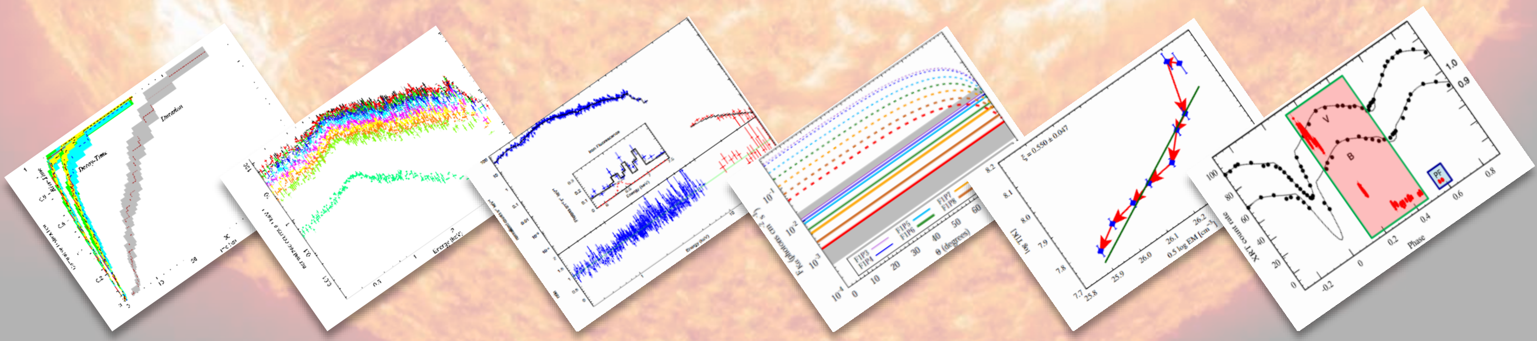

Research Centre

Aryabhatta Research Institute of Observational Sciences (ARIES)

Manora Peak, Nainital 263 002, Uttarakhand, India

Evolution of Magnetic Activities in Late-Type Stars

A

THESIS SUBMITTED

To

Pt. Ravishankar Shukla University, Raipur

For

The Degree of Doctor of Philosophy

in

PHYSICS

under the Faculty of Science

2017

Supervisor :
Dr. Jeewan C. Pandey
Scientist – E
ARIES, Nainital

Investigator :
Subhajeet Karmakar
ARIES, Manora Peak
Nainital – 263 002

Research Centre

Aryabhatta Research Institute of observational sciencES (ARIES)

Manora Peak, Nainital 263 002, India

Declaration by Candidate

I declare that the thesis entitled ***"Evolution of Magnetic Activities in Late-type stars"*** is my own work conducted under the supervision of ***Dr. Jeewan C. Pandey*** at ***Aryabhatta Research Institute of observational sciencES (ARIES), Nainital, Uttarakhand, India,*** approved by the Research Degree Committee. I have put in more than 200 days of attendance with the supervisor at the center.

I further declare that to the best of my knowledge the thesis does not contain any part of any work, which has been submitted for the award of any degree either in this University or in any other University/Deemed university without proper citation.

JPandey
11.07.2017

Dr. Jeewan C. Pandey
Signature of the Supervisor

Scientist "E"
ARIES, Manora Peak
Nainital.

SKarmakar
11.07.2017

Subhajeet Karmakar
Signature of the Candidate

Nameeta
13/07/2017

Signature of the Chairman, DRC

CHAIRMAN,
Deptt. Research Committee,
SOS in Physics & Astrophysics,
Pt. R.S. University, RAIPUR (C.G.)

Certificate by the Supervisor

This is to certify that the work entitled ***"Evolution of Magnetic Activities in Late-type stars"*** is a piece of research work done by ***Mr. Subhajeet Karmakar*** under my guidance and supervision for the degree of Doctor of Philosophy in ***PHYSICS*** of Pt. Ravishankar Shukla University, Raipur (Chhattisgarh), India. That the candidate has put in an attendance of more than 200 days with me.

To the best of my knowledge and belief this thesis

1. Embodies the work of the candidate himself.
2. Has duly been completed.
3. Fulfills the requirements of the Ordinance relating to the Ph.D. degree of the University;

   and
4. Is up to the standard both in respect of contents and language for being referred to the examiner.

JPandey
11.07.2017

Dr. Jeewan C. Pandey
Signature of the Supervisor

Scientist "E"
ARIES. Manora Peak
Nainital.

Forwarded

Nameeta
13/07/2017

Signature of the Chairman, DRC

CHAIRMAN,
Deptt. Research Committee,
SOS in Physics & Astrophysics,
Pt. R.S. University, RAIPUR, (C.G.)

Certificate No: 2012 /01

ARYABHATTA RESEARCH INSTITUTE OF OBSERVATIONAL SCIENCES

Manora Peak, Nainital

[An Autonomous Institute under the Department of Science and Technology (DST), Government of India]

Pre Ph.D. Course Work- 2011-12

It is certified that Mr. Subhajeet Karmakar attended and successfully completed the post-MSc coursework at ARIES, Nainital during the session August 2011-June 2012.

His performance in the course was found to be satisfactory and he obtained an aggregate of 67.2%

wVddi
for
Director
SCIENTIST 'F'
ARIES, NAINITAL

Indranil Chattopadhyay
Chairman Academic Committee
Chairperson
Academic Committee
ARIES, Nainital

SCHOOL OF STUDIES IN PHYSICS AND ASTROPHYSICS
PT. RAVISHANKAR SHUKLA UNIVERSITY,
RAIPUR - 492010, CHHATTISGARH (INDIA)

Dr. Nameeta Brahme
M. Phil, Ph. D.
Professor & Head

Phone : (M) 96913-18995
: (O) (0771) 2262864
Email : namitabrahme@gmail.com

Ref. : 2467

Date : 10-04-2017

CERTIFICATE

This is to certify that **Mr. Subhajeet Karmakar** has given Pre-Ph.D. seminar on his thesis entitled **"Evolution of Magnetic Activities in Late-Type Stars"** on **10.04.2017** at School of Studies in Physics & Astrophysics, Pt. Ravishankar Shukla University, Raipur.

Nameeta
10/04/2017

Chairman
Departmental Research Committee
SoS in Physics & Astrophysics
Pt. Ravishankar Shukla University, Raipur

APPENDIX – 5

Copy Right Transfer Approval Form

(Clause 14e of the Ordinance - 45)

Name of the Candidate:	SUBHAJEET KARMAKAR
Department:	School of Studies in Physics and Astrophysics
Degree :	Doctor or Philosophy in Physics
University:	Pt. Ravishankar Shukla University, Raipur
Supervisor:	Dr. Jeewan C. Pandey
Late-type stars Thesis Title:	Evolution of Magnetic Activities in Late-type stars
Year of Award:	....

Agreement

1. I hereby declare that, if appropriate, I have obtained and attended hereto a written permission/statement from owner(s) of each third party copyrighted matter to be included in my thesis/dissertation, allowing distribution as specified below.

2. I hereby grant to the university and its agents the non-exclusive license to archive and make accessible, under the condition specified below, my thesis/dissertation, in whole or in part in all forms of media, now or hereafter known. I retain all other ownership rights to the copyright of the thesis/dissertation. I and my Supervisor, also retain the right to use in future works (such as articles or books) all or part of this thesis, dissertation, or project report.

Condition:

1. Release the entire work for access worldwide ☐

Karmakar

Signature of the Candidate
Place Raipur
Date 17.07.2017

JPandey

Signature and Seal of the Supervisor

Scientist "E"
ARIES. Manora Peak
Nainital.

URKUND

Urkund Analysis Result

Analysed Document:	EVOLUTION OF MAGNETIC ACTIVITIES IN LATE TYPE STARS (SUBHAJEET KARMAKAR).pdf (D29627590)
Submitted:	2017-07-13 09:56:00
Submitted By:	library_prsu@rediffmail.com
Significance:	0 %

Sources included in the report:

Instances where selected sources appear:

0

13/7/17

SCHOOL OF STUDIES IN PHYSICS AND ASTROPHYSICS
PT. RAVISHANKAR SHUKLA UNIVERSITY,
RAIPUR - 492010, CHHATTISGARH (INDIA)

Dr. Nameeta Brahme
M. Phil, Ph. D.
Professor & Head

Phone : (M) 96913-18995
: (O) (0771) 2262864
Email : namitabrahme@gmail.com

Ref. : 3026

Date : 13-07-2017

PLAGIARISM VERIFICATION REPORT

This is to certify that plagiarism check of the Ph.D. thesis submitted by **Mr. Subhajeet Karmakar** entitled **"Evolution of Magnetic Activities in Late-Type Stars"** has been carried out by **Pt. Sunder Lal Sharma Library of Pt. Ravishankar Shukla University, Raipur (C.G.) India**. On the basis of this report it has been found that the percentage of similarity is 0%, therefore no plagiarism was found.

Hence DRC recommends the thesis may be dispatched to the reviewers for further action.

Nameeta 13/07/2017

Chairman
Departmental Research Committee
SoS in Physics & Astrophysics
Pt. Ravishankar Shukla University, Raipur

CHAIRMAN,
Deptt. Research Committee,
SOS in Physics & Astrophysics,
Pt. R.S. University, R... (C.G.)

To,

My Loving Parents

“Each piece, or part, of the whole of nature is always merely an *approximation* to the complete truth, or the complete truth so far as we know it. In fact, everything we know is only some kind of approximation, because *we know that we do not know all the laws* as yet. Therefore, things must be learned only to be unlearned again or, more likely, to be corrected.

The principle of science, the definition, almost, is the following: *The test of all knowledge is experiment.* Experiment is the *sole judge* of scientific ‘truth’. But what is the source of knowledge? Where do the laws that are to be tested come from? Experiment, itself, helps to produce these laws, in the sense that it gives us hints. But also needed is *imagination* to create from these hints the great generalizations — to guess at the wonderful, simple, but very strange patterns beneath them all, and then to experiment to check again whether we have made the right guess.”

— RICHARD P. FEYNMAN,
“The Feynman Lectures on Physics”
(Volume 1, Chapter 1, Page 1)

Acknowledgments

It is a great joy to reach the first milestone of my research career, and I am deeply indebted to everyone who helped, supported, loved and guided me in this journey both personally and professionally. First of all, I would like to thank to my parents, my teachers, and the institutions I have studied, who/which helped me to reach at this platform.

I express my heartful respect and gratefulness to my supervisor Dr. Jeewan Chandra Pandey, who introduced me the very exciting fields of "Stellar astrophysics" and "X-ray astronomy". I am greatly inspired by his hardworking, and very thankful to him for the support and guidance on my way to become an independent researcher. He always pushed me to achieve my upperlimit and showed me the way several times to get out of difficult situations. I am very proud to be his first Ph.D. student.

It is my pleasure to thank all my collaborators and colleagues, including Drs. Igor S. Savanov (INASAN, Russia), G. Taş (EUO, Turkey), V. S. Airapetian (NASA GSFC, USA) for their contributions as well as sharing their knowledge through the comments and suggestions.

I like to express my heartful gratitudes and appreciations to the present and past directors of ARIES, viz. Dr. A. K. Pandey, Prof. Ram Sagar, and Dr. Wahab Uddin, for the continuous support, over all guidance, and the inspiration they have given during my Ph.D. I also sincerely acknowledge the moral support, scientific discussions, and constructive scientific criticisms I have received at different stages of my Ph.D. career from Drs. Brijesh Kumar, Indranil Chattopadhyay, Kuntal Misra, Santosh Joshi, Yogesh Joshi, M. Gopinathan, Manish Naja, Biman J. Medhi, S. B. Pandey, Alok Chandra Gupta, Amitesh Omar, D. V. Phani Kumar, Hum Chand, Manish Naja, han, Narendra Singh, Ramakant Yadav, Sneh Lata, Saurabh, U. C. Dumka, and M. Singh for the discussions on various issues.

My heartfully thanks to all of my past and present colleagues for the golden moments we have spent together. A special thanks to my research group members, viz Arti Joshi, Bharti Arora, and Manoj Patel for their useful discussions and active support several times during my Ph.D. I express my happiness and thanks to my friends Neha and Abhishek, my past room-mates Praveen and Vinit, my time-to-time office-mates Subhash, Krishna, Arti, Aditi, Sumit, Devesh, Shilpa, Priyanka, Ugam, and Vishi for spending those wonderful moments.

I also thank my seniors Subhash, Krisna, Rupak, Sumana, Tapas, Manoj, Arun, Sarvan, Ram Kesh, Brajesh, Ravi, Narendra, Tapaswini, Sumit, Rajiv, Subhash, Hema, Archana, Piyush, Alka, and Sravanti for always being ready to support in every aspects and caring as a family member. My loving and caring juniors and friends like Arti, Aabha, Mukesh, Aditi, Parveen, Bhaskar, Provakor, Gaurav, Pallavi, Vivek, Ansul, Jhilik, Inakshi, Aparna, Chayan, Baisakhi, Milan, Saikat, Vinit, Mridweeka, Raman, Nibedita, Anjasha, Piyali, Raya, Sapna, Pankaj, Kuldeep, Ashwini, Ekta, Navdip, Vidushi, Rakesh, Gaurav, Priyanka (Jalan), Tirthendu, Jayanand, Shilpa, Bharti, Krishan, Sadhna, Priyanka (Srivastava), and Alaxender also deserves to be acknowledged for the nice unforgettable moments they have shared with me during these years of Ph.D. I also acknowledge Pradip da, Abhijit da, and their family members for the pro-active help and support they have given during my Ph.D. years.

I heartily acknowledge ARIES, for being my home for all these years of Ph.D. I also acknowledge DST for funding me. Moreover, part of my research was funded by the Indo-Russian DST-RFBR project reference INT/RUS/RFBR/P-167 which is also sincerely acknowledged. This research is made with the ground-based as well as space-based observatories. I acknowledge the entire team of 2.0-m IUCAA Girawali Observatory telescope, 1.3-m Devasthal Fast optical telescope, 1.04-m Sampurnand Telescope, 0.36-m Goddard Robotic Telescopes, *Swift*, *XMM-Newton*, *Hipparcos*, *SuperWASP*, *ASAS* observatories and the NASA Exoplanet Archive, All Sky Automated Survey archive, *Hipparcos* archive, *Swift* archive facilities.

I am also thankful to all the ARIES staff and office employees who helped me several times at library, administration, computer section, account section, electrical section, civil and mechanical sections etc. The canteen staffs, the security guards and the gardeners at ARIES who made a very helping and pleasant environment at ARIES and hence also deserve to be acknowledged. A handful of thanks also goes to Prof. S. K. Pandey, Drs. N. Brahme, N. K. Chakradhari, and all the members of physics department of Pt. Ravishankar Shukla University, Raipur for their support. I also want to thank Mr. Goswami and Sheetal for all their support at Raipur.

Karmakar
16.07.2017
Subhajeet Karmakar

Abstract

Late-type stars with an similar internal structure to that of the Sun, supposed to operate a similar type of dynamo mechanism. However, the observations of these stars have introduced a range of stellar rotation periods, gravities, masses, and ages, which put into the debate on the existing magnetic dynamo theory. In order to provide useful constraints for the dynamo theory, in this thesis, we have investigated several magnetic activities such as the presence of dark spots on the surface, short- and long-term variations in spot-cycles, and flares on five active late-type stars with luminosity class V to IV. These active stars are LO Peg, 47 Cas, AB Dor, CC Eri and SZ Psc.

In order to carry out the observations, we have used several ground based observatories for observations in optical wavelength including 2-m IUCAA Girawali Observatory, 1.04-m ARIES Sampurnanand Telescope, and 0.36-m Goddard Robotic Telescope, and two space based observatories (*XMM-Newton* and *Swift*) for observations in X-ray and UV band. Using $\sim$24 yrs long multi-band data, we found that the activity of LO Peg does not remain constant through out the observations. We derive rotational period of LO Peg to be 0.4231 ± 0.0001 d. A long-term periodicity of $\sim$5.98 and $\sim$2.2 yr is also found to be present. We found that the surface of LO Peg rotates differentially showing solar-like SDR pattern with a period of $\sim$2.7 yr. The surface coverage of cool spots is found to be in the range of $\sim$9–26% in LO Peg. It appears that the high and low latitude spots are interchanging their positions. Quasi-simultaneous observations in X-ray, UV, and optical photometric bands show a signature of an excess of X-ray and UV activities in spotted regions.

A total of 164 flares including 20 optical flares and 144 X-ray flares are studied in this thesis. The optical flares are detected on LO Peg with a flare frequency of $\sim$1 flare per two days and with flare energy of $\sim 10^{31-34}$

erg. Using $\sim$11 years *XMM-Newton* data of AB Dor $\sim$140 X-ray flares are detected with a flare frequency of $\sim$4 flares per rotation (or $\sim$2 flares per solar day). Based on the light curve morphology, we have classified the flares on AB Dor into five category namely typical, double, multile, complex and slow-rise-top-flat flares. The e-folding rise (τ_r) and decay (τ_d) times of the flares are correlated with each other in the form of $\tau_d \propto \tau_r^{0.78\pm0.05}$, which is slight different from the theoritically obtained relation of $\tau_d \propto \tau_r^{0.5}$ with the assumption that the decay time equals to radiative cooling time.

We carried out time-resolved spectral analysis on a normal flare from main-sequence (MS) star 47 Cas, two superflares on MS binary CC Eri, and a large flare on evolved RS CVn type eclipsing binary SZ Psc. The flare on SZ Psc is found to be out of the eclipse. The coronal temperature, emission measure, and abundances are found to vary during the flares. The emission measures and global coronal abundances follow the same pattern as the light curve. The peak temperatures observed in the moderate flare from 47 Cas, two superflares from CC Eri, and the large flare form SZ Psc is found to be $\sim$73, 174, 128, and 204 MK, respectively. Whereas, The peak luminosity of these respective flares are found to be $10^{30.6}$, $10^{32.2}$, $10^{31.8}$, and $10^{33.6}$ erg s^{-1}. The peak abundances of the flares from 47 Cas and SZ Psc are found to be subsolar, wheras for both the superflares from CC Eri it is more than the solar value. This indicates higher amount of evaporation of the chromospheric materials within the flaring loop during the superflares. Using the hydrodynamic loop modeling, we derive loop-lengths of the flares of the order of 10^{10-11} cm. We found that the flaring loop-length for evolved stars are $\sim$100 times more than the loop-length of the MS stars with a $\sim$10–40 times larger coronal magnetic fields. In case of both the superflares on CC Eri, Fe Kα emission at 6.4 keV is also detected in the X-ray spectra and we model the Kα emission feature as fluorescence from the hot flare source irradiating the photospheric iron. The presnt investigations shows a higher level of magnetic activity in the evolved RS CVn type binary than both the normal flares and the superflares on MS stars. This could be due to their extended convection zone and tidal locking of binary components, which makes them rotate fast.

List of Publications

Refereed Journal

To be Submitted

1. "A very long and hot X-ray flare on an RS CVn type eclipsing binary SZ Psc".
__Karmakar, Subhajeet__; Pandey, Jeewan C., 2017, Monthly Notices of the Royal Astronomical Society, to be submitted **[IF[1] = 4.961]**

2. "*XMM-Newton* observations of AB Dor : X-ray flares".
__Karmakar, Subhajeet__ & Pandey, Jeewan C., 2017, Astrophysical Journal Suplimentary Series, in preperation **[IF = 11.257]**

Published

3. "X-ray Superflares on CC Eri".
__Karmakar, Subhajeet__; Pandey, Jeewan C.; Airapetian, V. S.; Misra, K, 2017, Astrophysical Journal, 840, 102 **[IF = 5.909]**

4. "LO Peg: surface differential rotation, flares, and spot-topographic evolution".
__Karmakar, Subhajeet__; Pandey, Jeewan C.; Savanov, I. S.; Taş, G.; Pandey, S. B.; Dmitrienko, E. S.; Joshi; S. Misra, K; Sakamoto, T.; Gehrels, N.; Okajima, T., 2016, Monthly Notices of the Royal Astronomical Society, 459, 3112 **[IF = 4.952]**

5. "Broad-band linear polarization in late-type active dwarfs".
Patel, Manoj K.; Pandey, Jeewan C.; __Karmakar, Subhajeet__; Srivastava, D. C.; Savanov, Igor S., 2016, Monthly Notices of the Royal Astronomical Society, 457, 3178 **[IF = 4.952]**

6. "Photometric Observations of LO Peg in 2014-2015".
Savanov, I. S. et al. 2016, Acta Astronomica, 66, 381 **[IF = 2.000]**

7. "An X-Ray Flare from 47 Cas".
Pandey, Jeewan C.; __Karmakar, Subhajeet__, 2015, Astronomical Journal, 149, 47 **[IF = 4.617]**

[1]IF = Impact Factor for the year of publication (see *http://www.scijournal.org/astronomy-journal-impact-factor-list.shtml* for further details.)

8. "Phase-resolved *XMM-Newton* and *Swift* Observations of WR 25".
*Pandey, Jeewan C.; Pandey, S. B.; **Karmakar, Subhajeet**, 2014, Astrophysical Journal, 788, 84* **[IF = 5.993]**

Conference Proceeding

1. "An F-type ultra-fast rotator KIC 6791060: Starspot modulation and Flares".
__Karmakar, Subhajeet__ and Pandey, Jeewan C., 2017, blrss, p-21 [The 1st Belgo-Indian Network for Astronomy and Astrophysics Workshop (BINA), Held 15-18 November 2016, ARIES, Nainital, India]

2. "*Swift* Observations Of CC Eri: X-Ray Superflare".
__Karmakar, Subhajeet__ and Pandey, Jeewan C., 2016, csss.confE, 144 [The 19th Cambridge Workshop on Cool Stars, Stellar Systems, and the Sun (CS19), Held 06-10 June 2016, Uppsala, Sweden]

3. "Flares In Time-Domain Surveys".
Kowalski, Adam et al., 2016, csss.confE, 126 [The 19th Cambridge Workshop on Cool Stars, Stellar Systems, and the Sun (CS19), Held 06-10 June 2016, Uppsala, Sweden]

4. "Long-term spot topography and multi-band flare analysis of active ultra-fast rotator LO Peg".
*Pandey, S. B., Pandey, Jeewan C., **Karmakar, Subhajeet**, Savanov, Igor S.; 2014, styd.confE, 155* [Proceedings of Swift: 10 Years of Discovery (SWIFT 10), Held 2-5 December 2014 at La Sapienza University, Rome, Italy.]

5. "Study of X-ray flares in AB Dor by *XMM-Newton*".
__Karmakar, Subhajeet__; Pandey, Jeewan C., 2014, cospar, 40E, 1403 [40th COSPAR Scientific Assembly. Held 2-10 August 2014, in Moscow, Russia]

6. "X-ray rotational modulation and coronal abundances of AB Doradus".
__Karmakar, Subhajeet__; Pandey, Jeewan C., 2013, ASInC, 9, 119 [31st ASI Meeting, ASI Conference Series, Held 20-22 February 2013, Thiruvananthapuram, India]

NOTATIONS AND ABBREVIATIONS

The most commonly used notations and abbreviations in the thesis are given below. If a symbol has been used in a different connection than listed here, it has been explained at the appropriate place.

Notations

Å	Angstrom
α, RA	right ascension
A_V	total absorptions in the visual magnitude
A	Amplitude
B	Magnetic Field strength
c	color-index
χ	Chi
cm	centi-meter
ct	coutns
c(t)	count rate as a function of time
d	distance to the star/cluster from earth in parsec (pc)
d	day/days
$^\circ$, deg	degree
δ, Dec	declination
D_n	duration
$\mathrm{E}_{tot,X}$	Total energy
E_H	Heating rate per unit volume
F_x	X-ray Flux
F_{rad}	Radio Flux
F_{lm}	Local mean flux
Fe_t	Intregated excess flux
$\mathrm{F}_{K\alpha}$	Flux of Fe Kα
f	filling factor
g	Surafce gravity of the star
hr	hours
H	Heating rate
Hz	Hertz
H_m	Maximum height

I	Cousin I band magnitude
i	Inclination of object
$J2000$	epoch of observation
Jy	Jansky
k	Boltzmann constant
K	Kelvin
K_λ	extinction coefficient
kpc	kiloparsec (unit of distance)
keV	kiloelectron volt
kG	Kilo Gauss
eV	kiloelectron volt
ks	kilosec
kg	kilogram
km	kilmeter
L	Loop-length
L_{bol}	Bolometric Luminosity
L_{rad}	Radio Luminosity
L_X	X-ray Luminosity
$L_\odot$	Solar Luminosity
L_*	Luminosity of star
L_{rad}	Radio Luminosity
$L_\odot$	Solar Luminosity
L_{pb}	Magnetic loop length
λ	wavelength
L_{qs}, L_{ha}, L_{hd}, and L_{hr}	Half loop length
m	apparent visual magnitude
M_V	absolute visual magnitude
Myr	million Years
M_{bol}	Absolute bolometric magnitude
M_V	Absolute V band magnitude
$M_\odot$	Mass of Sun
M_*	Mass of star
mcrab	milliCrab
mag	magnitude
n_H	Hydrogen Column density

n_e	Electron density
nm	nanometer
p	pressure
P	Period
P_{rot}	Rotational Period
pc	parsec
π	Parallax
P(T)	Plasma emissivity
Ψ	Active longitude region
R_0	Rossby number
$'$, arcmin	arc minute
$''$, arcsec	arc second
mG	Milli Gauss
MK	Million Kelvin
mM	Mega Meter
ms	millisec
μ	Mean molecular weight
μG	micro Gauss
μm	micro meter
n_c	Pre-flare density
ω	Angular velocity
Ω	Diferential Roattion
R	Cousin R band magnitude
r_c	core radius
r	radius
R_V	Radial velocity
S_p	Spottedness
T_e	Electron tempearture
t_0	Characteristic time constant
$R_\odot$	Sun's radius
R_*	Star's radius
σ	Standard deviation
T	Temperature
T_{max}	Maximum Temperature
t_{pk}	Time at falare peak

$T_{\rm eff}$	Effective temperature
τ	optical depth
τ_c	Convective turnover time
τ_r	e-folding rise time
τ_d	e-folding decay time
τ_A	Alfven time
U	Johnson U band magnitude
V	Johnson V band magnitude
V_W	*SuperWASP* V band magnitude
V_H	*Hipparcos* V band magnitude
v_A	Alfven velocity
W	Watt
X	air mass
yr	year/years
Z	Solar metallicity
τ_{rad}	radiative cooling time
τ_{cond}	conductive cooling time
τ_{th}	thermodynamic scale of decay time
τ_r	Reconnection rate
θ	Astrocentric angle
$Z_\odot$	Solar abundances

Abbreviations

2MASS	Two Micron All-Sky-Survey
47 Cas	47 Cassiopeia
AB Dor	AB Doradus
APEC	Astrophysical Plasma Emission Code
ARIES	Aryabhatta Research Institute of observational SciencES
ASAS	All Sky Automated Survey
BAT	Burst Alert Telescope
BC	Bolometric correction
BY Dra	BY Draconis
CABS	Chromospherically Active Binary System

CCD	Charge Coupled Device
CC Eri	CC Eridani
CMD	Colour-Magnitude Diagram
CTTS	Classical T-Tauri stars
CVs	Cataclysmic Variables
CZ	Convective Zone
dble	double flares
DOF, dof	Degree of freedom
DR	Differential Rotation
DSS	Digitized Sky Survey
EPIC	European Photon Imaging Camera
ESA	European Space Agency
ESO	European Southern Observatory
ESS	Einstein Slew Survey
EM	Emission Measure
EUO	Ege University Observatory
EUV	Extreme Ultraviolet
EXOSAT	European X-ray Observatory Satellite
EW	Equivalent Width
FAP	False Alarm Probability
FIR	Far Infrared
FK Com	FK Comae Berences
FOV, FoV	Field of view
FR Cnc	FR Cancri
FUV	Far Ultraviolet
FWHM	Full Width at Half Maximum
GOES	Geostationary Operational Environmental Satellite
GRT	Goddard Robotic Telescope
GSFC	Goddard Space Flight Center
GSC	Gas Slit Camera
GHz	Giga Hertz
GYr	Giga year
HD	Henry Draper Catalogue
HR	Hertzsprung-Russell
IGO	IUCAA Girawali Observatory

IGT	IUCAA Girawali Telescope
IIA	Indian Institute of Astrophysics
IMF	Initial Mass Function
IR	Infra-Red
IRAF	Image Reduction and Analysis Facility
IRAS	Infrared Astronomical Satellite
ISM	Interstellar Matter/Medium
IUCAA	Inter University Center for Astronomy and Astrophysics
Jy	Jansky
JKT	Jacobus Kapetyn Telescope
K-S	Kolmogorov-Smirnov
LO Peg	LO Pegasi
MAXI	Monitor of All-sky X-ray Image
MEKAL	Mewe-Kaastra-Leidahl
MIR	Mid-infrared
mJy	milli-Jansky
MS	Main-Sequence
MSSL	Mullard Space Science Laboratory
Myr	Million year
MOS	Metal Oxide Semi-conductor
MS	Main-sequence
NGC	New General Catalogue
NIR	Near Infra-red
OAB	Brera Astronomical Observatory
OBFs	Optical Blocking Filters
ODF	Observation Data Files
OM	Optical Monitor
PD	Photo-Diode
PMS	Pre-Main-sequence
PHOT	Photometry
PMS	Pre-Main Sequence
PSC	Point Source Catalog
PSF	Point Spread Function
PSPC	Position Sensitive Proportional Counter

RASS	ROSAT All-Sky Survey
ROSAT	ROntgen SATellite
RS CVn	RS Cannum Venaticorum
RGB	Red Green Blue
RGS	Reflection Grating Spectrometer
SAS	Science Analysis System
SDR	Surface Differential Rotation
SED	Spectral Energy Distribution
SIMBAD	Set of Identifications, Measurements, and Bibliography for Astronomical Data
SOHO	Solar and Heliospheric Observatory
srf	Slow rise top flat flares.
SSC	*Spitzer* Science Center
ST	Sampurnanand Telescope
SuperWASP	Super Wide Angle Search for Planets
SZ Psc	SZ Pisces
TT	T-Tauri
TTS	T Tauri Star
typ	typical flares
UV	Ultraviolet
UVOT	UV/Optical Telescope
XMM-Newton	X-ray Multi-Mirror Mission
WT	Windowed-Timing mode
WTTS	Weak-line T-Tauri stars
W UMa	W Ursa Majoris (W UMa)
XRT	X-ray Telescope
ZAMS	Zero-Age-Main-Sequence

Contents

List of Figures

List of Tables

Chapter 1

Introduction

In the early 20^{th} century, stars were assumed to be powered by the gravitational contraction, as a consequence, they were thought to start their lives as very hot "early-type" stars, and as they evolve they gradually cool down into "late-type" stars. However, by the discovery of the fact that the stars are powered by nuclear fusion instead of gravitational contraction the model was rendered obsolete, but the names persisted due to historical reason. The cool stars with spectral type F, G, and K are still called the late-type stars. These stars also have similar internal structure to that of the Sun (a G-type star), i.e. an outer convective envelope above a radiative interior with an interface known as "tachocline". According to the current understanding, the magnetic field in the Sun is supposed to be generated by a naturally occurring dynamo mechanism operating inside the Sun. The magnetic field is also associated with several magnetic activities. The common observational evidences of these magnetic activities are surface inhomogeneities due to the presence of dark spots, short- and long-term variations in spot-cycles, and flares.

Stars with a similar internal structure to that of the Sun are also expected to show the solar-type dynamo operation. However, the observations of these stars with a ranges of rotation periods, gravities, masses, and ages have introduced a debate on the magnetic dynamo. Therefore, the investigations of these stars are necessary both in observational and theoretical aspects. The goal of this thesis is to investigate the evolution of magnetic activities such as the temporal evolution of surface inhomogeneities, surface differential rotations (SDRs), and flares on few late-type main sequence (MS) as well as evolved stars in order to provide important constrains in the existing dynamo theory.

In this chapter, I will briefly review the current understanding of the topic taking into account of the dynamo mechanism and different observational evidences of the stellar activities. At the end of the chapter, I describe aim and objectives of the thesis.

1.1 Late-type stars

The late-type stars (excluding the Sun) are not spatially resolved with the naked eye and the ground/space based observatories. Our basic understanding of the late-type stars are developed on the basis of the nearest late-type star Sun. This provides a very important advantage to the stellar astronomers, that due to its proximity it became an ideal object, that we can observe at high spatial and angular resolution. Therefore, before getting started with the discussion of the late-type stars here I briefly discuss about the Sun.

1.1.1 The Sun: The nearest late-type star

The Sun is the nearest star with an age of 4.5 billion years and spectral type of G2V. The Sun has a mass of $M_{\odot} = 1.99 \times 10^{30}$ kg, a radius of $R_{\odot} = 696$ Mm, a luminosity of $L_{\odot} = 3.85 \times 10^{26}$ W, and an effective temperature of $T_{\rm eff} = 5780$ K (Phillips, 1992). It was formed by the gravitational collapse of an interstellar gas cloud. While on the main sequence, its energy is supplied by the hydrogen fusion reactions in the core. When this reaction will cease (after $\sim 10^{10}$ years), the Sun will progress to the red giant phase. Red giants are larger, more luminous stars, of spectral type K or M, with lower effective surface temperatures. After another 150 million years, the red giant sheds its outer layers to form a planetary nebula (a ring-shaped nebula formed by an expanding shell of gas around the aging star), and leaving behind the core, becoming a compact object known as a white dwarf.

The current Sun shows variety of magnetic activities (Priest, 2000). The solar magnetic flux distribution can give rise to the dark spots on the surface of the Sun, also known as the sunspots, which cover up to 0.5% of the Sun's surface (Deng et al., 2016). The Sun follows an approximately 11 year activity cycle during which it returns to its minimum activity. The polarity of the global magnetic field is also reversed during a sunspot cycle. The smallest solar flares observed in the active region of the Sun lasts for only approximately tens of seconds and amounts to energy of $\sim 10^{26}$ erg (Hannah et al., 2008). Whereas in active Sun, large solar flares are found to be of the order of 10^{33-34} erg (Kane et al., 1995, 2005).

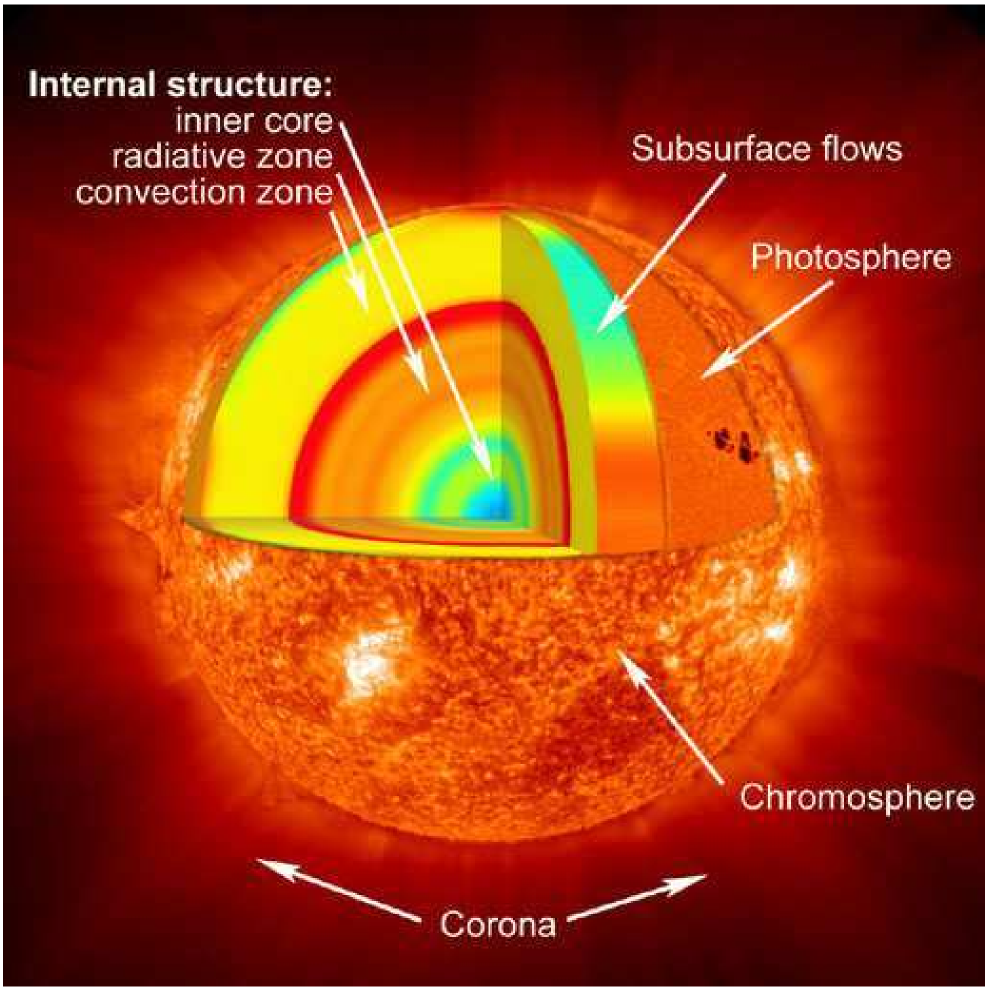

Figure 1.1: A cut away schematic view of the Sun (*courtesy of NASA*). The solar core is the source of energy, where fusion heats plasma up to $\sim$ 15 MK. Radiative diffusion transports the energy from the core in the radiative zone, out to 0.7 $R_{\odot}$. The convection zone is heated from the base of the tachocline, allowing convective currents to flow to the photosphere, the visible surface of the Sun. Temperatures rise from $\sim 10^3$ K in the photosphere to $\sim 10^4$ K in the chromosphere, then rise rapidly in the transition region to over 10^6 K in the solar corona.

1.1.2 The internal structure

The interior of the Sun/star cannot be directly observed since the stellar atmospheres become optically thick within a very shallow depth. At present, the only means to probe the interior of stars is by using seismic information, characterizing the propagation of waves throughout the stellar interior to infer the radial density profile and rotation structure. Late-type stars are also thought to have a solar-like internal structure, which consists of three main parts – an outer convective envelope, a radiative interior, and the core. Fig. 1.1 shows the inner structure of the Sun.

In the inner core, nuclear fusion of hydrogen into helium accounts for the energy source (extent to $\sim$0.25 $R_\odot$, temperature of $\sim$15 MK, and density of 1.6 $\times 10^5$ kg m^{-3}). The fusion produces a strong pressure, which acts against the gravity, so that the stellar core does not collapse. The dominant process is the proton-proton chain reaction, which provides 99% of the star's energy. This process is less sensitive to the core temperature, and less efficient at burning hydrogen than the CNO cycle found operating in higher mass stars, and as a result low-mass stars have long lifetimes on the main sequence, from $\sim 10^{10}$ years in G dwarfs to more than 10^{12} years for M dwarfs.

From the core, the energy is transported via radiation core out to a radius of $\sim$0.7 $R_\odot$ called the radiation zone. The temperature in this zone drops to $\sim$5 MK, with the radiation field closely approximated by a black body. The radiation zone is very dense which causes the pressure waves tend to occur standing waves. Although, there are only a few possibilities to observe the structures and dynamics in these regions. The radiation zone is well known to rotate as a solid body.

At the outer layer of the radiation zone, the temperature rate is steep enough that the convection acts as the primary medium of the energy transport. The motion of the plasma occurs with the formation of convective cells. The sizes of the convective cells are comparable with the local pressure scale height, which are in general quite big in the lower part and become smaller near the surface of the star, where they form granules. The Schwarzschild criterion (Schwarzschild, 1906) indicates that the convection is likely to occur, when the radial gradient of the temperature is greater than the adiabatic temperature gradient. In the standard picture of the solar/stellar magnetic dynamo, the interface between the convective and the radiative zones is called the "tachocline". It is where the Sun's magnetic field is strengthened and organized. The shearing from the differential rotation and the convective layer is also important and discussed in detail in Section 1.2.1. For the Sun, the convection zone extend from $\sim$0.713 $R_\odot$ to the surface (Kosovichev & Fedorova, 1991). The convective zone extends much deeper into the stellar interior for later spectral types (from F- to M-type dwarfs) i.e. with the decreasing stellar mass, until the stars become fully convective throughout their entire interiors at a mass around 0.35 $M_\odot$ (spectral type M3–M4) (e.g. Reiners & Basri, 2009).

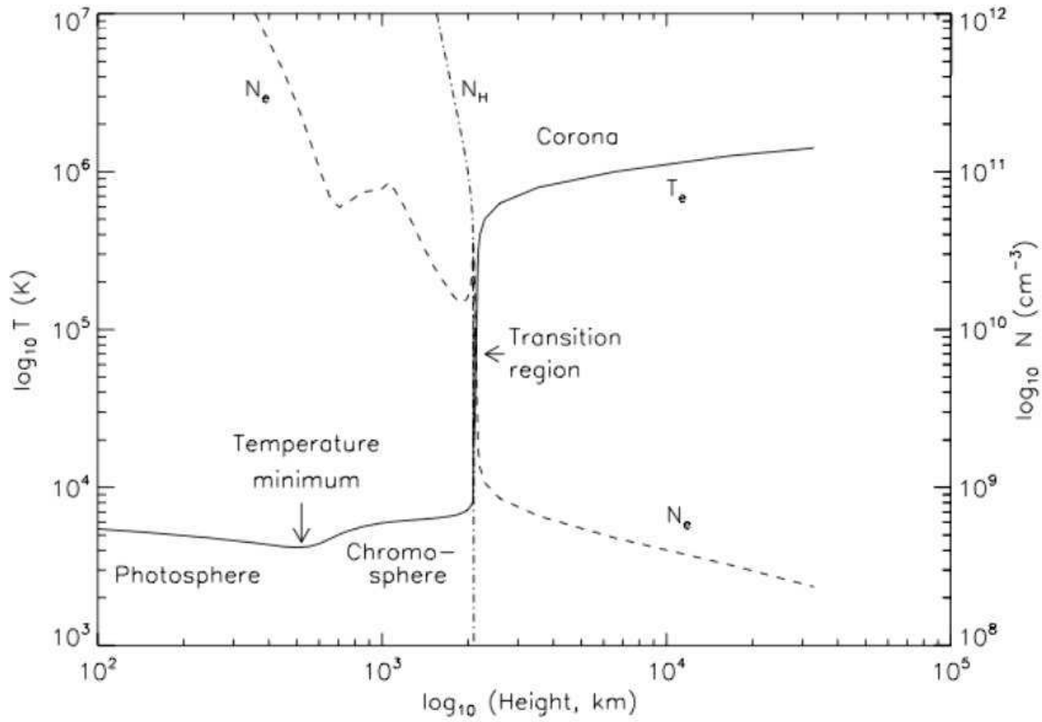

Figure 1.2: Variation of solar electron temperature, electron density, and neutral Hydrogen density as a function of height. [Adopted from the modified figure by Phillips et al. (2008), based on the 1D model calculations by Vernazza et al. (1981)].

1.1.3 The atmosphere

The visible solar/stellar atmosphere lies above the convective zone and can be divided into four layers: the photosphere, chromosphere, transition-region and corona. Fig. 1.2 illustrates how the temperature and density varies with height above the solar surface. The photosphere is one of the constituent parts of solar outer atmosphere and has a negative temperature gradient. It is a thin ($\sim$ 100 km), dense layer of plasma that emits the major part of solar radiation. The gas density in this area is $\approx 10^{17} cm^{-3}$ (Priest, 1984), where the peak photospheric temperature is 6600 K (decreasing to 4300 K at the temperature minimum where photosphere joins the chromosphere). The chromosphere is less dense than the photosphere and extends to about 2500 km above the photosphere. This region is more transparent with temperatures rising monotonically up to 10^5 K, where the transition-region begins. The chromosphere emits in the ultraviolet and is also detected via narrow bands of emission in optical photospheric line profile. The transition region is a thin region above the chromosphere, where temperatures rise rapidly, from about 20000 to a few million K. This region is characterised by a steep positive temperature gradient. Finally, the corona is the outermost area, extended out to several solar radii with temperature of $\sim 10^6$ K. It can be detected at extreme ultraviolet and X-ray wavelengths.

1.2 Magnetic fields in late-type stars

1.2.1 Stellar dynamo mechanism

Stellar magnetic fields are measured directly through the Zeeman effect (see Landstreet, 1992, for a review) or are detected indirectly through chromospheric and coronal emissions associated with the magnetic activity (see Schrijver, 1991). In the outer convective envelop of the stellar interior the energy is transported by the motion of the plasma forming the convection cells, which could build up certain current that can maintain the magnetic field of the star (first prposed by Larmor, 1919, in case of the Sun). As the star rotates the plasma rotates differentially where the surface at the equator rotates much faster than the poles (respectively 27 d to 35 d in case of the Sun), whereas the base of the convection zone, i.e. the tachocline, rotates as a rigid body (with a period of 30 d for the Sun). These conditions cause a strong shearing and rotation force on the fluid. Parker (1955) made a breakthrough by averaging over the complicated non-axisymmetric components of the solar magnetic fields, and showed that the solutions favor the concept of a dynamo operating in the Sun. Steenbeck et al. (1966) introduces "mean-field" dynamo theory by referring to a model that only predicts large scale magnetic features, which are necessarily much larger than the surface turbulence size scales or individual sunspots. This theory is the simplest and most popular dynamo theory used to explain magnetic field properties of the Sun as well as stars. Although, this is not the only model used to study the Sun (see Charbonneau, 2005), it also gives an excellent framework to understand the global properties of the solar/stellar dynamo.

According to the mean filed theory, before the onset of a new starspot cycle, the magnetic field is approximated to be a dipole field symmetric about the rotation axis, i.e. a pure poloidal field as shown in left panel of Fig. 1.3. The differential rotation converts an existing dipolar field of the Sun/star into an almost fully toroidal one. This effect is known as the Ω effect, after the Greek letter Ω is commonly used in physics to represent rotation. The sub-surface toroidal magnetic flux tubes, while begins to rise towards the surface due to a buoyant force exerted from the

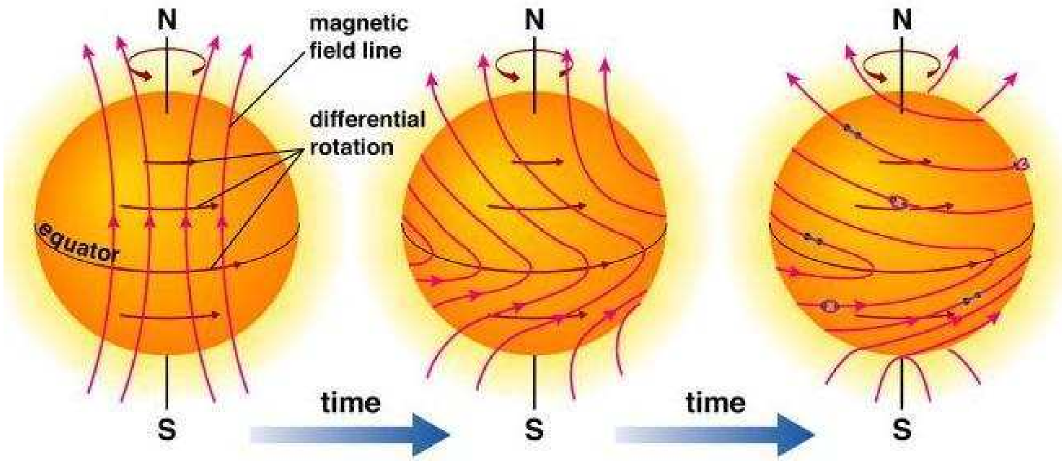

Figure 1.3: Illustration of the α–Ω effect that is the source of the solar magnetic field, beginning with a poloidal field on the left, winding up towards a toroidal field in the middle, and the emergence of complex active regions on the right (Carroll & Ostlie, 2006).

surrounding gas, become distorted, twisted (also called "helicity"), and more complex in shape under the effect of the rotation of stellar material. This is known as the α effect because of the resulting twisted shape of the magnetic field lines at the stellar surface resembles the Greek letter α and shown in the middle panel of Fig. 1.3. These flux tubes pierce the photosphere and hinders its temperature almost 1000 K below from that of the surrounding creating starspot pairs with opposite polarity at the footpoints of their emergence (see right panel of Fig. 1.3). This twisting in the flux tube also produces a latitude dependent tilt of the starspot pair due to the winding the surface magnetic field by differential rotation. The inclination of the tilt becomes more prominent with increasing latitude of the spot pair. This phenomenon is known as Joy's law, and is a critical component of the famous Babcock–Leighton mean-field solar dynamo model (Babcock, 1961; Leighton, 1964). Although most of the small magnetic features or the spots neutralize each other, a small fraction migrate to the poles via surface meridional flow. This helps to build up magnetic flux at the stellar poles which is preferentially of the opposite polarity from the initial dipolar field. Thus the toroidal magnetic field converts gradually back to a poloidal field, which allows the process to begin again.

The combination of the differential rotation, the convectively driven helicity, and the presence of a tachocline interface region work together at the star to operate the $\alpha - \Omega$ dynamo. The tachocline region creates additional shear and store the toroidal fluxtubes until the buoyant forces are strong enough to make them rise towards the surface. Now a days lots of observations are present which successfully explained the solar/stellar magnetic activities within this theoretical framework.

In the case of low mass stars, the convective zone extends much deeper into the stellar interior until the late M-dwarfs the stars are fully convective. This means that, due to the lack of tachocline interface region, the $\alpha - \Omega$ dynamo likely cannot function, instead the α^2 dynamo is thought to operate. The α^2 dynamo relies on the convective turbulence to convert from toroidal to poloidal magnetic flux and vice versa (Brandenburg & Subramanian, 2005). These stars are predicted to have less differential rotation both on and below the surface. The dynamo is thought to be driven by the convection that dominates the stellar interior (Durney et al., 1993). In these stars, the Ω effect may also contribute to the global or mean magnetic fields. So the possibility of an $\alpha^2 - \Omega$ dynamo cannot be ruled out. According to this dynamo, the rotation and the convection both play dominant roles, whereas weak differential rotation helps to organize the large scale magnetic field. However, the specific nature of the α effect, whether it is driven by convective cell motions throughout the envelope, or through the Coriolis force acting on the flux tubes due to the stellar rotation, is still debated (Charbonneau, 2005). The surface morphology of magnetic fields produced by an α^2 dynamo are still debated. Many simulations have shown that an α^2 dynamo will produce non-axisymmetric surface magnetic fields for even modest rotation rates (e.g. Chabrier & Küker, 2006). However, other models show that the weak differential rotation is present in fully convective stars, and that these dynamos still possess significant axisymmetric magnetic fields (Browning, 2008).

1.2.2 Stellar rotation–activity relation

Stellar rotation plays a key role in both the $\alpha - \Omega$ and α^2 dynamo through the α-effect. For both the dynamo models, a faster rotation is linked to a larger total magnetic field strength (Browning et al., 2010), and therefore, it exhibits a strong correlation with the magnetic activity and X-ray luminosities (L_x; Pallavicini et al., 1981). The young main-sequence stars rotate fast, and as the age increases, they slow down due to the loss of angular momentum by the magnetic stellar wind. Therefore, magnetic activity is also anti-correlated with age. The dynamo efficiency also depends on the depth of the convection zone, which usually increases for the late-type star with the age. The magnetic activity is therefore often been correlated with the Rossby number (R_0) instead of the rotation period, where the Rossby number is defined as the ratio between the rotation period (P_{rot}) and the convective turnover

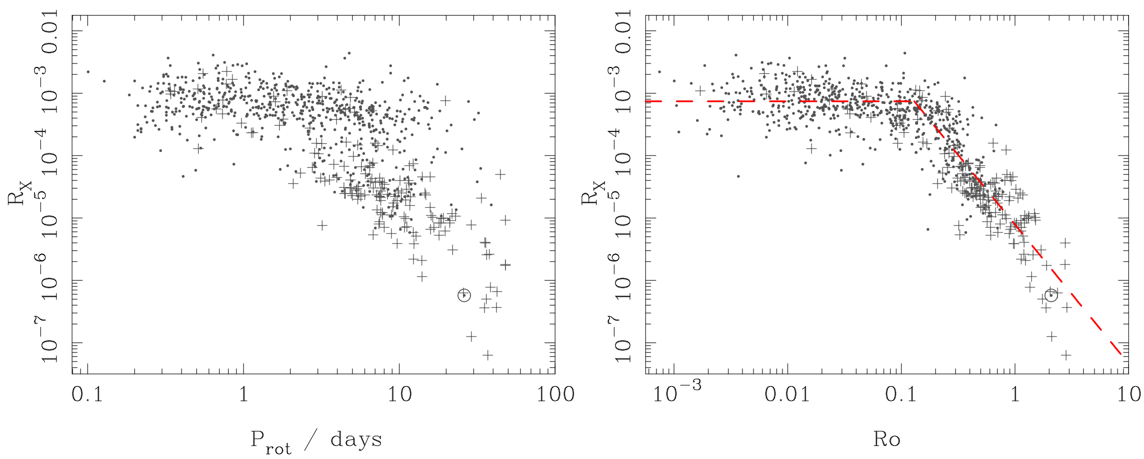

Figure 1.4: X-ray to bolometric luminosity ratio plotted against rotation period (left panel) and the Rossby number, $R_0 = P_{rot}/\tau$ (right panel).

time (τ_c) i.e. $R_0 = P_{rot}/\tau_c$. The overall rotation-activity relation was perhaps best clarified by using large samples of stars from stellar clusters. The comprehensive diagram in Fig. 1.4 clearly shows a regime where $L_X/L_{\rm bol} \propto Ro^{-2}$ for intermediate and slow rotators (Randich, 2000). However, in fast rotators L_X appears to become a unique function of $L_{\rm bol}$, $L_X/L_{\rm bol} \approx 10^{-3}$ regardless of the rotation period (Agrawal et al., 1986; Fleming et al., 1988; Pallavicini et al., 1990). The tendency for a corona to "saturate" at this level once the rotation period (or the Rossby number) is sufficiently small, or v sufficiently large, was identified and described in detail by Vilhu & Rucinski (1983), Vilhu (1984), Vilhu & Walter (1987), and Fleming et al. (1989). It is valid for all classes of stars but the onset of saturation varies somewhat depending on the spectral type. Once MS coronae are saturated, L_X also becomes a function of mass, colour, or radius simply owing to the fundamental properties of MS stars.

1.2.3 Magnetic fields in the stellar coronae

The structures, dynamics, and most of the features of the solar/stellar coronae are caused and dominated by the magnetic field. Since the ratio of the plasma pressure to the magnetic pressure (also known as "plasma-β") is very low, the motions of the plasma follow the magnetic field lines. This results in the formation of the coronal loops, where the heat conduction along the field lines is very efficient, however, it is strongly suppressed perpendicular to the loop. The footpoints of the coronal magnetic fields lie in the photosphere and move around by the granulation, which

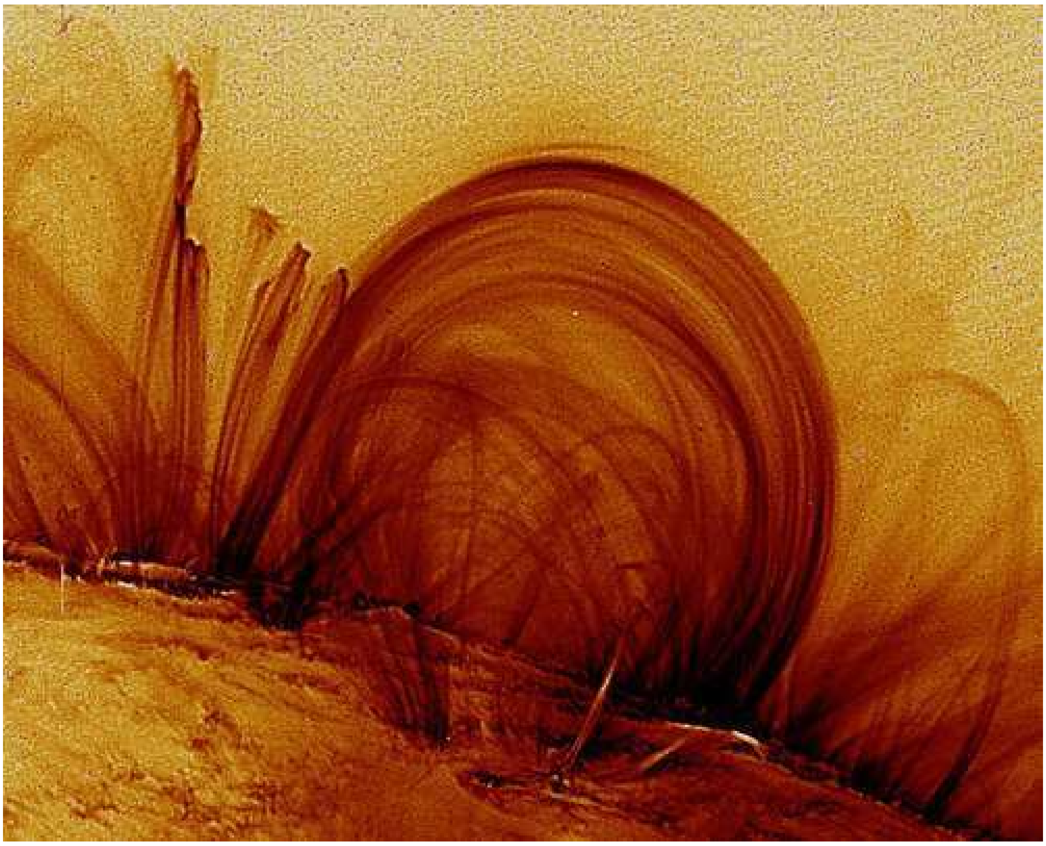

Figure 1.5: Image of a coronal loop observed with the TRACE satellite in 171 Å pass band. This filter corresponds to a temperature of one million Kelvin. The height of the loop is roughly 70 Mm.

are convective motions in the photosphere. Due to these motions, the magnetic field lines get twisted and interlinked. When the twisted and interlocked magnetic field lines reconnect, they release a large amount of energy to the corona as a result coronal heating and features like flares and CMEs can occur. The direct observation of the magnetic field is very difficult even in the solar corona. One can only observe the coronal emissivity coming from the magnetic field lines as shown in Fig. 1.5. However, with this method, one can get a qualitative idea about the magnetic field line structure. A much efficient method for estimating the magnetic field is the force-free extrapolation techniques (see Sakurai, 1981; Wiegelmann, 2008; Woltjer, 1958). In the stellar case, since the coronal magnetic loops are not even resolvable, the only way to estimate the coronal magnetic field strength by studying different magnetic activities in X-rays as the coronal emission is detectable in these wavebands.

The magnetic loops emerges from the stellar surface, traps and heats a tenuous coronal plasma to millions of degrees, which then emits X-rays. The mechanism by which the X-rays are emitted from the coronal plasma is 'Thermal Bremsstrahlung'. The L_x of the active late-type stars ranges from 10^{29} to 10^{32} erg s^{-1}, which is 10^{2-5} times more than the L_x of the Sun. However, free-free emission, gyroresonance, and gyrosynchrotron emission is responsible for the radio emission from the stellar corona. The radio luminosity of late-type active stars ranges from 10^{14-17} erg s^{-1} Hz^{-1} (Drake et al., 1989, 1992; Güdel, 1992). For late-type stars radio luminosity appears to be tightly and linearly correlated with L_x (Gudel et al., 1993; Pandey, 2006).

1.3 Stellar magnetic activities: The observable evidences

The stellar dynamo produces the magnetic field which in turn drives various activities on the stellar surface and also in its atmosphere. In this section, I have given a brief description of the different magnetic activities observed on the Sun as well as the stars. Some of the magnetic activities are produced due to the surface inhomogeneities and observed over a longer period of time, whereas others are transient in nature occur due to local magnetic events in the photosphere, chromosphere, or corona.

1.3.1 Starspots: The surface inhomogeneities

The cool regions on the stellar surface, which are due to local strong magnetic field appears darker than the surrounding of the photosphere are known as the starspots. These flux tubes appear as the magnetic loops in the upper atmosphere, and the footpoints of the loops form a pair of spots with a N – S magnetic dipole on the surface.

Our understanding about the starspots are developed on the solar analogy. Left panel of Fig. 1.6 shows the spots on the surface of the Sun. The sunspots are characterized by two concentric regions, which are shown in right panel of Fig. 1.6. The central region of a sunspot is known as the umbra, and is the darkest portion of the sunspot, with a typical temperature contrast of ∼1700 K with photosphere (Berdyugina, 2005). This is the area where the magnetic flux tubes are aligned nearly vertically, and create the greatest inhibition of convection. The outer portion of the spot is known as the penumbra, which surrounds the entire umbra. The

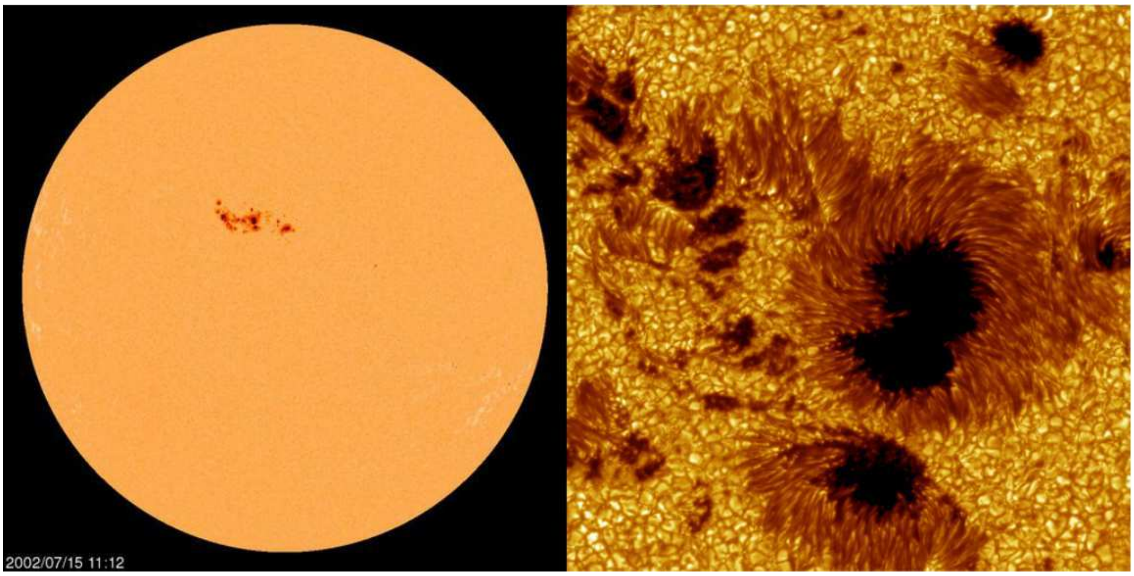

Figure 1.6: Left shows a full-disk SOHO/MDI continuum image of NOAA AR 10030 on2002 July 15. Right shows a zoom-in of this region using observations from the Swedish Solar Telescope. Images are courtesy of SOHO (NASA & ESA) and the Royal Swedish Academy of Sciences.

penumbra appears lighter than the umbra, though still darker than the photosphere with a temperature contrast of ∼750 K. Here the magnetic flux tubes are more inclined towards the photospheric surface. The relative coolness of the spatially resolved sunspots is evident by the existence of absorption bands of TiO molecules which would normally be disassociated at photospheric temperatures (Tandberg-Hanssen, 1967).

Spots on the surface of the distant stars cannot be spatially resolved. Instead we infer their presence by variations in the brightness of the star over the time. This idea of the light variations in the stars was initially proposed by Kron (1947), however extensive study in this field was statred after the work of Hall (1976). Dark spots move across the stellar disk due to the stellar rotation and thus modulate the total brightness with the rotational period of the star which in turn allow us to derive the stellar rotational period. A schematic diagram to show the variability mechanism is shown in Fig. 1.7. This results in periodic modulations in the stellar light curve, which are larger in amplitude if the starspots are larger or darker (Strassmeier, 2009).

Starspots on tidally synchronized binaries have been observed to display additional modulations at a period close to the binary revolution period. Starspots are also known to affect the light curves of eclipsing binary systems, causing the eclipse

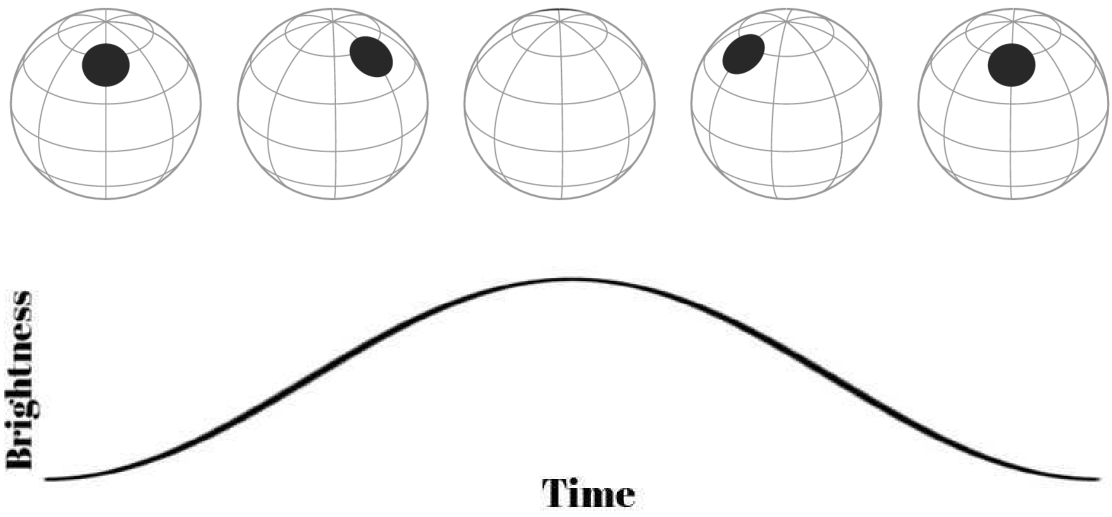

Figure 1.7: A schematic diagram to the show the rotational variability in brightness due to the inhomogeneities (cool spots) on the surface of a star.

depths to be asymmetric or to change over time as the spots evolve. Photometric data indicating brightness modulations due to starspots dates back almost 70 years; they were first discovered on RS CVn type eclipsing binary systems that had very high amplitudes of magnetic activity (Kron, 1947, 1950).

The spots on the stellar surface have been imaged by using a variety of techniques like Doppler imaging (Vogt & Penrod, 1983b) and interferometric technique (Parks et al., 2011). However, high-resolution spectroscopic observations with a high signal-to-noise ratio and a good phase coverage as required for Doppler imaging are limited. Further, the Doppler imaging technique can only be applied for fast-rotating stars with low inclination, whereas, the interferometric technique can be used for nearby stars of large angular size. The vast majority of spotted stars cannot be imaged with either of these techniques. Therefore, long-term traditional photometric observations are important to understand the active region evolution and the stellar activity cycles (e.g. Järvinen et al., 2005a; Oláh et al., 2009; Roettenbacher et al., 2013). Since a light curve represents a one-dimensional time series, the resulting stellar image contains information mostly in the direction of rotation, i.e., in the longitude, rather than spot size and locations in the latitude (Savanov & Strassmeier, 2008). Although the projection effects and limb darkening allow the inversion technique to recover more structures than is obvious at first glance.

1.3.2 Spot cycles

Although, the sunspots were discovered by Galileo Galilei 400 years ago, a oscillation behavior in the numbers of sunspots was first discovered by Schwabe (1844). This cycle has a maximum in every 11 years which is followed by a minimum. But the origin of the cycle was not clearly understood until Hale (1908) discovered the existence of magnetic field in sunspots. According to the modern dynamo theory (see § 1.2.1), due to the surface meridional flow on the Sun/stars, the photospheric spots migrate towards the poles, and the magnetic flux is deposited from the spot pairs with one polarity preferentially changes to the opposite to that of the poles. Over the time, this opposite polarity builds up, and gives rise to the 11-years periodic magnetic polarity reversal. In Fig. 1.8, the time evolution of the emergence of sunspots according to their average sunspots number, latitude, and average sunspots area are displayed.

Many of the active stars also show evidence of a long term variation in the light amplitude and in the mean light level of their light curves that could be similar to the 11 years solar activity cycle (Evren, 1990; Ibanoglu, 1990; Rodono, 1981). Hall (1990), Dorren & Guinan (1990), Henry et al. (1995), and Messina & Guinan (2003) found cyclic alternating changes in the orbital periods of active binaries and concluded that this may be due to the solar type magnetic cycle. The change in the orbital periods of close binaries is due to the variation of gravitational acceleration of the companion star, which is induced by a change in angular momentum and the magnetic field distribution (Lanza et al., 1998). Single late-type stars also show the activity cycles. Järvinen et al. (2005b) found 20 years spot cycle in a single active star AB Dor (K0V; P=0.51479d). Henry et al. (1995) have proposed other indicators of activity cycle, i.e. the modulation of mean colour indexes.

1.3.3 Surface differential rotation

Surface differential rotation (SDR) and its dependence on the global stellar properties are very important as it is one of the key ingredients of the dynamo theory in the generation and sustainment of stellar magnetic fields. These are thought to be responsible for all the activity phenomena observed in late-type stars (see e.g. Catalano et al., 1999; Guinan & Dorren, 1992; Rodonò, 2000). Moreover, observational studies of the SDR are fundamental since they provide empirical relations which allow us to test dynamo theories. They are also indicative of the conditions

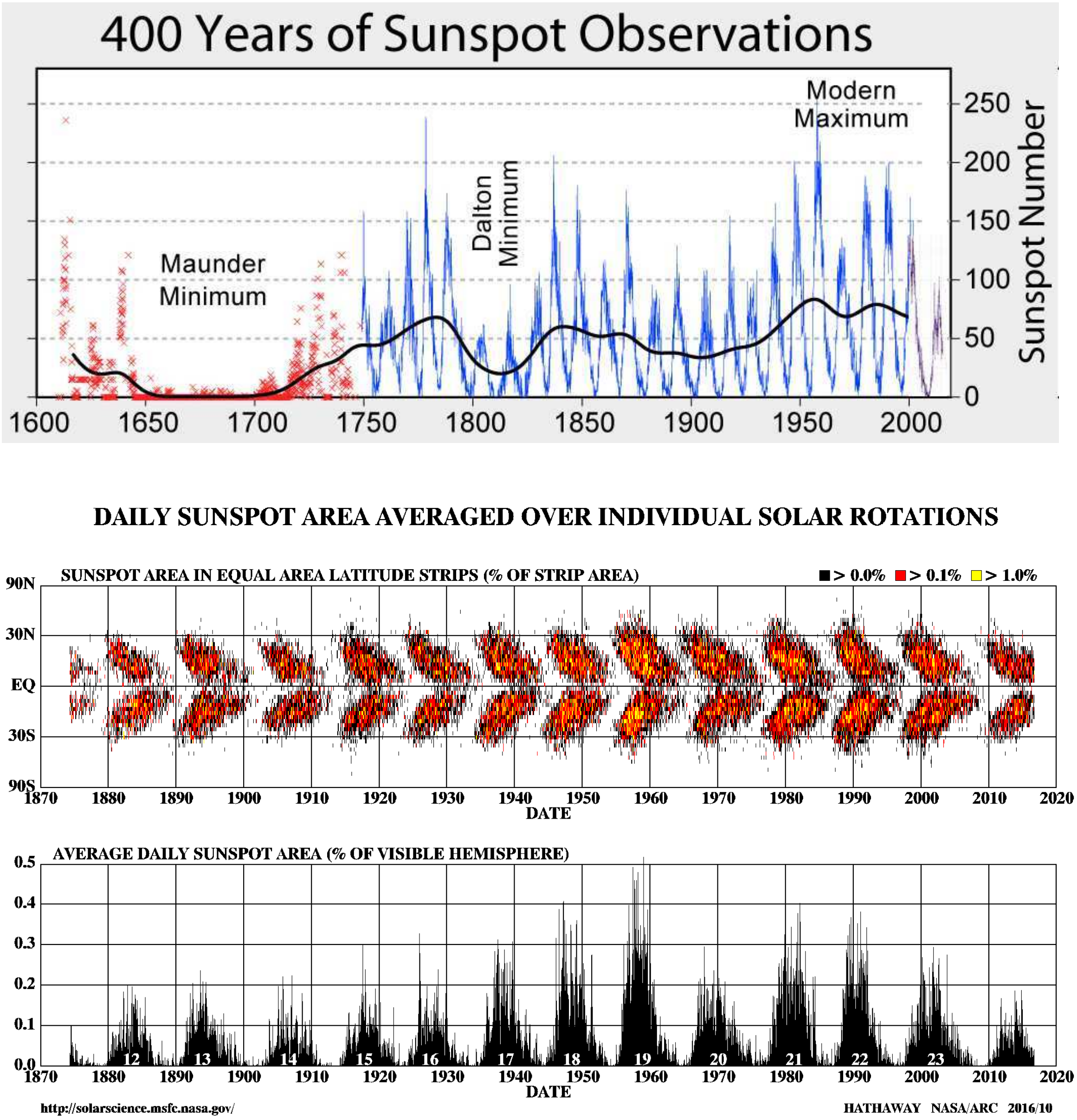

Figure 1.8: *Upper panel* : 400 years of regular sunspot number observations, based on an average of measurements from multiple observatories worldwide. The sunspot records are shown in blue, with a polynomial fit in black. Prior to 1749 (shown in red) only sporadic observations of sunspots are available. *Middle panel* : Sunspot area in the dependence to the latitude over time in equal area latitude strips (colours indicate % of strip area as per legend) over 140 years of observations. Both images courtesy of NASA. *Lower panel* :Tthe average daily sunspots area is given over time.(Taken from the NASA Marshall Space Flight center for Solar Physics.)

in the stellar interior and put significant constraints to the amplitude of the internal differential rotation. Fig. 1.9 shows the radial profile for Sun. In active stars, differential surface rotation provides a consistent explanation of wave migration or changing periods observed in the light curve (e.g. Baliunas & Vaughan, 1985).

Measurements of the stellar SDR are currently obtained in different ways: (i) Doppler Imaging maps (i.e. latitude-by-latitude cross-correlation analysis to pairs of surface images obtained several days apart; Vogt & Penrod, 1983a), (ii) from χ^2 landscape imaging methods (Collier Cameron & Donati, 2002a; Donati et al., 2000), (iii) from line profile analysis (Reiners & Schmitt, 2002), (iv) from stellar butterfly diagrams, that is from the season-to-season variations of the rotational period, as measured from spectro-photometric or broad-band photometric observations (Baliunas & Soon, 1995; Baliunas & Vaughan, 1985; Donahue & Dobson, 1996; Wilson, 1978) . By analogy with the solar case, such diagrams are interpretable in terms of migration of activity centers towards latitudes with different angular velocities. In this thesis, we have used the stellar butterfly diagrams to investigate the SDR. This method can allow us to investigate the existence of correlations with other global stellar parameters, the existence of different patterns of SDR and how they are connected with the phase of the starspot cycle. This will be discussed in a greater detail in Chapter 3.

1.3.4 Flares: The transient magnetic activities

Flares on the Sun and solar-type stars are generally interpreted as a rapid and transient release of magnetic energy in coronal layers driven by reconnection processes, associated with electromagnetic radiation from radio waves to γ-rays. As a consequence, the charge particles are accelerated and gyrate downward along the magnetic field lines, producing synchrotron radio emission, whereas these electron and proton beams collide with the denser material of the chromosphere and emit in hard X-rays (>20 keV). Simultaneous heating of plasma up to tens of MK evaporates the material from the chromospheric footpoints, which in turn increases the density on newly formed coronal loops emitting at extreme UV and X-rays. Since the non-flaring coronal emission only contains the information about an optically thin, multi-temperature, and possibly multi-density plasma in coronal equilibrium; therefore, it is very important to understand the dynamic behavior of the coronal flaring events. Extreme flaring events are even more useful to understand the extent to which the dynamic behavior can vary within the stellar environments.

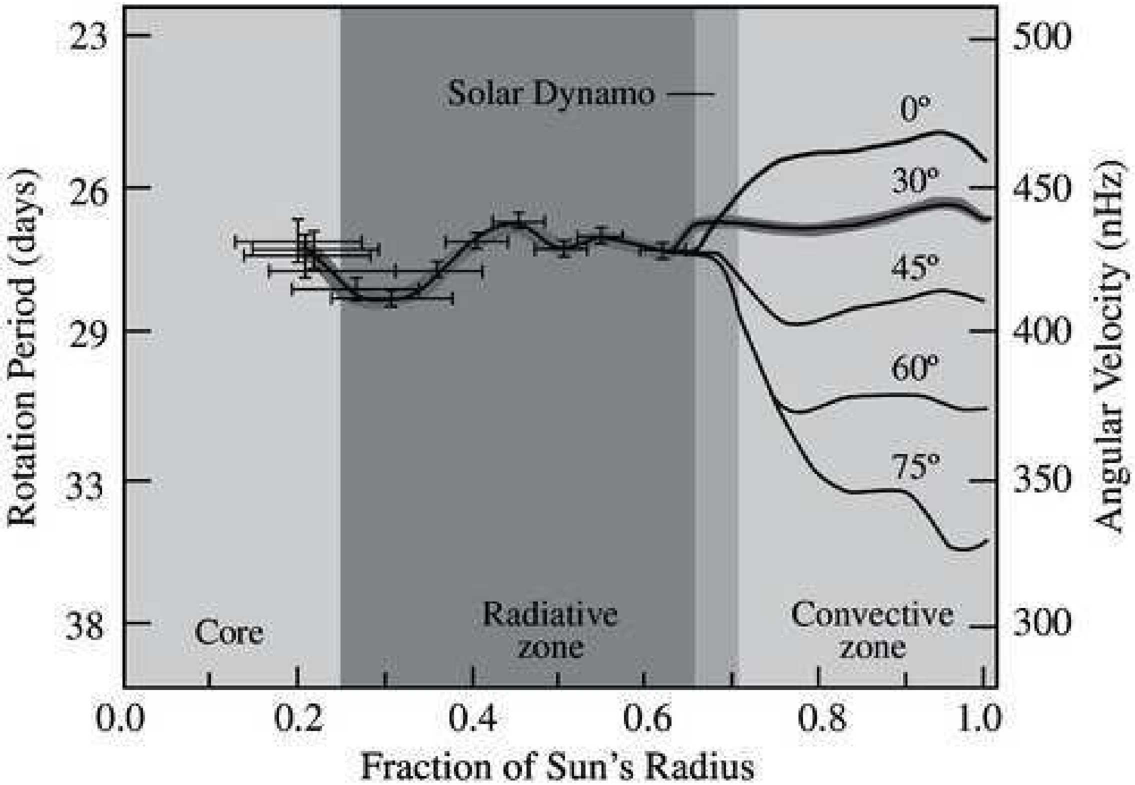

Figure 1.9: The rotation rate inside the Sun, determined by helioseismology using instruments aboard the SOHO. The outer parts of the Sun exhibit differential rotation, with material at high solar latitudes rotating more slowly than equatorial ones. This differential rotation persists to the bottom of the convective zone at 28.7 percent of the way down to the center of the Sun.

The typical total energy of solar flares ranges from 10^{29-32} erg, whereas the flares on normal solar-type stars having a total energy range of 10^{33-38} erg, are generally termed as "superflares" (Schaefer et al., 2000; Shibayama et al., 2013). X-ray superflares have been observed and analyzed in the late-type stars like Algol (Favata & Schmitt, 1999), AB Dor (Maggio et al., 2000), EV Lac (Favata et al., 2000; Osten et al., 2010), UX Ari (Franciosini et al., 2001), II Peg (Osten et al., 2007), and DG CVn (Fender et al., 2015).

1.3.4.1 Classification of flare

In case of solar flares, the classification of flare is based on the 1.54-12.4 keV (1-8 Å) soft X-ray flux observed by the *Geostationary Operational Environmental Satellite* (*GOES*). The largest flare have Xn-class with a peak flux of $n \times 10^{-1}$ Watt m^{-2}, where n starts from 1. The other classes of the solar flares are Mn, Cn, Bn and

An-class, where flux decreases through a decade from one class to next lower class and n varies from 1 to 9. However, classification of stellar flare is more complex as the amount of energy releases is much higher than the solar one. Early X-ray observations with the *European X-ray Observatory Satellite* (*EXOSAT*) observatory of flare stars revealed examples of two different type of flares: (1) impulsive flares and (2) long-decay/gradual flares.

An impulsive flare in this context means a high emission on short time scale. It is assumed to be similar to solar compact flares (Pallavicini et al., 1990). Wheras a gradual flare indicate a emission with lower amplitude on a larger time scale. This type of flare is assumed to be similar to two-ribbon solar flares (Pallavicini et al., 1990). The compact flares are less energetic ($\sim 10^{30}$ erg s^{-1}), short in duration (< 1 h) and confined to a single loop while the long decay flares are more energetic ($\sim 10^{32}$ erg s^{-1}), of long duration (≥ 1 h) and release the energy in an entire arcade of loops. The impulsive flares occur in hard X-rays and microwaves, whilst the gradual ones have been observed mostly in radio, Hα, EUV and soft X-ray (Benz, 2002).

1.3.4.2 Phases of flare

The solar/stellar flare light curves at different wavelengths do not peak at the same time, as well as their evolution also corresponds to the physical processes involved in each one of the flare phases. The general pattern of the time of emission in different wavelength ranges is shown in Fig. 1.10. In typical large solar flares, the preflare phase lasts ∼10 min, the impulsive phase ∼1 min, the flash phase ∼5 min and the decay phase ∼1 h.

(a) Pre-flare phase

This phase often start with a brightening in soft X-rays and extreme ultraviolet wavelengths. Magnetic flux continues to emerge and the field configuration is thought to become more sheared and twisted. One of the outstanding questions, still unanswered, is the conditions under which a flare is triggered. The pre-flare phase for solar flare typically last for 10 minutes.

(b) Impulsive phase

this phase starts with the onset of hard X-ray and centimetric gyrosynchrotron radiation of the energetic electrons as well as gamma-ray line emission caused by

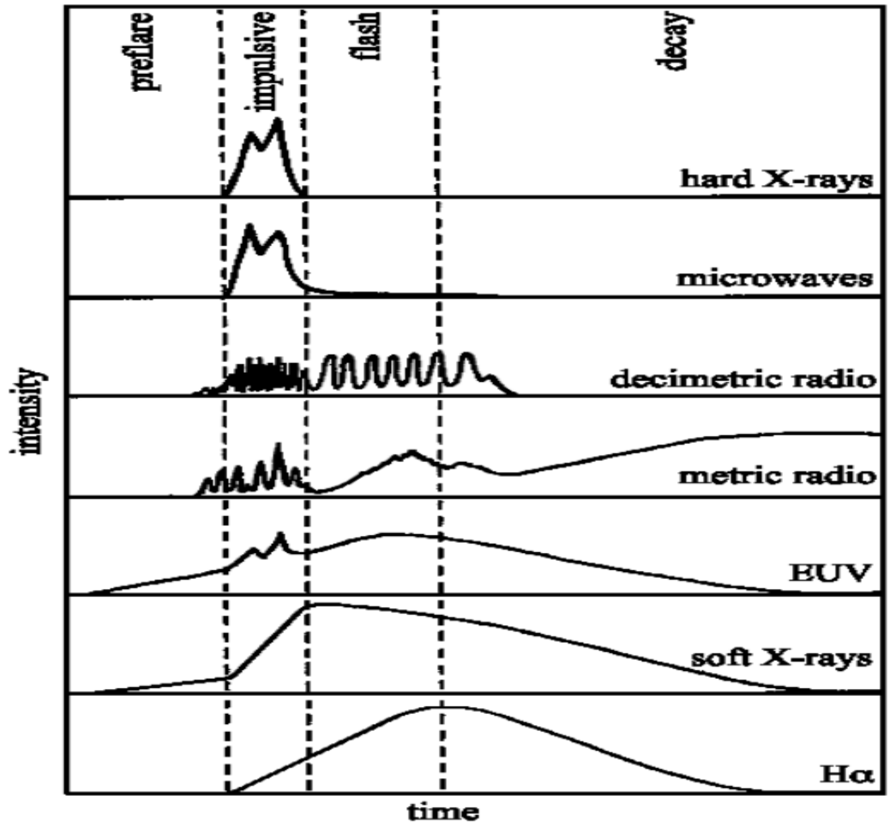

Figure 1.10: A schematic time evolution of flare intensities at different wavebands. The wavebands indicated at the top vary greatly in duration (adopted from Murdin, 2001).

energetic ions. Throughout the impulsive phase, the soft X-ray emission increases in both size and total flux. Growing emission in Balmer lines indicates that also the lower chromosphere is increasingly affected. The bulk of the flare energy is released in the impulsive phase. Typically, this phase has ∼1 min duration in the case of solar flares.

(c) Flash phase

In this phase, the non-thermal particles and their emissions have mostly disappeared but the impact of the energy released in the previous phases is still visible. During this phase, the temperature of the hot plasma decreases. Sometimes, however, gigantic soft X-ray emitting loops cool slowly, indicating that energy is still being released in this phase, which lasts for ∼5 minutes in case of solar flares.

(d) Decay phase

Finally, the flare gradually moves into the decay phase, during which the thermal flare emissions disappear. In the dense flaring plasma evaporated into the coronal post-flare loops, hydrogen recombines making these structures visible in Balmer lines. The post-flare loops often show down-moving material. It is the signature of a cooling loop. Thus the plasma evaporated by the flare is "raining" back to the chromosphere. The decay times for solar flares are typically of $\sim$1 hr.

1.3.4.3 Solar flare models

Fig. 1.11 shows schematically a well-developed model that describes the hard and soft X-rays radiation of solar flares. According to this picture, a solar flare is triggered by an instability or rearrangement in the magnetic configuration (magnetic reconnection) in the lower corona (Kopp & Pneuman, 1976; Tsuneta et al., 1992). This results in the rapid release of stored, non-potential magnetic energy and the acceleration of non-thermal particles (electrons and ions, primarily protons) to high speed by processes that are still not well understood. Using Yohkoh observations of solar flares, Masuda et al. (1994) and Masuda et al. (1995) detected, in addition to double-footpoint sources, a hard X-ray source well above the corresponding soft X-ray flaring loop structure around the peak time of the impulsive phase. This hard X-ray source showed an intensity variation similar to double-footpoint sources and a spectrum that is relatively hard compared with that of loop-top gradual source which appeared later in the flare. They suggested that either this "loop-top" hard X-ray source represents the reconnection site itself or the site where the downward plasma stream, ejected from the reconnection point far above the hard X-ray source, collides with the underlying closed magnetic loop. The accelerated (non-thermal) particles are beamed into the lower, denser layers of the solar chromosphere, along the newly linked coronal loop, or hurled out into space along open magnetic field lines. As the non-thermal electrons move either out or down along magnetic channels, they generate intense radio emission. Those non-thermal electrons that were channeled down the loop strike the chromosphere at nearly the speed of light, emitting hard X-rays by electron-ion bremsstrahlung at the loop footpoints. The chromospheric material at the loop footpoints is then heated (to temperatures which can be as large as tens of millions of degrees) very quickly (in seconds) by the accelerated particles that slam into it. The high-temperature material in the chromosphere is driven upward by the large pressure gradients and rises into the loop along the guiding

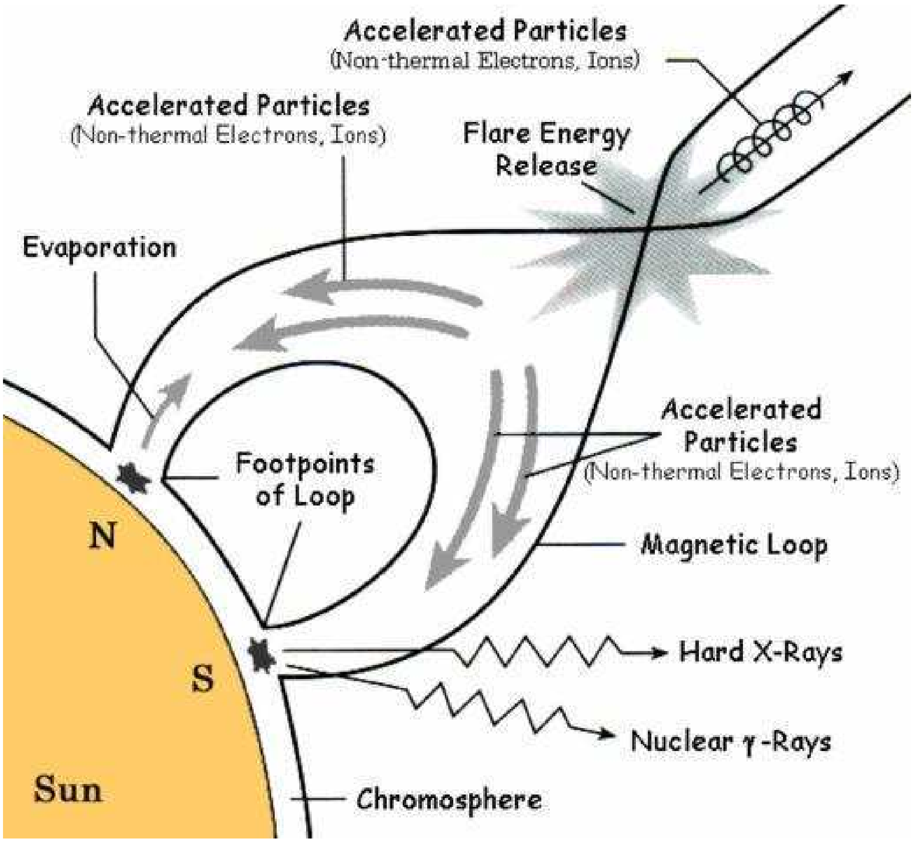

Figure 1.11: A schematically a well-developed model that describes the hard X-ray and soft X-ray radiation of solar flares (adapted from Lang, 2009).

magnetic field, accompanied by a slow, gradual increase in soft X-ray radiation by thermal bremsstrahlung that lasts tens of minutes. This upwelling of heated material is called chromospheric evaporation. Thus, the thermal decay phase, detected by the gradual build up of soft X-rays, is viewed as an atmospheric response to the energetic charged particles during the impulsive hard X-ray phase.

1.3.4.4 Models for stellar flares

Analysis of light curves during flares can provide us with insights into the characteristics of the coronal structures and, therefore, of the magnetic field (e.g. Favata et al., 2000; Reale et al., 2004; Schmidt et al., 1999). Even though stellar flares are spatially unresolved, a great deal of information on the coronal heating and on the plasma structure morphology can be inferred from a detailed modeling of stellar flares. For instance, if sufficient data are available for moderately time-resolved spectral analysis, a study of the complete evolution of a flare can allow us to (a) infer whether the flare occurs in closed coronal structures (loops), (b) determine the size of the flaring structures, (c) determine whether continuous heating is present throughout the flare and (d) put constraints on the location and distribution of the heating (see Reale et al., 2004). Many loop models with different assumption and solar analogy were developed in past. We will discuss some of them which are used frequently.

(a) The classical Haisch approach

Based on quasi static radiative and conductive cooling during the early phase of the decay, Haisch (1983) suggested an approach to model a loop. He assumed that near the flare maximum the observed decay time (τ_d), the radiative cooling time (τ_{rad}) and the conductive cooling time (τ_{cond}) are equal i.e.

$$\tau_d = \tau_{rad} = \tau_{cond} \tag{1.1}$$

$$\tau_{rad} = \frac{3kT}{n_e P(T)} \quad \text{and} \quad \tau_{cond} = \frac{3nKL_{rad}^2}{\kappa T^{5/2}} \tag{1.2}$$

where T is loop temperature, n_e is electron density, k is Boltzmann constant and $P(T) = 10^{-26.2}\sqrt{T}$ is the plasma emissivity. Additionally, assuming that the flaring loops are with constant cross section, the time equality near the flare maximum results following relations among the τ_d, T, n_e, loop length (L_{ha}) and emission measure (EM).

$$T\ (^\circ K) = 4 \times 10^{-5} EM^{1/4} \tau_d^{3/4} \tag{1.3}$$

$$n_e\ (cm^{-3}) = 10^9 EM^{1/8} \tau_d^{-9/8} \tag{1.4}$$

$$L_{ha}\ (cm) = 5 \times 10^{-6} EM^{1/4} \tau_d^{3/4} \tag{1.5}$$

This approach is very simple approach and applied to model the loops in various past studies (e.g. Mullan et al., 2006). In the hypothesis of flares occurring inside closed coronal structures, the decay time of the X-ray emission roughly scales as the plasma cooling time. In turn, the cooling timescales with the length of the structure which confines the plasma, therefore longer the decay results larger flaring structure.

(b) Quasi-static cooling model

This model is described by Serio et al. (1991), where they assumed that the flare decay starts when the loop is at hydrostatic and energy equilibrium i.e. system is initially in steady state. The method is based on the underlying set of hydrodynamic equations and assuming semicircular loops with constant cross section cooling from equilibrium condition and uniformly heated by an initial heat pulse. Assuming that the heating rate during the decay of flare is completely switched and using the the RTV scaling laws (Rosner et al., 1978), Serio et al. (1991) derived the thermodynamic scale of decay time as

$$\tau_{th} = \frac{3.7 \times 10^{-4} L_{qs}}{\sqrt{T_{max}}} \tag{1.6}$$

where L_{qs} is half loop length, and T_{max} is the maximum temperature. Reale et al. (1993) have modified this approach by considering the effect of gradually decaying heating function and to account for loops comparable or larger than the pressure scale height.

(c) Hydrodynamic loop model

As mentioned in the § 1.3.4.4, the quasi-static model do not consider the loop heating during the decay. It has been shown that the slope of the trajectory of the flare decay in the density-temperature (n-T) plane depends significantly on the heating decay time (Reale et al., 1993; Sylwester et al., 1993). Reale et al. (1997) used the slope of n-T diagram to derive the heating decay time, so to better constrain the loop length. The working hypotheses of this method similar to the quasi-static model with inclusion of heating as well as cooling during the decay. They described the ratio of light curve decay time and thermodynamic decay in the form of hyperbolic function:

$$\frac{\tau_d}{\tau_{th}} = \frac{c_a}{\zeta - \zeta_a} + q_a = F(\zeta) \tag{1.7}$$

The coefficients c_a, ζ_a and q_a depends on the energy response of the instrument used. Please see Table A.1 of Reale (2007) for values of c_a, ζ_a and q_a, and limiting values of ζ for different instruments. Using equations 1.6 and 1.7, Reale et al. (1997) found the relation of half loop length as

$$L_{hd} = \frac{\tau_d \sqrt{T_{max}}}{3.7 \times 10^{-4} F(\zeta)} \tag{1.8}$$

The above method is purely based on the decay phase, Reale (2007) derived the half loop length (L_{hr}) from the rise and peak phases of the flare as

$$L_{hr}\ (\ cm\ )\ = 9.5 \times 10^2\ \tau_M \frac{T_{max}^{5/2}}{T_M^2} \tag{1.9}$$

where τ_M and T_M (= 7.76×10^7 K) are time and temperature when the emission measure peaks.

(d) Magnetohydrodynamic model

Shibata & Yokoyama (1999, 2002) developed a method, which is based on a balance between heating due to magnetic reconnection and chromospheric evaporation. They assumed that, to maintain stable flare loops, the gas pressure of the evaporated plasma must be smaller than the magnetic pressure. The derived equations for a magnetic loop length L_{pb} is given by the equation

$$L_{pb}\ (cm) = 10^9 \left(\frac{EM}{10^{48}\ cm^{-3}}\right)^{3/5} \left(\frac{n_e}{10^9\ cm^{-3}}\right)^{-2/5} \left(\frac{T}{10^7\ \ K}\right)^{-8/5} \tag{1.10}$$

The Magnetic field strength is given as

$$B = 50 \left(\frac{EM}{10^{48} cm^{-3}}\right)^{-1/5} \left(\frac{n_e}{10^9 cm^{-3}}\right)^{3/10} \left(\frac{T}{10^7 K}\right)^{17/10} \tag{1.11}$$

Using this method Mitra-Kraev & Harra (2005) and Pandey & Srivastava (2009) derived the loop of flare from ξ Boo and AT Mic, respectively. There are many other example, where the loop length were derived from this method.

(e) Two ribbon flare model

The two-ribbon flare model was developed by Kopp & Poletto (1984) for the solar flares, and later extended it to stellar flares by Poletto et al. (1988). A modified version of the this model was applied by Güdel et al. (1999) for a long duration flare from UX Ari. This model assumes that a flaring event opens an arcade of loops; the open field lines are then driven towards a neutral sheet, where they reconnect at progressively higher altitudes, forming a growing system of loops. The magnetic energy released in the reconnection process provides the continuous heating responsible for the X-ray emission during the flare. The flare model describes the magnetic loop shape along meridional planes by Legendre polynomials P_n of order n, up to the height of the neutral point; above this level the magnetic field is directed radially. One loop arcade corresponds to one lobe between two zeros of P_n in latitude, axisymmetrically continued over some longitude in the east-west direction. The propagation of the neutral point in height, h(t), with a time constant t_0 (in units of R_*, measured from the star's center), is

$$h(t) = 1 + \frac{H_m}{R_*}(1 - e^{-t/t_0}) \tag{1.12}$$

where H_m is the maximum height reached by the neutral point during the reconnection event, and t_0 is the characteristic time constant of the process. H_m is assumed to be equal to the latitudinal width of the lobes (Poletto et al., 1988) and for $n \gg 2$

$$H_m \approx \frac{\pi}{n + 1/2} R_* \tag{1.13}$$

For n = 2, $H_m = (\pi/2)R_*$. The loop arcade is assumed to have a longitudinal extent of $1.5H_\mathrm{m}$, as typically observed in solar two ribbon flares.

For some flares, the loop lengths from different methods were found consistent with each other. However, for other flares inconsistency was found. Covino et al. (2001) have also compared the loop length from the hydrodynamic model of Reale et al. (1997) with a simple order of magnitude estimates of the radiative and conductive cooling times for a single flaring loop with no additional heating in the decay phase (Haisch, 1983; Pallavicini et al., 1990). They concluded that the loop lengths derived from these two approaches are not too dissimilar with each other. For the flare observed in the star LQ Hya, Covino et al. (2001) found similar loop lengths from two methods. Using hydrodynamic method, Favata et al. (2001) found small loop lengths to that derived from quasi-static cooling method van den Oord & Mewe (1989). Pandey & Singh (2011) also found larger loop lengths from Haisch approach. Shibata & Yokoyama (2002) showed the inconsistency between the loop lengths derived from the pressure balance method and the hydrodynamic method. However, they also noted that by increasing the pre-flare electron density from 10^9 cm^{-3} to 10^{10} cm^{-3}, loop lengths derived from both methods are consistent. Bhatt et al. (2014) also found the consistent loop lengths derived from the rise and decay method, and the Haisch approach for most of the flares observed in young stars. The hydrodynamic method is one of the current and a well developed method which additionally considers the reheating mechanism during the flare decay. Therefore, in this thesis, loop modeling was performed using this method.

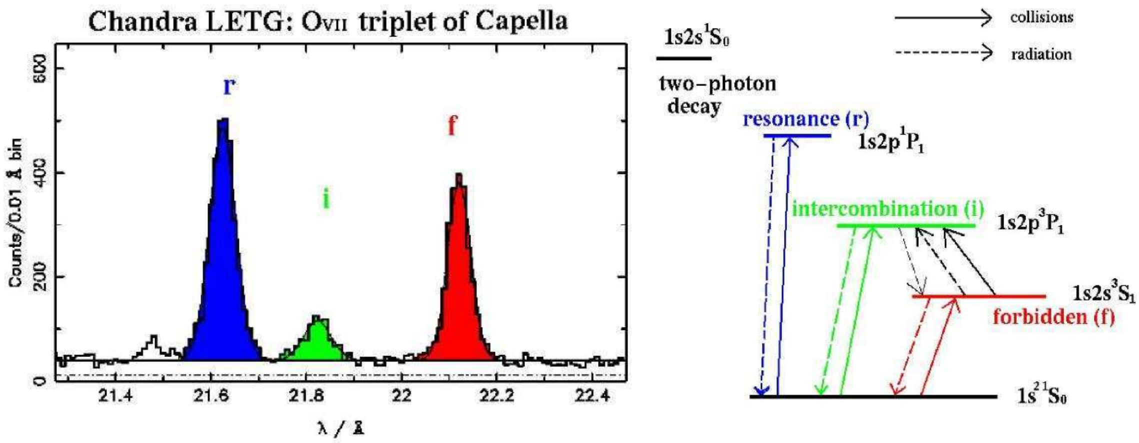

Figure 1.12: (left). Chandra LETGS measurements of the OVII triplet of Capella,taken from Ness et al. (2003) (right) Simplified energy-level diagram of the He-like triplets, taken from Ness et al. (2003).

1.3.4.5 Fe Kα fluorescence emission: Estimation of flare height/location

The X-ray emissions during the solar and stellar flares interact with the photospheric layers and become reprocessed through scattering and photoionization. These processes also produce characteristic fluorescent emission from astrophysically abundant species. Recent observations of X-ray superflares reveal an important aspect of the detection of iron Kα fluorescence emission during flaring events (Ercolano et al., 2008; Testa et al., 2008). Previously, this iron Kα fluorescence emission line at 6.4 keV was detected on the solar flares (Parmar et al., 1984; Zarro et al., 1992). The X-ray emissions during the solar and stellar flares interact with the photospheric layers and become reprocessed through scattering and photoionization. These processes also produce characteristic fluorescent emission from astrophysically abundant species. In the stellar context, the detected iron Kα line is generally attributed to a fluorescent process, where the fluorescing material is a neutral or low ionization state of photospheric iron (Fe I–Fe XII), which shines on the X-ray continuum emission arising from a loop-top source. Thus the detection of this line constraints the height of the flaring loop. The process involves photoionization of an inner K-shell electron and the de-excitation of an electron from a higher level at this energy. Thus the total photon flux above the Fe Kα ionization threshold of 7.11 keV is one of the main contributors to the observed flux in the Fe Kα line. For the solar flares, Bai (1979) derived a formula for the flux of Fe Kα photons received on the Earth, which was later extended to stellar context by Drake et al. (2008) and is given by

$$F_{K\alpha} = f(\theta)\Gamma(T, h)F_{7.11} \quad \text{photons cm}^{-2}\ \text{s}^{-1} \tag{1.14}$$

where $F_{7.11}$ is the total flux above 7.11 keV, $f(\theta)$ is a function that describes the angular dependence of the emitted flux on the astrocentric angle (defined as an angle subtended by the flare and the observer), and Γ is the fluorescent efficiency.

1.3.4.6 High resolution spectra: The density and temperature diagnostics

The density of the flaring plasma is important as it determines the time scales of radiation, and it can be inferred either indirectly from a flare analysis (see details for Chapter 4, 5, and 6) or directly by measuring the density sensitive line ratio of a high reslution spectra (see Chapter 4 for details). In the left panel of Fig. 1.12, a zoomed version a high-resolution X-ray spectra (taken from *Chandra* LETGS instrument) is shown, where the He-like triplet of O VII lines are marked with red, green, and blue for the resonance (r), intercombination (i) and forbidden (f) lines, respectively. These most intense He-like lines correspond to transitions between the n = 2 shell and the n = 1 ground state shell. The excited state transitions from ^{1}P$_1$, ^{3}P$_1$ and ^{3}S$_1$ to the ground state ^{1}S$_0$ are named as resonance (r), intercombination (i) and forbidden (f) lines, respectively (see right panel of Fig. 1.12). In the X-ray spectra the ratio of the fluxes in the forbidden line and intercombination line (R = f/i) is potentially sensitive to density (n_e), while the ratio G = (f+i)/r is sensitive to temperature (Gabriel & Jordan, 1969; Porquet et al., 2001). The f/i ratio is related to the electron density as

$$\frac{f}{i} = \frac{R_0}{\frac{n_e}{N_c} + 1} \tag{1.15}$$

where R_0 is low density limit ($n_e \to 0$), and the critical density, N_c, depends entirely on atomic rates (see Pradhan & Shull, 1981). Of the He-like ions observed with the reflection grating spectrometer of *XMM-Newton*, O VII has lines that are strong and unblended to use in a measurement of n_e.

1.3.5 Other magnetic activities

There are few other localised magnetic activities which is detected on the Sun that increases/decrease the solar/stellar brightness, such as: faculare, spicules, plages, filaments, prominences, and fibrils. The faculae are the active regions on the solar photosphere, located near the sunspots, and have a strong magnetic field in a very small area between convection flows (the granules). These can be visualised as either by bright spots or networks of bright regions between convective cells. Spicules can be found on the solar limb, and typically reach heights of $\sim$3 – 10 Mm above the solar surface. They are very short-lived, rising and falling over $\sim$ 5 – 15 minutes. On the other hand, the plage is a typical example of a chromospheric feature. These are the bright regions above the photosphere that are typically found near sunspots, of opposite polarity to the main spot. Other interesting chromospheric features are the filaments, which are long, dark structures on the solar disk. If these features found on the solar limb, they are referred to as prominences. Some hair-like structures on the solar disk are known as fibrils.

Among these magnetic activity features, the plage and faculae are the local bright spots. With the stellar rotation these features also move in and out of the visible stellar disk, and could result in a sinusoidal variation in the light curve. But, unlike the starspots these features create peaks instead of dips in the light curve. Therefore, it is difficult to know a priori that a sinusoidal variation in a stellar light curve are due to the starspots or these bright regions, creating the "Zebra Effect" paradox (first coined by Pettersen et al., 1992). However, in the case of transiting exoplanets (see Llama et al., 2012), it can definitly be concluded that if the modulation is due to the hot spots or the cool spots on the stellar surface.

All the solar magnetic activity increases to its peak during the phase of solar maximum. At this phase, although the occurrence rates of spots and flares are increases, but the total solar irradiance becomes slightly higher due to the presence of facule and plages. It is observed that the optical brightness of the Sun increases during the solar maximum by $\sim$0.04% (Foukal & Lean, 1986; Willson & Hudson, 1988). Thus, the networks of faculae can rival the individual sunspot groups in terms of the impact on the solar brightness. However, very high levels of sunspot activity has been correlated with a decrease in the relative facular coverage on the Sun (Foukal, 1993). This result may indicate that, for the highly active late-type stars, where the starspot coverage fractions are generally observed to be very large, the bright facular regions may be smaller and have a weaker impact on light curve modulations.

In order to detect faculae on other stars, Gondoin (2008) searched for signatures of faculae on two active stars with light curves from the *Microvariability and Oscillations of Stars telescope* (*MOST*; Walker et al., 2003). However, no robust signal from faculae was detected using the light curve modeling, and the observed modulations was appeared to be degenerate with cool starspots, possibly indicating faculae had a weaker impact on the light curves for these active stars.

Karoff et al. (2013) attempted an entirely different approach to infer the presence of faculae from high-precision light curves. This method was based on the solar observations of faculae networks having longer decay timescales than their corresponding sunspots, which results in lingering bright regions after the sunspot had decayed away. Using the power spectrum of *Kepler* light curves, Karoff et al. (2013) searched for characteristic timescales that would only be the result of this slower decay. They found encouraging evidences for both faculae and surface granulation, in addition to the expected pulsation and starspot modulations in the light curves of the investigated solar-like stars. In this thesis, I have only focussed on the prominent magnetic activities, i.e. the starspots, spotcycles, and flares.

1.4 Common types of active stars

All the common properties of the active stars have been presented above. The level of the activity also depends on their evolutionary status. In this section, we discuss various types of active stars based on their evolutionary status.

1.4.1 RS Cannum Venaticorum (RS CVn) binary stars

The RS CVn type binaries named after the prototype are a particular class of the active binary systems which were originally defined by Hall (1976). In an RS CVn binary, the two stars are usually tidally locked so that the rotational period of each star is approximately the same as the orbital period; however, the two stars are not undergoing mass transfer (i.e. they form a detached system). One star is generally a spectral type F to G dwarf or a subgiant that is $\sim$1000 K hotter than its companion, which is usually a G to K type giant or sub-giant.

1.4.2 BY Draconis (BY Dra)

BY Dra stars are a class of late K and M type dwarfs which exhibit photometric rotational modulation of few hundredths to a few tenths of a magnitude (Bopp & Evans, 1973). The orbital or rotational period of BY Dra is in the range of $\approx$ 0.5 - 20 d. As originally defined by Bopp & Fekel (1977), BY Dra types may include active single main-sequence star as well as members of detached binary system.

1.4.3 FK Comae Berences (FK Com)

FK Com stars were first defined as a new group of active stars by Bopp et al. (1981). FK Com stars are late-type (G or K) giants with rotational period of only a few days. Spectroscopic observations reveal rotational velocity of these stars of 50 - 150 km s^{-1}. These star do not show any significant periodic radial velocity variations, and therefore, are most likely single stars.

Other stars which shows the similar type of magnetic types are: pre-main sequence T-Tauri star, W Ursae Majoris (W UMa), Algol, and Cataclysmic Variables (CVs). W Uma systems are eclipsing contact binaries with spectral types between F and K, and orbital period generally from 0.2 to 1.5 d (Rucinski, 1998) but strongly peaked between 0.25 - 0.6 d. Algol binaries are interacting semi-detached systems with B-to-early-F primary components and less massive, G-to-K secondary companions that are in contact with their Roche equipotential surfaces. CV binaries are a diverse class of short-period semi-detached binaries consisting of an accreting white dwarf primary and a low-mass main-sequence secondary star.

1.5 The aim and objectives of the thesis

Late-type stars with a similar internal structure to that of the Sun is expected to show similar kind of magnetic activities due to their similar internal structure. However, in practice, it is found to vary over a wide range which is not well explained by the existing dynamo theroy. In this thesis, we have investigated different magnetic activities from the observational point of view, in order to provide valuable constraints on the dynamo theory.

In this thesis, to fulfil the above aim, we have investigated both the long-lasting and transient magnetic activities where we have studied the temporal evolution of the activities as well as the evolution of activity with the stellar age. To be more specific, we have chosen the following research objectives for our investigation:

1. Evolution of surface inhomogeneities (cool spots) on stellar surface, and corresponding short and long-term activity cycles using long-term photometric data.

2. Making use of long term photometric observations to study the SDR pattern in solar analogous.

3. To study the magnetic activities on different height from the stellar surface. i.e. throughout the photosphere, chromosphere, and corona using multi-wavelength data (X-ray to optical).

4. To study the transient magnetic activities (flares) which are supposed to be a result of magnetic reconnection at coronal heights. A study of temporal evolution of X-ray spectral parameters (temperature, emission measure, abundances) and the energy budget during the flare is important to understand the dynamical behaviour of the corona.

5. To search for the dependence of flare occurrence on the spottedness, and its longitudinal location on the stellar surface.

In order to accomplish these objectives, we have chosen four MS late-type stars namely LO Peg, 47 Cas, AB Dor, and CC Eri, and one evolved RS CVn binary SZ Psc. These are highly active stars with $L_x/L_{bol} \sim 10^{-3}$, and are located in saturation regime of Fig. 1.4. Basic physical parameters of these stars are given in Table 1.1 and details are mentioned in the forthcoming chapters.

Table 1.1: The sample of late-type stars and their basic parameters.

Name	Spectral Type	V (mag)	Distance (pc)	Period (d)	Log(L_x) (in cgs)	Log(L_x/L_{bol}) –	Age (Gyr)
LO Peg	K8V	9.25	24.8	0.42	29.72	-3.2	∼0.05
47 Cas	F0V	5.28	33.0	1616	30.37	∼ -3	1.3
AB Dor	K0V	6.99	14.9	0.51	30.18	∼ -3	∼0.05
CC Eri	K7.5V – M3V	8.87	11.5	1.56	29.58	∼-3.1	0.01
SZ Psc	F8V – K1IV	7.44	97.0	3.97	31.07	-3.43	8.7

The above data are taken from Guirado et al. (2011), López-Santiago et al. (2010), Zuckerman & Song (2004), and Gáspár et al. (2013).

1.6 Thesis outline

This thesis is structured as follows:

Chapter 2: In this chapter, I give a brief description of the telescopes used for the multi-wavelength observations and the data reduction techniques followed to analyze these observations.

Chapter 3: Using long-term multi-band data, an in-depth study of the starspot cycles, Surface Differential Rotations (SDR), optical flares, evolution of starspot distributions, and coronal activities on the surface of young, single, main-sequence, Ultra Fast Rotator LO Peg are described in this chapter.

Chapter 4: In this chapter, using *XMM-Newton* observation, we investigate on flare properties from the very active and poorly known stellar system 47 Cas and an fairly known system AB Dor.

Chapter 5: In this chapter, we present an in-depth study of two superflares detected on an active binary star CC Eridani by *Swift* observatory. The Fe Kα emission at 6.4 keV is also detected in the X-ray spectra and we model the Kα emission feature as fluorescence from the hot flare source irradiating the photospheric iron.

Chapter 6: A detailed analysis of a large and long duration flare observed by *Swift* satellite in an RS CVn type eclipsing binary SZ Psc is studied in this chapter.

Chapter 7: Finally, in this chapter, I have summarised the main results described in the previous chapters of this thesis and concluded the key findings. In this chapter, I have also given a brief picture of the future prospectives.

Chapter 2

Telescopes, Observations, Softwares, and Data Processing

Observations for current study were obtained from various ground- and space-based observatories in optical, UV, and X-ray waveband. The optical observations were obtained using three ground based observatories from *Aryabhatta Research Institute of observational sciencES* (ARIES), India, *Inter-University Centre for Astronomy and Astrophysics* (IUCAA), India, and *Goddard Space Flight Center* (GSFC), United States of Ameria (USA). In addition to this, we have also compiled various other available datasets from literature and archives to supplement our datasets. The X-ray and UV observations were obtained from the X-ray Multi-Mirror Mission (*XMM-Newton*) and *Swift* observatory. This chapter briefly describes the telescopes used for the multi-wavelength observations, the instruments, the data acquisition and reduction techniques followed by the analses of these observations.

2.1 Optical band

2.1.1 Telescopes

Our observations in optical waveband were carried out using three optical telescopes: 2-m *IUCAA Girawali Observatory* (IGO; see Das et al., 1999), 1.04-m *ARIES Sampurnanand Telescope* (ST; see Sinvhal et al., 1972) and 0.36-m *Goddard Robotic Telescope* (GRT; see Sakamoto et al., 2009). Apart from this, we have used literature data from Jeffries et al. (1994) and Taş (2011) where data were taken from the 0.48-m *Ege University Observatory* (EUO) telescope, Turkey and 1-m *Jacobus Kapetyn Telescope* (JKT), Canary Islands. The archival data were taken from *Hip-*

parcos[1] (Perryman et al., 1997), *All Sky Automated Survey*[2] (*ASAS*; Pojmanski, 2002), and *Super Wide Angle Search for Planets*[3] (*SuperWASP*; Pollacco et al., 2006) observations. I will give brief descriptions about all the telescopes and their pictures are displayed in Fig. 2.1.

2.1.1.1 IGO

The 2-m IGO telescope is an alt-azimuth mount telescope of IUCAA situated 80 km north of Pune City in India. (Longitude: 73°40′00″ E, Latitude: 19°05′00″ N, Altitude ∼1000 m), equipped with a f/10 Cassegrain telescope. It operates in 350 to 900 nm waveband.

2.1.1.2 ST

The 1.04-m ST is a two-pier equatorial English mounting telescope at ARIES (Longitude: 79°27′24″ E, Latitude: 29°21′42″ N, Altitude ∼1951 m), equipped with a Ritchey-Chretien optics. We have used CCD chip of size 2048 × 2048 pixels (2k×2k) available at the Cassegrain focus of ST.

2.1.1.3 GRT

The Goddard Robotic Telescope (GRT) system consists of a 0.36-m Celestron optical telescope assembly with 1200GTO mount. With a focal reducer (Celestron f/6.3), it has achieved a 20′×20′ field of view (FOV).

2.1.1.4 *SuperWASP*

The two continuously operating, robotic observatories cover the Northern and Southern Hemisphere, respectively (at Roque de los Muchachos Observatory and at the site of South African Astronomical Observatory, near Sutherland, South Africa.) The *SuperWASP* is a Torus Fork Mount telescope system with a focal ratio of f/1.8.

2.1.1.5 *ASAS*

The *ASAS* is a Polish project, The *ASAS*-3 system was installed in the 10 inch astrograph dome of the Las Campanas Observatory. It consisted of two wide-field

[1]http://heasarc.gsfc.nasa.gov/W3Browse/all/hipparcos.html
[2]http://www.astrouw.edu.pl/asas/?page=main
[3]http://exoplanetarchive.ipac.caltech.edu/applications/TblSearch/tblSearch.html?app=ExoSearch&config=superwaspt

telescopes, each equipped with 200/2.8 Minolta telephoto lens and 2k×2k AP-10 CCD camera.

2.1.1.6 *Hipparcos*

The *Hipparcos* was a scientific satellite of the European Space Agency (ESA) launched on 1989 August 8. It was having a Schmidt telescope with a 0.29-m diameter and 1.4-m focal length. The satellite was deactivated on 1993 August 15.

2.1.1.7 EUO

The EUO is a ground-based astronomical observatory operated by the Astronomy and Space Sciences Department at Ege University's Faculty of Science situated 10 km east of Izmir in western Turkey. The observatory consists of four optical telescopes: a 0.48-m Cassegrain telescope, and 0.30-m, 0.35-m, and 0.40-m Meade telescope. 2 pieces of CCD cameras are attached with 0.35-m and 40 cm telescopes.

2.1.1.8 JKT

The JKT is owned by the Instituto de Astrofísica de Canarias, (Latitude: $28^{\circ}45'40.1''$ N, Longitude: $17^{\circ}52'41.2''$ W). The JKT has a parabolic primary mirror of diameter 1.0 m, and two interchangeable secondary mirrors. The telescope is usually fitted with the hyperboloid secondary mirror, which gives a conventional f/15 Cassegrain focus. The alternative f/8.06 Harmer-Wynne system uses a spherical secondary and a doublet corrector to give a field of 90 arcmin diameter for photographic astrometry over a wide field.

2.1.2 Filters

Filters are primarily used for two objectives (a) to restrict the wavelength band of the incoming light; (b) to reduce the intensity of the light coming from very bright source. Since the detectors have a wider range of wavelength response and sensitivity, filters are important for the flux measurement of the astronomical objects at various wavelengths. These filters provide information like temperature, colour and other properties of a distant source. Johnson U, B, V and Cousin R filters were used for the present study. The central wavelength of these filters are 365, 445, 551, and 658 nm, with the bandwidth of 66, 94, 88, and 138 nm, respectively.

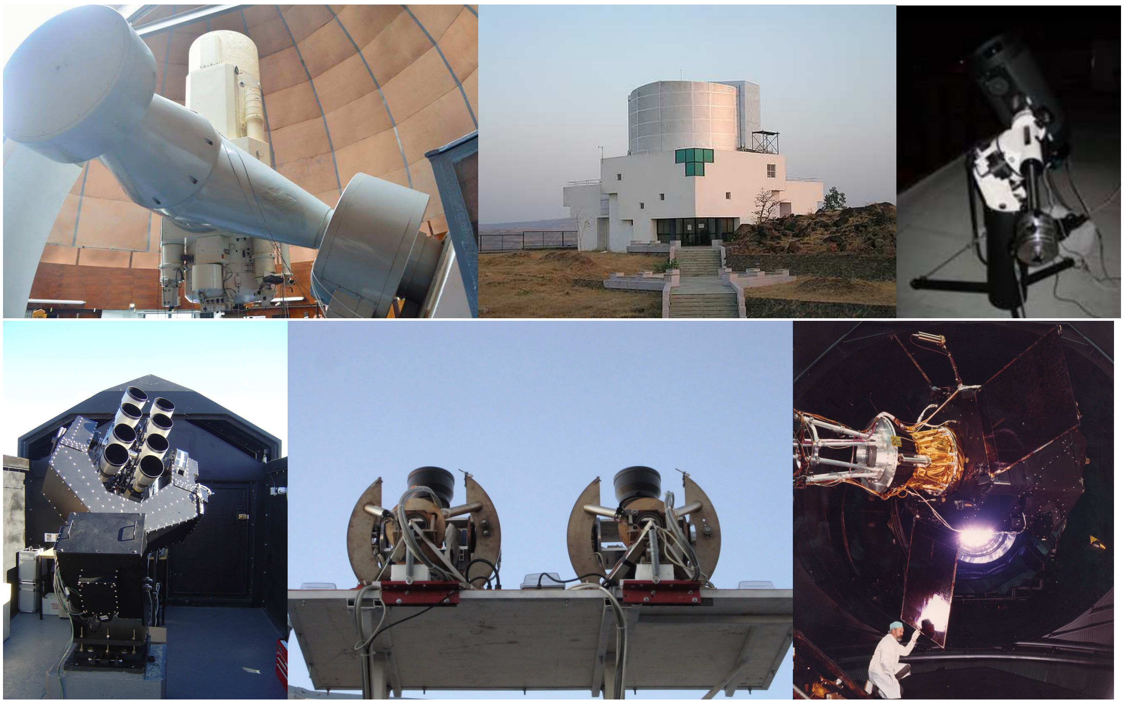

Figure 2.1: The pictures of different ground-based observatories used in our study. Clockwise (from top-left) – ST, IGO, GRT, *Hipparcos*, *ASAS*, *SuperWASP*.

2.1.3 CCD detectors

All of the above telescopes uses charge-coupled device (CCD) as detector for the observations. A typical CCD camera used for astronomical purpose consists of a two-dimensional array of photon detectors in a layer of semi-conducting material silicon. Each individual detector in the array is referred to as pixel. Each individual pixel is capable of collecting the photons and storing the produced electrons, which can be read out from the CCD array to a computer to produce a digital image of the varying intensities of light detected by the CCD. As photons come in contact with CCD surface and electrons build up in the wells (pixel) over the period of its exposure to light (the integration), a digital image is built up consisting of the pattern of electrical charge (intensity) present in each pixel. At the end of the integration period when light is no longer allowed to reach the CCD detector, the accumulated charge in each pixel is transferred to the on-chip amplifier, pixel by pixel.

During the read out process of the array, charge must be moved out of the imaging region of the array to a location where the amount of charge can be measured. Rows of pixels are moved in parallel down to a single row (the serial register) which is read out sequentially by Analog to Digital (A/D) converter where it is measured and then recorded. The measuring device is emptied and once again the rows of pixels are moved in parallel to the serial register, then each pixel is read out sequentially. This process continues until all of the pixels have been measured (read out).

At a room temperature and for a longer integration time (more than hundred milliseconds) thermal noise is created by the random generation of dark current. Therefore, to avoid the self generated dark signal, CCD must be cooled down to such a low temperature where thermal noise becomes negligible in comparison to the signal received from the astronomical source. During our observations it was cooled to about -110°C and -140°C respectively in a liquid nitrogen dewar to minimize the effect of thermal noise.

2.1.4 Observations

We observed the star LO Peg on 30 nights between October 25, 2009, and December 18, 2013, in Johnson U, B, V, and R photometric bands with the 2-m IGO, 1.04-m ST, and 0.36-m GRT telescopes. The exposure time was between 5 to 60 s depending on the seeing condition, filter, and telescope used. Several bias and twilight flat frames were taken in each observing night.

We have also compiled various other available datasets in U, B, V, and R bands from literature (Jeffries et al., 1994; Pandey et al., 2009, 2005; Taş, 2011) and from archives to supplement our datasets. The archival data were taken from *Hipparcos*, *ASAS*, and *SuperWASP* observations. The log of optical observations is given in Table 2.1. *Hipparcos* observations was spanned over ∼3 yr from November 27, 1989, to December 15, 1992. The *Hipparcos* magnitude (V_H) was converted to Johnson V magnitude by using the relation $V = V_H - (V - I)_c$, where $(V - I)_c$ is the catalog value corresponding to the colour $(V - I)$. With a $(V - I)$ colour of 1.288 mag for G-M dwarfs, we get the $(V - I)_c$ value of LO Peg to be 0.124 mag. *ASAS* survey was done in V-band and has a much longer observing span of ∼7 yr (April 26, 2003 - October 1, 2009). In the *ASAS* observations, we have used only 'A' and 'B' grade data within 1″ of the star LO Peg. *ASAS* photometry provides five sets of magnitudes corresponding to five aperture values varying in size from 2 to 6 pixels in diameter. For bright objects, Pojmanski (2002) suggested that magnitudes corresponding to the largest aperture (diameter 6 pixels) are useful. Therefore, we took magnitudes corresponding to the largest aperture for further

Table 2.1: Log of optical observations of LO Peg.

Observatories	**Start HJD (2400000+)**	**End HJD (2400000+)**	**Number of exposures**				**Ref**
			U	**B**	**V**	**R**	
ARIES ST	55130.118	56645.365	5	67	72	5	P
GRT	55766.811	55775.771	—	4	9	3	P
IGO	55130.100	55135.130	—	10	30	—	P
Archive							
Hipparcos	47857.501	48972.277	—	—	136†	—	a
ASAS	52755.911	55092.673	—	—	259	—	b
SuperWASP	53128.655	54410.482	—	—	8047†		c
Literature							
JKT	48874.519	48883.592	25	25	25	25	d
ARIES ST	52181.167	54421.047	—	90	119	—	e
EUO	52851.445	55071.521	5566	5566	5566	5566	f

Notes.
P - Present study; a - *Hipparcos* archive ; b - *ASAS* archive; c - *SuperWASP* archive
d - Jeffries et al. (1994); e - Pandey et al. (2009, 2005); f - Taş (2011).
† - *Hipparcos* and *SuperWASP* data were converted to corresponding V-band magnitude.

analysis. *SuperWASP* observations of LO Peg during May 3, 2004, to June 2006, were unfiltered which were not useful for our study (see Pollacco et al., 2006). A broadband filter with a pass-band from 400 to 700 nm (known as *SuperWASP* V-band) was installed on June 2006. In our analysis, we make use of the data taken from June 2006, onwards. Since the *SuperWASP* data were taken in a broader band than the Johnson V-band; it is necessary to convert *SuperWASP* band magnitude (V_W) to Johnson V magnitude. Fortunately, the Landolt standard field TPHE with seven standard stars was observed by *SuperWASP*. Fig. 2.2 shows the plot between V and V_W of Landolt standard stars, where the continuous line shows the best fit straight line. We derived the relation between V and V_W as $V = V_W - 0.09$, and converted the V_W magnitude into V. Further, we have restricted our analysis within magnitude error less than or equal to 0.04 mag both in *ASAS* and *SuperWASP* data. Including present observations along with the data compiled from literature and archive, LO Peg was observed for ∼24.1 yr from 1989 to 2013.

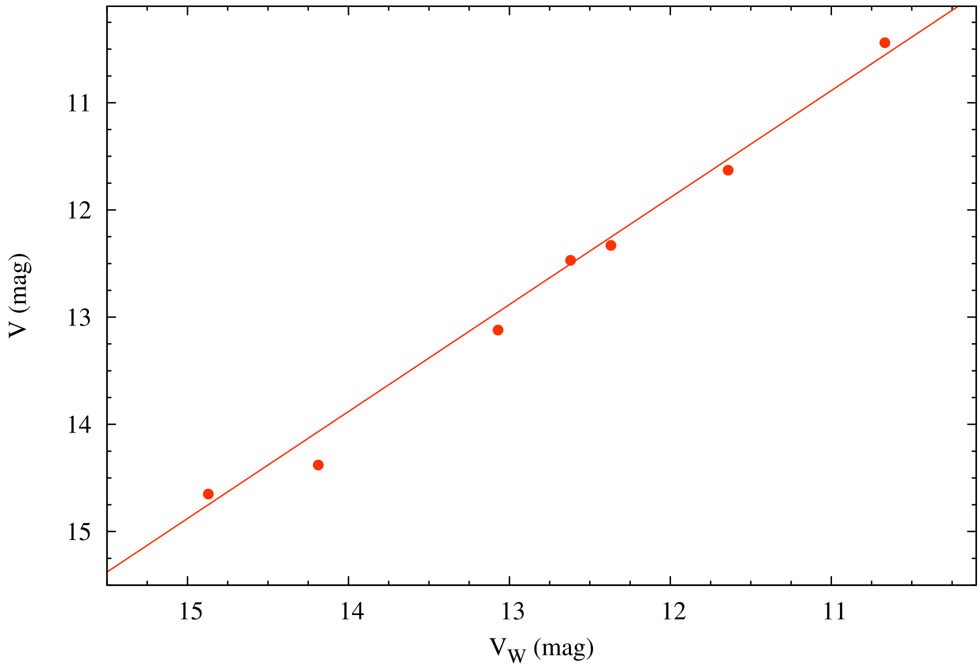

Figure 2.2: The relation between *SuperWASP* magnitude (V_W) and Johnson V-magnitude (V) of Landolt standard stars (TPHE field). Error bars shown in both axes are less than the size of the symbol. Continuous line shows the best fit straight line. We derived the relation between V and V_W as $V = V_W - 0.09$.

2.1.5 Data processing

The ground based telescopes suffer from the atmospheric extinction and seeing variations from one night to another. The seeing conditions of a night can severely affect the resolution of the instrument and the image quality, which is further degraded by the telescope optics (geometrical distortion), CCD effects (dark current, hot pixel) and the electronics associated with the CCDs (thermal noise). Along with the sources of interest, other unwanted cosmic signals also get detected on the CCD due to the cosmic rays which incident from all direction in the sky. All these effects described above can be removed from the raw CCD images using *Image Reduction and Analysis Facility* (IRAF[1]) software. The process of correcting the raw image to get an useful image on which further science can be done is known as *cleaning* or *pre-processing* of the image. The photometry *process* involves the measurement of intensity of the objects in terms of instrumental magnitude. The standard magni-

[1]IRAF is distributed by the National Optical Astronomy Observatories, Arizona which are operated by the Association of Universities for Research in Astronomy, Inc., under cooperative agreement with the National Science Foundation.

tude estimation from the instrumental magnitude is termed as the *post-processing* of the image. The various steps carried out in the reduction process of the images are summarized below.

2.1.5.1 Bias subtraction

An CCD image with an exposure time of zero seconds, i.e. the shutter remains closed and the CCD is simply read out, is known as “Bias” frame. The bias or zero frame allows the user to determine the underlying noise level within each data frame. The bias value in a CCD image is usually a low spatial frequency variation throughout the pixel-array, caused by the CCD on-chip amplifiers. The bias level of the CCD is determined from several bias frames (generally more than five) taken intermittently during observations in the course of a night. An average bias frame is created using the task *zerocombine* in IRAF and applying the *minmax* clipping algorithm, which was then subtracted from all the image frames, i.e., both target frames and the flat-field frames.

2.1.5.2 Dark subtraction

Dark frames are a method by which the thermal noise (dark current) in a, CCD can be measured. Subtraction of a dark frame from each target frame was not carried out for the observations reported here, as the CCDs used in the observations were cooled with liquid Nitrogen to -120° C at which the rate of accumulation of thermal charge is negligible for the exposure used in the present observations.

2.1.5.3 Flat fielding

Since all the pixels in a CCD do not possess the same response, it is necessary to correct the image for pixel-to-pixel variations in the CCD. This is accomplished by exposing the CCD to uniformly illuminated calibration field. In our observation, we took several (more than five) twilight sky frames in all U, B, V, and R photometric bands. They were median combined using the IRAF task *flatcombine* and employing the average sigma clipping algorithm. The combined flat-field frame was then normalized by mode and all the bias-subtracted target frames were then divided by this normalized flat-field frame.

2.1.5.4 Cosmic ray removal

The final step of the *pre-processing* of the images is the removal of cosmic ray strikes on pixel(s). Cosmic ray events are detected as few bright specks on the CCD image which are distinct from the stars in their intensity profile. The cosmic ray events are typically single-pixel events and easily distinguishable against clearly broader stellar (Gaussian-like) point spread function (PSF[1]). The cosmic ray is removed from the flat fielded frames using the *cosmicray* task in *crutil* package of IRAF.

2.1.5.5 Photometry

After pre-processing, in order to derive the instrumental magnitude aperture photometry was performed on both the object and the comparison stars in each frame. The CCD chip co-ordinates of these stars were found by the IRAF task *daofind*. Using the task *phot* we properly center the star, and with the given radius of the aperture as input, it derives the background subtracted sum of all the photons within that aperture. This task also allows us to specify a series of increasing aperture from a optimal small aperture (FWHM of the stellar profile) to larger aperture (seven times of the FWHM). We also took great care that the neighboring stars would not start influencing the sky background of the selected stars. The increment of the aperture was 0.5 pixel. The larger the aperture, more the flux of the star would be enclosed by the aperture. However, with larger aperture, the errors introduced due to sky subtraction would also be larger. Therefore, the optimal aperture is selected in such a way that it is large enough to enclose most of the flux, but otherwise is as small as possible.

Since, theoretically, a stellar (gaussian) profile extends up to infinity, the magnitude is restricted for the chosen aperture and needs to be corrected for the excess counts in the wings of the stellar profile. The correction from profile fitting magnitude to apperture magnitude is carried out by the process of determining the aperture growth curve, i.e. a plot of magnitude within a given aperture versus aperture size. The aperture correction is simply the magnitude difference between the asymptotic magnitude and the magnitude at the given aperture. The most straightforward way to determine the aperture correction is to measure it directly from a number of growth curves. A more advanced method for doing the aperture correction is the DAOGROW algorithm (Stetson, 1990), implemented in the task *mkapfile*

[1]The point spread function is a two dimensional brightness distribution profile produced in the detector by the point source object.

in digiphot.photcal. It fits a five parameter (with usually only 3 of them free) stellar profile model to the growth curves for one or more stars in one or more images. It then computes the aperture correction from a given aperture to the largest aperture.

2.1.5.6 Differential photometry and selection of comparison stars

In order to do photometric measurements of stars, two main methods are generally applied: (i) all-sky photometry and (ii) differential photometry. We have adopted differential photometry to get the standard magnitude of the program star. This method is also easier than All-Sky photometry and provides the maximum accuracy when measuring small variations. With a modest CCD field of view, the process becomes very simple and very effective as the comparison stars are often within the field of the program star at all times. In order to check any variation in the differential light curve of the target star, one or few comparison stars are chosen in the same field of view as close in the brightness and the colour to the target star (see details in next paragraph). Another star is also chosen from the same field of view in order to check the variability of the comparison star (Howell et al., 1988) is called check star. The non-variablility in the instrumental magnitudes of the differences between the comparison and check stars in each frames will confirm the non-variability of both the stars. Any variation in difference between the program star and comparison star would be referred as the intrinsic variability of the program star.

The atmospheric extinction and colour of the comparison stars may affect the variability of the program star. The standard equation which is used to correct the observations for both the atmospheric extinction and the colour of the star is

$$m_{\lambda_0} = m_\lambda + K'_\lambda X + K''_\lambda cX \tag{2.1}$$

where m_{λ_0} is the true magnitude, m_λ is the observed magnitude, K'_λ is the principle extinction coefficient, K''_λ is the colour dependent extinction coefficient, c is the colour index, and X is the airmass. Due to the identical atmospheric layers for the same frame the program star and the comparison star both will have same value of K'_λ. However, second order extinction coefficient can have an effect on the differential magnitude. From equation 2.1 the differential magnitude between two comparison stars of colour index c1 and c2 is given by

$$\Delta m_{\lambda_o} = \Delta m_\lambda + K''_\lambda X \Delta c \tag{2.2}$$

where $\Delta c = c1 - c2$ is the difference in colour indices. The principal extinction term cancels off as both the comparison stars have same airmass. In our study for the program star LO Peg we have chosen TYC 2188-1288-1 and TYC 2188-700-1 as the comparison and check stars, respectively. Comparison star TYC 2188-1288-1 has an exactly same color (B–V = 1.02) which leads to $\Delta c = 0$. Therefore, in equation 2.2 second term also vanishes.

The differences in the measured U, B, V, and R magnitudes of comparison and check stars did not show any secular trend during our observations. The nightly means of standard deviations of these differences were 0.009, 0.008, 0.008, and 0.007 mag in U, B, V, and R bands, respectively. This indicates that both the comparison and check stars were constant during the observing run. The standard magnitudes of comparison and check stars were taken from NOMAD Catalog (Zacharias et al., 2005). The derived photometric uncertainties for program star, check star, and comparison star were propagated to get the final photometric uncertainty of LO Peg.

2.2 X-ray and UV band

The atmosphere of the earth does not allow X-ray and UV from stellar sources to penetrate through it. Therefore, in order to study the celestial objects in these wavebands the X-ray observatories have to fly above the Earth's atmosphere with different instruments onboard. For the present work, we have used two X-ray observatories: *XMM-Newton* and *Swift* to study the late-type stars in X-ray and UV/Optical waveband. I will give brief descriptions of these two satellites, followed by our observations and the data extraction and processing techniques.

2.2.1 *XMM-Newton* observatory

The European Space Agency's (ESA) *XMM-Newton* was launched on December 10, 1999. This is the biggest science satellite ever built in Europe, thus far, and the telescope mirrors are the most powerful ever developed in the world. The spacecraft circulates around the Earth once in every ∼48 hours in an elliptical orbit with the apogee and the perigee distances of ∼107000 km and ∼27000 km, respectively. It is three-axis stabilized satellite with the absolute pointing accuracy is of the 10 m long XMM-Newton is 0.25 arcsec over a 10-second interval. *XMM-Newton* has an ability to make long uninterrupted exposures with highly sensitive observations.

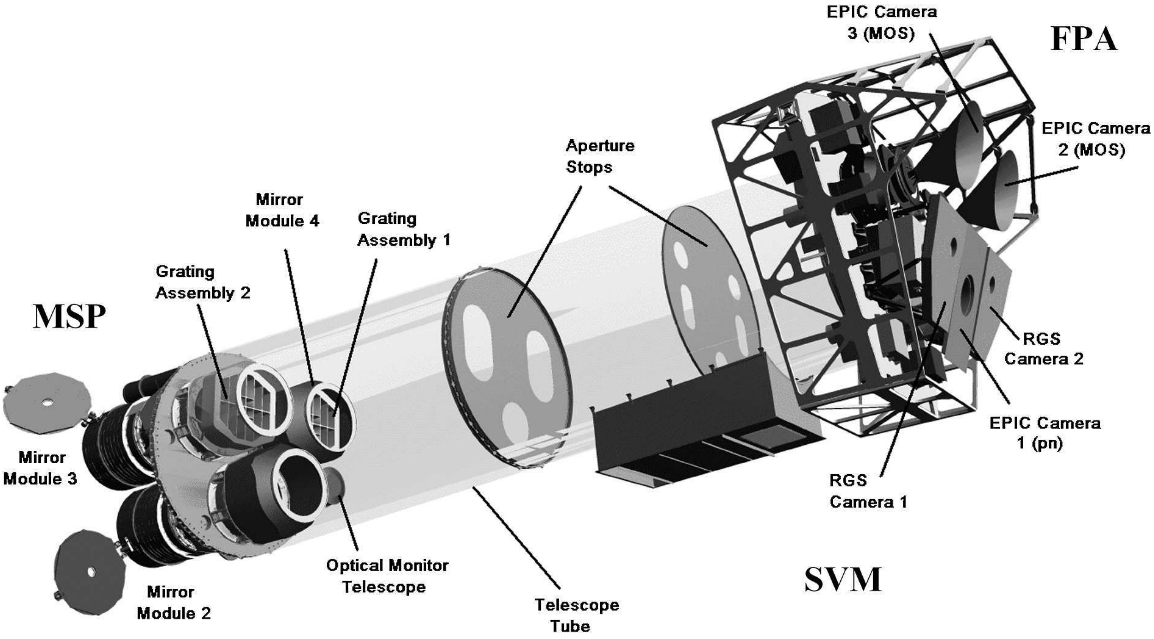

Figure 2.3: Schematic view of *XMM-Newton* satellite (*XMM-Newton* Community Support Team, 2010)

X-rays are very difficult to focus because of the high energy and their interaction with matter. When using mirrors, like XMM-Newton, the mirror surface has to be made of a material that does not readily absorb the X-rays, and the design has to ensure that the incoming rays hit the mirror surface at a shallow angle (grazing). Only in this way X-rays can be efficiently reflected and directed to a focus point. *XMM-Newton* carry three high throughput X-ray telescopes, each of which consists 'mirror modules' of 58 wafer-thin nickel mirrors, which are gold-plated and nested in each other just a few millimetres apart with a coaxial and confocal configuration (Jansen et al., 2001). The total mirror surface area of the three mirror modules together exceeds 120 m^2. Fig. 2.3 shows schematic view of *XMM-Newton* satellite.

There are three scientific instruments onboard in *XMM-Newton* observatory: the European Photon Imaging Camera (EPIC), the Reflection Grating Spectrometer (RGS) and the Optical Monitor (OM). For the present work, we have used only EPIC and RGS instruments onboard XMM-Newton satellite, the details of which are given below :

2.2.1.1 European Photon Imaging Camera (EPIC)

At the foci of the three X-ray mirror systems, there are three X-ray CCD cameras present onboard *XMM-Newton* satellite, with a FOV of 30′ (in diameter), and

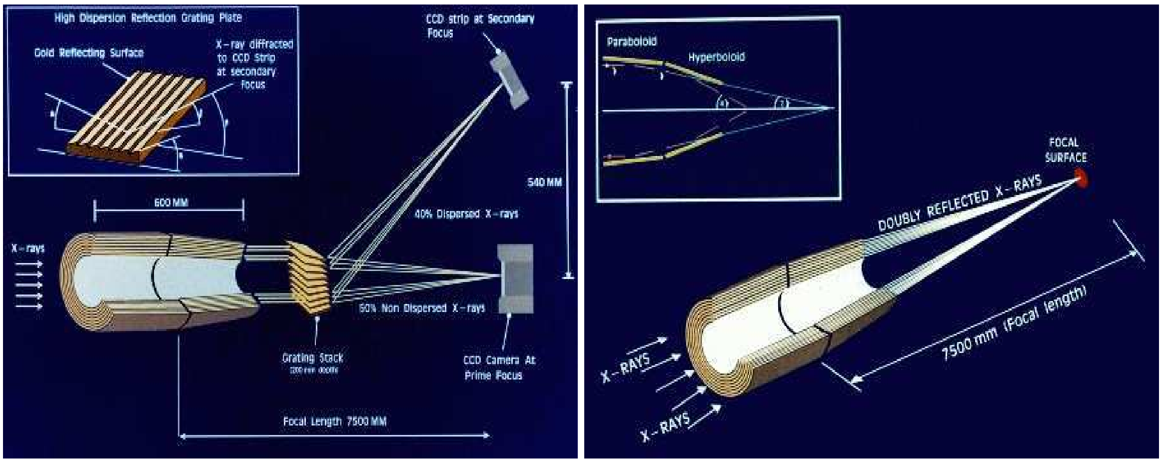

Figure 2.4: Schematic view of the mirror systems onboard *XMM-Newton* satellite (*XMM-Newton* Community Support Team, 2010)

moderate energy resolution (E/ΔE $\sim$ 20–50). Two of the three mirrors are designed for the two Metal Oxide Semi-conductor (MOS) detectors installed behind the telescope, which are also equipped with the reflection gratings assemblies. The zero'th order X-rays are focused on the EPIC-MOS for non-dispersive spectroscopy and higher order X-rays on the RGS for dispersive spectroscopy using the reflection grating assemblies. Therefore, incoming photons are divided into $\sim$44 % and $\sim$40 % for the EPIC-MOS and the RGS, respectively, and the rest of the light is lost due to structural obscuration. A schematic views of the two X-ray mirror systems are shown in Fig. 2.4. The MOS type CCDs are sensitive in the $\sim$0.15–12 keV energy range, wheras PN-type CCD is sensitive in the $\sim$0.15–15 keV energy range. The combination of the mirror system and the EPIC-PN module provide large effective area and a moderate energy resolution in the X-ray band. A constant degradation of the energy resolution is found at a rate of $\simeq$2.5 eV yr^{-1}. The absolute energy scale is accurate to $\sim$10–50 eV for the EPIC-PN.

For the EPIC instruments, three types of *Optical Blocking Filters* (OBFs) are installed for suppressing the optical contamination from the targets. The thick filter provides a capability of minimizing the optical contamination instead of a small effective area in the soft X-ray band. This is able to suppress efficiently the optical contamination for a point-like target with the V band magnitudes of 1–4 mag and -2–1 mag for the EPIC-MOS and the EPIC-PN. The medium filter is less efficient than the thick filter about 10^3, which is able to suppress the optical contamination for a point-like target with the V -band magnitudes of 6–9 mag. The remaining one, the thin filter, is used for the targets with the V-band magnitudes of >12 mag.

Both the EPIC-PN and the EPIC-MOS have several readout *modes* in operation. A full frame mode is the standard operation, in which all pixels of all CCDs are read out. Apart from this, a large window, a small window, and a timing mode can also be selected for each observation. A reduced number of read-out pixels provide a high temporal resolution with a stronger resistance to pile-up for bright targets. Typical images obtained in each mode are shown in Fig. 2.5.

2.2.1.2 Reflection Grating Spectrometer (RGS)

A reflection grating is a mirror with tightly controlled grooves on it. In case of RGS, there are about 645 grooves per mm. The X-rays reflected off the top and the valley of the grooves interfere with each other and cause a spectral image whereby X-rays of different wavelength/energy are reflected under slightly different angles. On *XMM-Newton* satellite two reflection grating arrays are installed, each of which composed of 182 such grating plates. Each plate consists of a silicon carbide substrate coated with a thin (2000 Å) film of gold. The grating plates, with stiffening ribs on their rear side are integrated onto a beryllium support structure.

Once the X-ray beam is splayed out into a spectrum, they are focused on the two RGS cameras in the spectral focal plane geometrically offset with respect to the EPIC cameras. The RGS cameras are composed of a strip of nine back-illuminated MOS CCDs which are operated in single photon counting and frame transfer mode. From the positions of the photons on the detector, the high resolution X-ray spectrum as diffracted by the grating array is determined. Combining the energy and position information allows us to separate the contributions from the various overlapping grating orders. In order to reduce background noise, the cameras are operated in a range of -80°C – -120°C. This low temperature is sustained using the coldness of space, captured by two passive radiators on the outside of the spacecraft.

2.2.2 *Swift* Observatory

The *Swift* satellite is a Medium-sized Explorer program by the National Aeronautics and Space Administration (NASA). This multi-wavelength observatory makes observations of celestial sources in the X-ray and the optical/ultra-violet wavebands simultaneously. The satellite was launched on November 20, 2004. The spacecraft (see Fig. 2.6) orbits around the Earth once in $\sim$95 minutes in a low-Earth orbit at a $\sim$600 km altitude with an inclination angle of $\sim$21°.

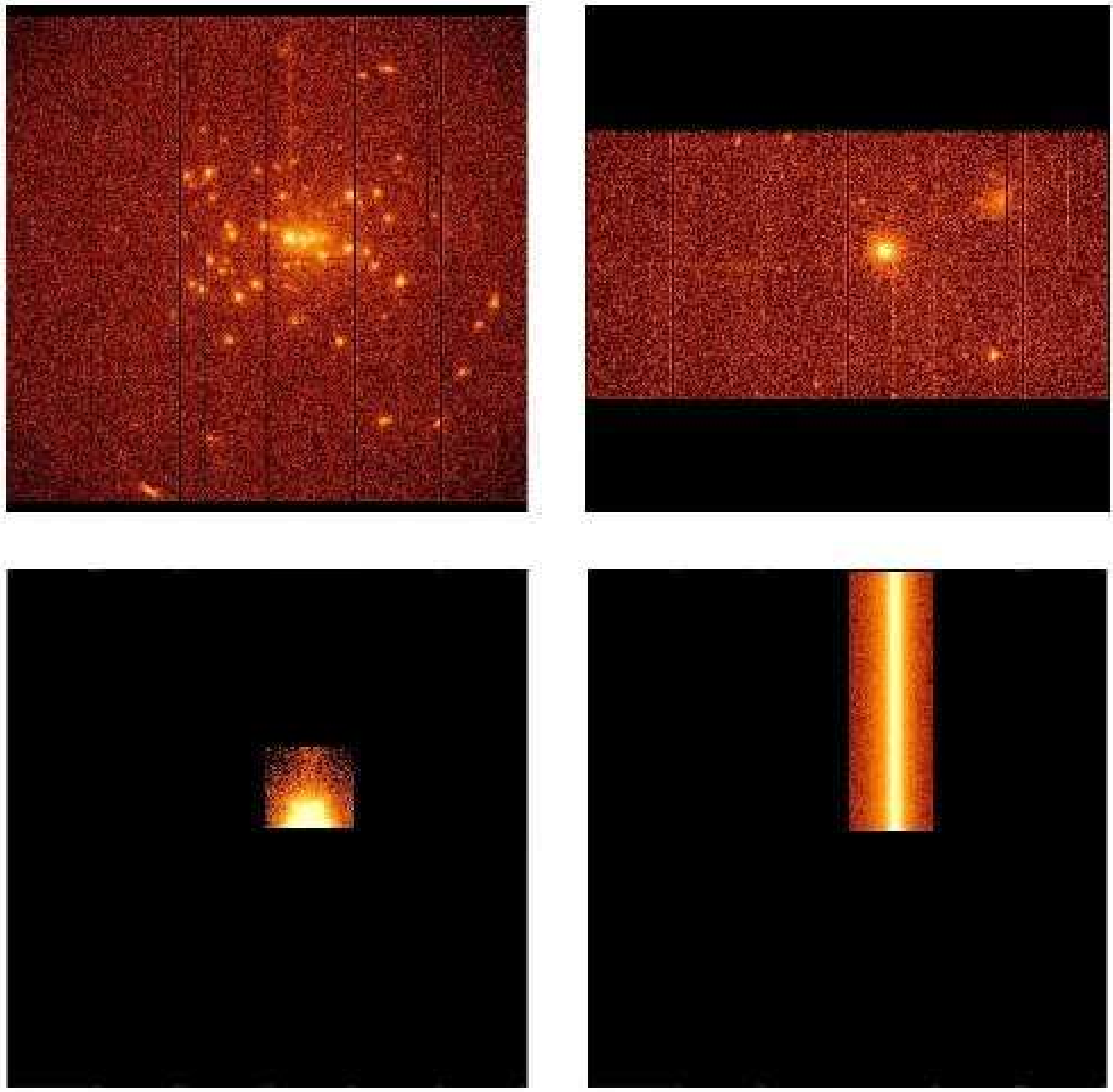

Figure 2.5: Typical images of four readout modes for the EPIC-PN (*XMM-Newton* Community Support Team, 2010). A full frame , a large window, a small window, and a timing mode are respectively shown in the top left, the top right, the bottom left, and the bottom right panels

Swift has three scientific instruments onboard in operation (Gehrels et al., 2004): the Burst Alert Telescope (BAT; Barthelmy et al., 2005) in hard X-ray, the X-Ray Telescope (XRT; Burrows et al., 2005) in soft X-ray, and the Ultra-Violet/Optical Telescope (UVOT; Roming et al., 2005b) in ultra-vioret and optical bands. Three independent instruments provide simultaneous observations in a wide-energy range. The spacecraft has an ability to point swiftly and autonomously a target position in less than approximately 90 s. All data products are promptly available in a public

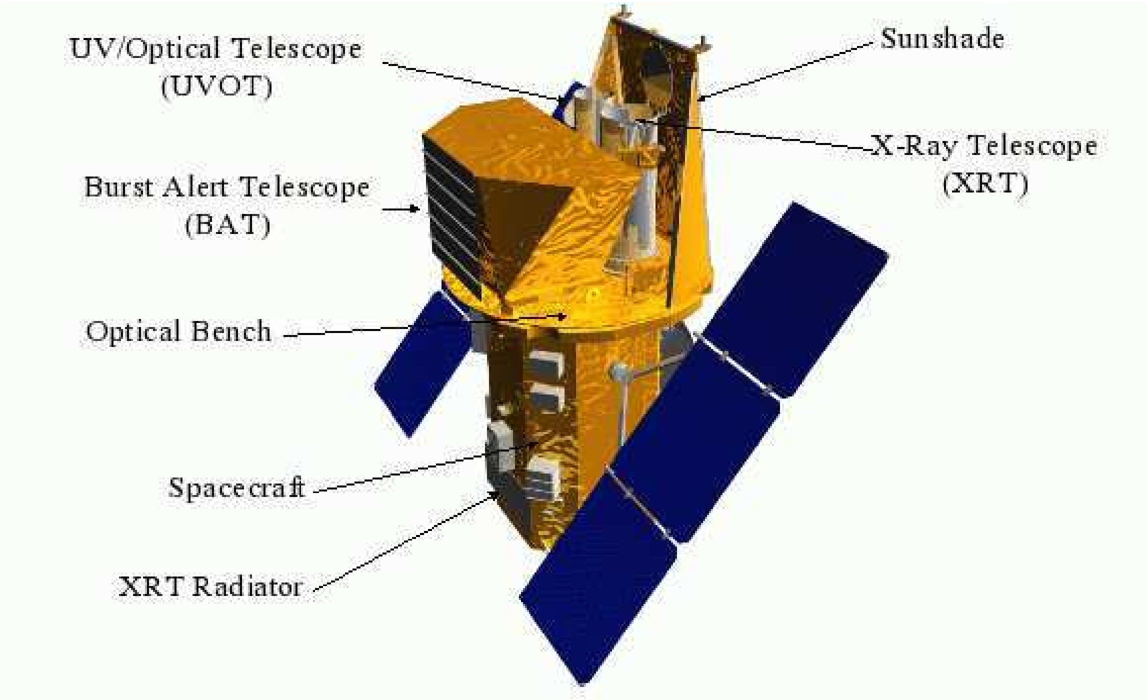

Figure 2.6: Schematic view of the mirror systems onboard *Swift* satellite (*Swift* Mission Participants, 2004)

archive.

2.2.2.1 Burst Alert Telescope (BAT)

The BAT is a highly sensitive, large FOV instrument produced by the Astrophysics Science Division at NASA's Goddard Space Flight Center (GSFC) with science flight software developed by the Los Alamos National Laboratory. It is designed to provide critical GRB triggers and it is also very useful to detect hard X-ray flares from the stellar sources. It is a coded aperture imaging instrument with a 1.4 steradians field-of-view (half coded), and the energy range is 15-150 keV for imaging with a non-coded response up to 500 keV. Within few seconds of detecting a burst, the BAT calculates an initial position, and check whether the burst merits a spacecraft slew and, if so, sends the position to the spacecraft.

The BAT uses a two-dimensional coded aperture mask and a large area solid state detector array to detect weak bursts, and has a large FOV to detect a good fraction of bright bursts. Since the BAT coded aperture FOV always includes the XRT and UVOT fields-of-view, moderate duration flares can be studied simultaneously with the X-ray and UV/optical emission.

The BAT runs in two modes: burst mode and survey mode. In the survey mode the instrument collects count-rate data in five-minute time bins for 80 energy intervals. When a burst occurs it switches into a photon-by-photon mode with a ring-buffer to save pre-burst information.

2.2.2.2 X-ray Telescope (XRT)

Swift's XRT is designed to measure the fluxes, spectra, and lightcurves over a wide dynamic range covering more than seven orders of magnitude in flux. It is a joint product of the Pennsylvania State University, the Brera Astronomical Observatory (OAB), and the University of Leicester. It works in the energy range 0.3 – 10 keV and provides the position of the X-ray sources with $\sim 5''$accuracy. The XRT has a total effective area of $\sim$110 cm^2 over a 0.2–10 keV energy range. Although the shape of the PSF of XRT is complex, the radial profile can be approximated by a King function as $\mathrm{PSF(r)} = (1 + (\mathrm{r}/\mathrm{r}_c)^2)^{-\beta}$, where r is the radius, r_c is the core radius, and β is the slope. The focal CCD detector is a three phase frame-transfer device. It has an imaging area of 600×600 pixels with a pixel size of 40 μm pixel^{-1} corresponding to a pixel scale of $2\overset{''}{.}36$ pixel^{-1}. Data of the imaging area is transferred to a framestore region of 600×600 array, and then it is read out according to an operating readout mode. The energy resolution of the CCD decreases from $\sim$190 eV (FWHM) at 10 keV to $\sim$50 eV (FWHM) at 0.1 keV.

There are four readout modes are available for XRT: (1) the Image-Long and Short (IM) mode, (2) Photo-Diode (PD) mode, (3) the Windowed-Timing (WT) mode, and (4) the Photon-Counting (PC) mode. A typical image with the WT and PC modes are shown in the left panel of Figure 2.7. This PC mode is a traditional frame transfer operation. It retains full imaging and spectroscopic resolution of the detector. The read-out time for a full frame is 2.5 s. We need to consider the photon pile-up for the measured count rates above $\sim$0.5 count s^{-1} in general observations. Whereas WT mode is suited for observing a moderately bright X-ray source. The narrow window and the restricted read-out provide a high-resolution X-ray light curves, spectra, and one-dimension images. The timing resolution is 1.7 ms. The photon pile-up is negligible for objects with a lower flux then $\sim$100 count s^{-1} in general observations (Romano et al., 2006).

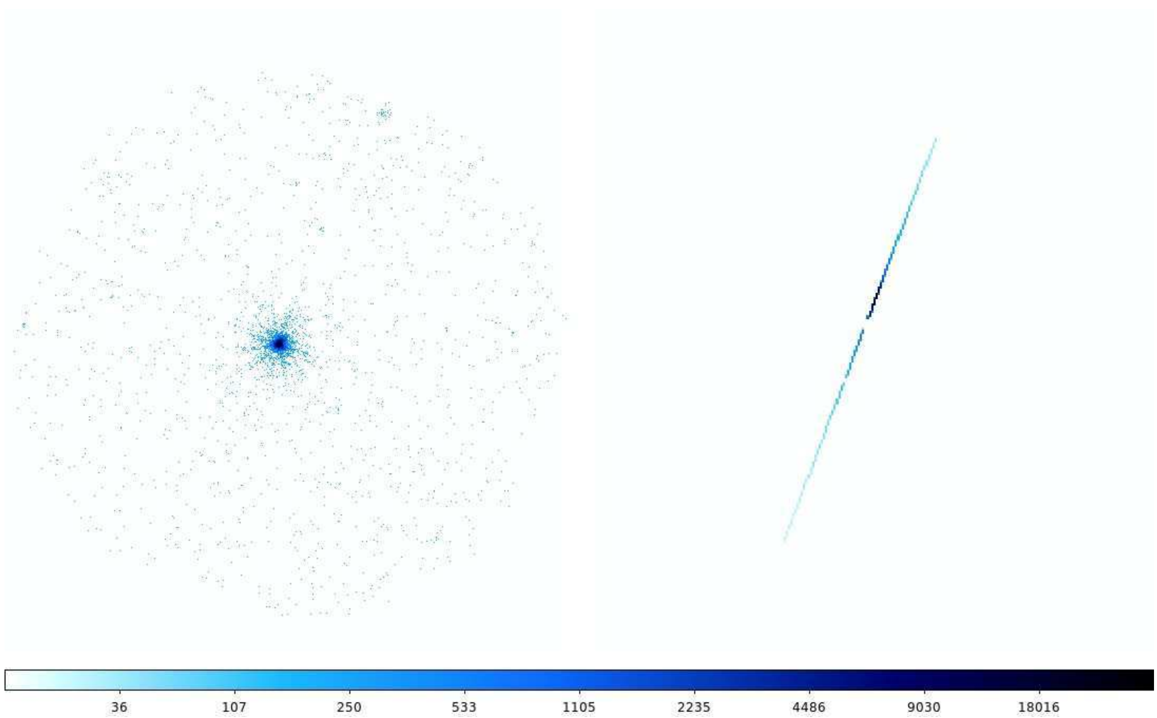

Figure 2.7: Typical images with PC (left) and the WT (right) modes

2.2.2.3 UV/Optical Telescope (UVOT)

The Ultra-Violet/Optical Telescope (UVOT) is a diffraction-limited 30 cm (12″ aperture) Ritchey-Chrétien reflector. It has an f/2.0 primary that is re-imaged to f/13 by the secondary. This results in pixels that are 0.502 arcsec over its 17 arcmin square FOV. The filter wheel includes a 4-times magnifier that results in 0.13 arcsec pixels for near diffraction limited imaging. The UVOT takes images and can obtain spectra (via a grism filter) during pointed follow-up observations. The UVOT is a joint product of the Pennsylvania State University and the Mullard Space Science Laboratory (MSSL).

The UVOT can detect a $m_B = 22.3$ mag point source in 1000 s using the open (white) filter. A comparable 30 cm ground-based telescope is limited to 20th mag due to sky brightness and seeing. Given an $m_B = 22.3$ source with a spectrum like an A0 star, the signal-to-noise ratio is ∼3 in 1000 s. Coincidence losses will start to degrade performance at count rates of greater than ∼10 count s^{-1} $pixel^{-1}$. Six UVOT broadband filters are available onboard: u, b, v, $uvw1$, $uvm2$, $uvw2$. The measured, on-orbit UVOT effective areas are shown in Fig. 2.8.

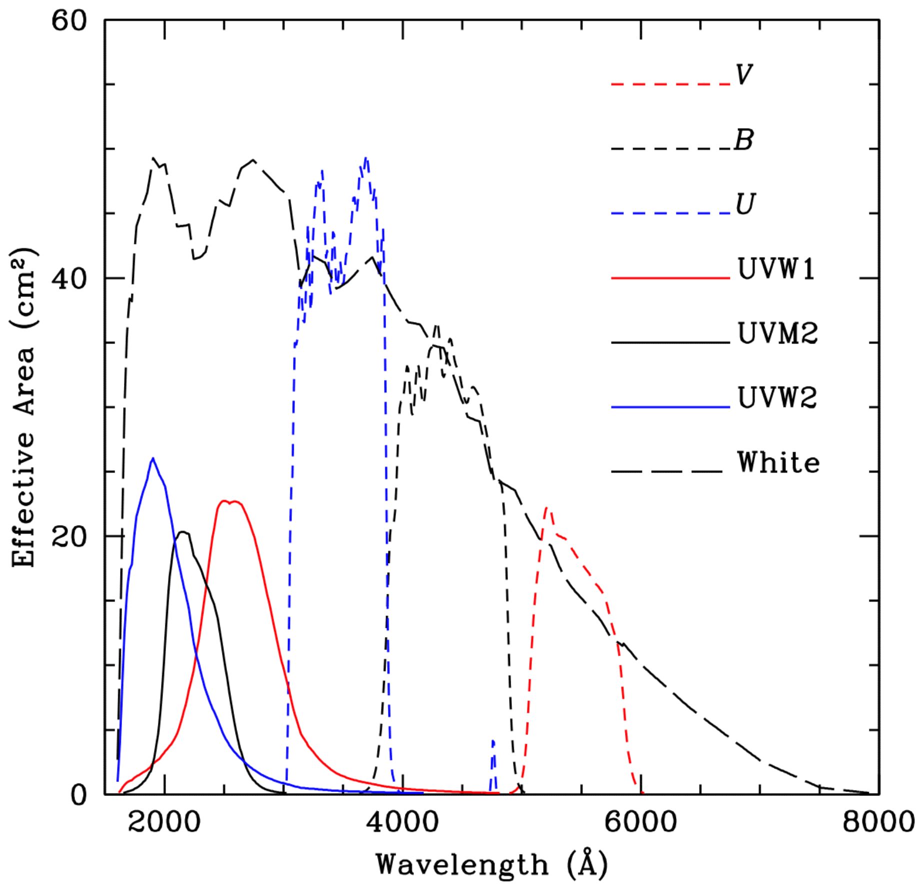

Figure 2.8: Effective area curves for the seven broadband UVOT filters shown. The white filter is shown in long dashed black. Other filters are: Dashed red–v, dashed black–b, dashed blue–u, solid red–uvw1, solid black–uvm2, solid blue–uvw2.

2.2.3 Observations

A log of X-ray and UV observations are given in Tables 2.3

2.2.3.1 *XMM-Newton*

47 Cas

47 Cas was observed by the *XMM-Newton* satellite using the European Photon Imaging Camera (EPIC) and Reflection Grating Spectrometer (RGS) instruments on 2001 September 11 at 02:21:19 UT for 40 ks. A log of X-ray and UV observations are given in Table 2.2 and 2.3.

Table 2.2: *XMM-Newton* Observation log: 47 Cas and AB DOR

Object	**Data**	**Rev.**	**Observation**	**Detector**	**Obs. Date**	**Time[3](UT)**	**Exposure**	**Off axis**
–	**set**	–	**ID**	**(Filter[2])**	(yyyy-mm-dd)	(hh:mm:ss)	**Time**(s)	(′)
47 Cas	–	0322	0111520101	PN(TH)	2001-09-10	23:30:24	50917	0.001
				M1(TH)		23:30:24	12287	
				M2(TH)		23:30:24	12292	
				RGS		15:23:24	61874	
AB Dor	S01	72	0123720201	PN(ME)	2000-05-01	02:52:31	60000	0.303
				RGS		02:30:21	62172	
AB Dor	S02	91	0126130201	PN(ME)	2000-06-07	09:44:12	41900	0.304
				RGS		05:29:46	59010	
AB Dor	S03	162	0123720301	PN(ME)	2000-10-27	15:23:55	55700	0.026
				M1(ME)		15:10:06	56039	
				M2(ME)		15:10:06	56039	
				RGS		15:01:40	58908	
AB Dor	S04a	185	0133120701	RGS	2000-12-11	14:38:38	58820	0.127
AB Dor	S04b	185	0133120101	RGS	2000-12-11	17:10:30	59420	0.127
AB Dor	S04c	185	0133120201	PN(TH)	2000-12-12	17:40:23	8497	2.211
				M1(TH)		20:22:00	6185	
				M2(TH)		20:22:00	6185	
				RGS		16:50:29	20909	
AB Dor	S05	205	0134520301	PN(ME)	2001-01-20	15:48:14	49100	0.132
				M1(ME)		15:34:37	49390	
				M2(ME)		15:34:37	49391	
				RGS		15:26:10	52309	
AB Dor	S06	266	0134520701	PN(ME)	2001-05-22	17:05:58	48219	0.275
				M1(ME)		16:50:15	49000	
				M2(ME)		16:50:15	49011	
				RGS		16:43:55	49610	
AB Dor	S07	338	0134521301	M1(ME)	2001-10-13	11:20:04	39147	0.110
				M2(ME)		11:20:04	39147	
				RGS		11:13:44	39745	
AB Dor	S08	375	0134521401	M1(ME)	2001-12-26	04:50:20	4200	0.156
				M2(ME)		04:50:20	4200	
				RGS		04:44:01	49732	
AB Dor	S09	429	0134521501	PN(ME)	2002-04-12	22:53:54	15932	0.175

Continued on Next Page…

Table 2.2 – Continued

Object –	**Data** set	**Rev.** –	**Observation** ID	**Detector** (**Filter**^{2})	**Obs. Date** (yyyy-mm-dd)	**Time**^{3}**(UT)** (hh:mm:ss)	**Exposure** **Time**(s)	**Off axis** (′)
				M1(ME)		22:34:35	16241	
				M2(ME)		22:34:37	16241	
				RGS		12:33:39	53220	
AB Dor	S10a	462	0155150101	PN(ME)	2002-06-18	03:12:38	5000	0.022
				M1(ME)		07:03:16	6084	
				M2(ME)		07:03:16	6084	
AB Dor	S10b	462	0134521601	PN(ME)	2002-06-18	16:49:58	17461	0.062
				M1(ME)		16:27:06	17117	
				M2(ME)		16:27:06	17117	
				RGS		09:30:06	47970	
AB Dor	S11	532	0134521801	RGS	2002-11-05	06:25:44	19912	0.159
AB Dor	S12	537	0134521701	M1(ME)	2002-11-15	05:45:10	19401	0.126
				M2(ME)		05:45:14	19652	
				RGS		05:44:24	19913	
AB Dor	S13	546	0134522001	M1(ME)	2002-12-03	05:00:00	18992	0.076
				M2(ME)		04:59:57	18992	
				RGS		04:59:07	20641	
AB Dor	S14	560	0134522101	M1(ME)	2002-12-30	10:49:02	48648	0.080
				M2(ME)		10:48:58	48400	
				RGS		10:48:08	50648	
AB Dor	S15	572	0134522201	RGS	2003-01-23	03:22:28	52368	0.086
AB Dor	S16	605	0134522301	M1(ME)	2003-03-30	20:19:57	3600	0.001
				M2(ME)		20:19:56	3600	
				RGS		10:30:52	48918	0.073
AB Dor	S17	636	0134522401	RGS	2003-05-31	16:39:30	28869	0.029
AB Dor	S18a	668	0160362501	M1(ME)	2003-08-02	10:05:29	5001	0.084
				M2(ME)		10:05:28	5001	
				RGS		05:13:56	22714	
AB Dor	S18b	668	0160362601	M1(ME)	2003-08-02	13:14:01	4999	0.118
				M2(ME)		13:14:01	4999	
				RGS		13:13:17	23919	
AB Dor	S19	709	0160362701	PN(TN)	2003-10-24	05:25:27	10400	0.110
				M1(ME)		03:22:56	17521	
				M2(ME)		03:22:56	17521	

Continued on Next Page…

Table 2.2 – Continued

Object –	**Data** **set**	**Rev.** –	**Observation** **ID**	**Detector** **(Filter²)**	**Obs. Date** (yyyy-mm-dd)	**Time³(UT)** (hh:mm:ss)	**Exposure** **Time**(s)	**Off axis** (′)
				RGS		17:54:57	51836	
AB Dor	S20	732	0160362801	RGS	2003-12-08	01:44:24	53694	0.116
AB Dor	S21	910	0160362901	RGS	2004-11-27	20:14:10	56340	1.669
AB Dor	S22	981	0160363001	RGS	2005-04-18	09:35:17	52098	0.073
AB Dor	S23	1072	0160363201	RGS	2005-10-16	22:28:17	50099	0.097
AB Dor	S24	1293	0412580101	RGS	2006-12-31	20:30:18	45019	0.066
AB Dor	S25	1393	0412580201	RGS	2007-07-19	03:37:30	56973	0.108
AB Dor	S26	1478	0412580301	RGS	2008-01-03	19:26:09	48901	0.080
AB Dor	S27	1662	0412580401	PN(TH)	2009-01-05	06:28:06	10000	0.099
				M1(TH)		06:25:18	9990	
				M2(TH)		06:25:22	9990	
				RGS	2009-01-04	19:24:54	49875	
AB Dor	S28	1825	0602240201	PN(ME)	2009-11-25	21:00:10	55971	1.120
				M1(ME)		20:55:00	56103	
				M2(ME)		20:54:55	55856	
				RGS		20:53:43	58442	
AB Dor	S29	1848	0412580601	PN(TH)	2010-01-12	00:56:59	10000	0.029
				M1(TH)		00:54:10	9990	
				M2(TH)		00:54:15	9990	
				RGS	2010-01-11	13:53:04	49917	
AB Dor	S30	2027	0412580701	PN(TH)	2011-01-03	02:10:27	10000	0.107
				M1(TH)		02:07:20	12287	
				M2(TH)		02:07:19	12292	
				RGS	2011-01-02	15:05:24	62871	
AB Dor	S31	2209	0412580801	M1(TH)	2012-01-01	02:06:59	9999	0.001
				M2(TH)		02:06:59	10000	
				RGS	2011-12-31	15:23:24	61874	

[1] M1,M2 stand for MOS1 and MOS2, respectively.
[2] TH, ME and TN stand for thick, medium and thin filters, resoectively.
[3] Exposure start time.

Table 2.3: *Swift* Observational log: LO Peg, CC Eri, and SZ Psc

.

Object	**Observation**	**Obs. Date**	**Time (UT)**	**Exposure Time (s)**			**Off axis**
–	**ID**	(yyyy-mm-dd)	(hh:mm:ss)	**XRT**	**UVOT**	**BAT**	(′)
LO Peg	00037810001	2008-04-30	20:26:01	2800	2770	2869	1.578
LO Peg	00037810002	2008-05-01	22:17:01	2008	1987	2042	2.590
LO Peg	00037810003	2008-06-20	16:07:01	1678	1622	1783	1.894
LO Peg	00037810004	2008-07-07	18:58:01	1698	1692	1768	2.112
LO Peg	00037810005	2008-08-21	15:25:00	4276	4234	4014	3.095
LO Peg	00037810007	2011-07-07	19:10:01	643	632	661	2.700
LO Peg	00037810008	2012-01-15	09:29:01	5041	4987	5074	4.177
LO Peg	00037810009	2012-01-16	23:59:01	402	918	942	1.327
LO Peg	00037810010	2012-01-18	01:42:00	1582	1558	1593	3.149
LO Peg	00037810011	2012-01-19	14:40:01	1220	1199	1233	4.354
LO Peg	00037810012	2012-01-20	14:40:01	4004	3959	4031	3.001
LO Peg	00037810013	2012-04-16	12:26:01	1717	1696	1730	1.110
LO Peg	00037810014	2012-06-23	07:02:00	443	433	450	1.599
LO Peg	00037810015	2012-06-24	05:22:00	1577	1554	1589	1.129
LO Peg	00037810016	2012-06-29	13:48:00	393	380	–	1.882
LO Peg	00037810017	2012-07-02	23:26:59	798	787	805	2.502
LO Peg	00037810018	2012-07-07	23:50:59	366	314	–	2.005
CC Eri	00331821000	2008-10-16	11:06:56	1781	10	5896	0.713
CC Eri	00331821001	2008-10-16	14:21:46	8601	8601	8030	0.592
CC Eri	00516027000	2012-02-24	18:49:51	1236	63	5386	2.859
SZ Psc	00625898000	2015-01-15	08:52:56	5309	4914	10027	3.407
SZ Psc	00625898001	2015-01-15	17:04:57	2000	1995	396	2.044
SZ Psc	00625898002	2015-01-16	01:06:59	1994	1988	2002	2.233
SZ Psc	00625898003	2015-01-16	04:10:29	1989	1980	2001	1.742
SZ Psc	00625898004	2015-01-16	07:37:31	1988	1973	2000	0.618
SZ Psc	00625898005	2015-01-16	14:10:20	1999	1987	2002	0.233
SZ Psc	00033606001	2015-01-21	00:54:59	224	217	600	3.938
SZ Psc	00033606002	2015-01-21	00:59:59	1999	1979	1671	5.876

AB Dor

AB Dor has frequently been observed for ∼12 years (40 occasions) as a calibration target of *XMM-Newton* satellite (see Jansen et al., 2001) since 1st May 2000 (revoulution #72) to 1st January 2012 (revolution #2209), with different combinations of on-board instruments operating simultaneously.

In 40 observations of *XMM-Newton*, on one occasion (obs ID 0123720101) data is not available in the archive, on two occasions (obs ID: 0134520601 and 0134520501) only PN-data, and on another two occasions (obs ID: 0160363101 and 0160363301) only MOS data were present but filter was closed during all four observations. Therefore, the rest 35 observations were used in present analysis and will be discussed further. Our *XMM-Newton* observational details are concised in Table 2.2. For the sake of our present analysis we account single revolution as a single set, which gives a total of 31 sets combining those 35 observations. The nomenclature of the sets are given as "Sij", where ij = 01, 02, ..., 31, (see the first three columns of Table 2.2 for further details). Among 31 sets 11 sets were observed with all PN, MOS and RGS, 8 sets were observed with MOS and RGS, 2 sets were observed with PN and RGS, and rest 10 sets were observed with only RGS instruments. The PN and MOS detectors were operated with the thick, medium or thin filters (see column 4 of Table 2.2 for individual observations). Exposure time varies from ∼4 ks to ∼63 ks (see column 5). In total AB Dor was observed for 336 ks by PN detector and 427 ks by MOS detectors and ∼1583 ks by RGS detector.

2.2.3.2 *Swift*

LO Peg

LO Peg was observed in 17 epochs with *Swift* satellite from April 30, 2008, to July 2, 2012. The observations were made in soft X-ray band (0.3 – 10.0 keV) with XRT in conjunction with UVOT in UV bands (170 – 650 nm). The offset of the observations lies between $1'.11$ and $4'.35$. The XRT exposure time of LO Peg ranges from 0.3 ks to 5.0 ks. X-ray light curves and spectra of LO Peg were extracted from on-source counts obtained from a circular region of $36''$ on the sky centered on the X-ray peaks. Whereas, the background was extracted from an annular region having an inner circle of $75''$ and outer circle of $400''$ co-axially centered on the X-ray peaks. Simultaneous observations of LO Peg with *Swift* UVOT were carried out in uvw2 (192.8 nm), uvm2 (224.6 nm) and uvw1 (260.0 nm) filters (Roming et al., 2005a) with exposure times between 0.02 ks to 3.06 ks.

CC Eri

Two superflares were detected on CC Eri (F1 and F2). The flare F1 triggered *Swift*'s BAT on 2008 October 16 UT 11:22:52 (=$T0_1$) during a preplanned spacecraft slew. The flare F2 was detected as an Automatic Target triggered on board on 2012 February 24 UT 19:05:44 (=$T0_2$).

Flaring events F1 and F2 were observed by the XRT from $T0_1$+147.2 and $T0_2$+397.5 s, respectively. The XRT observes in the energy range of 0.3–10 keV using CCD detectors, with the energy resolution of ≈ 140 eV at the Fe K (6 keV) region as measured at launch time.

In the case of flare F1, due to the large XRT count rate, the initial data recording was in Windowed Timing (WT) mode; whereas from $T0_1 + 11.7$ s until the end of the observation ($T0_1 + 31.1$ s), data were taken in Photon Counting (PC) mode. The flare F2 was observed only in WT mode after $T0_2$ for 1.2 ks.

SZ Psc

The flare triggered the *Swift*'s Burst Alert Telescope (BAT; Barthelmy et al., 2005) at T0 = 09:08:42 on 15 January 2015. XRT started observing SZ Psc at $T0_3$+380.5s. The soft X-ray (0.3 – 10 keV) rate was then 90 ct/s, corresponding to 3.7×10^9 erg s^{-1} cm^{-2}. The initial and all subsequent XRT observations during the first day were made in Windowed Timing mode. The UVOT began observing SZ Psc from $T0_3$+108 s with a 10s settling exposure. After a 4.2 ks gap in XRT/UVOT observations, UVOT observed in all 7 UVOT filters with regular cadence until 1.7 Ms after the trigger. The UVOT returned to the field 4 months later (11Ms after the trigger) to determine the quiesent level in the optical and UV filters.

2.2.4 Extracting X-ray data products

The observations made by different X-ray observatories are archived at their science centers and can be retrieved from there. Archived data can also be retrieved from NASA's High energy Astrophysics Science Archive Research Center (HEASARC). The observations taken with each X-ray observatory has to be processed using its data reduction tools and procedure to bring it to a standard format which can be further reduced using X-ray astronomical data analysis package FTOOLS. Below we summarize the procedures adopted for various X-ray observatories to extract standard products from their raw data.

2.2.4.1 *XMM-Newton*

X-ray data from *XMM-Newton* were reduced using the *Science Analysis System* (SAS) [1] software, version 14.0.0 with updated calibration files. The preliminary processing of raw EPIC observation Data Files was done using the EPCHAIN and EMCHAIN tasks which allow calibrations both in energy and astrometry of the events registered in each CCD chip. However, the metatask RGSPROC was used to generate the RGS event files. For the EPIC data, we have restricted our analysis to the energy band 0.3–10.0 keV due to the fact that the background contribution at high energies is particularly relevant where stellar sources have very little flux and often undetectable. Event list files were extracted using the SAS task EVSELECT. The EPATPLOT task was used for all the EPIC observations to check the existence of pile-up affecting region. For AB Dor [obs ID: 0133120101] EPIC data was heavily piled up which was also not removable even after taking annular source region so in this study only RGS data was included for present analysis. Data from all three cameras were checked for high background proton flares, taking a source free region as a background at nearly the same offset as the source. Although in three occassions of AB Dor observation [obs ID: 0134522301, 0160362501, 0160362601] the entire data were found to be affected by high background proton flares, we have taken it for further analysis since AB Dor and 47 Cas being a very much X-ray bright object, will not be affected much with high-background proton flare. X-ray light curves and spectra of AB Dor and 47 Cas were generated from on-source counts obtained from circular regions with a radius 36″ and 40″, respectively, around the source. The background was taken with same radius from a source free regions on the detectors at nearly the same offset as the source.

In order to correct the EPIC light curve for good time intervals, dead time, exposure, point-spread function, quantum efficiency, and background contribution, the SAS EPICLCCORR tool was used . However, to create a background subtracted and dead time corrected combined light curve of RGS instruments (RGS1 + RGS2) with both the orders (order 1 and 2) SAS task RGSLCCOR was used. The EPIC spectra were generated using SAS task ESPECGET, which also computes the photon redistribution as well as the ancillary matrix. Finally, both the EPIC and RGS spectra were rebinned to have a minimum of 20 counts per spectral bin.

[1] The *XMM-Newton* SAS user guide can be found at http://xmm.esac.esa.int/external/xmm_user_support/documentation/

2.2.4.2 *Swift*

Swift observations are archived at University of Leicester data base and at the ASI Science Data Center (ASDC) in Italy. Data can be obtained from any of the centers or from HEASARC Swift interface.

BAT

We have used BAT pipeline software within FTOOLS[1] version 6.20 with the latest CALDB version 'BAT (20090130)' to correct the energy from the efficient but slightly non-linear on board energy assignment. BAT light curves were extracted using the task BATBINEVT. For the spectral data reported here, the mask-weighted spectra in the 14–50 keV band were produced using BATMASKWTEVT and BATBINEVT tasks with an energy bin of 80 channels. The BAT ray tracing columns in spectral files were updated using the BATUPDATEPHAKW task, whereas the systematic error vector was applied to the spectra from the calibration database using the BATPHASYSERR task. The BAT detector response matrix was computed using the BATDRMGEN task. The sky images in two broad energy bins were created using BATBINEVT and BATFFTIMAGE, and flux at the source position was found using BATCELLDETECT, after removing a fit to the diffuse background and the contribution of bright sources in the field of view. The spectral analysis of all the BAT spectra was done using the X-ray spectral fitting package (XSPEC; version 12.9.0n; Arnaud, 1996). All the errors associated with the fitting of the BAT spectra were calculated for a confidence interval of 68% ($\Delta\chi^2 = 1$).

XRT

In order to produce the cleaned and calibrated event files, all the data were reduced using the *Swift* XRTPIPELINE task (version 0.13.2) and calibration files from the latest CALDB version 'XRT (20160609)' release[2]. The cleaned event lists generated with this pipeline are free from the effects of hot pixels and the bright Earth.

From the cleaned event list, images, light curves, and spectra for each observation were obtained with the XSELECT (version 2.4d) package. We have used only grade 0–2 events in WT mode and grade 0–12 events in PC mode to optimize the effective

[1]The mission-specific data analysis procedures are provided in FTOOLS software package; a full description of the procedures mentioned here can be found at https://heasarc.gsfc.nasa.gov/docs/software/ftools/ftools_menu.html

[2]See http://heasarc.gsfc.nasa.gov/docs/heasarc/caldb/swift/

area and hence the number of collected counts. Taking into account the point-spread function correction (PSF; Moretti et al., 2005) as well as the exposure map correction, the ancillary response files for the WT and PC modes were produced using the task XRTMKARF. In order to perform the spectral analysis, we have used the latest response matrix files (Godet et al., 2009), i.e. SWXWT0TO2S6_20010101V015.RMF for the flare F1 and SWXWT0TO2S6_20110101V015.RMF the flare F2 in WT mode and SWXPC0TO12S6_20010101V014.RMF for flare F1 in PC mode. All XRT spectra were binned to contain more than 20 counts bin^{-1}. The spectral analysis of all the XRT spectra was carried out in an energy range of 0.3–10 keV using XSPEC. All the errors of XRT spectral fitting were estimated with a 68% confidence interval ($\Delta\chi^2 = 1$), equivalent to $\pm 1\sigma$. In our analysis, the solar photospheric abundances ($Z_\odot$) were adopted from Anders & Grevesse (1989), whereas, to model N_H, we used the cross-sections obtained by Morrison & McCammon (1983).

While extracting the light curve and spectra, we took great care in order to correct the data for the effect of pile-up in both WT and PC modes. At high observed count rates in WT mode (several hundred counts s^{-1}) and PC mode (above 2 counts s^{-1}), the effects of pile-up are observed as an apparent loss of flux, particularly from the center of the PSF and a migration from 0–12 grades to higher grades and energies at high count rates. To account for this effect, the source region of WT data were extracted in a rectangular 40 × 20 pixel region (40 pixels long along the image strip and 20 pixels wide; 1 pixel = 2.″36) with a region of increasing size (0 × 20–20 × 20 pixels) excluded from its center, whereas the background region was extracted as 40 × 20 pixel region in the fainter end of the image strip. We produced a sample of grade ratio distribution using background-subtracted source event lists created in each region. The grade ratio distribution for the grade 0 event is defined as the ratio of the grade 0 event over the sum of grade 0–2 events per energy bin in the 0.3–10 keV energy range. Comparing the grade ratio distribution with that obtained using non-piled-up WT data, in order to estimate the number of pixels to exclude, we find that an exclusion of the innermost 5 pixels for F1 and 3 pixels for F2 were necessary when all the WT data are used. In order to carry out a more robust analysis for pile-up corrections, we also fit the spectra with an absorbed power law. The hydrogen column density N_H was fixed to the values that were obtained from the fit of the non-piled-up spectrum (exclusion of innermost 20 pixels was assumed to be unaffected by piled-up). This gives similar results of exclusion of the innermost pixels within its 1σ value. In PC mode, since the pile-up affects the center of the source radial PSF, we fit the wings of the source radial PSF profile with the XRT PSF model (a King function; see Moretti et al., 2005) excluding 15 pixels from the center and then extrapolated to the inner region. The PSF profile of the innermost 4 pixels was found to deviate from the King function, the exclusion of which enables us to mitigate the effects of pile-up from PC mode data.

UVOT

We have only performed the photometry for non-saturated images, we used a region of 5″ radius to extract the source counts and background counts were extracted using two circular regions of radius 12″ from a blank area of sky situated near to the source position. The UV magnitude and flux of each filter is obtained from the images using the *Swift* tools UVOTMAGHIST.

2.2.5 X-ray Temporal Analysis

The lightcurve (time versus counts or counts s^{-1}) of a source can be extracted from a circular region of a few arcsecond to a few arcminute radius centered on the source of interest in an X-ray image using the task XSELECT in FTOOLS. Similarly, the background lightcurve can be extracted from the source free region on the same CCD. We used a task LCMATH to subtract the background lightcurve from the observed source lightcurve (actually a sum of the source and the background lightcurve). The task LCMATH allows to weight the individual light curves according to the area of the corresponding region used before subtracting. The light curves thus obtained contain only source counts and can be plotted as well as re-binned using the task LCURVE.

2.2.6 Spectral Analysis

X-ray spectrum is computed by histogramming of PI values of all the photons within an extraction region. Source and background spectra are constructed separately. An observed X-ray spectrum is distribution of photon counts over the PI channels. The photon count rate (in count s^{-1})in PI channel is given by

$$C(I) = \int_0^\infty R(I, E) f(E) A(E) dE \tag{2.3}$$

where R(I, E) is probability of observing a photon with energy E in channel I, f(E) is photon flux density at energy E (source spectrum, in photons s^1 cm^{-2} keV^{-1}), A(E) is the effective area of the telescope and the detector system (Davis 2001). Usually it is not possible to determine the source spectrum f(E) by inverting the above equation. Therefore, a model source spectrum describable in terms of a few parameters, f(E, p1, p2, ...), is chosen and a model source count rates $C_P(I)$, are predicted which is compared to the observed data. This is usually done by varying the parameters and minimizing the χ^2 fit statistic. For this purpose, X-ray spectral fitting package XSPEC (Arnaud 1996) is used. The effective area is input into this program via a file called the ancillary response file (ARF) and the energy resolution of the detector is specified by the redistribution matrix file (RMF). The parameters corresponding to the minimum χ^2 are referred to as the best-fit parameters. χ^2 is defined as

$$\chi^2 = \sum (C_p(I)^2)/(\sigma(I)^2) \tag{2.4}$$

The χ^2 statistics provides a well-known goodness-of-fit criterion for a given number of degree of freedom or dof(ν). If χ^2 exceeds a critical value (Bevington 1969) one can conclude that $f_b(E)$ is not adequate to model for C(I). A general rule for an acceptable model is that reduced χ^2 (χ^2/ν) must be approximately one or $\chi^2 \sim \nu$ for an acceptable model.

2.2.7 Coronal plasma model

Coronal plasma models have been used extensively to model the solar coronal spectrum and the spectra of stellar coronae. A coronal plasma model is an 'ideal' where plasmas, viz: the plasma is (i) collisionally ionized and radiatively cooled, (ii) in ionization equilibrium, (iii) optically thin at all energies to its radiation, (iv) has electron and ion components with Maxwellian energy distribution, and (v) not affected by any external radiation through like photoionization. Conditions close to these are often found in low density ($n_e \leq 10^{10} cm^{-3}$), high temperature ($T_e = 10^{6-8} K$) plasma such as solar corona. Given these assumptions and assuming that the atomic physics for line and continuum is accurately described, for any specified T_e and n_e, and adopted set of elemental abundances, the emissivity per unit volume of the model plasma as function of energy can be calculated (Drake et al., 1997).

The current most efficient model to model the steller corona is the Astrophysical Plasma Emission Code (Smith et al., 2001), which uses atomic data in the companion Astrophysical Plasma Emission Database (APED) to calculate spectral models for hot plasmas. APEC calculates both line and continuum emissivities for a hot, optically thin plasma which is in collisional ionization equilibrium. It calculate the ionization balance directly (and thus handle nonequilibrium conditions). However APED does not yet contain all the necessary ionization/recombination rates, so we use tabulated values for the ionization balance in thermal collisional equilibrium.

Since there are thousands of lines of astrophysically abundant elements in the ultraviolet, EUV, and soft X-ray spectral regions that contribute, together with continuum processes such as free-free, bound-free, atomic data. The primary sources of uncertainty in these coronal models are probably (i) the particular ionization equilibrium that has been adopted, and (ii) error and emission in tabulated lines, their predicted energies and collisional strengths. This later problem is particularly acute in the Fe L-shell region of 0.5 to 1.5 keV (8 to 20 Å) which contains a large number of lines, principally the n=3 and n=4 to n=2 'L-shell' line complexes from a variety of ionization stages of Fe (Fe XVII - XIV), analogous to Ni L-shell complexes, as well as the resonance lines of the He- and H- like ions of N, O, Ne, and Mg. The standard way in which the spectra of astrophysical plasmas are compared with those predicted by coronal plasma models is to use global fitting procedures such as those incorporated into XSPEC.

Chapter 3

Evolution of magnetic activities in a UFR LO Peg

LO Peg has been an interesting object to study over the last two decades. It is a single, bright, young, K3V–K7V-type and a member of the Local Association (Gray & Bewley, 2003; Jeffries & Jewell, 1993; Montes et al., 2001; Pandey et al., 2005). It is one of the fast rotating active stars. From photometric observations Barnes et al. (2005) derived a rotational period of 0.42323 d. The fastest equatorial rotation rate of 65 km s^{-1} allows us to classify LO Peg as a UFR of the late spectral class. A presence of strong flaring activity was also identified by Jeffries et al. (1994) and Eibe et al. (1999) from H_α and He I D3 observations. Taş (2011) found evidence of flares in the optical band. Doppler imaging of LO Peg showed evidence of high polar activities (Barnes et al., 2005; Lister et al., 1999; Piluso et al., 2008). Several photometric, polarimetric, and X-ray studies were also carried out by Csorvási (2006); Dal & Taş (2003); Pandey et al. (2009, 2005), and Taş (2011). Using the polarimetric study Pandey et al. (2009) suggested the presence of prominence-like structure. The strong lithium line and the emission in the Hα, CaII H+K lines are observed in the optical spectrum of LO Peg, which indicates a high level of magnetic activities in this object. Zuckerman et al. (2004) have identified LO Peg as a member of a group of 50-Myr-old stars that partially surround the Sun. The above results encouraged us to observe and collect all available data, and analyze them with the aim to establish whether the star exhibits active longitudes and cyclic behavior in spot patterns and overall evolution of magnetic activities.

[1]**Results presented in this chapter have been published in (Karmakar et al., 2016).**

3.1 Short and long periods activity cycles

Fig. 3.1 shows the multi-wavelength light curves of LO Peg where bottom four panels indicate the optical U, B, V, and R photometric bands. The optical light curves display high amplitude both in short-term and long-term flux variations. The most populous V-band data was analyzed for the periodicity using Scargle-Press period search method (Horne & Baliunas, 1986; Press & Rybicki, 1989; Scargle, 1982) available in the UK Starlink PERIOD package (version-5.0-2; see Dhillon et al., 2001). Top panel of Fig. 3.2(a) shows the power spectra obtained from Scargle periodogram. We have also calculated the False Alarm Probability (FAP) for any peak frequency using the method given by Horne & Baliunas (1986). The significance level of 99.9% is shown by continuous horizontal line in the Fig. 3.2. Large and almost periodic gaps in the dataset led to further complications in the power spectrum. True frequencies of the source were further modulated by the irregular infrequent sampling defined by window function of the data. In order to resolve this problem we have computed window function with the same time sampling and photometric errors of the actual light curve, but contains only a constant magnitude as the average magnitude of the data (9.250 mag). We have repeated the process with many realization of noise, where we have generated 1000 random numbers within 3σ range of the mean value and taking these value as a constant we computed each periodogram. The resulting periodogram were averaged and shown in bottom panel of Fig. 3.2.

In Scargle power spectra the peak marked as 'S' corresponds to the rotational period of 0.422923 ± 0.000005 d, where the uncertainty in period was derived using the method given by Horne & Baliunas (1986). The uncertainty in the derived period was very small (< 1 s) due to the long base line of unevenly sample data. Further, there was a large gap in the data. Therefore, we derived the rotational period and corresponding error by averaging the seasonal rotational periods (see §3.2). The value of mean seasonal rotation period was found to be 0.4231 ± 0.0001 d, which is very similar to the previously determined period (Barnes et al., 2005). Two other smaller peaks at periods of ~ 0.212 d and ~ 0.846 d were identified in the power spectra as the harmonic and sub-harmonic, respectively. The former may indicate the existence of two active regions over the surface of LO Peg, whereas the later appears due to repeated occurrence of the same spot at multiple of it's period.

In order to search for the long term periodicity, we have zoomed the lower frequency range of Fig. 3.2(a) and shown in Fig. 3.2(b). Several peaks were found above the 99.9% confidence level, these peaks are marked by Li, where i = 1 to 11.

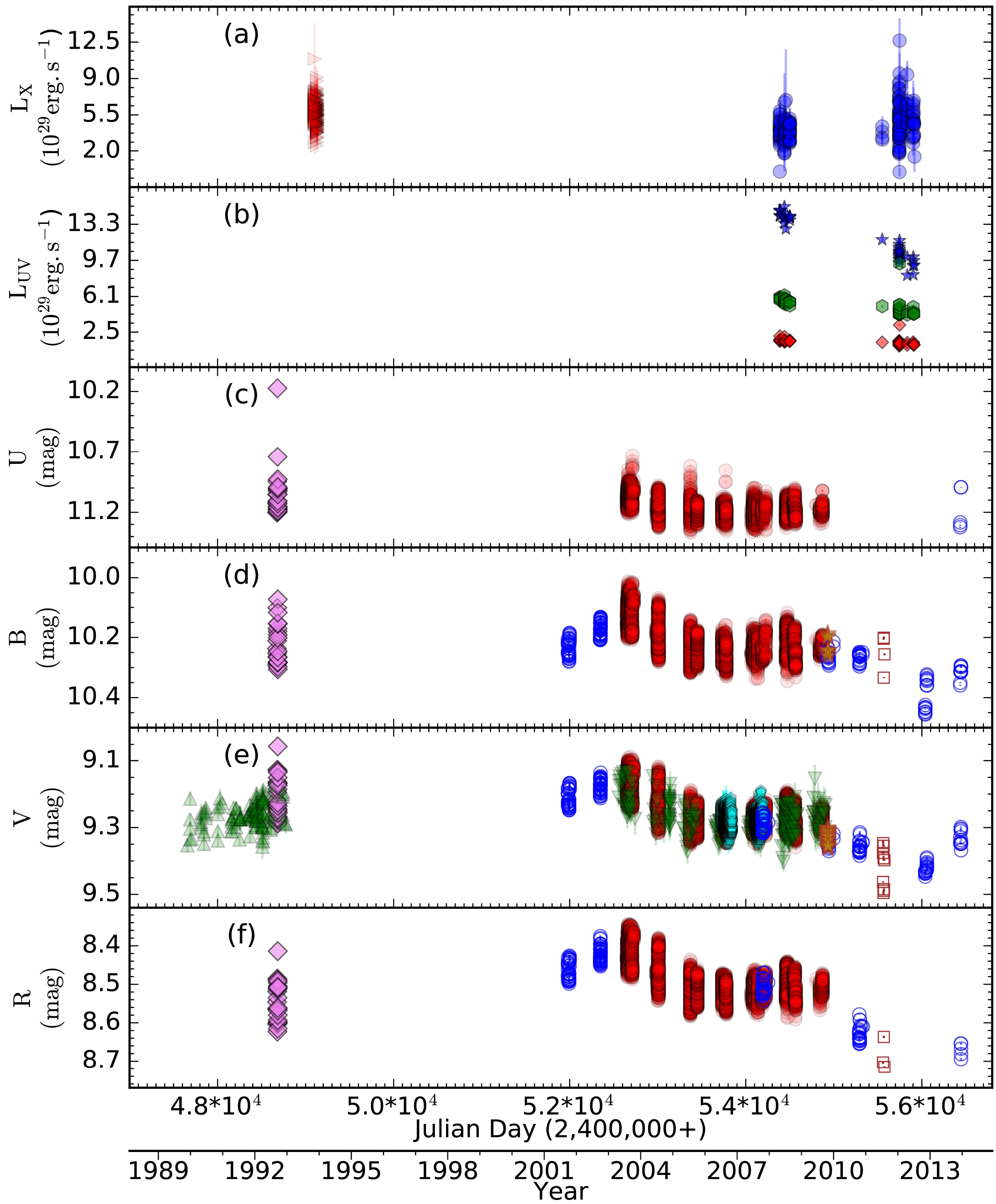

Figure 3.1: Multi-band light curve of LO Peg. From top to bottom – (a) The X-ray light curves obtained from *Swift* XRT (solid circle) and *ROSAT* PSPC (solid right triangle) instruments. (b) The UV light curve obtained from *Swift* UVOT in three different UV-filters: uvw2 (solid hexagon), uvm2 (solid diamond), and uvw1 (solid star). (c–f) The next four panels shows optical light curves obtained in U, B, V, and R bands, respectively. Observations were taken from ARIES (open circle), IGO (solid star), GRT (open square), EUO (solid circle), and JKT (solid diamond) telescopes and archival data were obtained from *Hipparcos* satellite (solid triangle), *SuperWASP* (solid pentagon), and *ASAS* (solid reverse triangle).

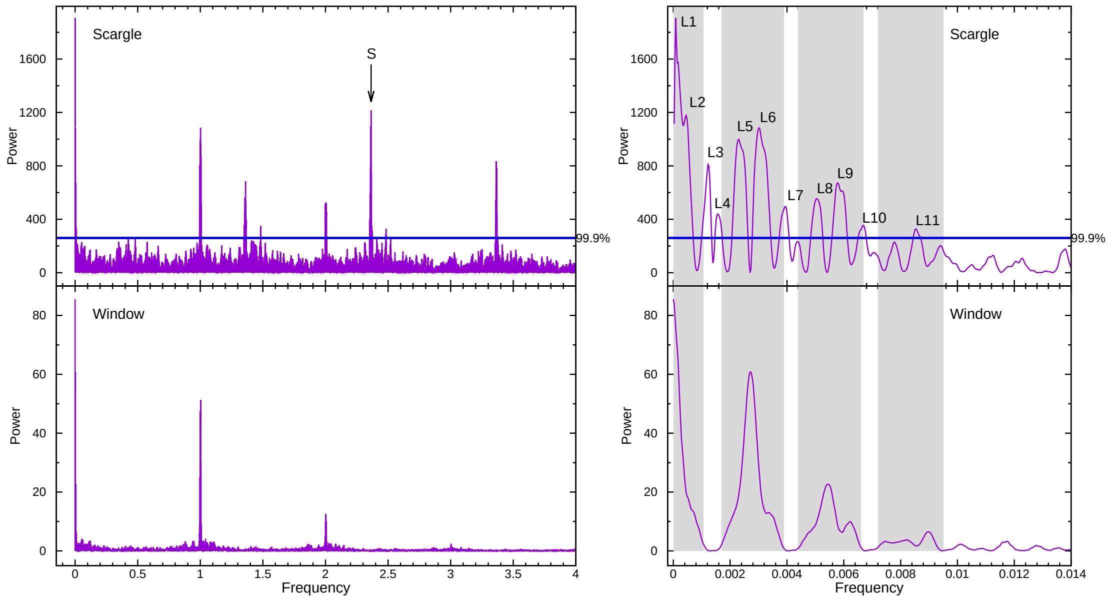

(a) (b)

Figure 3.2: (a) Scargle-Press periodogram obtained from V-band data (top) along with the calculated window function (bottom). The significance level of 99.9% is shown by continuous horizontal line. The peak marked as ‘S’ corresponds to the stellar rotation period. (b) The low frequency region is zoomed to show the long term periods, The shaded regions show the frequency domain ascribed to window function. Long-term peaks are marked by ‘L1 – L11’ (see the text for detailed description).

However many of the peaks were found under window function (see shaded region of Fig. 3.2(b)). Peaks corresponding to the periods L3 and L4 did not fall under the window function. Further, we have folded the data in each period and found periodic modulation only for periods 5.98 yr and 2.2 yr corresponding to L2 and L3. To avoid the modulation due to its rotation, we have made one point of every five-rotation period ($\sim$ 2 d). Further, the light curve evolved over a long time; therefore, for folding the data on the long periods, we have split the light curves for different times segments such that each segment has a length of minimum to those long periods. The top and bottom panels of Fig 3.3 show the folded light curves on periods 5.98 and 2.2 yr for different time segments, respectively. For the period 5.98 yr, we found only 3 time segments of $\sim$6 yr. For 2.2 yr period, we could make only 4 time-segments of each 3-4 yr.

Further, we have fitted sinusoids in the phase folded light curves for each interval. In the top panel of Figure 3.3, the best-fit sinusoids are shown by dashed and con-

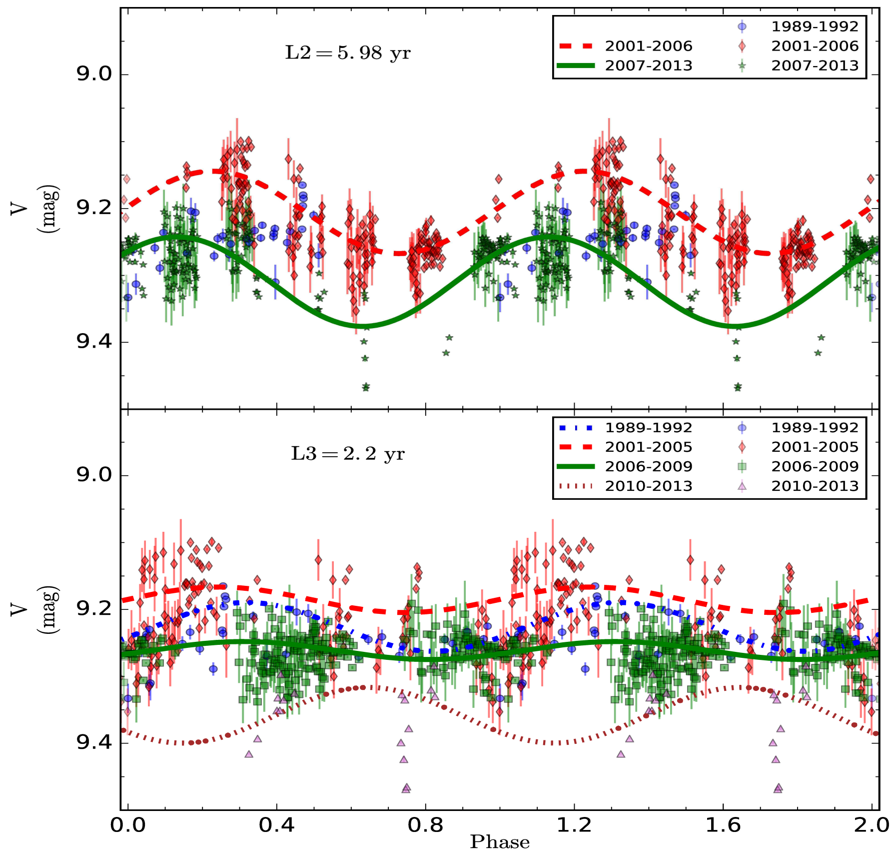

Figure 3.3: Folded light curve of LO Peg in V-band with periods of 5.98 yr (top) and 2.2 yr (bottom). The best-fit sinusoids are shown by dashed, dotted, dash-dotted and continuous lines for different time-intervals marked at the top-right corner of each panel. We could not fit the time-interval of 1989–1992 in top panel due to partial phase coverage of data points.

tinuous curves for the time interval 2001-2006 and 2007-2013, respectively. Sinusoid was not fitted to the time interval of 1989-1992 due to the partial phase coverage. The long-term evolution of the activity seems to present. Similar behaviour of the light curve was also seen while fitting sinusoid to the phase folded light curves on 2.2 yr in the bottom panel of Figure 3.3. The 2.2 yr period was also found to be similar to the latitudinal spot migration period derived from SDR analysis, which could be similar to the 11 yr cycle of the solar butterfly diagram. This type of activity cycle was also observed in similar fast-rotating stars such as AB Dor (Collier Cameron & Donati, 2002b; Järvinen et al., 2005b) and LQ Hya (Messina & Guinan, 2003). This was the first attempt to search the long-term periodicity in LO Peg.

3.2 Surface differential rotation: The butterfly diagram

The visibility of photospheric starspots is modulated by stellar rotation which causes quasi-periodic brightness variations on time scales of the order of the rotational period. The modulation period indicates the angular velocity of the latitude at which starspot activity is predominantly centered. Since the circumpolar spots will not affect the rotational modulation, with an inclination angle (i) of 45.0±2.5° on LO Peg (Barnes et al., 2005; Piluso et al., 2008), any modulation observed on stellar surface would be only due to the spot-groups present within a latitude of ±45° from the stellar equator. Similar to the solar case, the year to year variations of the rotational period can be described as the migration of stellar activity centers towards latitudes possessing different angular velocity. This migration is caused by the internal radial shear, which is assumed to be coupled with observed latitudinal shear (e.g. in $\alpha - \Omega$ dynamo model). In order to search for any change in the rotational period, we have determined photometric period of each observing season separately. We have chosen the observing seasons to derive the period due to the fact that the brightness of star in each season showed regular modulation which could be attributed to rotation of a stationary spot pattern of the star. Smaller time interval and hence smaller baseline introduces large uncertainty in determination of photometric period, whereas larger time intervals shows a significant change in shape of the light curve. In case of the sparse data obtained from *Hipparcos* satellite, the interval were chosen similar to the maximum data length of 0.7 yr obtained from ground based observations. In this way we could obtain 18 seasonal light curves, and average values of each seasonal light curve are shown in the top panel of Fig. 3.4 along with the time sequence of V-band magnitudes of LO Peg. Each seasonal data were analyzed using the Scargle-Press period search method. The uncertainty in photometric period and False Alarm Probability (FAP) were calculated following the method of Horne & Baliunas (1986). In the bottom panel of Fig. 3.4(a) we plot the seasonal values of the measured rotational periods (P_{sr}) and the results are summarized in Table 3.1. These modulation periods correspond to the angular velocity of the latitudes at which non-circumpolar spot-groups are present. Fig. 3.4(b) shows the Scargle power spectra of the measured seasonal rotational periods. Within the Nyquist frequency of 0.00124, we found maximum peak in the Scargle-Press periodogram is above 90% significance level and has an periodicity of 2.7 ± 0.1 yr. This period is well within 3σ level of the identified periodicity of brightness variation (see § 3.1). In ∼24 yr of observations 9 cycles of 2.7 yr period can be made, where we have detected six full cycles and one incomplete cycle (II). We found that the rotational period tends to decrease steadily during an 'cycle' of ∼2.7 yr, and jumping back to a higher value at the beginning of a new cycle. The abrupt changes in period of cycle-I may be a result of the sparse dataset obtained from *Hipparcos* satellite. However, in cycle-VII, we did not see any noticeable change in the rotational period.

Table 3.1: Parameters derived from the SDR analysis.

Cycle[a]	**Start HJD (2400000+)**	**END HJD (2400000+)**	**MEAN HJD (2400000+)**	**N$_0$**	**V$_{avg}$ (mag)**	**P$_{sr}$ (d)**	**FAP**
I	47857.500	48066.063	47961.782	19	9.268 ± 0.004	0.4243 ± 0.0003	0.05
	48113.175	48368.850	48282.378	13	9.255 ± 0.005	0.4313 ± 0.0005	0.12
	48368.850	48624.525	48490.262	30	9.248 ± 0.003	0.4203 ± 0.0002	0.03
	48624.525	48880.200	48756.841	73	9.233 ± 0.002	0.4231 ± 0.0001	3.28e-08
II	48880.200	48972.277	48926.410	25	9.194 ± 0.002	0.4237 ± 0.0004	2.31e-03
V	52181.166	52198.126	52189.646	37	9.1909 ± 0.001	0.4240 ± 0.0009	1.25e-06
	52546.207	52551.254	52548.731	50	9.154 ± 0.001	0.421 ± 0.001	1.99e-07
VI	52755.911	52942.538	52849.224	894	9.1522 ± 0.0003	0.42319 ± 0.00002	2.45e-165
	53142.922	53344.523	53243.722	574	9.2100 ± 0.0005	0.42308 ± 0.00005	6.20e-105
	53487.918	53650.354	53569.136	889	9.2546 ± 0.0003	0.41864 ± 0.00004	1.14e-144
VII	53853.920	54044.457	53949.188	4792	9.2617 ± 0.0002	0.42295 ± 0.00001	∼0
	54227.896	54454.050	54340.973	4700	9.2610 ± 0.0002	0.42331 ± 0.00001	∼0
	54590.916	54785.517	54688.216	1061	9.2487 ± 0.0004	0.42305 ± 0.00002	3.37e-177
VIII	54954.917	55196.045	55075.481	386	9.2603 ± 0.0008	0.4304 ± 0.0001	1.48e-09
	55489.158	55526.101	55507.630	23	9.338 ± 0.001	0.417 ± 0.001	0.05
IX	55758.817	55775.770	55767.294	9	9.402 ± 0.003	0.424 ± 0.001	0.22
	56239.143	56257.173	56248.158	20	9.402 ± 0.001	0.424 ± 0.001	0.01
	56636.357	56645.364	56640.861	12	9.312 ± 0.001	0.419 ± 0.002	0.05

Notes.
a - Detected starspot cycles of 2.7±0.1 yr (shown in bottom panel of Fig. 3.4(a)), N$_0$ is the number of data points during each season, V$_{avg}$ is the average V-band magnitude in each season, P$_{sr}$ is the seasonal rotational period, and FAP is false alarm probability.

The decrease in photometric periods within most of the cycles is reminiscent of the sunspot cyclic behaviour, where the latitude of spot forming region moves toward the equator, i.e., toward progressively faster rotating latitudes along an activity cycle, and spot-groups were present within ±45° latitude of LO Peg. This finding indicates that LO Peg has a solar-like SDR pattern. From spectroscopic analysis Piluso et al. (2008) also detected the presence of such lower latitude spots. It is interesting to note that the slope of the rotational period on LO Peg varies and therefore SDR amplitude ΔP ($= P_{max} - P_{min}$) changes from cycle to cycle. Similar behaviour was also observed in AB Dor (Collier Cameron & Donati, 2002b),

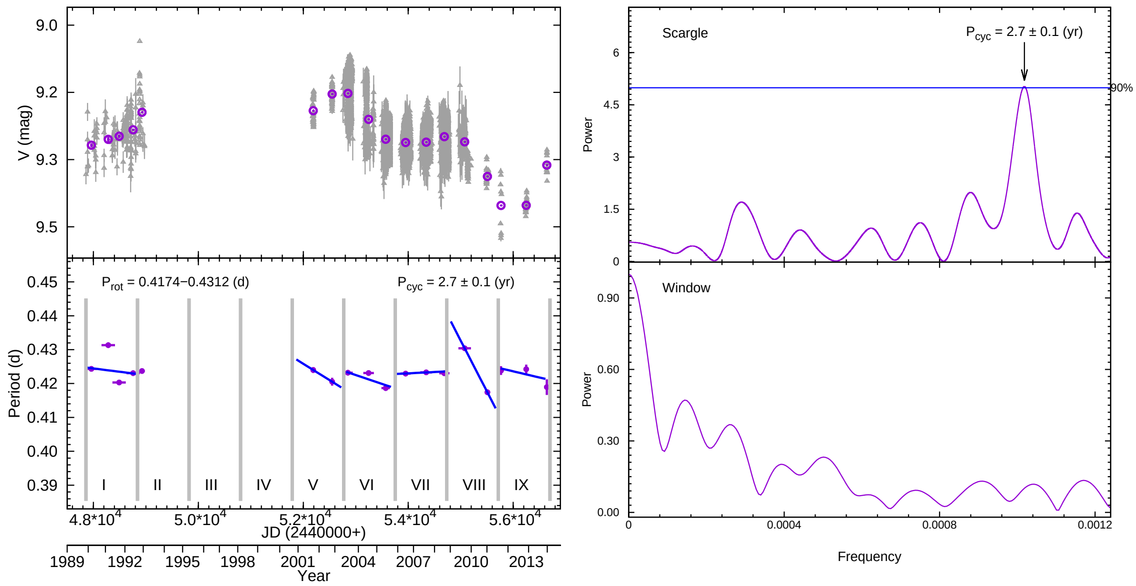

(a) (b)

Figure 3.4: Top panel of (a) shows the V-band light curve (solid triangles) along with the mean magnitude of each season (open circles). Solid circles in bottom panel of (a) shows the derived rotational periods in each season. The Scargle-Press periodogram of these seasonal periods along with calculated window function shown in top and bottom panel of (b), respectively, with 90% significance level marked with blue horizontal lines. The highest peak above 90% significance level indicates the cyclic period of 2.7 ± 0.1 yr. In bottom panel of (a) each period of 2.7 ± 0.1 yr is indicated with the vertical lines. The straight lines in each cycle show a linear fit to data during the cycle. The rotation period monotonically decreases along most the star-spot cycles showing a solar-like behaviour.

BE Cet, DX Leo, and LQ Hya (Messina & Guinan, 2003). This resembles either a wave of excess rotation on a time scale of the order of decades, or a variation of the width of the latitude band in which spots occur. LO Peg shows a change in rotation period from 0.43133 d to 0.41743 d, which corresponds to ~3 km s^{-1} change in $v$sin$i$, which is nearly 15 times more than AB Dor. We have estimated the differential rotation on LO Peg with $\Delta\Omega/\Omega$ ranging from 0.001 – 0.03, which is similar to that obtained by Barnes et al. (2005). AB Dor and LQ Hya having very similar spectral class and periodicity showed similar feature with the star LO Peg. Derived values of $\Delta\Omega/\Omega$ for AB Dor (Collier Cameron & Donati, 2002b) and LQ Hya (Berdyugina et al., 2002) are also similar to that for LO Peg. During more than two decades of observations only in September 2003 LO Peg was observed both photometrically (Taş, 2011) and spectroscopically (Piluso et al., 2008). In our SDR analysis, the first point of cycle-VI corresponds to that time interval (see Table 3.1 and Fig. 3.4). This time interval being at the starting of the cycle indicates the period corresponds to higher latitude. Therefore, we expect presence of spots on higher latitude on the surface of LO Peg. Piluso et al. (2008) have also found starspot concentration towards the polar region.

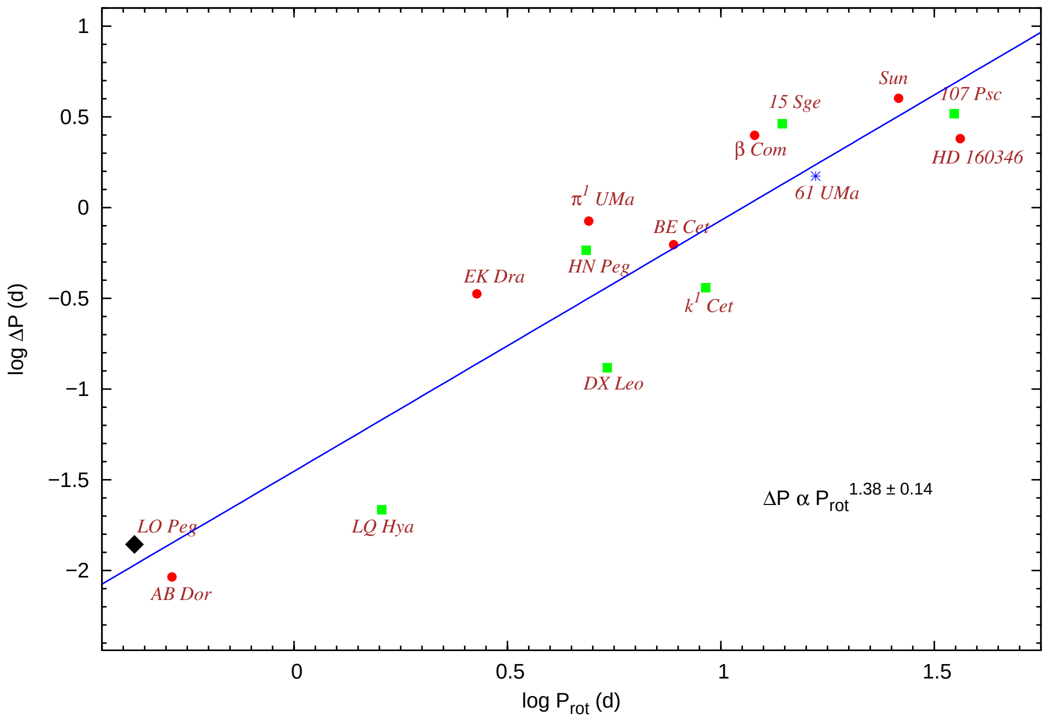

Figure 3.5: The log rotational period variations vs. the mean rotational period of stars. Solid circle, solid squares and asterisks denote the stars with solar, anti-solar and hybrid pattern. LO Peg is shown with solid diamond. The continuous line is a power law fit to the whole sample.

A positive correlation between the absolute value of SDR and the stellar rotation period was predicted by dynamo models according to a power law (Kitchatinov & Rüdiger, 1999) i.e. $\Delta P \ \alpha \ P_{rot}^{n}$; where ΔP is the SDR amplitude, P_{rot} is the rotational period and n is the power index. Kitchatinov & Rüdiger (1999) found that n varies with both rotation rate and with spectral type. This power law dependence is confirmed by observational data (Hall, 1991; Henry et al., 1995), although the observational and theoretical values of n differ (see Messina & Guinan, 2003). Fig. 3.5 shows the plot between ΔP and P_{rot} of LO Peg with other 14 stars with known activity cycles and SDR (Collier Cameron & Donati, 2002b; Donahue & Dobson, 1996; Gray & Baliunas, 1997; Messina & Guinan, 2003). We found LO Peg (solid diamond) follows the same trend with the nearest candidate AB Dor. Including LO Peg, we derive the relation $\Delta P \ \alpha \ P_{rot}^{1.4\pm0.1}$, which is very similar to the relations derived from other observational evidences such as Messina & Guinan (2003) (n = 1.4 ± 0.5), Donahue & Dobson (1996) (n = 1.30), Rüdiger et al. (1998) (n = 1.15 – 1.30). This indicates the disagreement between the observational (n = 1.1 – 1.4) and the theoretical (n > 2) values of power law index (Kitchatinov & Rüdiger, 1999).

3.3 Flares

Flares in LO Peg were searched using U, B, V, and R data. For this analysis, we have converted the magnitude into flux using the zero-points given in Bessell (1979). Fig. 3.6 shows two consecutive representative flares observed simultaneously in all four optical bands. The first flare was detected in all four bands while next flare was not detected in longer wavelengths (V and R band). Thus, a flare detected in one band is not necessarily detected in each of the optical bands. Due to the sparse data, we have not followed the usual flare detection methods as described in Osten et al. (2012), Hawley et al. (2014) and Shibayama et al. (2013). We have chosen different epochs such that, each epoch contains a continuous single night observation with at least 16 data-points and minimum observing span of $\sim$ 1 hr. A total of 501 epochs were found using the most populous V-band data, among which only 82 epochs have simultaneous observations with other three optical-bands.

The light curve of each epoch was first detrended to remove the rotational modulation by fitting a sinusoidal function. The local mean flux (F_{lm}) and standard deviation (σ_{ql}) of the flux were then computed at each time-sampled dataset. To avoid mis-detection of short stellar brightness enhancement as a flare, candidate flares were flagged as excursions of two or more consecutive data points above $2.5\sigma_{ql}$ from F_{lm} (see Davenport et al., 2014; Hawley et al., 2014; Lurie et al., 2015) with at least one of those points being $\geq 3\sigma_{ql}$ above F_{lm} in any of the optical band. Once the flare was detected using the above criteria, the flare segment was removed to calculate the exact value of σ_{ql}, where most of the flares were identified above the $3\sigma_{ql}$ from the quiescent state. This derived value of σ_{ql} was not used for further flare identification. Finally, each flare candidate, in each photometric band was inspected manually to confirm it as real flares. In this way, we have detected 20 optical flares. Flare nomenclatures were given as 'Fi', where i = 1, 2, 3, . . . 20; denotes the chronological order of the detected flares. Flare parameters of all the detected flares are listed in Table 3.2.

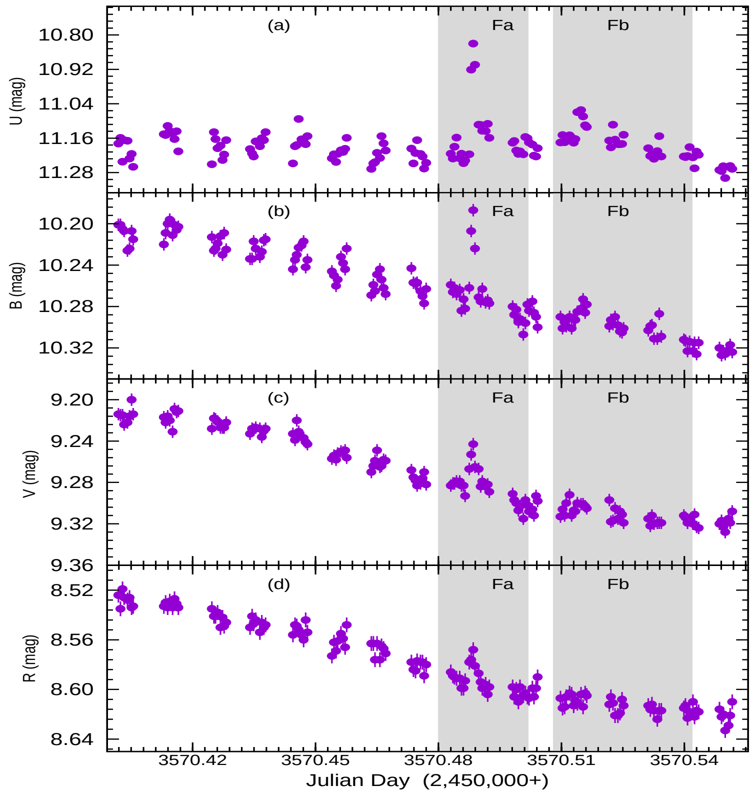

Figure 3.6: Two consecutive representative flares (shaded regions) on LO Peg simultaneously observed in U (a), B (b), V (c) and R (d) optical bands. The first flare shows activity level in all four optical bands. Whereas the second flare is detected only in shorter wavelengths (U and B bands).

Fig. 3.7 shows flares detected in V-band, where top panels of each plot show V-band magnitude variation during flares along with the fitted sinusoidal function and bottom panels show the detrended light curve with best fitted exponential function. Most of the flares of LO Peg show usual fast rise (impulsive phase) followed by a slower exponential decay (gradual phase). The e-folding rise (τ_r) and decay times (τ_d) have been derived from the least-squares fit of the exponential function in the form of $F(t) = A_{pk}e^{(t_{pk}-t)/\tau} + F_{lm}$ from flare-start to flare-peak, and from flare-peak to flare-end, respectively. In the fitting procedure $A_{pk}(= F_{pk} - F_{lm})$, F_{lm} and t_{pk} were fixed parameters. Here, F_{pk} is flux at flare peak at time t_{pk}. For the flare F13, the peak was not observed, therefore, the parameters A and t_{pk} were also kept as free parameters in exponential fitting. In order to get a meaningful fit, we restricted our analysis to those flares which contain more than two data points in rise/decay

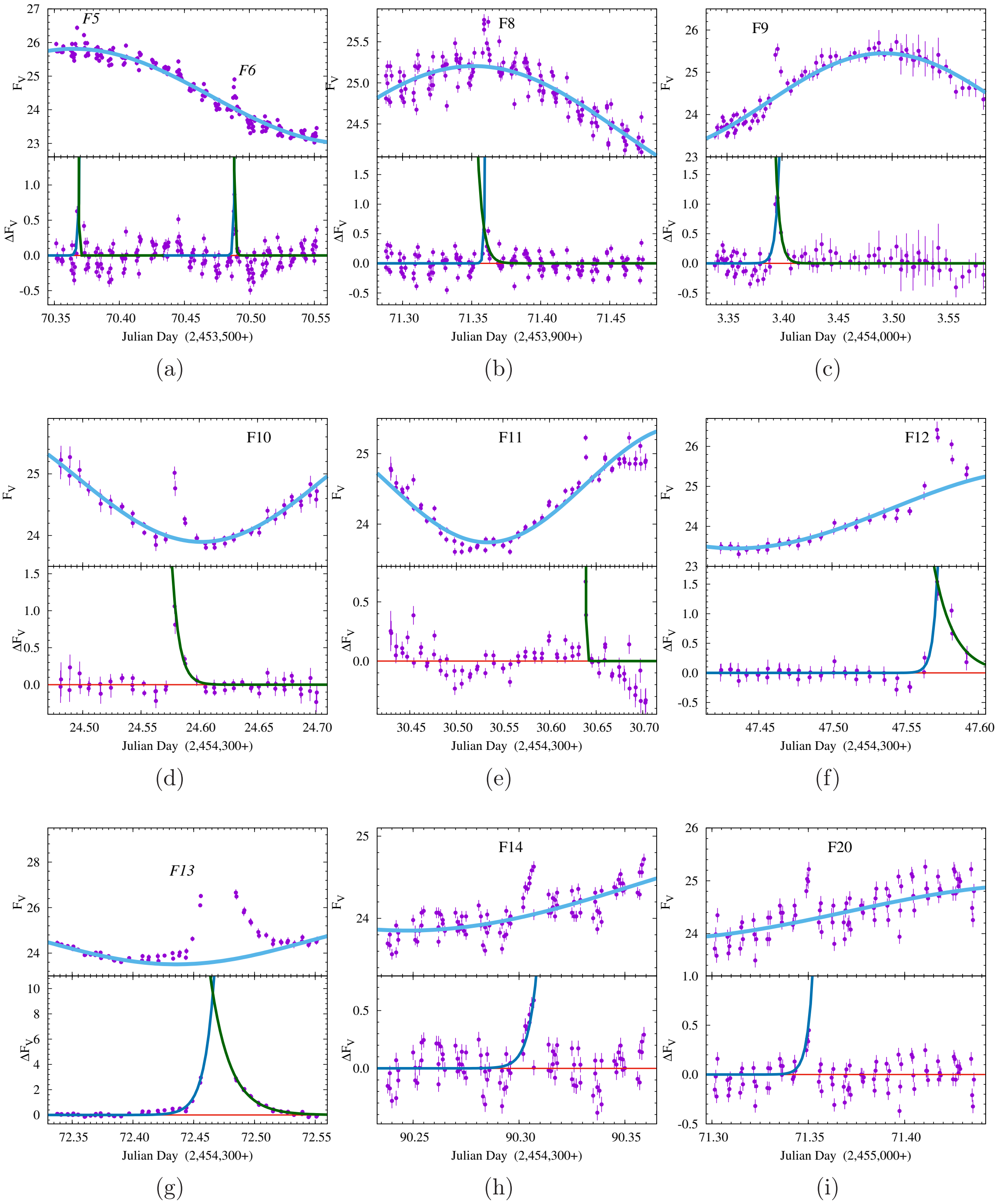

Figure 3.7: Light curves of all detected V-band flares on LO Peg. Top panel of each plot shows the light curve along with best-fitted sinusoid. The bottom panel shows the detrended light curve along with best fitted exponential functions fitted to flare rise and/or flare decay.

phase. The fitted values of τ_r and τ_d are given in columns 10 and 11 of Table 3.2. The values of τ_r were found to be in the range of 0.3 – 14 min with a median value of 2.5 min. Whereas, values of τ_d were derived in the range of 0.4 – 22 min, with a median of 3.3 min. Most of the time τ_d was found to be more than τ_r. Although most of the flares occurred on LO Peg show the usual fast rise and slow decay, there were a few flares that show the reverse phenomena. This was also previously observed on K-type star V711 Tau (Zhang et al., 1990), which may be the result of complex flaring activity at the rise phase of the flare which could not be resolved due to instrumental limitations. Davenport et al. (2014) show the existence of complex flares with high-cadence *Kepler* data which can be explained by a superposition of multiple flares.

The amplitude of a flare is defined as

$$A = \frac{A_{pk}}{F_{lm}} = \left(\frac{F_{pk} - F_{lm}}{F_{lm}} \right) \tag{3.1}$$

The amplitude of the flare is thus measured relative to the current state of the underlying star, including effects from starspots, and represents the excess emission above the local mean flux. The highest amplitude of 1.02 was found in the long lasting flare F13, while smallest amplitude of 0.016 was found for a small duration flare indicating that long lasting flares are more powerful than small duration flares. The derived flare amplitudes on LO Peg were found to be higher in shorter wavelengths than that in longer wavelengths (see two representative flares in Fig. 3.6). Similar feature was also found in multi-wavelength studies of the flare on FR Cnc (Golovin et al., 2012).

The duration (Dn) of a flare is defined as the difference between the start time (the point in time when the flare flux starts to deviate from the local mean flux) and the end time (when the flare flux returns to the local mean flux). The start and end times for each flare were obtained by manual inspection. Flare start time, flare peak time, flare durations, and flare amplitudes are given in 4nd, 6th, 5th, and 9th column of Table 3.2. Most of the flares are ~1 hr long with a minimum and maximum flare duration of ~12 min and ~3.4 hr. Flare observed on SV Cam (Patkos, 1981), XY UMa (Zeilik et al., 1982), DK CVn (Dal et al., 2012), FR Cnc (Golovin et al., 2012), AB Dor (Lalitha et al., 2013), and DV Psc (Pi et al., 2014) studied in optical bands also lie in the same range. Several flares observed on M-dwarfs by Hawley et al. (2014) show similar feature but with a flare duration of ~2 min.

Table 3.2: Parameters obtained from the flare analysis.

Sl. No.	Flare name	Filter	t_{st} [a] (HJD) (2400000+)	Dn [b] (min)	t_{pk} [c] (HJD) (2400000+)	F_{lm} [d]	$\left(\frac{A_{pk}}{\sigma_{ql}}\right)$ [e]	A [f] (frac)	τ_r [g] (min)	τ_d [h] (min)	Energy [k] (10^{32} erg)
1	F1	U	52857.437	26	52857.445	3.67	3.61	0.133	—	10.5 ± 2.6	> 2.31
2		B	52857.437	26	52857.445	11.26	3.37	0.026	—	21.9 ± 5.0	> 2.81
3	F2	U	53206.468	12	53206.513	3.50	3.03	0.062	3.0 ± 1.2	2.9 ± 1.2	0.57
4		B	53206.465	12	53206.511	11.11	2.61	0.016	∼0.4	∼0.7	0.09
5	F3	U	53570.317	29	53570.323	3.54	9.50	0.269	3.9 ± 1.4	4.8 ± 1.4	3.25
6		B	53570.318	26	53570.322	11.03	6.11	0.048	1.4 ± 0.4	1.0 ± 0.4	0.49
7	F4	U	53570.331	42	53570.344	3.45	6.78	0.200	6.9 ± 2.7	∼1.3	2.38
8		B	53570.331	42	53570.341	11.04	5.21	0.040	4.9 ± 1.7	2.0 ± 1.0	1.29
9	F5	U	53570.359	72	53570.384	3.40	8.42	0.256	13.8 ± 2.2	∼0.7	5.56
10		B	53570.354	72	53570.376	10.99	4.72	0.036	9.8 ± 2.5	9.2 ± 2.0	3.37
11		V	53570.354	68	53570.368	25.80	4.48	0.027	0.3 ± 0.1	5.5 ± 1.9	1.80
12		R	53570.353	63	53570.366	24.46	6.01	0.031	2.0 ± 0.6	7.9 ± 1.3	3.40
13	F6	U	53570.482	32	53570.488	3.22	14.55	0.454	1.0 ± 0.1	2.3 ± 0.3	2.18
14		B	53570.481	23	53570.488	10.22	10.54	0.090	1.3 ± 0.3	1.2 ± 0.1	0.99
15		V	53570.482	22	53570.488	23.96	6.52	0.040	1.3 ± 0.3	1.6 ± 0.4	1.26
16		R	53570.482	20	53570.488	23.00	4.68	0.024	1.3 ± 0.6	1.0 ± 0.4	0.58
17	F7	U	53570.500	71	53570.515	3.17	6.18	0.196	8.6 ± 1.3	18.7 ± 1.6	7.37
18		B	53570.508	49	53570.515	9.93	3.10	0.027	2.3 ± 0.9	15.0 ± 2.3	2.06
19	F8	U	53971.346	52	53971.359	3.47	10.79	0.302	1.7 ± 0.3	1.2 ± 0.3	1.34
20		B	53971.339	52	53971.359	10.77	6.10	0.048	2.5 ± 0.9	4.2 ± 0.7	1.55
21		V	53971.347	49	53971.359	25.17	3.43	0.023	2.6 ± 1.6	5.0 ± 1.4	1.98
22		R	53971.346	49	53971.358	24.07	2.56	0.015	—	5.5 ± 2.2	> 0.87
23	F9	V	54003.386	33	54003.396	24.48	7.44	0.045	4.5 ± 1.4	5.8 ± 1.6	5.16
24	F10	V	54324.568	58	54324.579	23.98	12.97	0.047	—	12.1 ± 1.7	> 6.22
25	F11	V	54330.631	25	54330.639	24.58	4.34	0.027	—	∼1.0	> 0.32
26	F12	V	54347.557	66	54347.572	24.95	24.25	0.062	5.0 ± 1.0	20.7 ± 3.3	14.63
27	F13	V	54372.403	202	54372.466	24.04	231.62	1.023	11.2 ± 0.7	22.0 ± 1.3	153.61
28	F14	U	54390.293	50	54390.305	3.28	5.56	0.127	3.2 ± 0.7	2.6 ± 0.9	1.10
29		B	54390.290	50	54390.307	10.27	8.15	0.041	5.8 ± 0.7	—	> 1.09
30		V	54390.293	49	54390.307	24.05	4.19	0.026	6.5 ± 1.4	—	> 1.83
31		R	54390.294	48	54390.306	23.15	3.28	0.018	1.9 ± 0.9	0.9 ± 0.6	0.54
32	F15	U	54657.392	22	54657.401	3.27	5.36	0.161	—	2.3 ± 1.0	> 0.54
33	F16	U	54657.503	46	54657.516	3.23	4.15	0.115	∼3.2	5.8 ± 1.3	1.48
34		B	54657.504	43	54657.517	10.27	3.45	0.028	7.3 ± 2.3	3.6 ± 1.0	1.42
35	F17	U	54747.324	33	54747.336	3.56	3.87	0.067	—	1.0 ± 0.4	> 0.11
36	F18	U	55070.300	26	55070.307	3.53	4.92	0.097	∼2.0	2.6 ± 1.3	0.71
37		B	55070.298	26	55070.308	10.77	3.14	0.017	∼2.6	∼0.4	0.26
38	F19	U	55071.261	72	55071.289	3.25	3.04	0.077	11.2 ± 4.5	9.1 ± 2.9	2.26
39	F20	U	55071.335	57	55071.350	3.29	3.13	0.078	∼4.2	7.8 ± 2.5	1.40
40		B	55071.337	56	55071.349	10.52	5.68	0.040	∼0.9	3.7 ± 1.4	0.87
41		V	55071.337	55	55071.350	24.60	3.17	0.022	11.1 ± 2.2	—	> 2.73
42		R	55071.338	52	55071.349	23.73	3.59	0.021	9.4 ± 2.6	—	> 2.09

Notes.
a - Flare start time; b - Flare duration; c - Flare peak time; d - Local mean flux (F_{lm}) in unit 10^{-11} erg s^{-1} cm^{-2}; e - measure of maximum flux increase during flare from quiescent level in multiple of σ_{ql}; f - Amplitude of the flare; g, h - e-folding rise and decay time of flare; k - Flare energy.

The flare energy is computed using the area under the flare light curve i.e. the integrated excess flux ($F_e(t)$) released during the flare as

$$E_{flare} = 4\pi d^2 \int F_e(t)\, dt \tag{3.2}$$

With a distance (d) of 25.1 pc for LO Peg (Perryman, 1997), the derived values of energy in different filters for all detected flares are given in column 12 of Table 3.2. The flare energies are found in between 9 $\times 10^{30}$ erg to 1.54 $\times 10^{34}$ erg. The most energetic flare is the longest flare. Seventeen out of twenty flares having energy less than 10^{33} erg, signifies more energetic flares are less in number. With *Kepler* data Hawley et al. (2014) also detected most of the flares on M-dwarf GJ 1243 having energy of the order of 10^{31} erg. One flare (F13) is found to have total energy more than 10^{34} erg, therefore, this flare can be classified as a Superflare (see Candelaresi et al., 2014). The derived energy of this flare was ∼10.5 times more than the next largest flare and 668 times more than the weakest flare observed on LO Peg. During the flare F13, the V-band magnitude increases up to 0.42 mag, similar enhancement in V-band mag also noticed in FR Cnc (Golovin et al., 2012). Since the total energy released by the flare must be smaller than (or equal to) the magnetic energy stored around the starspots (i.e. $E_{\rm flare} \leq E_{\rm mag}$), the minimum magnetic field can be estimated during the flare as $E_{\rm mag}\ \alpha\ B^2 l^3$. Assuming the loop-length of typical flares on G-K stars are of the order of 10^{10} cm (see Güdel et al., 2001; Pandey & Singh, 2008). The minimum magnetic field in the observed flares are estimated to be 0.1 – 3.5 kG.

We derive the flare frequency for LO Peg as ∼ 1 flare per two days. There are very few detailed studies of optical flares on UFRs due to constraints in their detection limit, detection timing and very less flare frequency. Recent studies on optical flares done with ground-based observatories on DV Psc (Pi et al., 2014) and CU Cnc (Qian et al., 2012) show flare frequencies of ∼2 flares per day and ∼1 flare per day, respectively, which are similar to that for LO Peg. However, several other studies done with *Kepler* satellite (Hawley et al., 2014; Lurie et al., 2015) on M-dwarfs reveal that flare frequency varies over a wide range of ∼1 flare per month to ∼10 flares per day.

3.4 Surface imaging with light curve inversion technique

In order to determine locations of spots on the stellar surface, we have performed inversion of the phased light curves into stellar images using the light curve inversion code (iPH; see Savanov & Dmitrienko, 2011; Savanov & Strassmeier, 2008). The model assumes that, due to the low spatial resolution, the local intensity of the stellar surface always has a contribution from the photosphere (I_P) and from cool spots (I_S) weighted by the fraction of the surface covered by spots, i.e., the spot filling factor f by the following relation: $I = f \times I_P + (1 - f) \times I_S$; with $0 < f < 1$. The inversion of a light curve results in a distribution of the spot filling factor (f) over the visible stellar surface. Although this approach is less informative than the Doppler imaging technique (see Barnes et al., 2005; Piluso et al., 2008; Strassmeier & Bartus, 2000); however, analysis of long time series of photometric observations allows us to recover longitudinal spot patterns and study of their long-term evolution.

We could make 47 time intervals by manual inspection such that each interval had a sufficient number of data points and had no noticeable changes in their shape. Individual light curves were analyzed using the iPH code. Several sets of time interval contain a large number of observations within it (e.g. set 33 includes 1007 measurement), in those cases we divided the time axis of the phase diagram into 100 bins and averaged the measurements. In our modelling, the surface of the star was divided into a grid of $6° \times 6°$ pixels (unit areas), and the values of f were determined for each grid pixel. We adopt the photospheric temperature of LO Peg to be $\sim$4500 K (see Pandey et al., 2005) and the spot temperature to be 750 K lower than the photospheric temperature (Piluso et al., 2008; Savanov & Dmitrienko, 2011). The stellar astrophysical input includes a set of photometric fluxes calculated from atmospheric model by Kurucz (1992) as a function of temperature and gravity. For LO Peg the 'i' was precisely determined with the analysis of a very extensive set of high resolution spectra (see Barnes et al., 2005; Piluso et al., 2008), therefore, in our reconstruction of the temperature inhomogeneity maps we safely fixed the inclination angle at 45°. Various test cases were performed to recover the artificial maps and include data errors and different input parameter errors which demonstrate the robustness of our solution to various false parameters.

Fig. 3.8 shows the reconstructed temperature inhomogeneity maps of LO Peg, which reveal that the spots have a tendency to concentrate at two longitudes corresponding to two active regions on the stellar surface. The difference between two

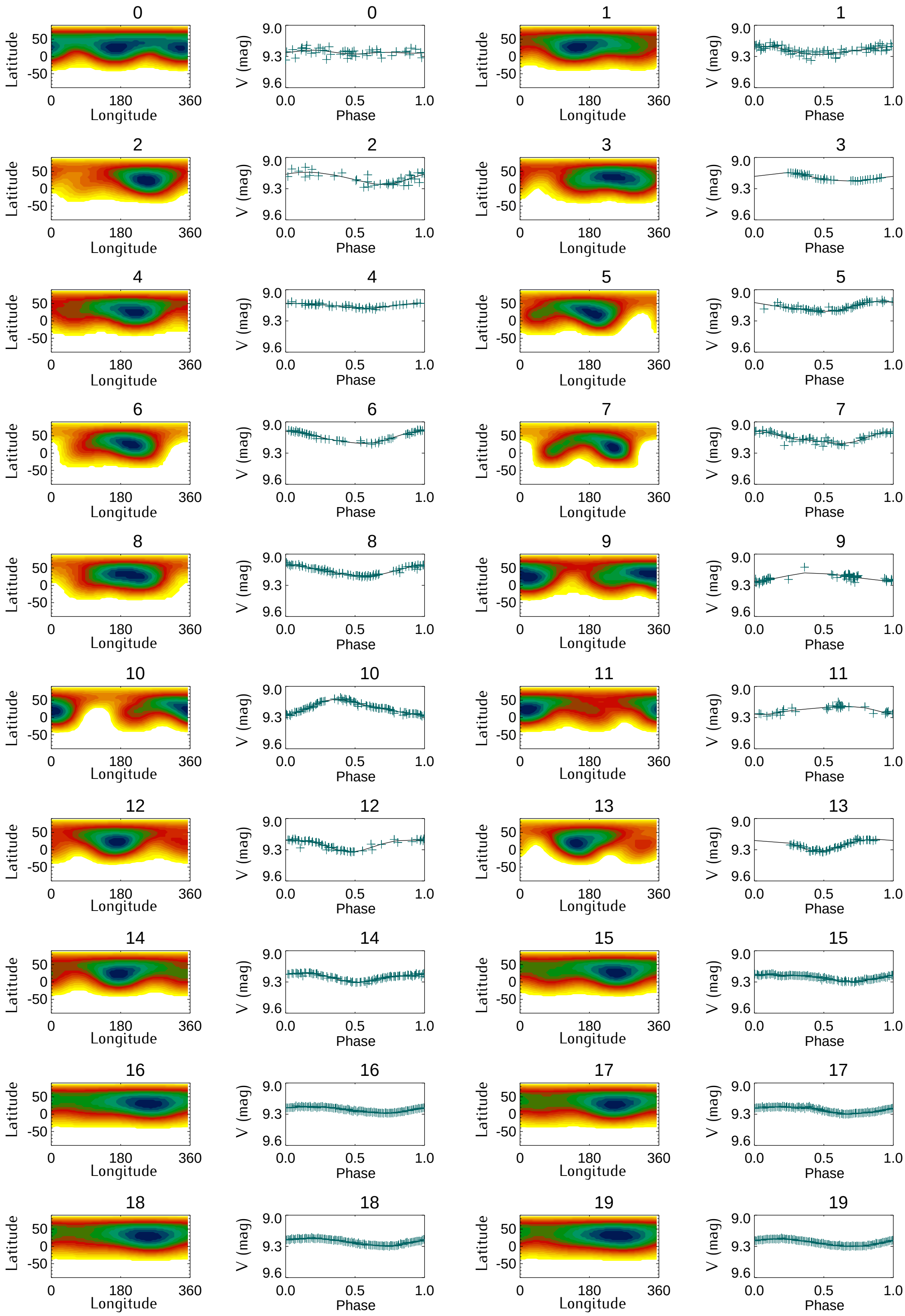

Figure 3.8: The surface temperature inhomogeneity maps of LO Peg — Continued

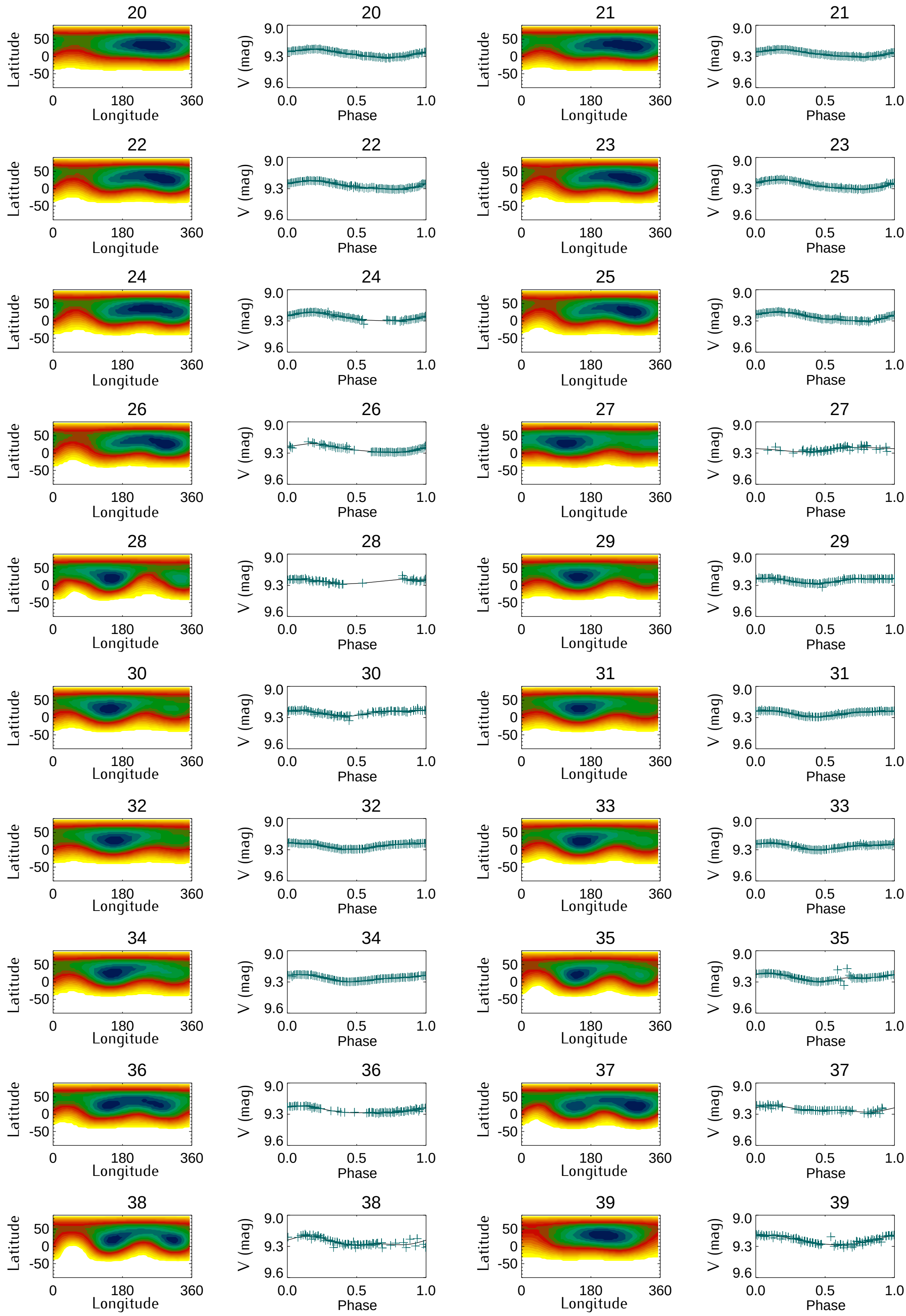

Figure 3.8: The surface temperature inhomogeneity maps of LO Peg — Continued

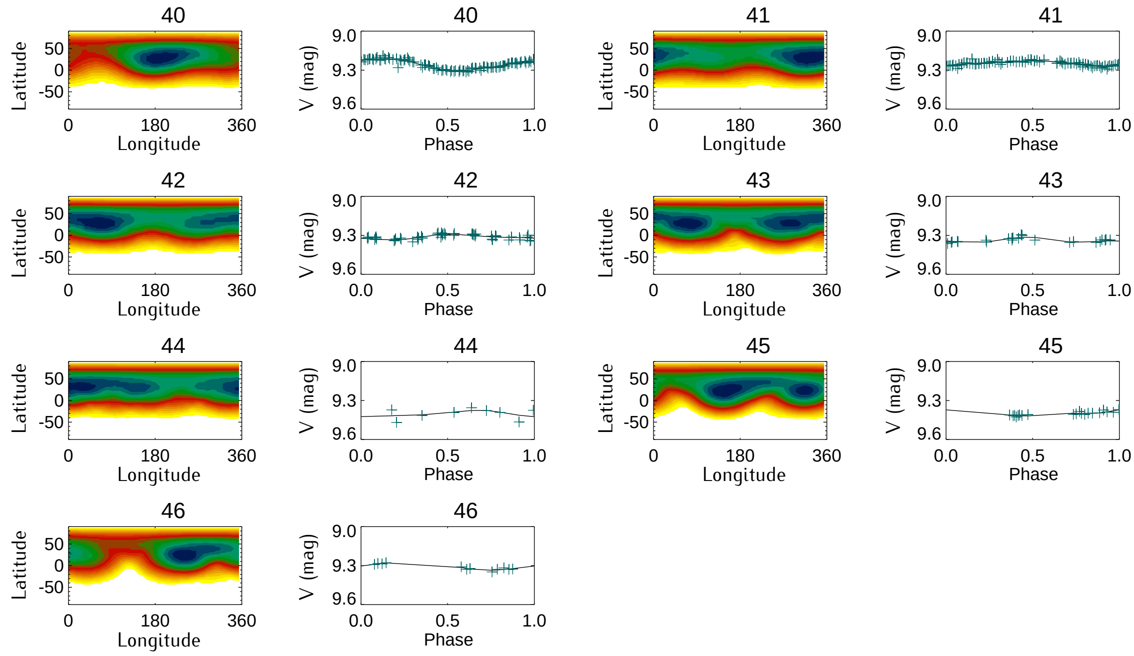

Figure 3.8: The surface temperature inhomogeneity maps of LO Peg for 47 epochs are shown in left panels (1st and 3rd columns). The surface maps are presented on the same scale, with darker regions corresponding to higher spot-filling factors. Right panels (2nd and 4th columns) show the light curves folded on each epoch. Observed and calculated V-band light curves are presented by crosses and continuous lines, respectively.

active longitudes was found to be inconstant and less than 180°. The uncertainty in the positions of the active longitudes on the stellar surface was on average of about 6° (or 0.02 in phase). The derived stellar parameters active longitude regions (ψ_1, ψ_2), spottedness (Sp), and V-band amplitudes (A_{LI}) corresponding to each surface brightness map shown in Fig. 3.8 are plotted with HJD in Fig. 3.9. The filled and open circles in Fig. 3.9(b) show high and low active regions, respectively. The derived parameters are also given in Table 3.3. First three surface maps were created with the sparse data of *Hipparcos* satellite, and to create good quality maps, data of ~2 yr, ~0.5 yr and ~0.5 yr were used. We get a signature of presence of two equal spot groups ~170° apart in first two years (1989 to 1991), whereas the presence of single spot group was indicated with the surface map of the third year (1992). From 2001 to 2013 with ground-based observations and archival data it became possible to create at least one surface map per year. Using high-cadence data of *SuperWASP* in 2006 and 2007, we created twelve surface maps (Set-15 to Set-26) in three months of 2006 (July 27th to November 4th) and ten surface maps (Set-27 to Set-36) in

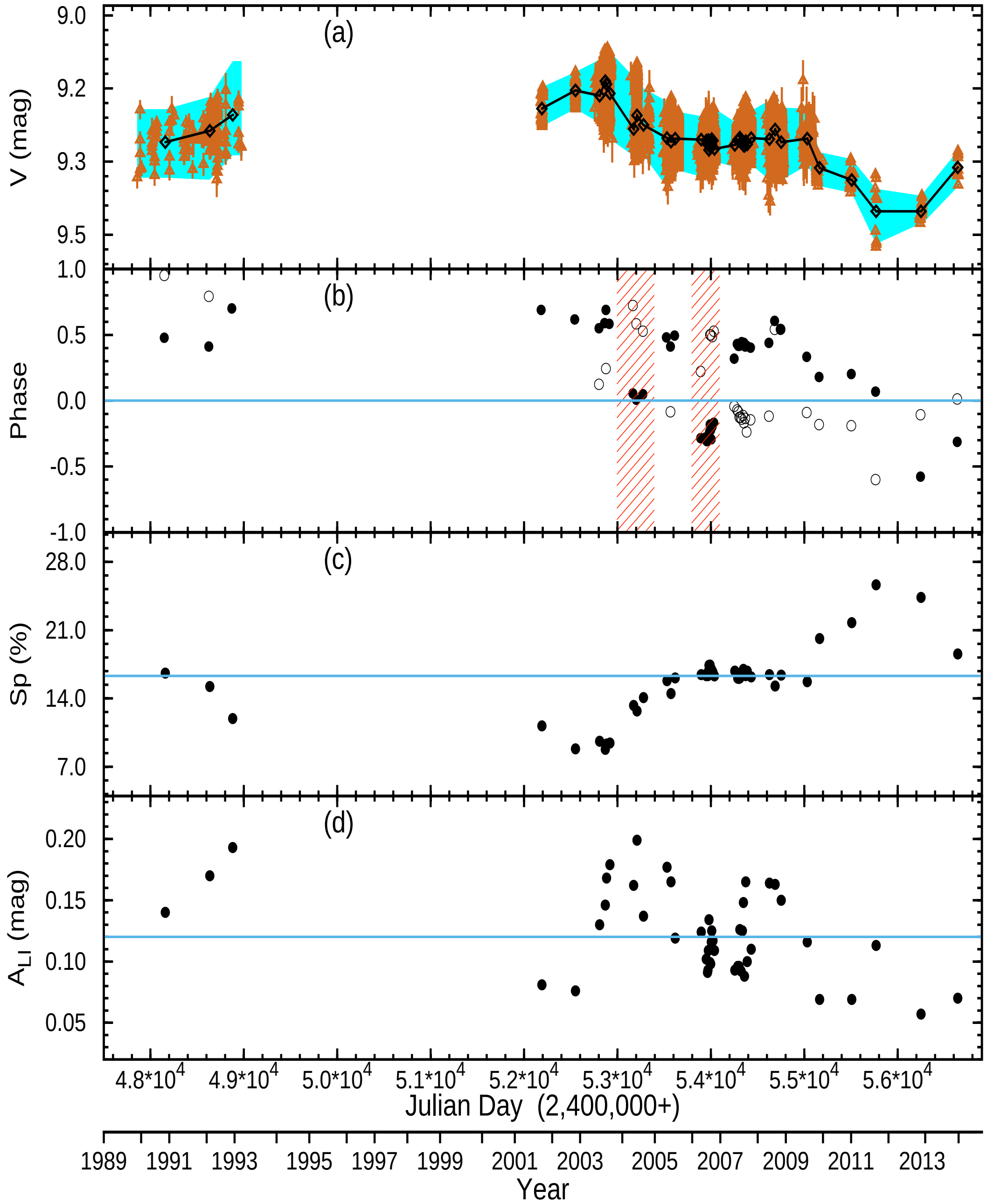

Figure 3.9: Parameters of LO Peg derived from modelling. From top to bottom – (a) V-band light curve of LO Peg (open triangles) plotted with mean magnitude of each epoch (open diamonds). The shaded regions shows the errors in data points. (b) Phases/longitudes of spots recovered from light curve inversion. Filled and open circles show primary and secondary active longitudes, respectively. Vertical shaded regions indicate the time intervals when the possible flip-flop events occur. (c) Recovered surface coverage of cool spots (per cent) on LO Peg. (d) The amplitude of brightness variations in unit of magnitude.

three months of 2007 (July 24th to December 19th). This enables us to make a detailed study on the surface structure of LO Peg. It appears that LO Peg consists only one spot group during the observations of August 2006 (Set-16 to Set-21). In September 2006 migration from single spotted surface to double spotted surface was clearly noticeable (Set-22 to Set-26). Both spots are separated by $< 115°$. Two spot groups were also observed during the 2007, but the separations of two spot groups were $> 125°$. It was also noticed that the active regions changed their position from 2006 to 2007, which indicates a flip-flop cycle of $\sim$1 yr (see shaded regions on the Fig. 3.9(b)). Similar phenomena were also noticed during the year 2004 and 2005 with an approximately same period. But due to uncertainty on the position of the spot-groups, it was not possible to say whether the flip-flop cyclic behaviour continues in later years. Indication of the flip-flop effect in LO Peg is quite similar to that observed by Korhonen et al. (2002) and Järvinen et al. (2005a). The flip-flop phenomenon has been noticed for the first time by Jetsu et al. (1991) in the giant star FK Com. Later it was found to be cyclic in RS CVn and FK Com-type stars, as well as in some young solar analogues (e.g. Korhonen et al., 2002). After its discovery in cool stars, the flip-flop phenomena have also been reported in the Sun (Berdyugina & Usoskin, 2003). This phenomenon is well explained by the dynamo based solution where a non-axisymmetric dynamo component, giving rise to two permanent active longitudes 180° apart, is needed together with an oscillating axis-symmetric magnetic field (Elstner, 2005; Korhonen & Elstner, 2005). Fluri & Berdyugina (2004) suggest another possibility with a combination of stationary axisymmetric and varying non-axisymmetric components. It also appears that, the flip-flop cycle is approximately one third of the latitudinal spot migration cycle.

The total area of the visible stellar surface covered by spots, known as spottedness (Sp), varies within a range of 8.8 – 25.7% (see Fig. 3.9(c)), with a median value of 16.3%. From the year 2001 to 2005, it was found to decrease until its minimum in August 2003, and then return to its median value in 2005. It remained constant for $\sim$4 yr at this value, and then increased to reach its maximum. Further the spottedness of the star has returned to its median value again. The time interval of returning to its median value was approximately same as 4 yr. The spottedness in LO Peg is very similar to that found in K-type stars XX Tri (Savanov, 2014), V1147 Tau (Patel et al., 2013), LQ Hya, and MS Ser (Alekseev, 2003). We did not see any relation between spottedness and cyclic behaviour or the rotational period. However, from the year 2005 to 2009 spottedness variation is found to be almost

Table 3.3: Parameters derived from the light curve modelling.

Epoch	**No. of Points**	**HJD$_{beg}$ (2400000+)**	**HJD$_{end}$ (2400000+)**	V$_{max}$ (mag)	V$_{min}$ (mag)	V$_{mean}$ (mag)	A_{LI} (mag)	**Sp %**	ψ_1 (°)	ψ_2 (°)	Note†
0	47	47857.50	48458.42	9.193	9.333	9.260	0.140	16.6	172	342	e
1	74	48550.46	48717.97	9.167	9.337	9.237	0.170	15.2	148	285	n
2	39	48788.25	48972.28	9.094	9.287	9.204	0.193	11.9	252	..	n
3	37	52181.17	52198.13	9.147	9.228	9.191	0.081	11.2	248	..	u
4	50	52546.21	52551.25	9.116	9.192	9.154	0.076	8.8	222	..	n
5	232	52755.91	52860.68	9.091	9.221	9.165	0.130	9.6	198	45	n
6	204	52863.39	52872.41	9.071	9.217	9.135	0.146	8.8	212	..	n
7	168	52874.64	52890.55	9.067	9.235	9.141	0.168	9.3	248	88	n
8	290	52893.59	52942.54	9.075	9.254	9.160	0.179	9.4	210	..	n
9	74	53142.92	53199.49	9.126	9.288	9.233	0.162	13.3	20	260	u
10	464	53203.42	53211.47	9.098	9.297	9.205	0.199	12.7	3	210	n
11	36	53212.39	53344.52	9.150	9.287	9.225	0.137	14.1	18	190	n
12	221	53487.92	53570.69	9.176	9.353	9.252	0.177	15.8	173	..	n
13	242	53571.30	53574.69	9.168	9.333	9.259	0.165	14.5	148	330	u
14	426	53584.66	53650.35	9.197	9.316	9.253	0.119	16.1	178	..	n
15	746	53853.92	53938.68	9.207	9.331	9.255	0.124	16.4	258	80	n
16	555	53943.57	53955.73	9.200	9.302	9.257	0.102	16.3	260	..	n
17	315	53960.41	53963.44	9.216	9.307	9.264	0.091	16.5	250	..	n
18	308	53966.46	53969.69	9.210	9.303	9.258	0.093	16.3	253	..	n
19	638	53970.41	53973.68	9.206	9.315	9.256	0.109	16.8	252	..	n
20	599	53975.40	53981.55	9.194	9.328	9.276	0.134	17.4	260	..	n
21	504	53987.40	53994.62	9.217	9.316	9.270	0.099	17.4	275	..	n
22	241	53995.36	53998.61	9.212	9.310	9.258	0.098	17.1	295	180	n
23	286	54001.34	54005.59	9.204	9.320	9.264	0.116	16.8	280	180	n
24	228	54006.39	54011.57	9.206	9.331	9.254	0.125	16.9	255	..	n
25	242	54017.33	54023.38	9.202	9.319	9.257	0.117	16.7	290	175	n
26	130	54029.40	54044.46	9.191	9.300	9.274	0.109	16.3	300	190	n
27	181	54227.90	54281.78	9.218	9.311	9.266	0.093	16.8	115	345	n
28	243	54283.77	54289.74	9.207	9.303	9.256	0.096	16.1	155	335	u
29	266	54293.75	54305.73	9.223	9.319	9.254	0.096	16.0	150	330	n
30	428	54306.49	54312.69	9.204	9.330	9.251	0.126	16.1	150	315	n
31	686	54315.69	54328.70	9.217	9.309	9.261	0.092	16.5	152	315	n
32	1007	54329.43	54340.68	9.206	9.331	9.261	0.125	16.7	160	310	n
33	557	54343.59	54352.64	9.179	9.327	9.267	0.148	17.0	155	320	n
34	546	54353.37	54364.53	9.219	9.307	9.268	0.088	16.8	158	300	n
35	320	54368.37	54377.43	9.169	9.334	9.258	0.165	16.3	148	312	n
36	333	54381.44	54394.27	9.203	9.303	9.265	0.100	16.8	150	275	e
37	133	54405.31	54454.05	9.196	9.306	9.252	0.110	16.2	145	308	n
38	224	54590.92	54661.78	9.174	9.338	9.254	0.164	16.4	158	318	n
39	385	54663.77	54710.68	9.169	9.332	9.234	0.163	15.3	218	..	n
40	452	54716.66	54785.52	9.189	9.339	9.260	0.150	16.4	195	..	n
41	339	54954.92	55105.62	9.191	9.307	9.253	0.116	15.7	120	328	n
42	47	55130.10	55196.05	9.281	9.350	9.313	0.069	20.1	65	295	n
43	23	55489.16	55526.10	9.295	9.364	9.338	0.069	21.8	73	292	u
44	9	55758.82	55775.77	9.356	9.469	9.402	0.113	25.7	25	145	u
45	20	56239.14	56257.17	9.370	9.427	9.402	0.057	24.3	153	322	u
46	12	56636.36	56645.36	9.278	9.348	9.312	0.070	18.6	248	5	u

Notes.
HJD$_{beg}$, HJD$_{end}$, and HJD$_{middle}$ are start, end, and middle time of each epoch. V$_{max}$, V$_{min}$, and V$_{mean}$ are maximum V$_{max}$, V$_{min}$, and V$_{mean}$ are maximum, minimum and mean magnitudes of LO Peg. A_{LI} is the amplitude of variability. Sp is the spottedness of the stellar surface. ψ_1 and ψ_2 are active longitudes.
† e – size of both spots were approximately equal; n – size of both spots were different; u – uncertain results due to incomplete light curve.

constant (shown in third panel of Fig 3.9). At the same time duration, SDR analysis also indicates that the seasonal rotational period and hence the latitude of the spot groups also remains constant (see cycle-VII in second panel of Fig. 3.4). This suggests that the magnetic activities remains constant within that period of time. In all other cycles the seasonal rotational period and hence latitudinal spot groups follows solar-like butterfly pattern with a ∼2.7 yr period. Whereas, spottedness variation does not show any periodic modulation. The observations of Set-8 (Sept 11 – Oct 30 2003) are quasi simultaneous with the spectroscopic observation of Piluso et al. (2008). During this period our analysis shows single spot at phase 210°. Whereas Doppler imaging study of Piluso et al. (2008) shows a signature of low-latitude spot at phase ∼0.7. Correcting for the difference in ephemeris, we get the corresponding starspot longitude to be ∼226°, which is almost similar to our derived value. The longer time span used in the generation of surface map may cause the difference between the two longitude positions.

As seen in Fig. 3.9(d) the amplitude of the brightness varies within a range 0.06 – 0.19 mag, with a median value of 0.12 mag. This value is very similar to variability amplitude of other K type stars such as V1147 Tau (Patel et al., 2013), LQ Hya (Berdyugina et al., 2002), AB Dor (Järvinen et al., 2005b), and MS Ser (Alekseev, 2003). Savanov (2014) detected the variability amplitude up to 0.8 mag in late-type star ASAS 063656-0521.0.

3.5 Flare vs Spottedness

We inspected the list of flares for further evidence of a correlation between flare timing and orientation of the dominant spot group. The phase minima as a function of flare phase is plotted in Fig. 3.10(a), where we did not find any correlation. This finding is also consistent with the flare study of Hunt-Walker et al. (2012) and Roettenbacher et al. (2013). From this result we conclude that most of the flares on LO Peg may not originate in the strongest spot group, but rather come from small spot structures or polar spots. In order to check whether the spottedness on the stellar surface is related to occurrence rate of flare, we plotted the distribution of detected flares in each percentage binning of spottedness shown in Fig. 3.10(b). Most of the flares detected on LO Peg are found to occur within a spottedness range of 13–18%, with a highest number of 9 flares occurred at a spottedness range of 16–17%.

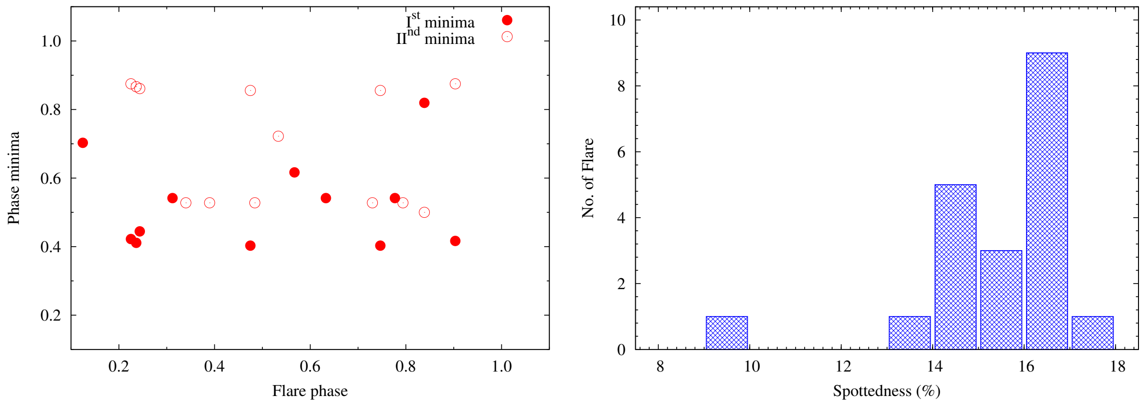

(a) (b)

Figure 3.10: (a) Phase minima is plotted as a function of flare peak phase. (b) Observed distribution of detected flares with stellar spottedness.

3.6 Coronal and chromospheric features

The background subtracted X-ray light curves of LO Peg as observed with *Swift* XRT and *ROSAT* PSPC instruments are shown in the top panel of Fig. 3.1. The temporal binning of the X-ray light curves are 100 s. XRT light curves were obtained in energy band 0.3 – 10.0 keV, whereas *ROSAT* light curves were obtained in an energy band 0.3 – 2.0 keV. *ROSAT* PSPC count rate were converted to *Swift* XRT count rate using WebPIMMS[1] where we assumed two temperature components 0.27 keV and 1.08 keV and 0.2 solar abundances. To check for the variability, the significance of deviations from the mean count rate were measured using the standard χ^2-test. For our X-ray light curves, derived value of χ^2 is 664 which is very large in comparison to the 190 degrees of freedom ($\chi^2_\nu = 3.5$). This indicates that LO Peg is essentially variable in X-ray band.

On one occasion (ID: 00037810011) sudden enhancement of X-ray count rates was detected along with a simultaneous enhancement in UV count rates in each of the UV filters. This enhancement could be due to flaring activity, where flare peak count rates were ∼3 times higher than a quiescent level of 0.20 counts s^{-1}. The close inspection of the X-ray light curve shows the decay phase of the flare. We could not analyze this flare due to poor statistics. However, the flare duration was found to be 1.2 ks.

[1]http://heasarc.nasa.gov/cgi-bin/Tools/w3pimms/w3pimms.pl

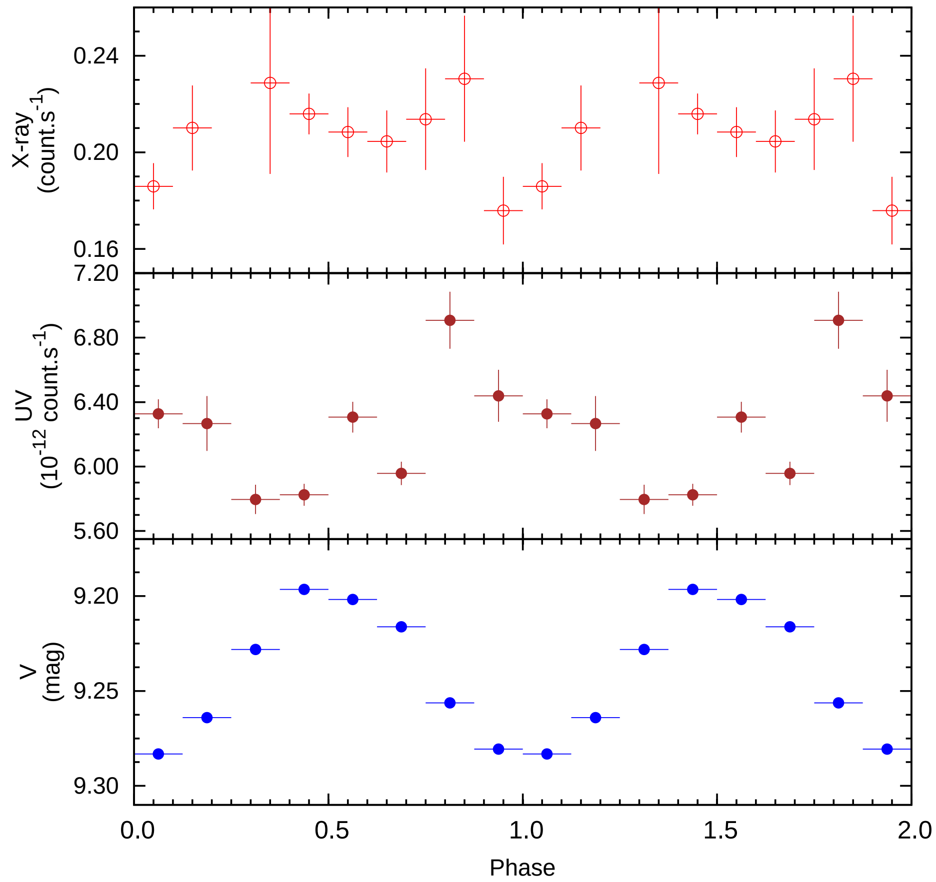

Figure 3.11: From top to bottom the X-ray, UV, and optical folded light curves are shown. Each folded light curve is binned at bin-size 0.1.

Fig. 3.11 shows the rotationally modulated X-ray, UV (uvm2 filter), and optical (V-band) light curves. Observations of the year 2008 were used for rotational modulation, where we have removed the flaring feature from X-ray light curve. Optical and X-ray observations are ~100 d apart. It appears that both X-ray and UV light curves were rotationally modulated. X-ray and UV light curves appear to be anti-correlated with V-band light curve. The Pearson correlation coefficients between X-ray and V-band, and UV and V-band light curve were found to be -0.22 and -0.57, respectively.

The *Swift* XRT spectra of the star LO Peg, as shown in Fig. 3.12, were best fitted with two temperature (2T) astrophysical plasma model (APEC; Smith et al., 2001), with variable elemental abundances (Z). The interstellar hydrogen column density (N_H) was left free to vary. Since all the parameters were found to be constant within a 1σ level, we determined the parameters from joint spectral fitting. The

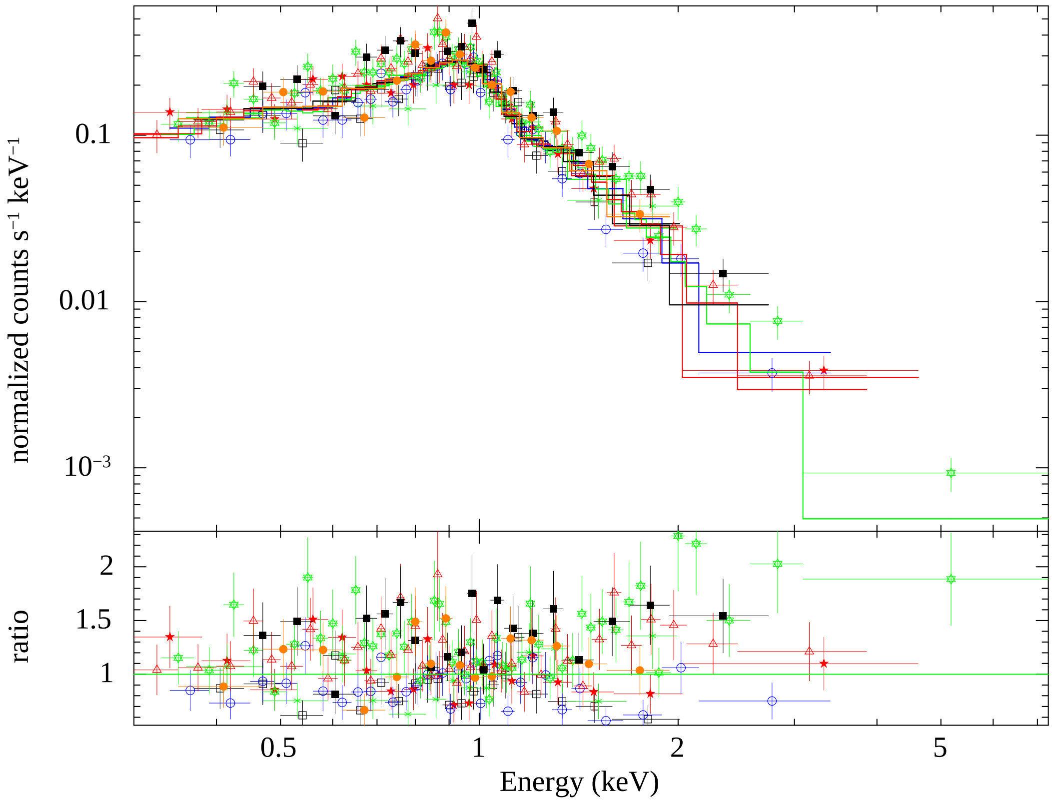

Figure 3.12: X-ray Spectra of LO Peg obtained from *Swift* XRT along with the best fit APEC 2T model (top panel). Different symbols denote different observation IDs. The bottom panel represents the ratio of the observed counts to the counts predicted by best-fit model.

two temperatures and corresponding emission measures were 0.28 ± 0.04 keV and 1.03 ± 0.05 keV, and $3.1 \pm 0.9 \times 10^{52}$ cm^{-3} and $4.6 \pm 0.6 \times 10^{52}$ cm^{-3}, respectively. Global abundances were found to be 0.13 ± 0.02 solar unit ($Z_{\odot}$). The derived value of unabsorbed luminosity is given by $1.4^{+0.5}_{-0.4} \times 10^{29}$ erg s^{-1} cm^{-2}.

3.7 Conclusions

In this study, with ∼24 yr long photometric observations from different worldwide telescopes, and X-ray and UV observations obtained with *Swift* satellite we have investigated the properties of an UFR LO Peg. No signature of long-term variations in X-rays is seen, whereas long-term periodic variability are clearly seen in the optical and UV bands. The rotational period of LO Peg steadily decreases along the activity cycle, jumping back to higher values at the beginning of the next cycle with a cycle of 2.7 ± 0.1 yr, indicating a solar-like SDR pattern on LO Peg. A total of 20 optical flares are detected, where the most energetic flare has energy of $10^{34.2}$ erg whereas the least energetic flare has energy of $10^{30.9}$ erg with flare duration range of 12 – 202 min. Our inversion of phased light curves show the surface coverage of cool spots are in the range of $\sim 9 - 26$ per cent. Evidence of flip-flop cycle of $\sim$1 yr is also found. We found that majority of the flares on LO Peg may not originate in the strongest spot group, but rather come from small spot structures or polar spots. However, majority of flares tend to originate from large spottedness. Corona of LO Peg consist of two temperatures of $\sim$3 MK and $\sim$12 MK. Quasi-simultaneous observations in X-ray, UV, and optical UBVR bands show a signature of high X-ray and UV activities in the direction of spotted regions.

Chapter 4

Flares from late-type main sequence stars 47 Cas and AB Dor

This chapter consists two parts. In the first part, we investigate physical properties of a flaring event from the very active and poorly known MS binary system 47 Cas, whereas in the second part we make use of a long-term X-ray data to study the flaring events from a fairly known MS quadruple system AB Dor. Observations in both cases were taken from *XMM-Newton* observatory.

4.1 47 Cas

47-Cas is an early F-type MS stellar system, which is supposed to consists of an unseen companion, 47 Cas B, which has been detected only in the radio wavelength by (Güdel et al., 1998) and for which no optical characterization is available thus far. The *Hipparcos* catalog lists the young and rapidly rotating F0V star, 47 Cas, as a close visual binary with a period of about 1616 days. Güdel et al. (1998, 1995) studied 47 Cas using X-ray (*ROSAT*) and radio (6 cm) observations. Their study suggests that X-ray and radio emissions from 47 Cas are due to the late-type companion. Garner & Etzel (1998) have also suggested that the X-ray and radio activities are similar to a chromospherically active solar type companion. Furthermore, signatures of coronal activity are not normally associated with early F-type main-sequence stars. Later, the high-resolution X-ray spectra of 47 Cas from XMM Newton were analyzed by Ness et al. (2003), Telleschi et al. (2005), and Nordon &

[1]**The results presented in this chapter have been published in Pandey & Karmakar (2015).**

Behar (2008) with an aim of abundance analysis. In this study, we have analyzed the flaring feature in the 47 Cas system.

4.1.1 X-ray light curves

Fig. 4.1 shows the background subtracted X-ray light curve of 47 Cas in the total (0.3–10.0 kev), soft (0.3–2.0 keV) and hard (2.0–10.0 kev) energy bands with a temporal binning of 200s. The light curves in all energy bands show variability, which resembles flaring activity. The flaring feature is marked with an 'F' in Fig. 4.1. The flare began after 11.2 ks from the start of PN observations and lasted for 4.8 ks. In the total energy band, the count rate at the peak of the flare was found to be 1.8 times more than that in the quiescent state. However, the flare peak to quiescent state count ratios were found to be 1.7 and 4.4 in the soft and hard energy bands, respectively. After the end of the flaring event an active level 'U' was identified where the average flux was 1.2 times more than that in the quiescent state. The level 'U' was identified only in the soft and total energy bands, and no such feature was seen in the hard energy band. We termed this level as post-flare state. The e-folding rise time (τ_r) has been derived from the least-squares fit of the exponential functions (see equation 4.1) between flare start and flare peak, whereas e-folding decay time (τ_d) has been derived similarly from the least-squares fit of the exponential functions between flare peak and flare end.

$$c(t) = A_{pk}.exp\left(\pm\frac{t-t_{pk}}{\tau_r,\tau_d}\right) + q \tag{4.1}$$

where c(t) is the count rate as a function of time t, t_{pk} and A_{pk} is the time and count rate at flare peak and q is the count rate in the quiescent state. In the total energy band, τ_r and τ_d of the flare observed in 47 Cas were derived to be 831 ± 100 s and 2494 ± 82 s, respectively. However, τ_r and τ_d were derived as 743 ± 89 s and 2446 ± 77 s, and 590 ± 108 s and 1203 ± 62 s in the soft and hard energy bands, respectively. These values of rise and decay times of the flare are found to be similar to those of the flares observed from G-K dwarfs (Pandey & Singh, 2008) and are smaller than those from evolved RS CVn-type and pre-main-sequence stars (Getman et al., 2008b; Pandey & Singh, 2012). These data along with the flare luminosity (see below) suggest that the flare from 47 Cas is an impulsive flare (Pallavicini et al., 1990), which is similar to a compact solar flare. The compact flares are less energetic ($\sim 10^{30}$), short in duration (< 1 hour) and confined to a single loop. The τ_d in the soft energy band was higher than that in the hard energy band. A similar tendency was also noticed in many flares observed from G-K dwarfs. This could probably be due to the softening of the spectrum during the decay due to the plasma cooling, i.e. emission gradually shifts from the high energy band to deeper in the soft energy band. We have also noticed the heightened emission after the flare in the soft energy band. Similar behavior in light curves was seen in the flares from ξ Boo (Pandey & Srivastava, 2009) and CC Eri (Crespo-Chacón et al., 2007; Pandey & Singh, 2008). It also appears that before the flaring event the X-ray light curve was not constant. Such small-scale variability in the X-ray light curve before and after the flaring event could be due to the emergence of smaller flares during the observations. Continuous low-level variability due to small flares has also been reported for active dwarfs and giants (Ayres et al., 2001; Kuerster et al., 1997a; Mathioudakis & Mullan, 1999; Vilhu et al., 1993).

The bottom panel of Fig. 4.1 shows the temporal variation of the hardness ratio (HR). The HR is defined as $(H - S)/(H + S)$; where H and S are the count rates in the hard and soft bands, respectively. The variation in the HR during the flares is indicative of changes in the coronal temperature. The HR varied in a fashion similar to its light curves, indicating an increase in the temperature at the flare peak and a subsequent cooling.

4.1.2 X-ray spectral analysis

4.1.2.1 Quiescent state spectra

The quiescent state X-ray spectra were extracted from the 'Q' part of the light curve. The quiescent state coronal parameters of 47 Cas were derived by fitting the X-ray spectra with a single (1T) and double (2T) temperature collisional plasma models known as APEC (Smith et al., 2001) as implemented in the X-ray spectral fitting package XSPEC (Arnaud, 1996) version 12.8.1. The global abundances (Z) and interstellar hydrogen column density (N_H) were left as free parameters. The N_H is modeled with cross sections obtained by Morrison & McCammon (1983); however, the solar photospheric abundances ($Z_\odot$) were adopted from Anders & Grevesse (1989). Both 1T and 2T plasma models with solar photospheric abundances were rejected due to the high value of χ^2. The 2T model with with sub-solar abundances was found to be acceptable with a reduced χ^2 of 1.2. By adding one more component to the temperature in fitting, we did not find any further improvement in the reduced χ^2; therefore, we assume that the quiescent coronae of 47 Cas were well represented by two temperatures plasma. The cool and hot temperatures and the corresponding

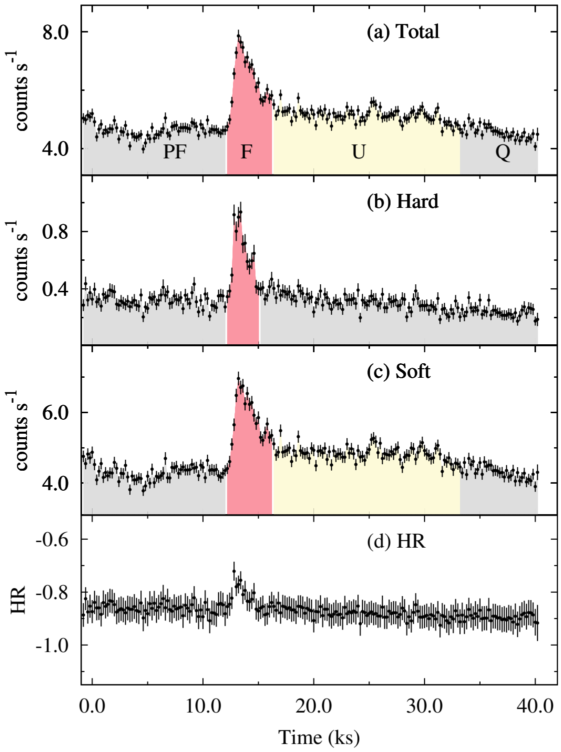

(a) PN

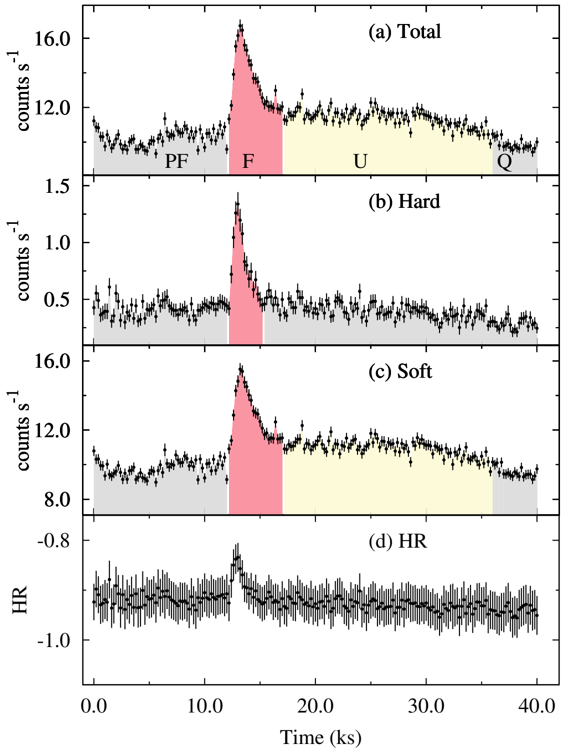

(b) MOS

Figure 4.1: X-ray light curve of the 47 Cas system at three different energy bands along with the hardness ratio curve. The hardness ratio is defined as $(H-S)/(H+S)$. The pre-flare state, flaring state, heightened post-flare emission and quiescent state are marked by PF, F, U, and Q, respectively.

emission measures were derived as 0.32 ± 0.02 keV and 0.95 ± 0.02 keV, and $9.0^{+1.3}_{-1.2}\times 10^{52}$ cm^{-3} and $17.7^{+1.4}_{-1.3}\times10^{52}$ cm^{-3}, respectively. The value of N_H was derived to be $1.6\pm0.7\times10^{20}$ cm^{-2}, which is lower than that of the total galactic HI column density (Dickey & Lockman, 1990) towards the direction of 47 Cas. The abundance during the quiescent state of 47 Cas was derived to be $0.135\pm0.009 Z_\odot$ The quiescent state X-ray flux of 47 Cas was estimated by using the CFLUX model in XSPEC and are corrected for N_H. The unabsorbed X-ray luminosity of 47 Cas during its quiescence was derived to be $1.90\pm0.02\times10^{30}$ erg s^{-1}.

4.1.3 Spectral evolution of flare

The X-ray light curve of 47 Cas was divided into 11 time bins, and spectra of each time interval were extracted and analyzed to trace the spectral changes during the flare. These divisions were made to ensure that spectra in each time bin have sufficient counts to provide reliable values of spectral parameters. Fig. 4.2 shows the spectra of different time intervals during the flaring and quiescent states. The spectral evolution can be seen clearly. In order to study the flare emission only, we have performed three temperature spectral fits of the data, with the quiescent emission taken into account by including its best-fitting 2T model as a frozen background contribution, which allows us to derive one "effective" temperature and one EM of the flaring plasma. Initially, N_H was a free parameter in the spectral fitting and appeared to be constant during the flare to the quiescent state value. Therefore, in the next stage of spectral fitting, N_H was fixed to the quiescent state value along with the parameters of the first two temperature components. Abundances and temperature and normalization of the third component were free parameters in the spectral fitting. The resulting temporal evolution of the spectral parameters of the flare is shown in Fig. 4.3 and derived parameters are given in Table 4.1.

Abundances, temperature, and the corresponding emission measure were found to vary during the flare. The peak value of Z was derived to be $0.199Z_{\odot}$, which is well above the 4σ level to the minimum value observed. The flare temperature peaked at 72.8 MK during the rise phase of the flare, which is ~ 3 times more than the minimum value at the end of the decay phase. The value of maximum temperature is more than that observed in many flares from similar dwarfs (Pandey & Singh, 2008). The EM followed the flare light curve and peaked later than the temperature at a value of 9.72×10^{52} cm^{-2}, which is ~ 9 times more than the minimum value observed at the end of the flare. A delay between EM and temperature has been observed both in solar and stellar flares oftenly (Favata et al., 2000; Maggio et al., 2000; Pandey & Singh, 2008, 2012; Stelzer et al., 2002; Sylwester et al., 1993). This could be due to a coherent plasma evolution during the flare and therefore, a flare occurring inside a single loop, or at least the presence of a dominant loop early in the flare. We found a significant increase in the abundances from 0.13 $Z_{\odot}$ to 0.2 $Z_{\odot}$during the flare. A possible explanation for an enhancement in abundances during the flare is due to the evaporation of fresh chromospheric material in the flaring loops. Using the RGS spectra of 47 Cas, Nordon & Behar (2008) and Telleschi et al. (2005) found a small enhancement of abundances of low first-ionization-potential metals. However, this enhancement in the abundances was well within a 1σ level. The L_x reached a value of 3.54×10^{30} erg s^{-1}, which is 1.8 times more than that of the quiescent state. The flux during the post-flare phase ("U") was 1.3 times more than that during quiescent state.

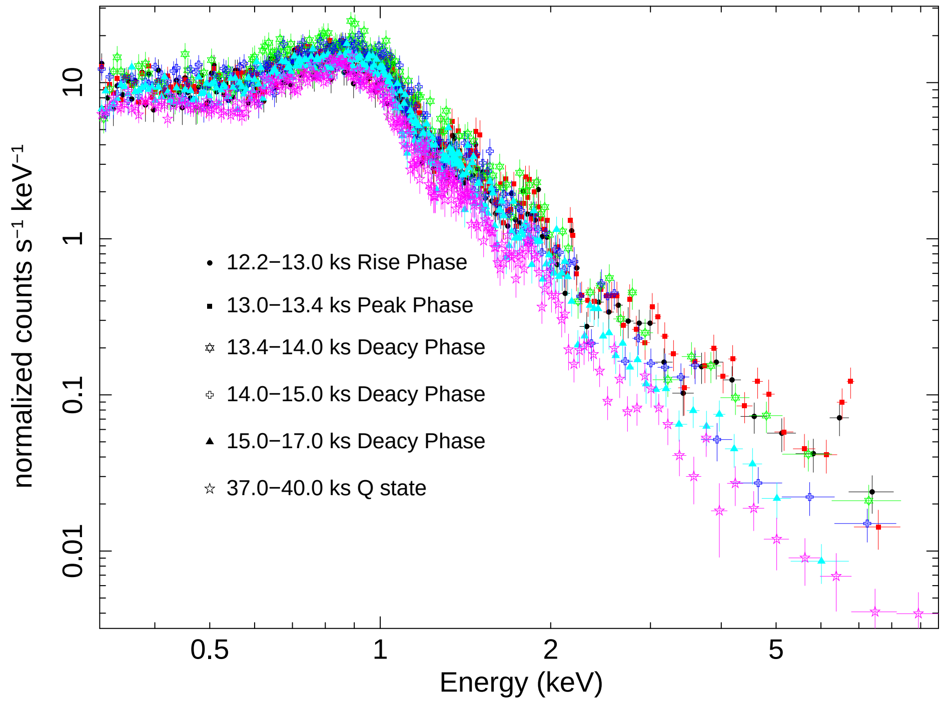

Figure 4.2: X-ray spectral evolution of 47 Cas during the flare with respect to quiescent state.

4.1.4 Density measurement: The RGS spectra

The RGS spectra of 47 Cas were analyzed in detail by Ness et al. (2003); Telleschi et al. (2005) and Nordon & Behar (2008); therefore, we have restricted our analysis to the OVII line only to determine the density. The density values during the flare and the quiescent state of 47 Cas were derived by using He-like triplets from OVII. The most intense He-like lines correspond to transitions between the $n = 2$ shell and the $n = 1$ ground state shell. The excited state transitions $^1P_1$, $^3P_1$ and $^3S_1$ to the ground state $^1S_0$ are called resonance (r), intercombination (i) and forbidden (f) lines, respectively. In the X-ray spectra, the ratio of fluxes in forbidden and intercombination lines ($R = f/i$) is potentially sensitive to density (n_e), while the ratio $G = (f + i)/r$ is sensitive to temperature (Gabriel & Jordan, 1969; Porquet et al., 2001). Of the He-like ions observed with the RGS, OVII has lines that are strong and unblended to use in a measurement of n_e. Figures 4.4 (a-d) show the He-like triplet from OVII line for total observations, pre-flare state, flaring state and quiescent state of 47 Cas B. Line fluxes were measured using the XSPEC package by fitting the RGS1 spectra with a sum of narrow Gaussian emission lines convolved

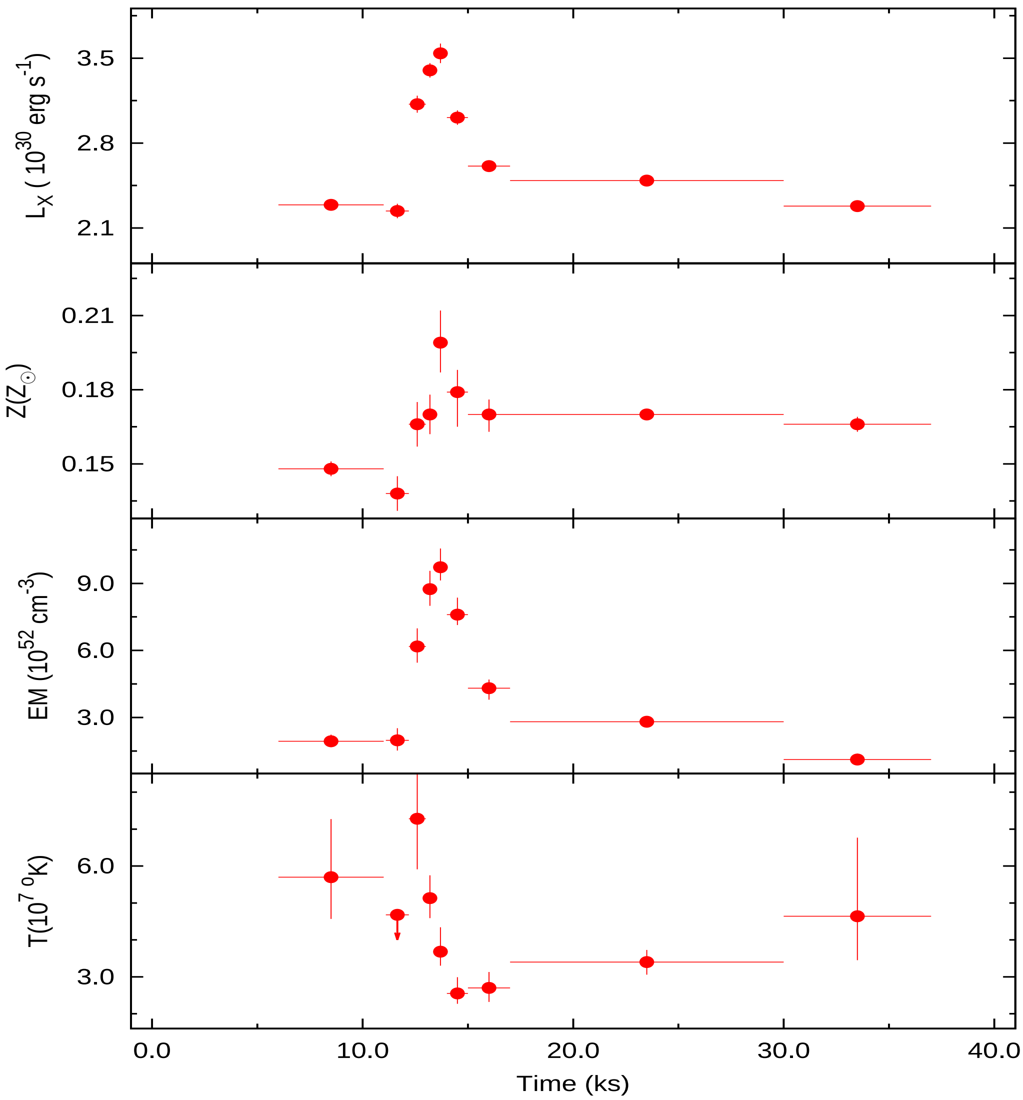

Figure 4.3: Evolution of X-ray spectral parameters of 47 Cas during the flare.

with the response matrices of the RGS instruments. The continuum emission was described using Bremsstrahlung models at the temperatures of the plasma components inferred from the analysis of the EPIC spectra during the quiescent state. The derived values of fluxes of r, i and f lines are given in Table 4.2. We have used the CHIANTI atomic database version 7.1 (Dere et al., 1997; Landi et al., 2013) to derive the $G-$ and $R-$ratios. Figures 4.5 (a) and (b) are plots of G-ratio and temperature, and R-ratio and density. The G-ratio for 47 Cas B implies a temperature in between 1–3 MK. Therefore, R-ratio was derived for the temperature range of 1–3

Table 4.1: Best-fit spectral parameters from different segment of the light curve.

Time bins (ks) (from-to)	Z ($Z_\odot$)	T (10^7 °K)	EM (10^{52} cm^{-3})	L_X (10^{30} erg s^{-1})	χ^2_ν(dof)
6.0-11.0	$0.148^{+0.003}_{-0.003}$	$5.70^{+1.57}_{-1.13}$	$1.94^{+0.29}_{-0.26}$	$2.29^{+0.02}_{-0.02}$	1.26(361)
11.1-12.2	$0.138^{+0.007}_{-0.007}$	$4.68^{+0.00}_{-0.00}$	$1.98^{+0.54}_{-0.46}$	$2.24^{+0.06}_{-0.06}$	1.10(223)
12.2-13.0	$0.166^{+0.009}_{-0.009}$	$7.28^{+1.38}_{-1.37}$	$6.18^{+0.81}_{-0.73}$	$3.12^{+0.07}_{-0.07}$	1.00(220)
13.0-13.4	$0.170^{+0.008}_{-0.008}$	$5.13^{+0.62}_{-0.54}$	$8.74^{+0.82}_{-0.74}$	$3.40^{+0.06}_{-0.06}$	1.02(272)
13.4-14.0	$0.199^{+0.013}_{-0.012}$	$3.68^{+0.66}_{-0.38}$	$9.72^{+0.84}_{-0.59}$	$3.54^{+0.08}_{-0.08}$	1.11(203)
14.0-15.0	$0.179^{+0.009}_{-0.014}$	$2.55^{+0.44}_{-0.28}$	$7.60^{+0.76}_{-0.46}$	$3.01^{+0.06}_{-0.06}$	1.11(241)
15.0-17.0	$0.170^{+0.006}_{-0.007}$	$2.70^{+0.43}_{-0.38}$	$4.31^{+0.39}_{-0.51}$	$2.61^{+0.04}_{-0.04}$	1.19(282)
17.0-30.0	$0.170^{+0.002}_{-0.002}$	$3.40^{+0.33}_{-0.34}$	$2.81^{+0.21}_{-0.21}$	$2.49^{+0.01}_{-0.01}$	1.08(487)
30.0-37.0	$0.166^{+0.003}_{-0.003}$	$4.64^{+2.13}_{-1.19}$	$1.12^{+0.20}_{-0.24}$	$2.28^{+0.02}_{-0.02}$	1.12(386)

MK. For these temperatures, we derive electron densities $2.5^{+2.1}_{-1.7} \times 10^{10}$ cm^{-3} and $4.0^{+2.3}_{-1.5}$ cm^{-3} for the quiescent and flaring states, respectively. The electron density during the flare was slightly higher than the quiescent state. However, this increase is well within a 1σ level.

4.1.5 Loop length and flare parameters

The loop length of the flare observed in 47 Cas was derived using the hydrodynamic model (see section 1.3.4.4 and equation 1.8). In this equation 1.8, the observed peak temperature must be corrected to a maximum value using the following equation

$$T_{max} = 0.13T^{1.16} \tag{4.2}$$

where T is the maximum best-fit temperature derived from spectral fitting to the data. This expression for loop maximum temperature can be derived from fitting hydrostatic model loops with isothermal models. The unitless correction factor for XMM-Newton is

Table 4.2: Flux of He-like OVII triplet during different segments of light curve as shown in Fig. 4.1. The derived values of densities are also given.

Line (OVII)	λ (Å)	Flux (10^{-4} $Photons$ cm^{-2} s^{-1}) Total	Pre-Flare	Flare	Quiescent
r	21.6	1.10 ± 0.17	1.14 ± 0.23	1.37 ± 0.21	1.07 ± 0.21
i	21.8	0.39 ± 0.12	0.35 ± 0.11	0.56 ± 0.20	0.30 ± 0.10
f	22.1	0.75 ± 0.14	0.72 ± 0.20	0.93 ± 0.21	0.63 ± 0.16
Density (cm^{-3})		$3.2^{+2.5}_{-1.4} \times 10^{10}$	$2.2^{+1.7}_{-1.2} \times 10^{10}$	$4.0^{+2.3}_{-1.5} \times 10^{10}$	$2.5^{+2.1}_{-1.4} \times 10^{10}$

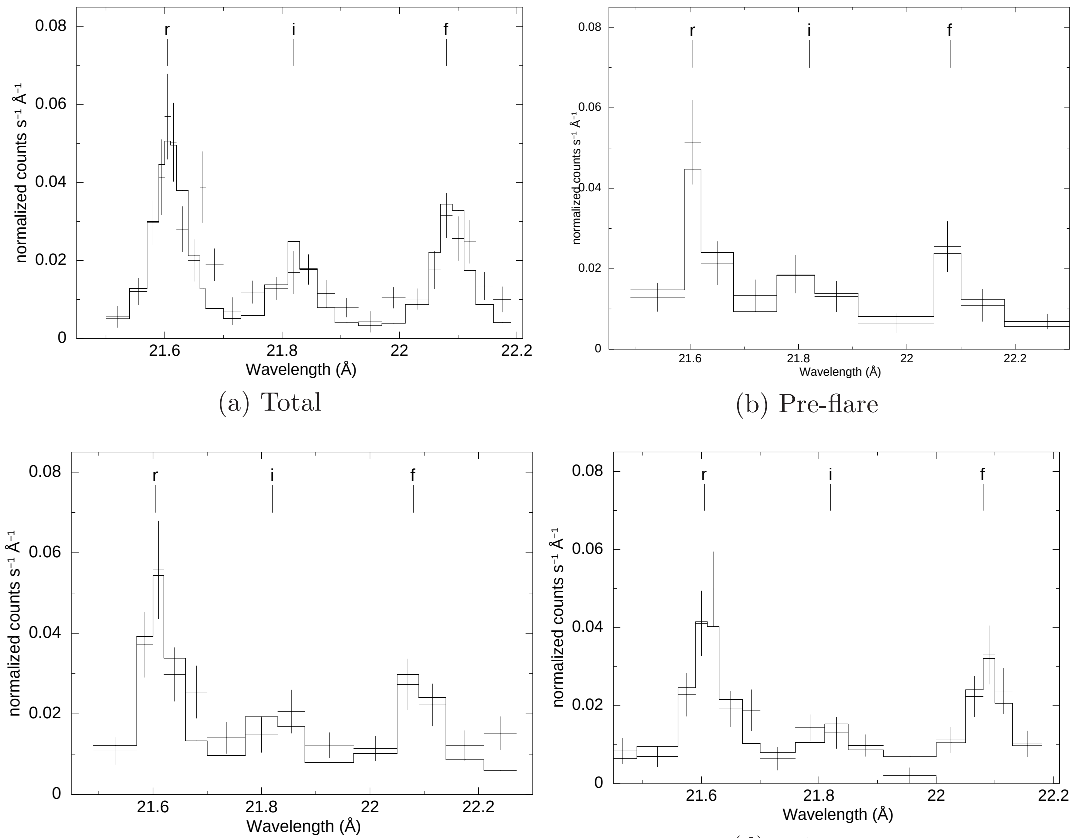

(a) Total (b) Pre-flare

(c) Flare (d) quiescent

Figure 4.4: He-like triplet of OVII extracted from the *XMM-Newton* RGS spectrum of 47 Cas during (a) quiescent plus flare state, (b) pre-flare state (c) flare state, and (d) quiescent state.

$$F(\zeta) = \frac{0.51}{\zeta - 0.35} + 1.35; \tag{4.3}$$

where ζ is the slope of the $\log \sqrt{\mathrm{EM}} - \log T$ diagram (Reale, 2007). Equations 4.2 and 4.3 are calibrated for spectral response of the detecter used for observations (Reale et al., 2004). Fig. 4.6 shows the $\log \sqrt{\mathrm{EM}} - \log \mathrm{T}$ diagram during the flare. We derive the value of ζ to be 1.54 ± 1.06, indicating the presence of sustained heating during the decay of the flare was negligible. The value of ζ in the upper extreme is outside the domain of the validity of the method, therefore, the loop length was derived by using the lower extreme value of ζ (i.e. 0.48) and estimated as 3.3×10^{10} cm.

The loop length is also derived from other methods as given by Haisch (1983),

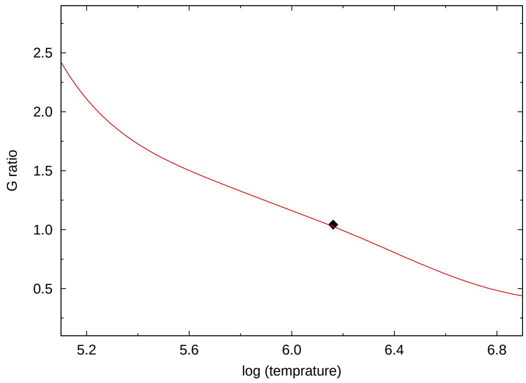

(a) Temperature

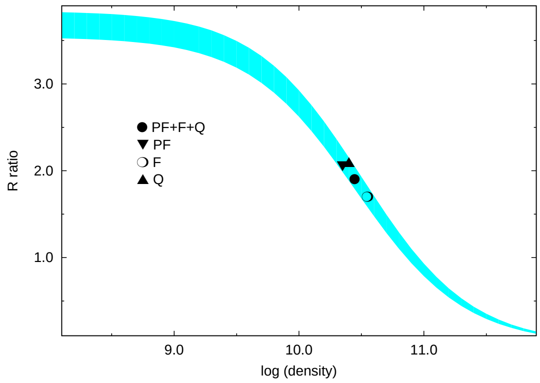

(b) Density

Figure 4.5: The ratio G = (i + f)/r of the summed intensities of the OVII intercombination and forbidden lines over the intensity of the recombination line and (b) intensity ratio R = f/i of the OVII forbidden and intercombination lines as a function of electron density, calculated using the CHIANTI database. The R-ratio was calculated for the temperature range of 1-3 MK.

Hawley et al. (1995), Shibata & Yokoyama (2002) and Aschwanden et al. (2008), and we found that the loop lengths from these methods are consistent with that from Reale et al. (1997)'s method. Many authors in the past have compared the loop lengths from the above methods and some of them found consistent loop lengths (Bhatt et al., 2014; Covino et al., 2001); however, others found inconsistencies in the loop length determination (Favata et al., 2001; Shibata & Yokoyama, 2002; Srivastava et al., 2013). Considering 47 Cas to be an early G-type star (Güdel et al., 1998), the loop length was found to be less than the half of the stellar radius and much less than the pressure scale height of $\sim 4 \times 10^{11}$ cm. Here, pressure scale height is defined as $h = kT/\mu g$; where k is the Boltzmann constant, T is the plasma temperature, μ is the mean molecular weight in terms of the proton's rest mass, and g is the surface gravity of the star.

After finding L, EM and n_e, we can derive the pressure (p), the volume (V), and the minimum magnetic field (B) to confine the flaring plasma as

$$n_e = \frac{p}{2kT_{\max}}\ \mathrm{cm}^{-3};\ V = \frac{\mathrm{EM}}{n_e^2}\ \mathrm{cm}^3; B = \sqrt{8\pi p}\ \mathrm{G} \tag{4.4}$$

using $n_e = 4.0 \times 10^{10}$ cm^{-3}, $EM = 9.72 \times 10^{52}$ cm^{-3} and $T = 7.28 \times 10^7$ K. The estimated values of p, V and B during the flare observed in 47 Cas were 804 dyne cm^{-2}, 6.0×10^{31} cm^3 and 142 Gauss, respectively. The pressure and density derived for the present flare are intermediate between those of the flares from G-K dwarfs (Pandey & Singh, 2008).

Due to the lack of multi-wavelength coverage, a detailed assessment of the energy budget of the present flare is not possible. However, using the scaling laws from Rosner et al. (1978), the heating rate per unit volume can be determined as $E_H = 10^{-6}\, T^{3.5}\, L^{-2}$ erg s^{-1} cm^{-3}, where T and L are plasma temperature and loop length. Using $L = 3.3{\times}10^{10}$ cm, the value of E_H was obtained as 3.2 erg s^{-1} cm^{-3}. The total heating rate at the flare maximum is estimated as, $H = E_H V \approx 2 \times 10^{32}$ erg s^{-1}. In order to satisfy the energy balance relation for the flaring as a whole, the maximum X-ray luminosity must be lower than the total energy rate (H) at the flare peak. For the present flare, the total energy rate was found to be ~ 40 times more than the peak X-ray luminosity. This value is in agreement with those reported for the solar flares where the soft X-ray radiation only accounts for up to 20 % of the total energy (Wu et al., 1986), but is smaller than many flares from solar-like stars. The total energy released from the flare was found to be 2×10^{34} erg over 4.8 ks, which is equivalent to ~ 3 s of the star's bolometric energy output. The total X-ray energy released during the flare from 47 Cas indicates that this flare was as energetic as flares from other G-K dwarfs ($2.3 \times 10^{32} - 6.1 \times 10^{34}$ erg; Pandey & Singh, 2008). If we assume heating is constant for the initial rise phase, which lasts for $\tau_r \approx 831$ s, and then decays exponentially, with an e-folding time of $\tau_d \approx 2494$ s, the total energy [$E_{tot} = H(\tau_d + \tau_r)$] is estimated as $\sim 6 \times 10^{35}$ erg, which is approximately 30 times more than the energy radiated in X-rays.

It is believed that the magnetic field provides the main source of energy for the solar/stellar activities including flares. In order to know the strength of the magnetic field (B_0) required to accumulate the emitted energy, we assume that the energy released during the flare is indeed of magnetic origin and it occurs entirely within a single coronal loop structure. The total energy can be estimated as

$$E_{\rm X,tot} = \frac{(B_0^2 - B^2)}{8\pi} \times V \tag{4.5}$$

Using the values of $E_{\rm X,tot}$, B and V, the total magnetic field required to produce the flare is estimated to be ~ 517 Gauss.

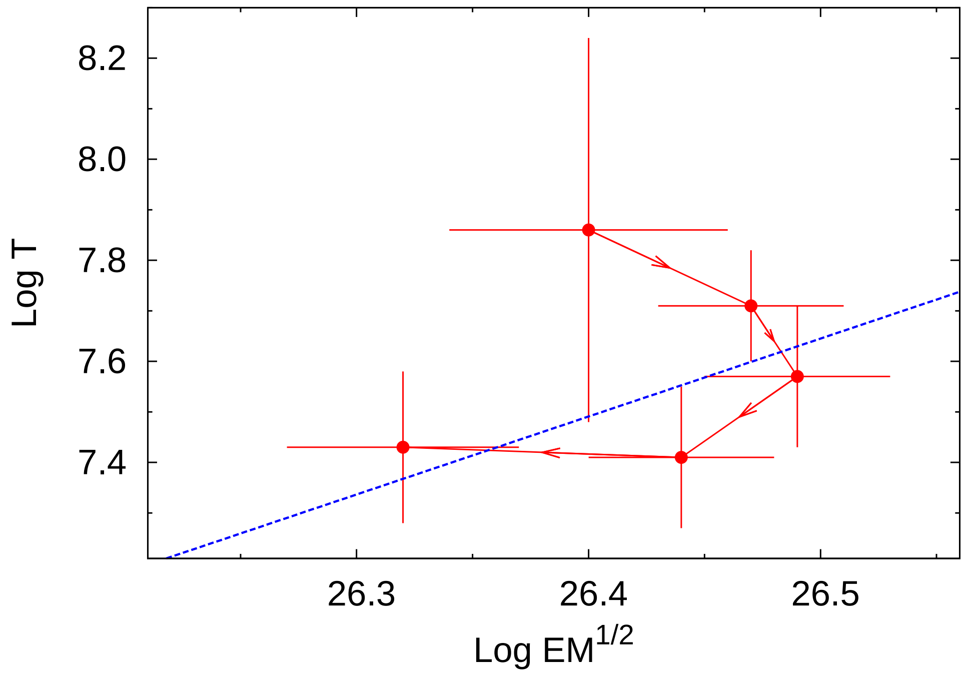

Figure 4.6: Evolution of flare in log $\sqrt{\mathrm{EM}}$ – log T plane. The dashed line show the best fit straight line during the decay phase with slope $\zeta = 1.54 \pm 1.06$.

4.1.6 conclusions

The luminosity at the peak of the flare from 47 Cas is found to be 3.54×10^{30} erg s^{-1}, which is $\sim$ 2 times higher than that at a quiescent state. The time-resolved X-ray spectroscopy of the flare show the variable nature of the temperature, the emission measure, and the abundance. The maximum temperature during the flare is derived as 72.8 MK. The density during the flare is estimated as 4.0×10^{10} cm. The parameters derived from the present analyses indicate that the X-ray flare on 47 Cas is similar to a solar impulsive flare whose height (L/π) is only 15% of the stellar radius.

4.2 AB Dor

In this part of the chapter, a comprehensive analysis of all X-ray flares observed on the nearest quadruple system AB Dor, with *XMM-Newton* satellite was done. The brightest star of this quadruple system (Close et al., 2007), AB Dor A, is a well-known, closest ultra-fast rotator (P_{rot} = 0.51 days, d = $\sim$14.9 pc, see Guirado et al., 1997; Pakull, 1981) and one of the brightest coronal X-ray sources in the sky. It has a mass of about 0.86 ± 0.054 $M_\odot$ (Strassmeier, 2009), and a radius of about 0.96 ± 0.06 $R_\odot$ (Guirado et al., 2011) with an age of about ∼20–30 Myr (Collier Cameron & Foing, 1997). It's visual companion AB Dor B (or Rst 137B) is an active M-dwarf (Vilhu & Linsky, 1987), ∼60 times bolometrically fainter and located ∼9.5″ away from AB Dor A. AB Dor B is discovered as a binary system after the advent of adaptive optics (Close et al., 2005). The fourth component AB Dor C is a very low mass star (0.08–0.11 $M_\odot$) located ∼ 0.16″ away from AB Dor A (Close et al., 2007). The contribution from the companions to the X-ray spectrum of AB Dor A can be considered to be negligible, essentially because the quiescent X-ray emission of the companions scales as their bolometric luminosity (for their young age, all the stars in the system emit close to the saturation level of $L_x/L_{bol} \sim 10^{-3}$). After first detection of AB Dor in X-ray by the *Einstein Observatory* (see Pakull, 1981; Vilhu & Linsky, 1987), it has been a frequent target of extensive investigation across all wavelength bands. Further X-ray observations were carried out with ROSAT (Kuerster et al., 1997b), *XMM-Newton* (Güdel et al., 2001; Lalitha et al., 2013; Sanz-Forcada et al., 2003), and *Chandra* (García-Alvarez et al., 2008; Hussain et al., 2007; Sanz-Forcada et al., 2003). High activity levels were consistently reported with frequent flaring Vilhu et al. (1993) estimated flare frequency to be one flare per rotation) on time scales from minutes to hours. Considering these facts and making use of twelve year's XMM-Newton data, we investigated all X-ray flares observed on AB Dor A.

4.2.1 Light curves of flaring events

The background subtracted X-ray light curves of all 31 sets (S01 to S31) of AB Dor, as observed with EPIC and RGS detectors are shown in Figure 4.7. The PN (marked as solid red circles) and MOS (summed MOS1+MOS2; marked as solid black squares) light curves were obtained in the energy band 0.3-10.0 keV, whereas, the RGS light curves (summed RGS1+RGS2; marked as solid blue triangle) were obtained in the 0.3-2.5 keV energy band. The temporal binning of all the light curves was 200 s. The entire light curve of each observations were inconstant; therefore, it was hard to find the quiescent level of AB Dor. However, the minimum count rates were found during the observations S04, S08 and S24, which we considered as quiescent state as marked by Q1, Q2 and Q3 in Figure 4.7. The median values of the quiescent state count rates were found to be 20.3, 10.4 and 2.33 counts s^{-1} for PN, MOS, and RGS detectors, respectively.

Table 4.3: Parameters obtained from light curvs of the flaring events.

Sl.	**Flare**	**Dn.**	τ_r **(ks)**			τ_d **(ks)**			F_p/F_q			**Type**
No.	**name**	(ks)	**PN**	**MOS**	**RGS**	**PN**	**MOS**	**RGS**	**PN**	**MOS**	**RGS**	–
1	S01-F1	6.30	4.24 ± 0.52	—	4.82 ± 2.56	2.00 ± 0.18	—	1.92 ± 0.49	1.18	—	1.18	typ
2	S01-F2	9.19	0.69 ± 0.09	—	0.55 ± 0.17	7.71 ± 0.46	—	6.99 ± 0.88	1.25	—	1.29	typ
3	S01-F3	13.75	1.23 ± 0.12	—	1.60 ± 0.11	3.00 ± 0.07	—	2.71 ± 0.11	3.04	—	2.81	typ
4	S01-F4a		0.98 ± 0.07	—	1.14 ± 0.11	2.32 ± 0.22	—	1.80 ± 0.29	2.21	—	2.19	
5	S01-F4b	> 20.94	2.77 ± 0.42	—	2.76 ± 0.54	4.28 ± 0.66	—	4.38 ± 1.17	1.77	—	1.93	mpl
6	S01-F4c		3.69 ± 0.74	—	3.27 ± 1.49	1.48 ± 0.38	—	1.13 ± 0.65	1.61	—	1.58	
7	S01-F4d		0.90 ± 0.20	—	1.09 ± 0.39	—	—	—	> 1.79	—	> 1.94	
8	S02-F1	> 10.31	—	—	2.24 ± 1.58	—	—	5.09 ± 0.40	—	—	> 1.41	inc
9	S02-F2	6.39	—	—	0.24 ± 0.11	—	—	1.58 ± 0.20	—	—	1.25	typ
10	S02-F3a	18.46	2.43 ± 0.20	—	2.25 ± 0.21	3.37 ± 0.69	—	2.06 ± 1.04	1.27	—	1.44	srf
11	S02-F3b		2.86 ± 0.55	—	2.99 ± 1.58	3.17 ± 0.19	—	3.05 ± 0.35	1.30	—	1.38	
12	S02-F4	7.43	4.46 ± 0.50	—	4.66 ± 0.73	6.58 ± 0.37	—	6.59 ± 0.58	1.43	—	1.52	typ
13	S02-F5	5.92	1.06 ± 0.15	—	2.06 ± 0.38	4.14 ± 0.26	—	3.74 ± 0.42	1.26	—	1.32	typ
14	S02-F6	> 4.02	0.36 ± 0.02	—	0.36 ± 0.13	1.39 ± 0.16	—	1.81 ± 0.42	> 1.25	—	> 1.29	inc
15	S03-F1a	11.10	0.39 ± 0.03	0.41 ± 0.05	0.46 ± 0.04	1.27 ± 0.15	1.33 ± 0.23	1.20 ± 0.22	2.51	2.43	2.30	dbl
16	S03-F1b		1.49 ± 0.25	1.45 ± 0.33	1.93 ± 0.42	3.58 ± 0.08	3.83 ± 0.08	3.83 ± 0.16	2.06	2.06	2.04	
17	S03-F2	11.09	0.73 ± 0.05	1.28 ± 0.06	1.08 ± 0.09	7.49 ± 0.18	8.87 ± 0.32	7.36 ± 0.31	1.70	1.50	1.74	typ
18	S03-F3	7.78	2.27 ± 0.31	2.19 ± 0.27	1.23 ± 0.28	6.25 ± 0.29	5.61 ± 0.32	4.88 ± 0.40	1.32	1.31	1.45	typ
19	S04-F1	6.21	—	—	0.42 ± 0.14	—	—	0.99 ± 0.20	—	—	1.27	typ
20	S04-F2a		—	—	3.03 ± 0.16	—	—	15.93 ± 0.81	—	—	1.71	
21	S04-F2b	41.11	—	—	1.56 ± 0.29	—	—	2.30 ± 0.31	—	—	1.49	mpl
22	S04-F2c		—	—	0.96 ± 0.23	—	—	3.65 ± 0.34	—	—	1.49	
23	S04-F2d		—	—	0.33 ± 0.25	—	—	3.35 ± 0.55	—	—	1.49	
24	S04-F3	> 8.36	—	1.21 ± 0.14	0.94 ± 0.17	—	4.64 ± 0.44	3.91 ± 0.40	—	1.55	1.64	typ
25	S05-F1a		22.33 ± 0.96	23.04 ± 1.46	19.68 ± 0.98	30.23 ± 0.61	29.58 ± 0.58	31.02 ± 0.91	2.19	2.18	2.26	
26	S05-F1b		0.24 ± 0.09	0.23 ± 0.12	0.66 ± 0.20	1.29 ± 0.17	1.33 ± 0.16	1.29 ± 0.27	2.21	2.18	2.11	
27	S05-F1c	> 52.41	0.21 ± 0.12	0.19 ± 0.17	0.39 ± 0.20	1.77 ± 0.29	1.56 ± 0.30	1.78 ± 0.25	2.14	2.12	2.16	cpx
28	S05-F1d		0.40 ± 0.06	0.53 ± 0.11	0.34 ± 0.08	1.19 ± 0.09	1.46 ± 0.15	1.14 ± 0.13	2.16	2.06	2.16	
29	S05-F1e		1.58 ± 0.42	1.34 ± 0.17	0.92 ± 0.33	1.28 ± 0.29	1.51 ± 0.20	1.90 ± 0.55	1.58	1.56	1.63	
30	S05-F1f		2.42 ± 0.15	2.44 ± 0.27	2.11 ± 0.28	—	—	—	> 1.82	> 1.74	> 1.84	
31	S06-F1a	15.78	1.50 ± 0.13	1.72 ± 0.25	1.97 ± 0.25	2.76 ± 0.23	3.21 ± 0.42	3.00 ± 0.69	1.74	1.68	1.65	dbl
32	S06-F1b		2.43 ± 0.33	2.59 ± 0.51	3.00 ± 1.03	4.12 ± 0.14	4.43 ± 0.23	4.75 ± 0.41	1.48	1.51	1.43	
33	S06-F2a		0.58 ± 0.13	0.57 ± 0.11	0.57 ± 0.10	0.64 ± 0.09	0.65 ± 0.08	0.69 ± 0.09	2.13	2.21	2.00	
34	S06-F2b	> 19.79	2.86 ± 0.16	3.11 ± 0.18	2.83 ± 0.15	3.08 ± 0.20	3.22 ± 0.34	3.19 ± 0.34	2.55	2.41	2.33	tpl
35	S06-F2c		3.92 ± 0.15	4.24 ± 0.31	3.83 ± 0.23	—	—	—	3.53	3.12	> 3.26	
36	S07-F1	> 4.49	—	—	—	—	2.79 ± 0.35	2.45 ± 0.26	—	> 1.25	> 1.31	inc
37	S07-F2	18.05	—	3.76 ± 0.31	3.39 ± 0.39	—	6.28 ± 0.40	7.05 ± 0.47	—	1.32	1.43	typ
38	S07-F3a	> 6.98	—	1.46 ± 0.13	1.15 ± 0.10	—	4.86 ± 1.79	4.04 ± 1.89	—	2.48	3.52	dbl
39	S07-F3b		—	0.39 ± 0.18	0.33 ± 0.24	—	3.45 ± 0.55	2.73 ± 0.26	—	2.50	3.37	

Continued on Next Page...

Table 4.3 – Continued

Sl. No.	Flare name	Dn. (ks)	τ_r(s) PN	τ_r(s) MOS	τ_r(s) RGS	τ_d(s) PN	τ_d(s) MOS	τ_d(s) RGS	F_p/F_q PN	F_p/F_q MOS	F_p/F_q RGS	Type –
40	S09-F1a	13.14	—	—	1.38 ± 0.16	—	—	0.31 ± 0.18	—	—	1.44	dbl
41	S09-F1b		—	—	2.85 ± 1.75	—	—	5.08 ± 0.48	—	—	1.31	
42	S09-F2	5.81	0.30 ± 0.12	0.20 ± 0.08	0.28 ± 0.09	0.89 ± 0.06	0.91 ± 0.11	0.93 ± 0.13	1.33	1.22	1.33	typ
43	S10-F1a	30.05	—	—	4.68 ± 0.12	—	—	6.10 ± 0.94	—	2.78	2.83	mpl
44	S10-F1b		—	—	1.69 ± 0.92	—	2.46 ± 0.27	2.33 ± 0.21	—	2.56	2.62	
45	S10-F1c		—	—	1.97 ± 0.63	—	—	—	—	—	> 2.10	
46	S10-F1d		—	—	—	—	—	1.75 ± 0.10	—	—	> 2.10	
47	S10-F2	11.72	—	—	1.48 ± 0.13	—	—	3.49 ± 0.33	—	—	1.30	typ
48	S10-F3	11.71	0.00 ± 0.00	5.91 ± 2.47	2.35 ± 0.26	16.06 ± 1.44	15.79 ± 1.46	12.67 ± 0.89	> 1.42	> 1.29	1.60	typ
49	S10-F4a	> 12.17	1.93 ± 0.22	2.09 ± 0.23	1.95 ± 0.32	0.93 ± 0.23	1.18 ± 0.27	1.68 ± 0.53	1.80	1.50	1.39	tpl
50	S10-F4b		0.36 ± 0.50	1.19 ± 0.23	0.57 ± 1.35	1.70 ± 0.44	16.20 ± 2.52	1.06 ± 0.45	1.81	1.60	1.41	
51	S10-F4c		0.71 ± 0.26	—	0.46 ± 0.24	4.38 ± 0.17	—	3.62 ± 0.37	1.91	—	1.59	
52	S11-F1	19.94	—	—	8.77 ± 0.37	—	—	9.14 ± 0.45	—	—	2.28	typ
53	S12-F1	19.79	—	—	—	—	6.02 ± 0.06	6.36 ± 0.12	—	3.88	3.90	inc
54	S13-F1	6.58	—	3.94 ± 0.30	4.37 ± 0.35	—	8.49 ± 0.17	6.41 ± 0.50	—	2.64	2.85	typ
55	S13-F2	> 3.78	—	2.98 ± 0.11	3.03 ± 0.17	—	—	—	—	> 3.03	> 3.24	inc
56	S14-F1	> 16.75	—	7.78 ± 2.11	9.03 ± 2.08	—	9.97 ± 0.10	9.38 ± 0.12	—	3.72	3.42	inc
57	S14-F2	5.03	—	3.38 ± 0.19	3.88 ± 0.34	—	4.81 ± 0.09	5.27 ± 0.45	—	2.06	1.87	typ
58	S15-F1	> 14.79	—	—	—	—	—	8.16 ± 0.22	—	—	2.32	inc
59	S15-F2	5.22	—	—	0.13 ± 0.02	—	—	0.27 ± 0.02	—	—	2.61	typ
60	S15-F3	> 19.44	—	—	9.28 ± 0.37	—	—	—	—	—	1.74	inc
61	S16-F1	> 17.86	—	—	—	—	—	5.88 ± 0.15	—	—	2.36	inc
62	S16-F2	7.98	—	—	1.40 ± 0.13	—	—	4.80 ± 0.35	—	—	1.43	typ
63	S16-F3a	9.15	—	—	1.14 ± 0.28	—	—	5.40 ± 1.59	—	—	1.32	dbl
64	S16-F3b		—	—	0.30 ± 0.22	—	—	4.49 ± 1.06	—	—	1.29	
65	S16-F4a	> 12.76	—	—	2.08 ± 0.11	—	—	1.62 ± 0.18	—	—	2.93	dbl
66	S16-F4b		—	—	1.71 ± 0.49	—	—	4.01 ± 0.33	—	—	1.92	
67	S17-F1	7.18	—	—	1.63 ± 0.18	—	—	2.27 ± 0.25	—	—	1.46	typ
68	S18-F1a	> 15.62	—	—	—	—	4.24 ± 0.22	3.99 ± 1.15	—	> 1.79	> 1.85	dbl
69	S18-F1b		—	—	2.09 ± 1.12	—	—	4.99 ± 0.49	—	—	1.46	
70	S19-F1	> 10.42	—	—	0.59 ± 0.10	—	—	3.09 ± 0.38	—	—	> 1.45	inc
71	S19-F2a	25.66	—	—	2.01 ± 0.25	—	—	3.73 ± 0.88	—	—	1.43	mpl
72	S19-F2b		—	—	1.06 ± 0.78	—	—	1.76 ± 0.63	—	—	1.56	
73	S19-F2c		—	—	1.63 ± 0.58	—	4.10 ± 0.83	4.33 ± 0.97	—	1.41	1.58	
74	S19-F2d		—	3.33 ± 0.48	2.77 ± 0.83	4.24 ± 0.37	3.85 ± 0.25	3.96 ± 0.53	1.54	1.47	1.62	
75	S19-F2e		0.23 ± 0.18	0.18 ± 0.08	0.18 ± 0.07	1.50 ± 0.25	1.87 ± 0.39	2.06 ± 0.40	1.31	1.25	1.30	

Continued on Next Page. . .

Table 4.3 – Continued

Sl.	Flare	Dn.	τ_r(s)			τ_d(s)			F_p/F_q			Type
No.	name	(ks)	PN	MOS	RGS	PN	MOS	RGS	PN	MOS	RGS	–
76	S19-F3	> 2.55	1.30 ± 0.10	0.82 ± 0.08	1.02 ± 0.24	—	—	—	1.53	1.55	> 1.50	inc
77	S20-F1	7.94	—	—	1.76 ± 0.31	—	—	2.07 ± 0.26	—	—	1.37	typ
78	S20-F2a	21.38	—	—	1.58 ± 0.18	—	—	3.40 ± 2.19	—	—	1.64	tpl
79	S20-F2b		—	—	2.01 ± 1.39	—	—	6.17 ± 0.49	—	—	1.63	
80	S20-F2c		—	—	0.44 ± 0.15	—	—	1.24 ± 0.17	—	—	1.35	
81	S20-F3a	22.50	—	—	4.34 ± 0.27	—	—	1.21 ± 0.64	—	—	1.28	tpl
82	S20-F3b		—	—	0.63 ± 0.21	—	—	2.56 ± 0.19	—	—	1.56	
83	S20-F3c		—	—	0.19 ± 0.15	—	—	1.69 ± 0.38	—	—	1.15	
84	S21-F1	> 4.47	—	—	1.20 ± 0.35	—	—	2.46 ± 0.23	—	—	> 1.73	inc
85	S21-F2a	21.73	—	—	8.30 ± 0.80	—	—	8.96 ± 4.94	—	—	1.62	dbl
86	S21-F2b		—	—	1.73 ± 1.23	—	—	6.14 ± 0.45	—	—	1.51	
87	S21-F3	9.94	—	—	4.22 ± 0.77	—	—	4.73 ± 0.54	—	—	1.41	typ
88	S21-F4	6.46	—	—	0.70 ± 0.07	—	—	3.38 ± 0.46	—	—	1.75	typ
89	S22-F1a	> 26.25	—	—	—	—	—	6.93 ± 0.34	—	—	> 2.22	cpx
90	S22-F1b		—	—	0.26 ± 0.37	—	—	0.93 ± 0.17	—	—	1.97	
91	S22-F1c		—	—	0.15 ± 0.03	—	—	5.01 ± 0.73	—	—	2.11	
92	S22-F1d		—	—	1.34 ± 0.10	—	—	1.16 ± 0.11	—	—	1.38	
93	S23-F1	> 3.73	—	—	4.06 ± 1.56	—	—	1.29 ± 0.13	—	—	> 1.51	inc
94	S23-F2	9.09	—	—	2.89 ± 0.34	—	—	3.23 ± 0.41	—	—	1.42	typ
95	S23-F3a	13.23	—	—	0.74 ± 0.12	—	—	1.70 ± 0.30	—	—	2.59	dbl
96	S23-F3b		—	—	1.75 ± 0.18	—	—	3.56 ± 0.16	—	—	3.28	
97	S23-F4	10.67	—	—	3.57 ± 0.42	—	—	5.33 ± 0.22	—	—	1.92	typ
98	S24-F1a	> 9.71	—	—	1.72 ± 0.24	—	—	1.92 ± 0.55	—	—	1.49	dbl
99	S24-F1b		—	—	1.10 ± 0.55	—	—	3.88 ± 0.35	—	—	1.35	
100	S24-F2a	> 16.68	—	—	3.72 ± 0.14	—	—	6.39 ± 3.81	—	—	2.68	dbl
101	S24-F2b		—	—	2.54 ± 0.98	—	—	10.05 ± 2.69	—	—	> 3.37	
102	S25-F1a	> 12.08	—	—	—	—	—	2.53 ± 1.15	—	—	> 1.59	dbl
103	S25-F1b		—	—	0.27 ± 0.10	—	—	5.45 ± 0.38	—	—	1.46	
104	S25-F2a	11.10	—	—	2.37 ± 0.20	—	—	3.55 ± 0.98	—	—	1.48	dbl
105	S25-F2b		—	—	2.15 ± 1.01	—	—	4.05 ± 0.38	—	—	1.46	
106	S25-F3a	> 19.03	—	—	3.20 ± 0.30	—	—	13.48 ± 4.72	—	—	1.57	dbl
107	S25-F3b		—	—	0.98 ± 0.10	—	—	3.56 ± 0.17	—	—	2.60	
108	S26-F1a	> 13.16	—	—	2.95 ± 0.47	—	—	7.42 ± 7.96	—	—	1.49	tpl
109	S26-F1b		—	—	0.85 ± 0.51	—	—	3.41 ± 0.82	—	—	1.55	
110	S26-F1c		—	—	0.57 ± 0.25	—	—	3.04 ± 0.34	—	—	1.46	
111	S26-F2a	33.52	—	—	1.14 ± 0.07	—	—	1.77 ± 0.24	—	—	3.93	mpl
112	S26-F2b		—	—	2.90 ± 0.56	—	—	2.12 ± 0.33	—	—	2.96	
113	S26-F2c		—	—	1.96 ± 0.31	—	—	6.72 ± 0.20	—	—	2.92	
114	S26-F2d		—	—	0.80 ± 0.13	—	—	2.24 ± 0.14	—	—	1.83	
115	S26-F2e		—	—	0.11 ± 0.08	—	—	1.23 ± 0.20	—	—	1.34	

Continued on Next Page…

Table 4.3 – Continued

Sl. No.	**Flare name**	**Dn.** (ks)	τ_r**(s)** PN	τ_r**(s)** MOS	τ_r**(s)** RGS	τ_d**(s)** PN	τ_d**(s)** MOS	τ_d**(s)** RGS	F_p/F_q PN	F_p/F_q MOS	F_p/F_q RGS	**Type** –
116	S27-F1	15.09	—	—	3.06 ± 0.22	—	—	8.95 ± 0.42	—	—	1.66	typ
117	S27-F2	26.25	1.40 ± 0.31	1.78 ± 0.34	3.08 ± 0.19	12.30 ± 0.28	13.00 ± 0.28	12.13 ± 0.48	> 1.20	> 1.23	1.66	typ
118	S27-F3	> 2.62	1.14 ± 0.18	1.40 ± 0.24	1.62 ± 0.24	—	—	—	> 1.21	> 1.23	> 1.35	inc
119	S28-F1	> 7.50	—	—	—	6.89 ± 0.19	8.01 ± 0.33	7.52 ± 0.50	1.61	1.52	1.63	inc
120	S28-F2a	33.40	2.69 ± 0.35	2.66 ± 0.38	2.25 ± 0.37	6.24 ± 5.25	5.36 ± 4.17	5.92 ± 3.47	1.38	1.47	1.47	mpl
121	S28-F2b		0.95 ± 0.19	0.96 ± 0.20	0.98 ± 0.18	2.54 ± 0.27	2.51 ± 0.28	2.19 ± 0.25	3.24	3.59	3.13	
122	S28-F2c		2.87 ± 0.46	2.76 ± 0.47	3.37 ± 0.51	4.92 ± 0.09	4.74 ± 0.10	5.34 ± 0.15	2.47	2.71	2.55	
123	S28-F2d		0.76 ± 0.05	0.87 ± 0.07	0.83 ± 0.09	2.51 ± 0.05	2.84 ± 0.06	3.44 ± 0.13	1.93	1.97	1.88	
124	S28-F3a	> 6.50	1.37 ± 0.28	1.27 ± 0.19	1.16 ± 0.21	1.67 ± 0.65	1.46 ± 0.19	1.43 ± 0.44	1.19	1.27	1.42	dbl
125	S28-F3b		0.61 ± 0.17	0.57 ± 0.08	0.65 ± 0.25	—	—	—	> 1.28	> 1.38	> 1.48	
126	S29-F1	23.24	—	—	1.66 ± 0.18	7.07 ± 0.19	6.81 ± 0.33	7.08 ± 0.33	> 1.18	> 1.18	1.65	typ
127	S29-F2	2.58	0.45 ± 0.10	0.22 ± 0.03	0.24 ± 0.06	—	—	—	> 1.46	> 1.51	> 1.54	inc
128	S30-F1	> 8.66	—	—	—	—	—	4.28 ± 0.36	—	—	> 2.83	inc
129	S30-F2	16.57	—	—	8.78 ± 0.81	—	—	7.74 ± 0.46	—	—	1.59	typ
130	S30-F3a	29.55	—	—	6.31 ± 0.86	—	—	7.41 ± 1.28	—	—	1.54	tpl
131	S30-F3b		4.70 ± 0.68	4.35 ± 0.62	4.84 ± 1.03	5.67 ± 0.57	5.62 ± 0.37	5.78 ± 0.69	1.51	1.59	1.45	
132	S30-F3c		0.43 ± 0.03	0.47 ± 0.04	0.68 ± 0.09	1.34 ± 0.04	1.45 ± 0.06	1.65 ± 0.10	2.68	2.81	2.31	
133	S30-F4	3.21	—	—	0.96 ± 0.16	—	—	0.49 ± 0.13	—	—	1.35	typ
134	S30-F5	> 3.85	—	—	2.28 ± 0.21	—	—	—	—	—	1.47	inc
135	S31-F1	6.81	—	—	3.36 ± 0.44	—	—	2.20 ± 0.08	—	—	1.99	typ
136	S31-F2a	> 27.34	—	—	1.02 ± 0.11	—	—	2.52 ± 0.14	—	—	2.03	cpx
137	S31-F2b		—	—	0.84 ± 0.19	—	—	2.48 ± 0.41	—	—	1.46	
138	S31-F2c		—	—	0.75 ± 0.09	—	1.33 ± 0.05	1.32 ± 0.06	—	2.45	2.06	
139	S31-F2d		—	0.90 ± 0.23	1.08 ± 0.22	—	3.98 ± 0.47	3.53 ± 0.25	—	1.24	1.25	
140	S31-F3	11.83	—	—	1.96 ± 0.13	—	—	3.68 ± 0.21	—	—	1.60	inc

The variable nature of X-ray light curves was on a time scale of hours and most of which resembles a flaring activity. Significant increase in intensity (above 3σ level of quiescent state) followed by a gradual decay is defined as flares. Such patterns were observed in the light curves of AB Dor as shown in Figure 4.7, where the flare regions are represented by arrows (separated by gray vertical lines) and marked by "Sij-Fk", where ij=01, 02, ... , 31 refers to the set number, whereas 'k' refers to the flare number in each set starting from 1.

4.2.2 Flare classification

Although the shape of a typical flare light curve was expected as a sudden increase in intensity followed by a exponential decay, we found several light curves with different shapes corresponds to different temporal morphology. Based on flare morphology Getman et al. (2008a) classified COUP flares in four different types – typical flares (*typ*, step flares (*stp*, double flares (*dbl*) and slow rise top flat flares (*srf*). The X-ray lightcurves with rapid monotonic rise and generally slower monotonic decay was described as *typ* flare. The *stp* flares are described as a typical flare but with a shoulder or bump overlayed on its decay phase. These morphologies are commonly seen on the Sun and are due either to a reheating event or to a triggered reconnection in a nearby magnetic loop. The *dbl* are defined as two overlapped typical flares or a bump in flare rise phase. The *srf* flares are more complex events where variations appear to occur more slowly than in most flares. They have slow rises, long duration peaks, and/or very long decays.

To adopt this classification scheme in AB Dor flares, we found, while a flare is identified as stp flare for broad energy range light curves, whereas two or multiple well-defined peaks in the softer energy band (e.g. flare S01-F4), so that it is not inherently very different from double or multiple peak flares. So in our study, we drop the 'stp' flare category and added multiple flare (*mpl*; more than two overlapped typical flares) and complex flare (*cpx*; one large predominated flares and other small flares superposed on it) category. Although, we have classified these flares according to flare morphology, it is unclear that the flares other than typ-flares (dbl, mpl, cpx, and srf flares) are caused by overlapping of emissions from spatially separated different flaring events or by the overlapping of emissions of multiple heating events of a single magnetic loop or a sequence of triggered reconnection events in a loop arcade. We have marked the different peaks of these multiple peaks flares (dbl, mpl, cpx, and srf) with lower-case alphabets (a, b, c, ...etc.) from the starting of the flare,

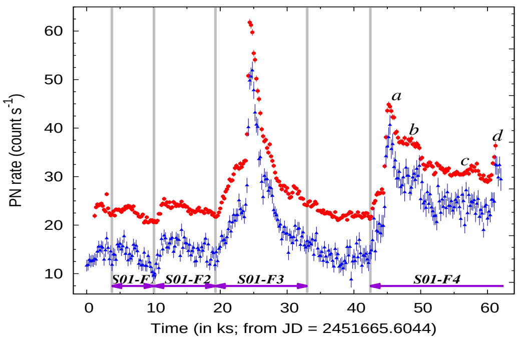

set-01

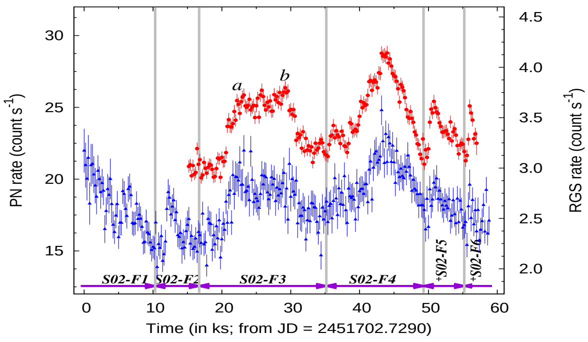

set-02

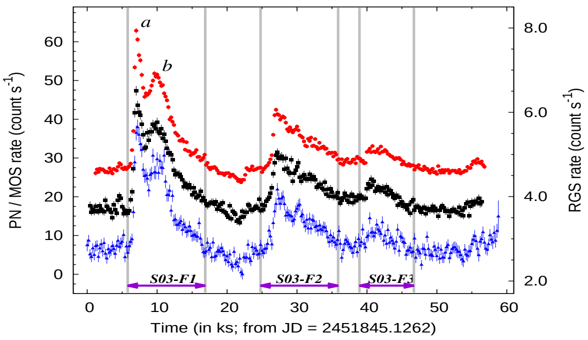

set-03

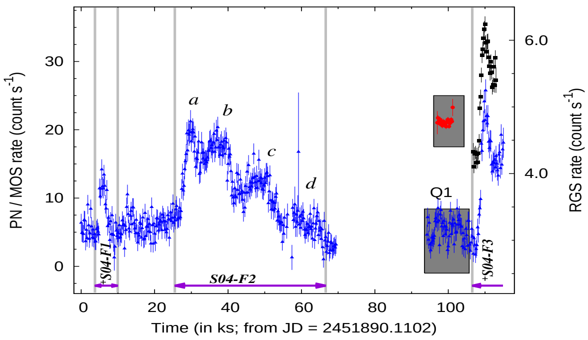

set-04

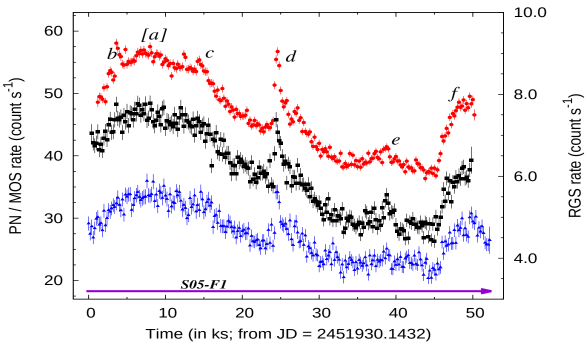

set-05

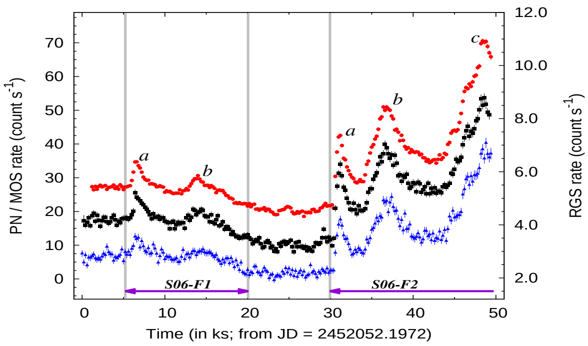

set-06

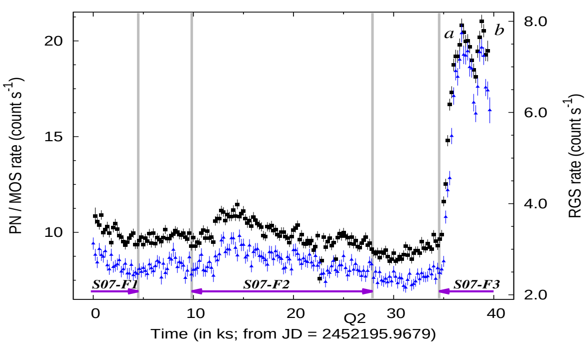

set-07

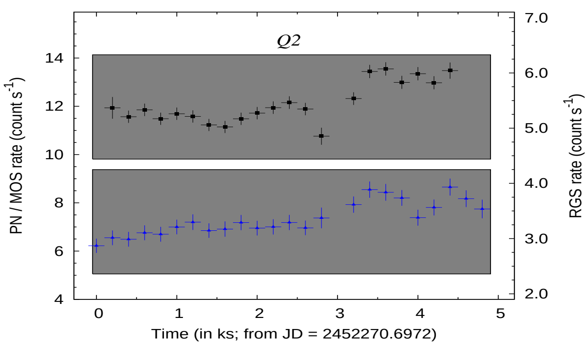

set-08

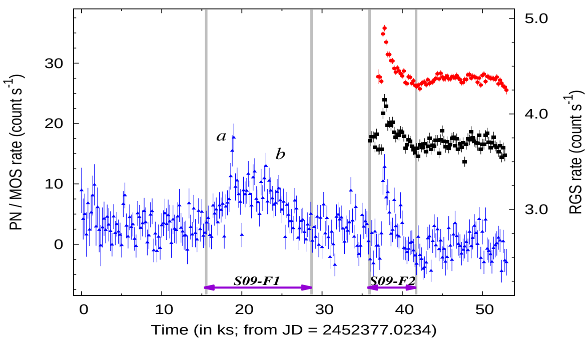

set-09

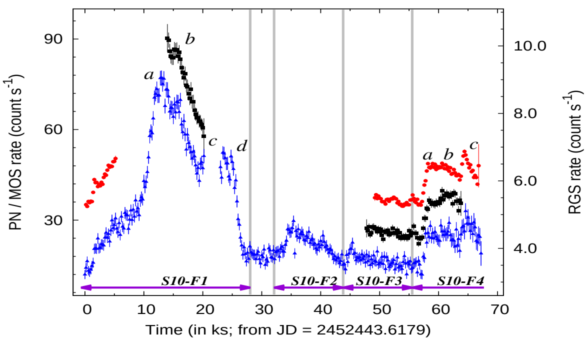

set-10

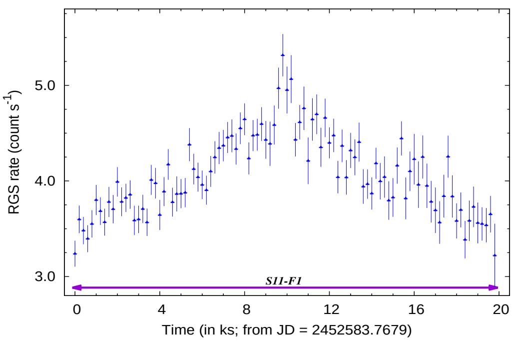

set-11

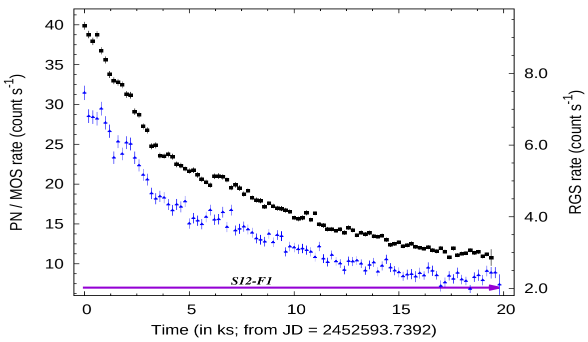

set-12

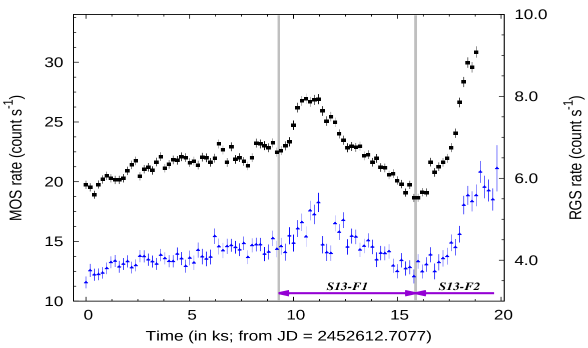

set-13

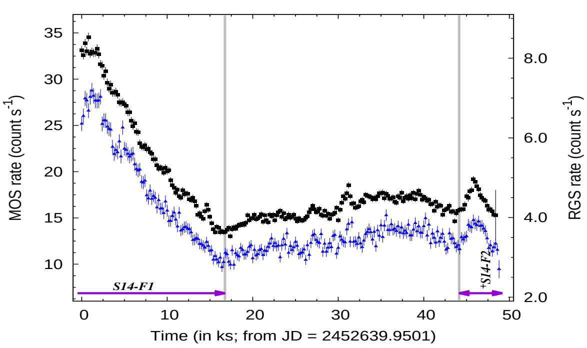

set-14

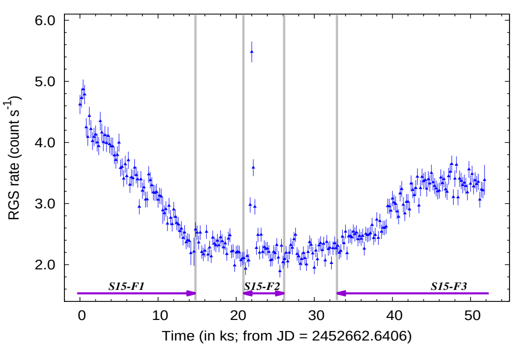

set-15

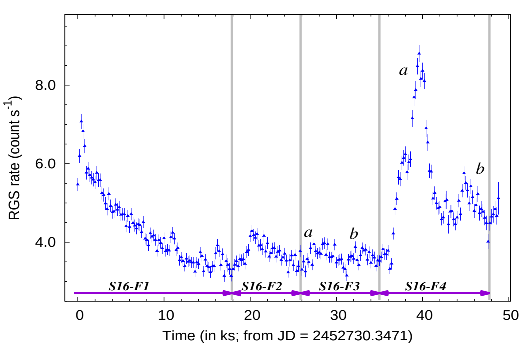

set-16

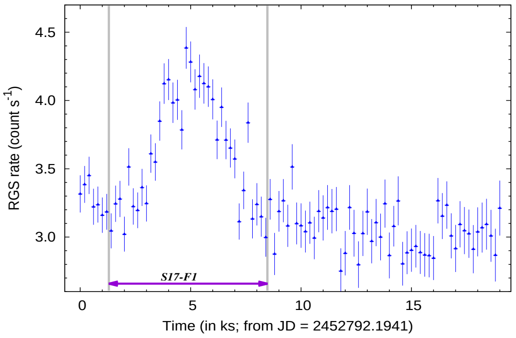

set-17

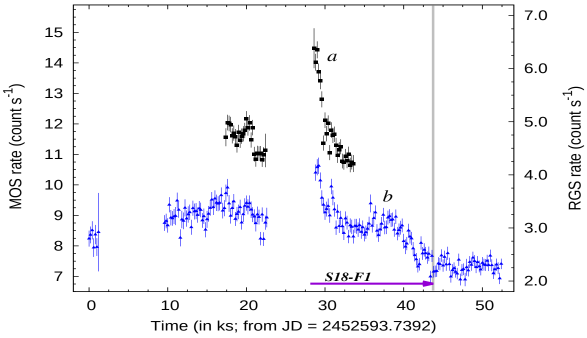

set-18

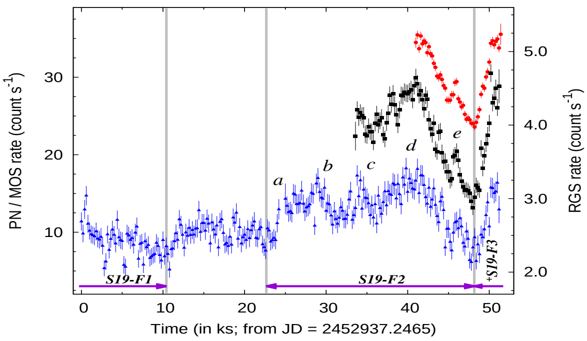

set-19

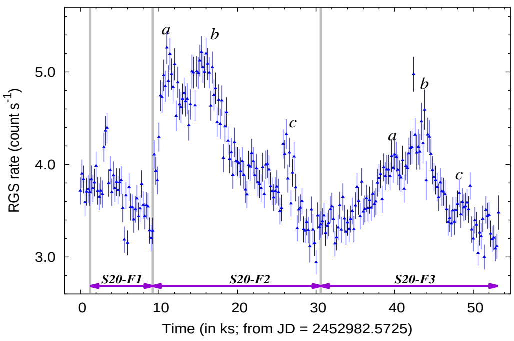

set-20

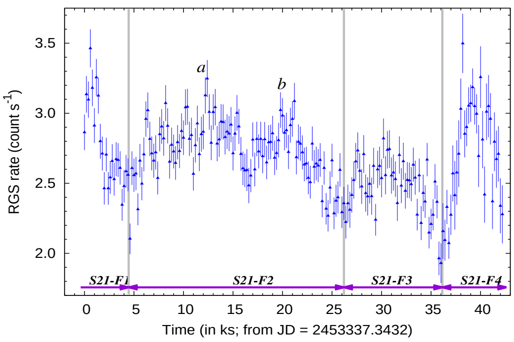

set-21

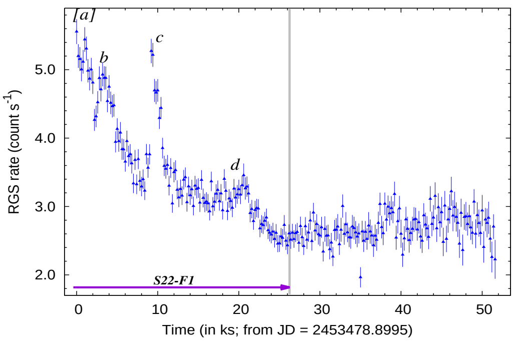

set-22

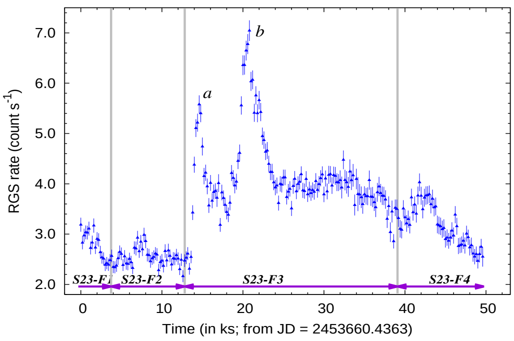

set-23

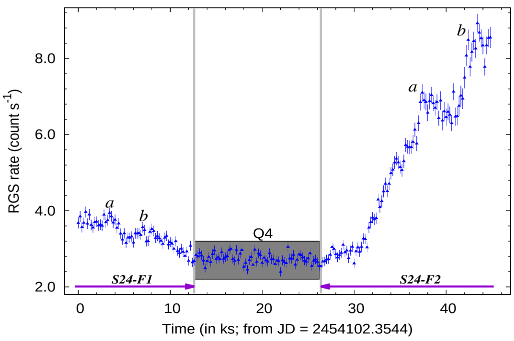

set-24

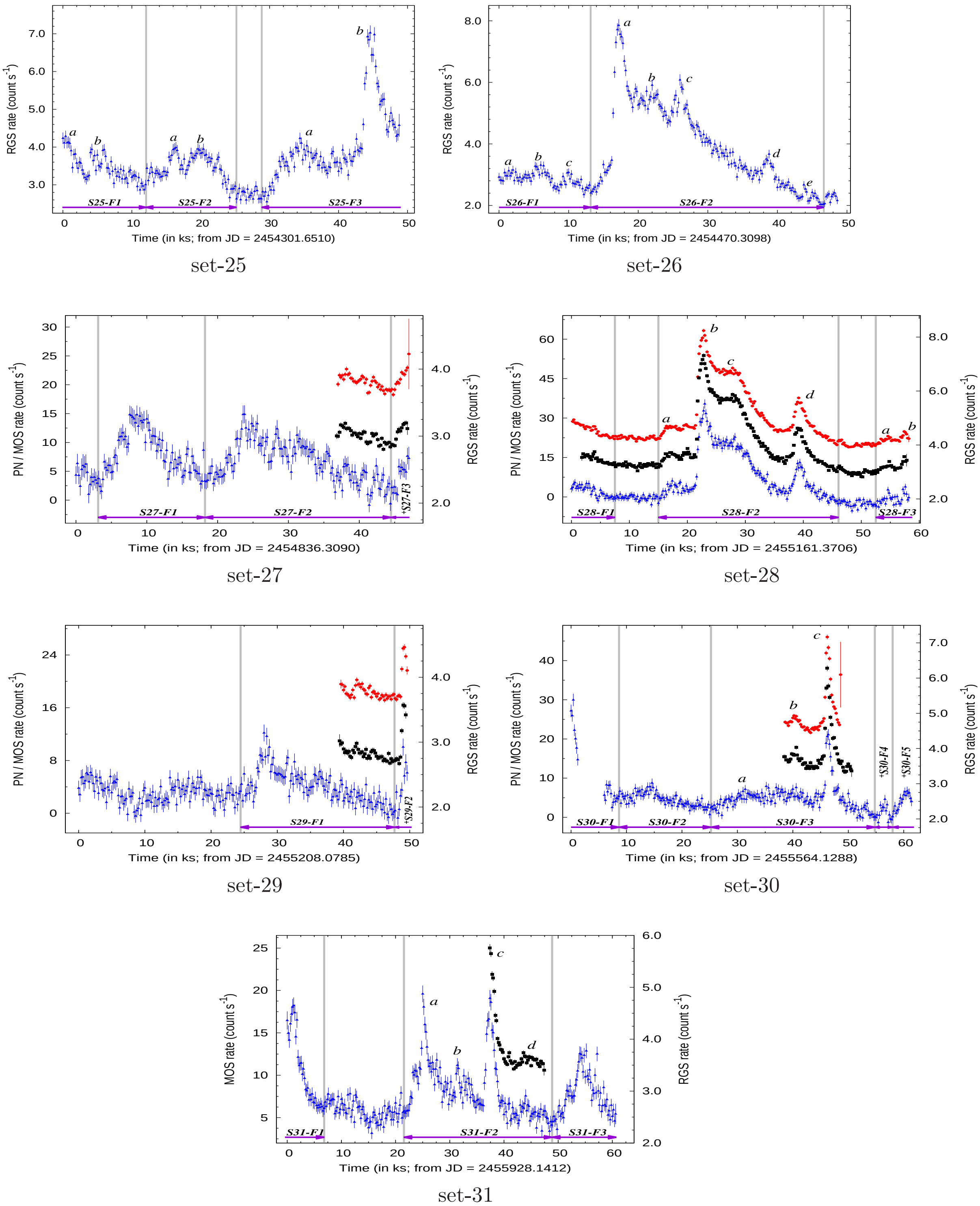

Figure 4.7: X-ray light curves of the AB Dor during different epoch of observations. PN, MOS and RGS are shown with red solid circle, black solid box and blue solid triangle respectively. The MOS count rates were scaled as $3.84 \times MOS - 21.7$ for sets S03, S04, S05, S06, S09, S10 and S19, and 1.89 x MOS - 8.7 for sets S27, S28, S29 and S30 in order to plot the light curves from all threeinstruments in the same panel.

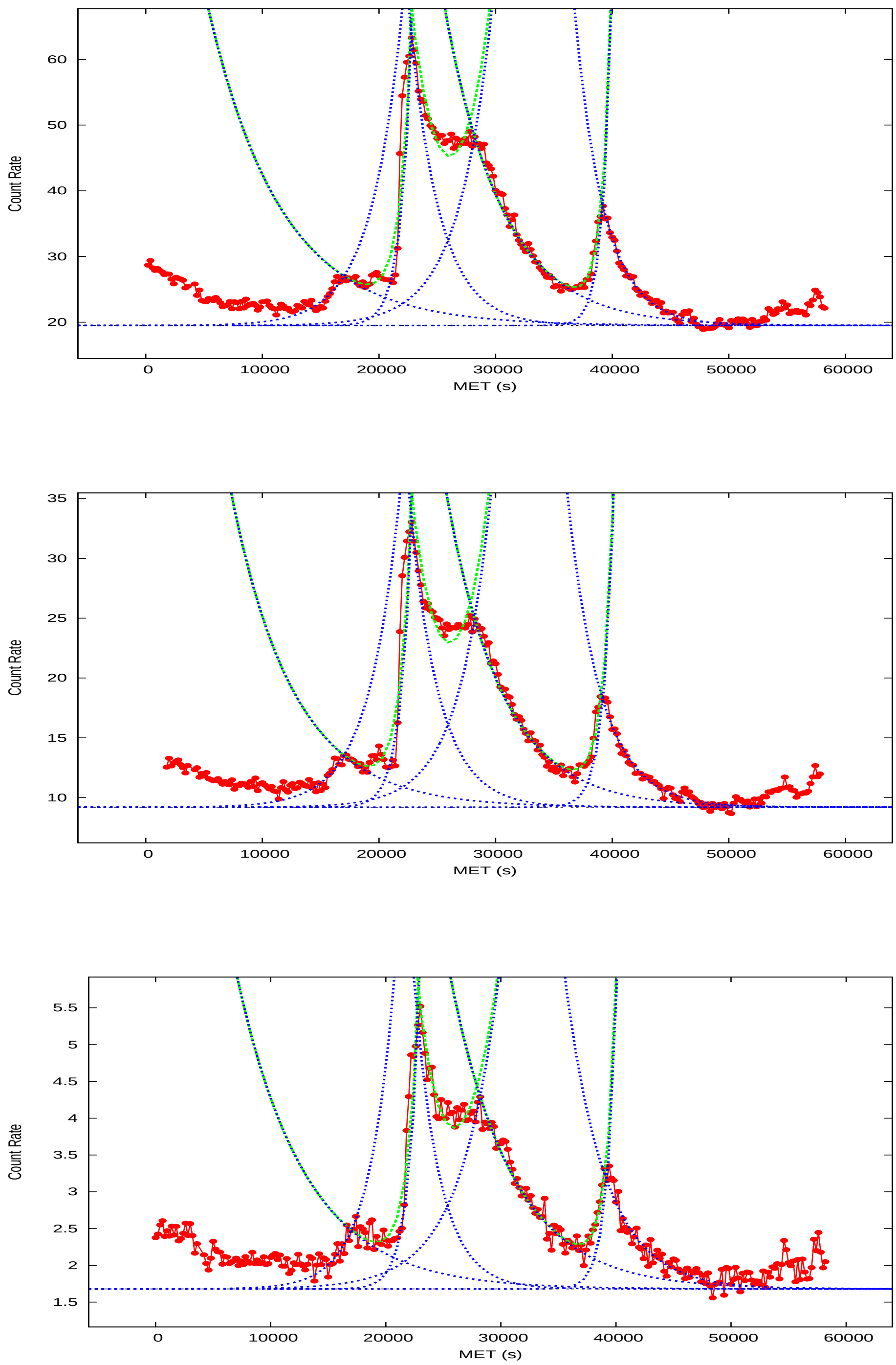

(a) S28-F2

Figure 4.8: An examples of the best-fit of a multiple peak flare S28-F2. All the peaks were fitted simultaneously with exponential rise ane exponential decay. From top to bottom, the fitted PN, MOS, and RGS light curve is shown.

whereas, the “predominant flare" of cpx flare is marked with lower-case alphabets surrounded by square brackets (e.g. [a], see S05-F1, S22-F1 etc.).

The *typ* flares (e.g. S01-F1, S01-F3, S02-F2, S03-F2) are the most populous class of the flares from AB Dor with 31 in numbers. The values of τ_d and τ_r were found to be in the range of 0.11 - 6.53 ks and 0.21 - 7.28 ks, respectively. Fifteen flares (e.g. S03-F1, S06-F1, S07-F3) are classified as *dbl* flare with the values of τ_d and τ_r in the range of 0.11 - 30.14 ks and 0.21 - 27 ks, respectively. A total 13 flares fall into the category of *mpl* flare (e.g. S01-F4, S04-F2, S10-F1). Only three flares are *cpx* flare. Apart from this flares in our study 19 flares are incomplete (inc) flares which we could not classify according to the above classification scheme.

Consider all flaring events as a individual flares, we detect 140 flares during the $\sim$ 11 years of XMM-Newton observations, with a derived flare frequency to be $\sim$ 4 flares per rotation. Whereas, considering all flaring events corresponds to dbl, mpl, cpx or srf flares to be single event, we detect only 81 flares with a derived flare frequency to be 2.25 flares per rotation.

4.2.3 Flare parameters

The duration (Dn) of the flare is defined as the difference between the start time (the point in time when the count rate begins to increase from the quiescent level) and the end time (when the flare counts returns to the quiescent level). The start and end times for each flare were obtained during the manual inspection. Flare durations are found within a range of 43 minutes (2.55 ks; smallest flare S19-F3) to 14.6 hrs (52.4 ks; longest duration flare S05-F1) with a median value of 4.6 hrs (16.5 ks). Flare duration of all the flares are given in 2nd column of Table 4.3.

In the case of *typ* flares, the e-folding rise time (τ_r) has been derived from the least-squares fit of the exponential functions (see equation 4.1), whereas for ‘dbl’ and ‘mpl’ flares τ_r and τ_d were derived the double or multiple exponential function of the following form

$$c(t) = \sum_{i=1}^{N}(A_{pk})_i.exp\left(\pm\frac{t-(t_{pk})_i}{\tau_r,\tau_d}\right)+q \tag{4.6}$$

where N is the number of peaks in a flaring event. To analyse ‘cpx’ flares, we first exclude the smaller superimposed flares from the light curve and fit the equation 4.1 to derive the values of τ_r and τ_d of the ‘predominant’ flare. In order to derive the values of τ_r and τ_d of smaller superimposed flares, firstly we detrended the predominant flare by fitting equation 4.1, then fitted the equation 4.6 in the residual. Although the procedure of analyzing the 'srf' flares were similar to that of 'mpl' flares, due to slow rise and top flat nature, we got large τ_r values compare to any other types of flares. Fig. 4.9 shows the best exponential(s) from equations 4.1 and 4.6 for all type of flares described above in section 4.2.2. The best fit values of τ_r and τ_d for all flares derived for PN, MOS and RGS instruments are given in column 4–9 of Table 4.3, whereas the flare-types were marked in the last column.

Fig. 4.9(a) shows the distribution of the Dn, τ_r and τ_d. The distribution of τ_r and τ_d are shown for different detectors. The median value of flare duration was found to be 2.28 hr.

Flares F04-F2, S10-F1, S19-F2 and S26-F2 were found to be long lasting ($>$ 7 h) flares. Infact, the flare F04-F2 is longest flare observed with total duration of $\sim$ 12.1 h. The shortest duration flare observed completly was S20-F1 with flare duration of 1.1 h. The values of τ_d and τ_r were found to be in the range of 0.11 - 30.14 ks and 0.21 - 27 ks, respectively. Most of the time τ_d was found to be more than τ_r. Fig. 4.9(a) shows the distribution of rise and decay times of the flares observed from AB Dor using PN, MOS and RGS detectors. The median values of τ_r and τ_d derived for PN, MOS and RGS detectors are given in Table 4.4.

4.2.4 τ_d vs τ_r

Based on a standard reconnection model, τ_r is equal to the interval of magnetic reconnection. Petschek (1964) showed that the reconnection timescale is proportional to the Alfven time ($\tau_A = l/v_A$), where v_A is the Alfven velocity. Hence τ_r is given as

$$\tau_r = \frac{\tau_A}{M_A} \propto \frac{l}{B} \frac{M_A}{n_c^{1/2}} \tag{4.7}$$

where reconnection rate, M_A, is in the range of 0.001 - 0.1 (Isobe et al., 2002; Petschek, 1964), n_c is a pre-flare density, l is semi-loop length. Assuming the decay phase of the flare is dominated by radiative cooling and magnetic pressure is comparable to the plasma pressure at the flare peak, the τ_d is given as

Table 4.4: Median values of τ_r and τ_d of the flares observed from AB Dor.

Detector	τ_r (ks)	τ_d (ks)
PN	2.027 ± 0.493	4.518 ± 0.799
MOS	2.432 ± 0.557	5.247 ± 0.797
RGS	2.183 ± 0.211	4.254 ± 0.322

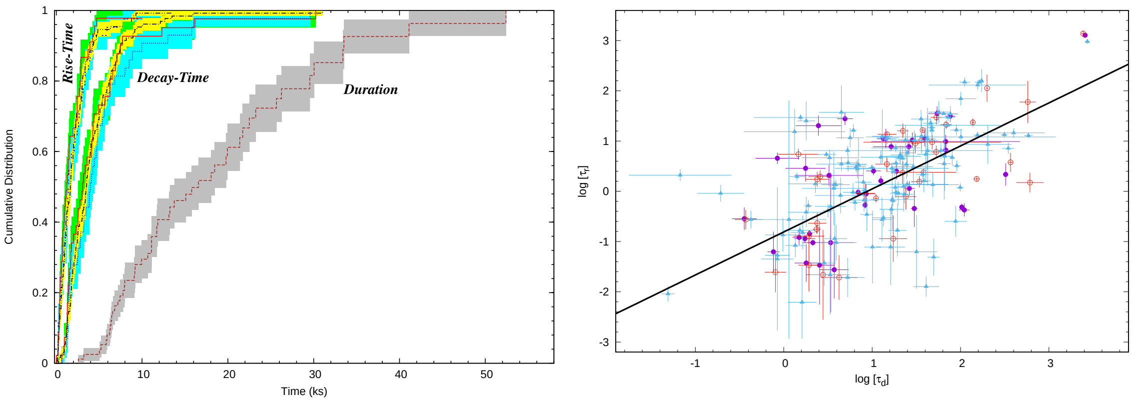

(a) (b)

Figure 4.9: (a) Cumulative distribution function for rise-time, decay-time and flare durations of all the flaring events observed with EPIC PN (red), MOS (black), and RGS (blue). (b). The rise-time vs. decay-time is plotted in logerithmic scale. The black straight line represents the best-fit.

$$\tau_d \propto \sqrt{\frac{l}{B}\frac{1}{n_c^{1/4}}} \tag{4.8}$$

Using equations 4.7 and 4.8 one can obtained the following relation

$$\tau_d \propto \sqrt{\tau_r} \tag{4.9}$$

Fig. 4.9(b) shows the plot between rise and decay times of the flares observed in AB Dor. A clear correlation was observed between τ_d and $\tau_r$with Pearson correlation coefficient of 0.76. The straight line is linear regression fit in the form of $\tau_d \propto \tau_r^{0.78\pm0.05}$. The observed relation between $\tau_r$and $\tau_d$is slightly differ from the theoretically predicted relation as described in equation 4.9.

4.2.5 Conclusions

We detected a total 140 flares from AB Dor using *XMM-Newton* data with flare frequency of 2 flares per rotation period of AB Dor. These flares show variety of light curve shapes and flare amplitudes. Based on the light-curve, we classified them into five category namely typical, double, multiple, complex and slow rise top flat flares. The rise and decay times of the flares are correlated with each other in the form of $\tau_d \propto \tau_r^{0.78\pm0.05}$, which is slight different from the theoretically obtained relation of $\tau_d \propto \tau_r^{0.5}$ with the assumption that the decay time equals to radiative cooling time.

Chapter 5

Superflares from late-type main sequence star CC Eri

CC Eri is a SB2 binary system, which consists of a K7.5Ve primary and M3.5Ve secondary (Amado et al., 2000), and is located at a distance of $\sim$ 11.5 pc. With a mass ratio ≈ 2 (Evans, 1959), the system is tidally locked and the primary component is one of the fastest rotating K dwarfs in the solar vicinity with a rotation period of 1.56 day. Gáspár et al. (2013) estimated the age of the CC Eri system to be 10 Myr. The chromospheric emission was found to vary in anti-phase with its optical continuum, suggesting the association of active emission regions with starspots (Amado et al., 2000; Busko et al., 1977). The polarization of the quiescent radio emission was found to be 10%-20% (Osten et al., 2002; Slee et al., 2004), which implies the presence of a large-scale magnetic field. The first X-ray detection was done with HEAO1 showing X-ray luminosity of $10^{29.6}$ erg s^{-1} in the 2-20 keV energy band (Tsikoudi, 1982). Later several X-ray observations were made with other satellites such as Einstein IPC (Caillault et al., 1988) and EXOSAT (Pallavicini et al., 1988). Using XMM-Newton observations, the quiescent state coronae of CC Eri were well described by two-temperature plasma models (3 and 10 MK) with a luminosity of 10^{29} erg s^{-1} in 0.3–10 keV energy band (Pandey & Singh, 2008). CC Eri has a record of frequent flaring activity observed across a wide range of the electromagnetic spectrum. The first ever X-ray flare on CC Eri was detected with the ROSAT satellite (Pan & Jordan, 1995). Later several X-ray flares were detected with *XMM-Newton* (Crespo-Chacón et al., 2007; Pandey & Singh, 2008), *Chandra* (Nordon & Behar, 2008), *Swift* (Barthelmy et al., 2012; Evans et al., 2008), and MAXI GCS (Suwa

[1]**The results presented in this chapter have been published in Karmakar et al. (2017).**

et al., 2011). Among the previously observed flares, the largest one was observed with Chandra, having a peak X-ray flux that is $\sim$ 11 times more than that of the quiescent value. Superflares from CC Eri are expected to be driven by strong surface magnetic fields as estimated by Bopp & Evans (1973). This background motivated us to study the flares from CC Eri.

5.1 X-ray light curves of flaring events

X-ray light curves of CC Eri obtained in 0.3–10 keV and 14–150 keV energy bands are shown in Fig. 5.1. The BAT observation in 2008, which began at $T0_1$–243 s, shows a rise in intensity up to $T0_1$+100 s, where it reached a peak intensity with a count rate of 0.024±0.005 counts s^{-1}, which is $\sim$24 times higher than the minimum observed count rate. A sharp decrease in intensity up to nearly $T0_1$+450 s was observed followed by a shallower decay until the end of the BAT observations at $\sim T0_1$+950 s. The XRT count rate of flare FCC1 was already declining as it entered the XRT field of view at $T0_1$+142 s. The peak XRT count rate for the pile-up corrected data was found to be 437±7 counts s^{-1}, which was $\sim$100 counts s^{-1} lower than the previously reported count rate (Evans et al., 2008). Flare FCC1 survived for the entire WT mode of observation of 1.8 ks, after that the observation was switched over in PC mode where count rates were found to be constant and marked as 'PF' in Fig. 5.1(a). The BAT observation of flare FCC2, which began at $T0_2$–240 s, shows a rise in intensity and peaked around $T0_2$, followed by a decline in intensity until the end of the BAT observation. The peak BAT count rate for flare FCC2 was found to be $\sim$0.004 counts s^{-1}, which was $\sim$4 times more than the minimum count rate observed. The flare 'FCC2' was also already declining when it entered in the XRT field of view with a pile-up corrected peak count rate of 99±2 counts s^{-1}. The XRT count rates at the peak of the flares FCC1 and FCC2 were found to be 474 and 108 times more than the minimum observed count rates, respectively. The durations of the flares were more than 2.2 for FCC1 and 1.8 ks for FCC2. The e-folding rise times (τ_r) of the flares FCC1 and FCC2 derived from BAT data were found to be 150±12 and 146±34 s, respectively; whereas e-folding decay times (τ_d) with BAT and XRT data were found to be 283±13 and 539±4 s for flare FCC1 and 592±114 and 1014±17 s for flare FCC2, respectively. This indicates a faster decay in the hard X-ray band than in the soft X-ray. Both flaring events were clearly identified in the energy band of 14–50 keV, but they were barely detectable above 50 keV.

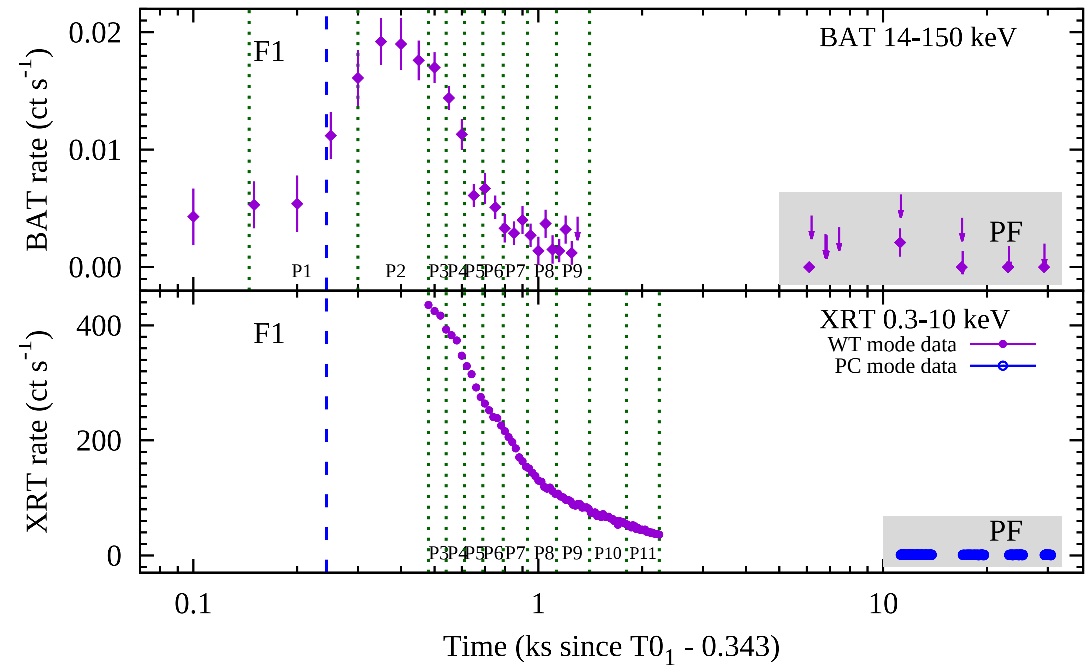

(a) Observations in 2008 shows flare FCC1 with a post-flare (PF) region

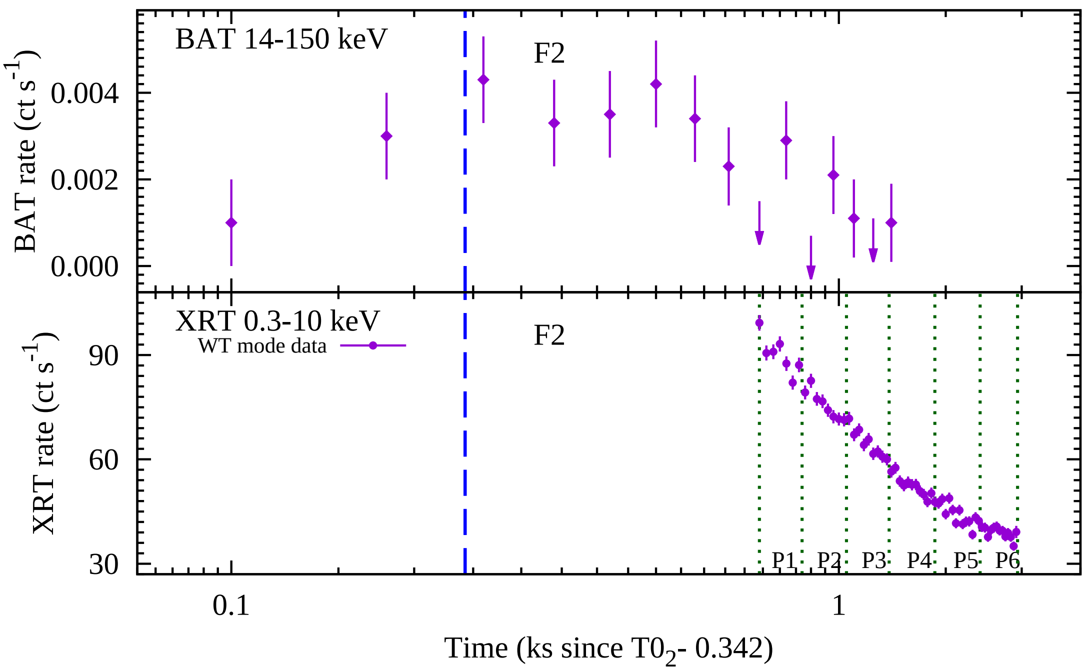

(b) Observations in 2012 shows flare FCC2

Figure 5.1: X-ray light curves of the flares (a) FCC1 and (b) FCC2 of CC Eri. Temporal binning for BAT light curves is 50 and 80 s for flares FCC1 and FCC2, respectively, whereas the binning for XRT light curves is 10 s for both flares. Dashed vertical lines indicate the trigger time, whereas dotted vertical lines show the time intervals for which time-resolved spectroscopy was performed. The time intervals are represented by P_i, where $i = 1 - 11$ for FCC1 and 1– 6 for FCC2.

Table 5.1: Spectral parameters derived for the post-flare emission of CC Eri from *Swift* XRT PC mode spectra during the time interval "PF" as shown in Fig. 5.1 using APEC 2-T and APEC 3-T models.

Parameters	2T	3T
N_H (10^{20} atoms cm^{-2})	$0.9^{+0.8}_{-0.8}$	$2.8^{+1.1}_{-1.1}$
kT_1 (keV)	$0.83^{+0.02}_{-0.02}$	$0.25^{+0.02}_{-0.02}$
EM_1 (10^{52} cm^{-3})	$3.4^{+0.6}_{-0.6}$	$1.4^{+0.4}_{-0.4}$
kT_2 (keV)	$3.9^{+2.4}_{-0.9}$	$0.94^{+0.03}_{-0.03}$
EM_2 (10^{52} cm^{-3})	$0.8^{+0.2}_{-0.2}$	$1.7^{+0.4}_{-0.4}$
kT_3 (keV)	–	$3.4^{+0.7}_{-0.6}$
EM_3 (10^{52} cm^{-3})	–	$0.9^{+0.2}_{-0.1}$
Z ($Z_\odot$)	$0.13^{+0.03}_{-0.02}$	$0.29^{+0.09}_{-0.05}$
$L_{X,[0.3-10]}$ (10^{29} erg s^{-1})	$3.88^{+0.06}_{-0.06}$	$4.33^{+0.07}_{-0.07}$
χ^2(DOF)	1.56 (120)	1.08 (118)

Notes.N_H, kT, and EM are the galactic HI column density, plasma temperature, and emission measures, respectively. Z is global metallic abundances and $L_{X,[0.3-10]}$ is the derived luminosity in the XRT band.

5.2 Hard X-ray spectra from BAT

Spectral parameters during the flares evolve with time as flare emission rises, reaches its peak, and later decays similarly to the X-ray light curve. Therefore, in order to trace the spectral change, we have divided the BAT light curve of the flare FCC1 into nine time segments and extracted the spectra of each segment, whereas we could not divide the flare FCC2 into any further segments due to poor statistics. The combined BAT and XRT spectra near the peak phase of the flare FCC1 (i.e. part P3) of CC Eri are shown in Fig. 5.2. The dotted vertical lines in the top panel of Fig. 5.1(a) indicate the time intervals during which BAT spectra were accumulated. In this section, we analyze those time segments where only the BAT observations were available, i.e. the first two time segments for flare FCC1 (P1 and P2), and only one for flare FCC2. The hard X-ray spectra were best-fitted using single temperature Astrophysical Plasma Emission Code (APEC; see Smith et al., 2001) as implemented for collisionally ionized plasma. The addition of another thermal or non-thermal component does not improve the fit-statistics. Since the standard APEC model included in the XSPEC distribution only considers emission up to photon energies of 50 keV; therefore, we restricted our analysis in 14–50 keV energy band. The abundances in this analysis were fixed to the mean abundances derived from XRT spectral fitting (see § 5.3) given in a multiple of the solar values of

Anders & Grevesse (1989). The galactic $^{h}1$ column density (N_H) in the direction of CC Eri is calculated according to the survey of Dickey & Lockman (1990) and kept fixed at the value of 2.5×10^{20} cm^{-2}. The unabsorbed X-ray fluxes were calculated using the CFLUX model. The variation in hard X-ray luminosity ($L_{X,[14-50]}$), plasma temperature (kT), emission measure (EM), and abundances (Z) derived from the BAT spectra are illustrated in Fig. 5.3 and given in Table 5.4. The peak plasma temperatures were derived to be >14.4 keV and ∼11 keV for flares FCC1 and FCC2, whereas peak $L_{x,[14-50]}$ were derived to be $1.2\pm0.1\times10^{32}$ and $1.1\pm0.1\times10^{31}$ erg s^{-1}.

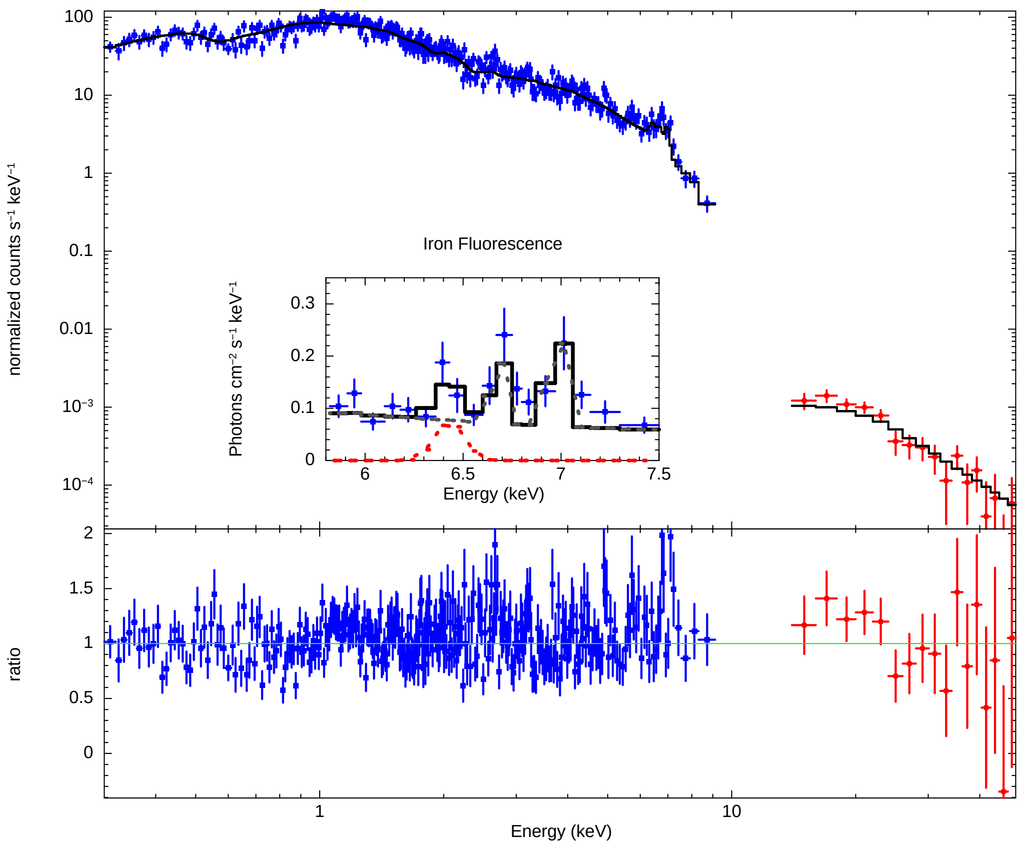

Figure 5.2: Combined XRT and BAT spectra near the peak phase of flare FCC1 (i.e. part P3) are shown as representative spectra. In the top panel, the XRT and BAT spectra are shown with solid squares and solid circles, respectively, whereas the best-fit APEC 3-T model is over-plotted with a continuous line. The bottom panel plots the ratio between data and model. The inset of the top panel shows a close-up view of the Fe Kα complex, where the 6.4 keV emission line is fitted with a Gaussian. The contribution of APEC component and the Gaussian component is shown by dashed lines.

5.3 Soft X-ray spectra from XRT: Time resolved spectroscopy

Time-resolved spectral analysis was also performed for the XRT data of both flares. The WT mode data for flares FCC1 and FCC2 were divided into nine and six time bins, respectively, so that each time bin contains sufficient and a similar number of counts. The length of time bins is variable, ranging from 60–440 s for the flare FCC1 and 130–261 s for the flare FCC2. The dotted vertical lines in the bottom panel of Fig. 5.1(a and b) show the time intervals for which the XRT spectra were accumulated. The first seven time segments of XRT data were common with BAT data for the flare FCC1.

5.3.1 Post-flare phase of the flaring event FCC1

The coronal parameters of the PF phase were derived by the fitting single (1-T), two (2-T), and three (3-T) temperatures APEC model. The global abundances (Z) and interstellar ^{h}1 column density (N_H) were left as free parameters. None of the plasma models (1-T, 2-T, or 3-T) with solar abundances ($Z_\odot$) were formally acceptable because large values of χ^2 were obtained. The 2-T plasma model with sub-solar abundances was found to have a significantly better fit than the 1-T model with reduced χ^2 (χ^2) of 1.56 for 120 degrees of freedom (dof). Adding one more plasma component improves the fit significantly with χ^2 = 1.08 for 118 dof. The F-test applied to the χ^2 resulting from the fits with APEC 2-T and 3-T models showed that the 3-T model was more significant with an F-statistics of 27.7 with a null hypothesis probability of 1.4×10^{-10}. The addition of one more thermal component did not show any further improvement in the χ^2; therefore, we assume that the post-flare coronae of CC Eri were well represented by three temperature plasma. Table 5.1 summarizes the best-fit values of the 2-T and 3-T plasma models of various parameters along with their χ^2 value. The first two temperatures in the 3-T model were derived as 0.25±0.02 and 0.94±0.03 keV. These two temperatures are consistent to that derived by Crespo-Chacón et al. (2007) and Pandey & Singh (2008) for quiescent coronae of CC Eri using *XMM-Newton* data. This indicates that the post-flaring region has not yet returned to the quiescent level and has a third thermal component of $3.4^{+0.7}_{-0.6}$ keV. With the preliminary analysis of the same data, Evans et al. (2008) also suspected that the post-flare region was not a quiescent state. The X-ray luminosity in the 0.3–10.0 keV band during the post-flare

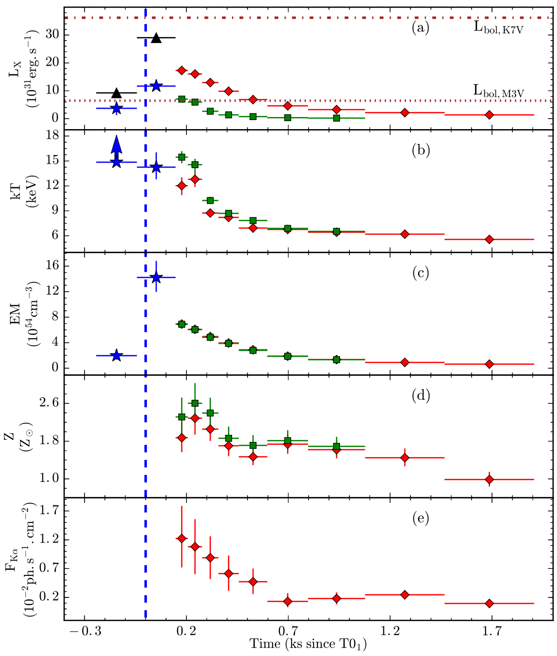

((i)) Flare FCC1

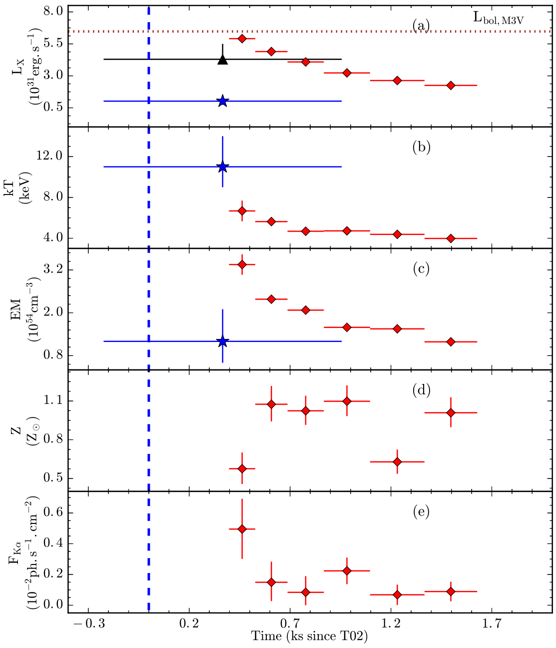

((ii)) Flare FCC2

Figure 5.3: Evolution of spectral parameters of CC Eri during the flares FCC1 (i) and FCC2 (ii).Parameters derived with the XRT, BAT, and XRT+BAT spectral fitting in all the panels are represented by the solid diamonds, solid stars, and solid squares, respectively.In the top panel (a), the X-ray luminosities are derived in 0.3–10 keV (solid diamond) and 14–50 keV (solid star and solid squares) energy bands. For the first two segments, BAT luminosity derived in the 14–50 keV energy band is extrapolated to the 0.3–10 keV energy band (solid triangles). The dashed–dotted and dotted horizontal lines correspond to bolometric luminosity of the primary and secondary components of CC Eri, respectively.Panels (b)–(e) display the variations of plasma temperature, EM, abundance, and Fe Kα line flux, respectively.The dashed vertical line indicates the trigger time of the flares FCC1 and FCC2.Horizontal bars give the time range over which spectra were extracted;vertical bars show a 68% confidence interval of the parameters.

region was derived to be $4.33 \pm 0.07 \times 10^{29}$ erg s^{-1}, which was $\sim$5 times higher than the previously determined quiescent state luminosity in the same energy band by Pandey & Singh (2008) using *XMM-Newton*.

5.3.2 The flaring event FCC1

A 3-T plasma model was found to be acceptable in each segment of flaring event FCC1. The first two temperatures, corresponding EMs, and N_H were found to be constant within a 1σ level. The average values of all the segments of the first two temperatures were 0.3 ± 0.1 and 1.1 ± 0.2 keV, respectively. These two temperatures were very similar to that of the first two temperatures of the PF phase. Therefore, for the further spectral fitting of flare-segments of the flare FCC1, we fixed the first two temperatures to the average values. The free parameters were temperature and corresponding normalization of the third component along with the abundances. The time evolution of derived spectral parameters of flare FCC1 is shown in Fig. 5.3(a) and are given in Table 5.2. The abundance, temperature, and corresponding EM were found to vary during the flare. The peak values of abundances were derived to be 2.3±0.4 $Z_\odot$, which was ∼8 times more than the post-flaring region and ∼13 times more than that of the quiescent value of CC Eri (Pandey & Singh, 2008). The derived peak flare temperature of 12.3 ± 0.9 keV was ∼3.6 times more than the third thermal component observed in the PF phase. The EM followed the flare light curve and peaked at a value of $6.9{\pm}0.3{\times}10^{54}$ cm^{-3}, which was ∼766 times more than the minimum value observed at the post-flare region. The peak X-ray luminosity in 0.3–10 keV energy band during flare FCC1 was derived to be $10^{32.2}$ erg s^{-1}, which was ∼400 times more luminous than that of the post-flare regions, whereas ∼1922 times more luminous than that of the quiescent state of CC Eri derived by Pandey & Singh (2008). The amount of soft X-ray luminosity during the time segments when only BAT data were collected were estimated by extrapolating the 14–50 keV luminosity derived from the best-fit APEC model of the BAT data using WEBPIMMS[1] and is shown by solid triangles in the top panels of Fig. 5.3(i).

5.3.3 The flaring event FCC2

For the flaring event FCC2, no pre-/post-flare or quiescent states were observed; therefore, a time-resolved spectroscopy was done by fitting 1-T, 2-T, and 3-T plasma models. A 2-T plasma model was found suitable for each flare segment as the minimum value of χ^2 was obtained. Initially, in the spectral fitting N_H was a free parameter and was constant within a 1σ level; therefore, in the next stage of spectral fitting, we fixed N_H to its average value. The derived spectral parameters are given in Table 5.3. Both the temperatures and the corresponding EM along with the global abundances were found to be variable during the flare. In order to compare

[1] https://heasarc.gsfc.nasa.gov/cgi-bin/Tools/w3pimms/w3pimms.pl

Table 5.2: X-ray spectral parameters of CC Eri during the flare FCC1 derived from the XRT time-resolved spectra.

Parts	**Time Interval**	$\mathbf{kT_3}$	$\mathbf{EM_3}$	**Z**	Fe Kα			$\mathbf{L_{x,[0.3-10]}}$	χ^2_ν **(DOF)**	**P**
					E	**EW**	$\mathbf{F_{K\alpha}}$ $\mathbf{(10^{-2}}$			
	(s)	**(keV)**	$\mathbf{(10^{54}\ cm^{-3})}$	($Z_\odot$)	**(keV)**	**(keV)**	**ph** $\mathbf{cm^{-2}\ s^{-1})}$	$\mathbf{(10^{31}\ erg\ s^{-1})}$		(%)
P3	$T0_1$+137:$T0_1$+197	$11.6^{+1.0}_{-1.1}$	$6.9^{+0.3}_{-0.3}$	$1.9^{+0.3}_{-0.3}$	$6.37^{+0.06}_{-0.08}$	132^{+64}_{-67}	$1.2^{+0.6}_{-0.5}$	$17.3^{+0.2}_{-0.2}$	1.179 (303)	89.3
P4	$T0_1$+197:$T0_1$+267	$12.3^{+0.9}_{-0.9}$	$6.1^{+0.3}_{-0.3}$	$2.3^{+0.4}_{-0.4}$	$6.38^{+0.07}_{-0.07}$	124^{+46}_{-66}	$1.1^{+0.5}_{-0.5}$	$16.0^{+0.2}_{-0.2}$	1.119 (312)	88.5
P5	$T0_1$+267:$T0_1$+347	$8.3^{+0.5}_{-0.3}$	$5.0^{+0.2}_{-0.2}$	$2.1^{+0.3}_{-0.3}$	$6.21^{+0.05}_{-0.05}$	173^{+90}_{-73}	$0.9^{+0.4}_{-0.4}$	$13.0^{+0.1}_{-0.1}$	0.951 (303)	93.9
P6	$T0_1$+347:$T0_1$+447	$7.7^{+0.4}_{-0.4}$	$3.9^{+0.2}_{-0.2}$	$1.7^{+0.2}_{-0.2}$	$6.34^{+0.06}_{-0.05}$	132^{+80}_{-77}	$0.6^{+0.3}_{-0.3}$	$9.9^{+0.1}_{-0.1}$	1.149 (292)	78.9
P7	$T0_1$+447:$T0_1$+587	$6.5^{+0.2}_{-0.2}$	$2.9^{+0.1}_{-0.1}$	$1.5^{+0.2}_{-0.2}$	$6.41^{+0.06}_{-0.07}$	77^{+92}_{-37}	$0.4^{+0.2}_{-0.2}$	$6.85^{+0.07}_{-0.07}$	1.238 (288)	80.3
P8	$T0_1$+587:$T0_1$+787	$6.3^{+0.2}_{-0.2}$	$1.88^{+0.08}_{-0.08}$	$1.7^{+0.2}_{-0.2}$	6.39	23^{+25}_{-23}	<0.24	$4.62^{+0.05}_{-0.05}$	1.134 (282)	48.6
P9	$T0_1$+787:$T0_1$+1067	$6.0^{+0.2}_{-0.2}$	$1.34^{+0.05}_{-0.05}$	$1.6^{+0.2}_{-0.2}$	$6.38^{+0.08}_{-0.10}$	77^{+68}_{-48}	$0.2^{+0.1}_{-0.1}$	$3.26^{+0.03}_{-0.03}$	1.273 (276)	55.1
P10	$T0_1$+1067:$T0_1$+1457	$5.8^{+0.3}_{-0.3}$	$0.90^{+0.04}_{-0.04}$	$1.5^{+0.2}_{-0.2}$	$6.40^{+0.05}_{-0.05}$	118^{+131}_{-24}	$0.22^{+0.08}_{-0.08}$	$2.18^{+0.02}_{-0.02}$	1.179 (266)	96.4
P11	$T0_1$+1457:$T0_1$+1897	$5.1^{+0.2}_{-0.3}$	$0.63^{+0.03}_{-0.03}$	$1.0^{+0.2}_{-0.2}$	6.41	68^{+55}_{-52}	$0.06^{+0.05}_{-0.05}$	$1.37^{+0.02}_{-0.02}$	1.043 (220)	77.4

Notes.kT_3, EM_3, and Z are the "effective" plasma temperature, emission measures, and abundances during different time intervals of flare decay, respectively. E is the Gaussian peak around 6.4 keV, EW is the equivalent width, $F_{K\alpha}$ is the Kα line flux, $L_{X,[0.3-10]}$ is the derived luminosity in XRT band, and P is the F-test probability, which indicates how much of an addition of the Gaussian line at 6.4 keV is significant, i.e. the emission line is not a result of random fluctuation of the data points. All the errors shown in this table are in the 68% confidence interval.

Table 5.3: Time-resolved spectral parameters of CC Eri during the flare FCC2 derived from the XRT spectra.

Parts	**Time Interval** (s)	**kT_1** (keV)	**kT_2** (keV)	**EM_1** (10^{54} cm^{-3})	**EM_2** (10^{54} cm^{-3})	**Z** ($Z_\odot$)	Fe Kα **E** (keV)	Fe Kα **EW** (keV)	Fe Kα **$F_{K\alpha}$** (10^{-2} ph cm^{-2} s^{-1})	**$L_{x,[0.3-10]}$** (10^{31} erg s^{-1})	χ^2_ν **(DOF)**	**P** (%)
P1	$T0_2$+397:$T0_2$+527	$1.63^{+0.05}_{-0.07}$	$8.7^{+1.8}_{-1.0}$	$1.0^{+0.3}_{-0.2}$	$2.4^{+0.1}_{-0.1}$	$0.54^{+0.13}_{-0.12}$	$6.46^{+0.05}_{-0.05}$	181^{+108}_{-75}	$0.50^{+0.20}_{-0.19}$	$5.91^{+0.06}_{-0.06}$	1.298 (288)	92.2
P2	$T0_2$+527:$T0_2$+687	$1.25^{+0.04}_{-0.06}$	$6.0^{+0.4}_{-0.4}$	$0.20^{+0.05}_{-0.04}$	$2.18^{+0.07}_{-0.07}$	$1.03^{+0.14}_{-0.13}$	$6.28^{+0.13}_{-0.11}$	101^{+42}_{-83}	$0.15^{+0.13}_{-0.12}$	$4.90^{+0.05}_{-0.05}$	1.205 (289)	46.2
P3	$T0_2$+687:$T0_2$+867	$1.05^{+0.02}_{-0.03}$	$4.9^{+0.2}_{-0.2}$	$0.13^{+0.02}_{-0.02}$	$1.94^{+0.06}_{-0.06}$	$0.98^{+0.12}_{-0.11}$	6.35	47^{+56}_{-47}	$0.08^{+0.11}_{-0.08}$	$4.09^{+0.04}_{-0.04}$	1.164 (285)	91.6
P4	$T0_2$+867:$T0_2$+1096	$1.02^{+0.03}_{-0.03}$	$4.9^{+0.2}_{-0.2}$	$0.09^{+0.01}_{-0.01}$	$1.50^{+0.05}_{-0.05}$	$1.06^{+0.12}_{-0.11}$	$6.19^{+0.06}_{-0.06}$	244^{+76}_{-106}	$0.22^{+0.09}_{-0.09}$	$3.23^{+0.03}_{-0.03}$	0.968 (283)	96.7
P5	$T0_2$+1096:$T0_2$+1366	$1.25^{+0.05}_{-0.07}$	$4.9^{+0.4}_{-0.3}$	$0.21^{+0.07}_{-0.05}$	$1.34^{+0.05}_{-0.05}$	$0.59^{+0.09}_{-0.19}$	6.24	94^{+83}_{-80}	$0.07^{+0.07}_{-0.07}$	$2.63^{+0.02}_{-0.03}$	1.134 (277)	66.4
P6	$T0_2$+1366:$T0_2$+1627	$1.04^{+0.02}_{-0.03}$	$4.2^{+0.2}_{-0.2}$	$0.08^{+0.01}_{-0.01}$	$1.11^{+0.04}_{-0.04}$	$0.97^{+0.12}_{-0.11}$	$6.25^{+0.13}_{-0.13}$	162^{+112}_{-114}	$0.09^{+0.06}_{-0.06}$	$2.25^{+0.02}_{-0.02}$	0.925 (253)	65.2

Notes. Parameters have similar meanings as in Tables 5.1 and 5.2.

Table 5.4: Time-resolved spectral parameters of the BAT and XRT+BAT spectra of the flares FCC1 and FCC2

Flare	**Parts**	**Time Interval** (s)	**kT** (keV)	**EM** (10^{54} cm^{-3})	**Z** ($Z_\odot$)	**$F_{7.11-50}$** (10^{-2} ph cm^{-2} s^{-1})	**$L_{x,[14-50]}$** (10^{31} erg s^{-1})	χ^2_ν **(DOF)**
F1	P1*	$T0_1$–243 : $T0_1$–43	> 14.4	$2.0^{+1.1}_{-0.6}$	$1.64^\dagger$	–	$3.7^{+0.6}_{-0.6}$	0.893 (15)
	P2*	$T0_1$–43 : $T0_1$+137	14^{+2}_{-1}	$14.2^{+2.6}_{-2.3}$	$1.64^\dagger$	–	$11.7^{+1.0}_{-1.1}$	0.581 (15)
	P3	$T0_1$+137 : $T0_1$+197	$15.0^{+0.7}_{-0.7}$	$6.9^{+0.3}_{-0.3}$	$2.3^{+0.4}_{-0.4}$	$37.3^{+0.4}_{-0.4}$	$7.02^{+0.07}_{-0.07}$	1.193 (322)
	P4	$T0_1$+197 : $T0_1$+267	$14.1^{+0.7}_{-1.1}$	$6.1^{+0.3}_{-0.3}$	$2.6^{+0.4}_{-0.4}$	$33.1^{+0.3}_{-0.3}$	$5.95^{+0.06}_{-0.06}$	1.104 (331)
	P5	$T0_1$+267 : $T0_1$+347	$9.80^{+0.4}_{-0.4}$	$4.8^{+0.2}_{-0.2}$	$2.4^{+0.3}_{-0.3}$	$20.3^{+0.2}_{-0.2}$	$2.67^{+0.03}_{-0.03}$	0.978 (322)
	P6	$T0_1$+347 : $T0_1$+447	$8.25^{+0.3}_{-0.3}$	$3.9^{+0.2}_{-0.2}$	$1.9^{+0.3}_{-0.2}$	$12.7^{+0.1}_{-0.1}$	$1.38^{+0.01}_{-0.01}$	1.173 (311)
	P7	$T0_1$+447 : $T0_1$+587	$7.39^{+0.4}_{-0.4}$	$2.8^{+0.1}_{-0.1}$	$1.7^{+0.2}_{-0.2}$	$7.88^{+0.08}_{-0.08}$	$0.752^{+0.008}_{-0.008}$	1.256 (307)
	P8	$T0_1$+587 : $T0_1$+787	$6.44^{+0.2}_{-0.2}$	$1.86^{+0.07}_{-0.07}$	$1.8^{+0.2}_{-0.2}$	$4.58^{+0.05}_{-0.05}$	$0.364^{+0.004}_{-0.004}$	1.134 (300)
	P9	$T0_1$+787 : $T0_1$+957	$6.08^{+0.2}_{-0.2}$	$1.33^{+0.05}_{-0.05}$	$1.7^{+0.2}_{-0.2}$	$2.94^{+0.03}_{-0.03}$	$0.217^{+0.002}_{-0.002}$	1.247 (295)
F2*	–	$T0_2$–242 : $T0_2$+938	11^{+3}_{-2}	$1.2^{+0.9}_{-0.6}$	$1.00^\dagger$	–	$1.1^{+0.1}_{-0.1}$	0.683 (15)

Notes.kT, EM, and Z are the "effective" plasma temperature, emission measures, and abundances during different time intervals of flare decay, respectively.$F_{7.11-50}$ is the flux derived in the 7.11–50 keV energy band. $L_{X,[14-50]}$ is the luminosity derived in the 14–50 keV energy band.All the errors shown in this table are in the 68% confidence interval.

*** -** In these time segments, only BAT spectra were available and best-fitted with the single temperature APEC model, whereas in other segments, XRT+BAT spectra were fitted with three temperature APEC with the first two temperatures fixed to the quiescent value.

† **-** The abundances were kept fixed at the average abundance derived from XRT spectral fitting.

the plasma properties of the flare represented by two-temperature components, the total emission measure and temperature were calculated as EM = $(\mathrm{EM}_1 + \mathrm{EM}_2)$ and T = $(\mathrm{EM}_1.\mathrm{T}_1 + \mathrm{EM}_2.\mathrm{T}_2)/\mathrm{EM}$. The time evolution of spectral parameters along with the X-ray luminosity in 0.3-10 keV energy band for the flare FCC2 is shown in Fig. 5.3(ii). The abundances were varied from 0.5 to 1.1 $Z_\odot$. The flare temperature (weighted sum) and total EM were peaked at 6.7 ± 1.0 keV and $3.3{\pm}0.3{\times}10^{54}$ cm^{-3}, respectively. These values are two to three times higher than the respective minimum observed values. At the end of the flare, the X-ray luminosity was found to be 38% of its maximum value of $10^{31.8}$ erg s^{-1}.

5.3.4 The emission line at 6.4 keV

In the spectral fitting of XRT spectra with the 3-T APEC model for FCC1 and the 2-T APEC model for FCC2, a significant positive residuals redward of the prominent Fe K complex at ≈6.7 keV were detected. This excess emission occurs at the expected position of the 6.4 keV Fe fluorescent line, which is not included in the APEC line list. To determine whether indeed such emission is present in the XRT spectrum, we have fitted again the spectra with an additional Gaussian line component along with the best-fit plasma model. Initially, keeping free the width of the Gaussian line (σ), it converges to a very large value than the actual line width. Therefore, in order to get a best fit, we fixed the σ in every value from 10–200 eV with an increment of 10 eV. In this analysis, we have used the σ corresponding to the minimum χ^2 value, ranging from 40–80 eV for a different time segment of the flare. The line centroid (E) and the normalization along with the temperature, abundances, and EM were left free to vary. The best-fit parameters are given in Table 5.2 and 5.3, for the flares FCC1 and FCC2, respectively. In each segment, the best-fit line energy agrees with the Fe fluorescent feature at E $\sim$ 6.4 keV (see the sixth column of Table 5.2 and eighth column of Table 5.3). We applied the F-test to the χ^2 resulting from the fits with and without an additional Gaussian line, which shows the significance of the Fe Kα feature with a probability of the line not being a result of random fluctuation (see the last column of Table 5.2 and 5.3). The derived Fe Kα line flux shows variability and follows the light curve and peaked at a value of $1.2^{+0.6}_{-0.5}{\times}10^{-2}$ photons s^{-1}cm^{-2} for the flare FCC1 and $5.0^{+2.0}_{-1.9}{\times}10^{-3}$ photons s^{-1}cm^{-2} for the flare FCC2, which is $\sim$20 and $\sim$7 times more than the minimum observed Fe Kα flux, respectively. The equivalent width (EW) was found to be in the range of 23–173 eV for the flare FCC1 and 47–244 eV for the flare FCC2.

5.4 XRT+BAT spectra

Time-resolved spectroscopy for the flare FCC1 was also performed with the XRT+BAT data. Very poor statistics of the BAT spectra did not allow us a time-resolved spectral analysis of the XRT+BAT spectra for the flare FCC2. A similar approach, as applied for the XRT spectral fitting was also applied for the XRT+BAT spectral fitting. For the flare FCC1, we choose seven time bins (P3–P9) similar to the spectral fitting of only-XRT data as described in the previous section (see Fig. 5.1). Since galactic $^{\mathrm{h}}1$ column density was not found to be variable during only-XRT spectral analysis; therefore, we fixed N_H to its average value. The global abundances, temperature, and corresponding EMs of the third component were free parameters in the spectral fitting. The derived parameters are given in Table 5.4 and the variations of the spectral parameters are shown in Fig. 5.3. The peak temperature derived in this spectral fitting was found to be 15.0±0.7 keV, which is higher than the highest temperature derived from XRT spectral analysis. The EM was found to have the similar values as those derived from XRT spectral fitting, whereas the peak abundance was found to be ~1.1 times higher than to that derived from XRT data.

5.5 Hydrodynamic modeling of flare decay

Although stellar flares cannot be spatially resolved, it is possible to infer the physical size and structure of flares from the flare loop models. The flares observed from CC Eri were also modeled using state-of-art hydrodynamic model of Reale et al. (1997). Details on the model is given in section 1.3.4.4. Using equation 1.8, we estimated the loop lengths of flaring structure from CC Eri, where $T_{\max}$ and $F(\zeta)$ are calibrated for spectral response of *Swift* XRT by Osten et al. (2010) as

$$T_{\max} = 0.0261 \times T_{\mathrm{obs}}^{1.244} \tag{5.1}$$

$$\frac{\tau_{\mathrm{d}}}{\tau_{\mathrm{th}}} = F(\zeta) = \frac{1.81}{\zeta - 0.1} + 0.67 \qquad 0.4 < \zeta \lesssim 1.9 \tag{5.2}$$

The value of ζ was derived as slope of density-temperature diagram. For stellar observations, no density determination is normally available; therefore, we used the quantity $\sqrt{\mathrm{EM}}$ as a proxy of the density assuming the geometry of the flaring loop during the decay. Fig. 5.4 shows the path $\log \sqrt{\mathrm{EM}}$ versus $\log T$ for flares FCC1 and FCC2. A linear fit to the data provided the value of ζ as 0.550 ± 0.047 for flare

FCC1 and 0.819 ± 0.179 for flare FCC2. This indicates the presence of sustained heating during the decay phase of both flares.

The relationship between $T_{\rm max}$ and observed peak temperature ($T_{\rm obs}$) was also calibrated for *Swift* XRT by Osten et al. (2010) as $T_{\rm max} = 0.0261 \times T_{\rm obs}^{1.244}$, where both temperatures are in K. For flares FCC1 and FCC2, $T_{\rm max}$ was calculated to be 365±33 and 170±32 MK, respectively. The flaring loop length was derived as $1.2 \pm 0.1 \times 10^{10}$ cm for flare FCC1 and $2.2 \pm 0.6 \times 10^{10}$ cm for flare FCC2. Assuming a semi-circular geometry, the flaring loop height (L/π) was estimated to be 0.1 and 0.2 times the stellar radius (R_*) of the primary component of CC Eri of the flares FCC1 and FCC2. The loop parameters for both the flares are given in Table 5.5.

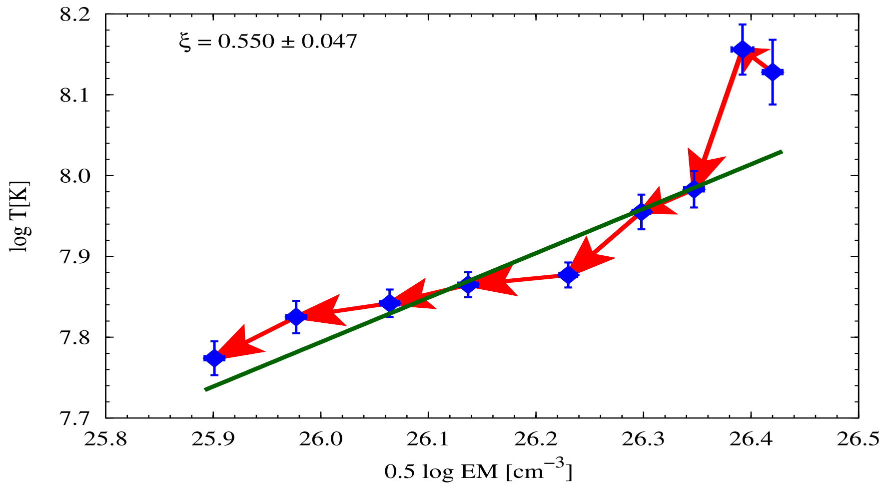

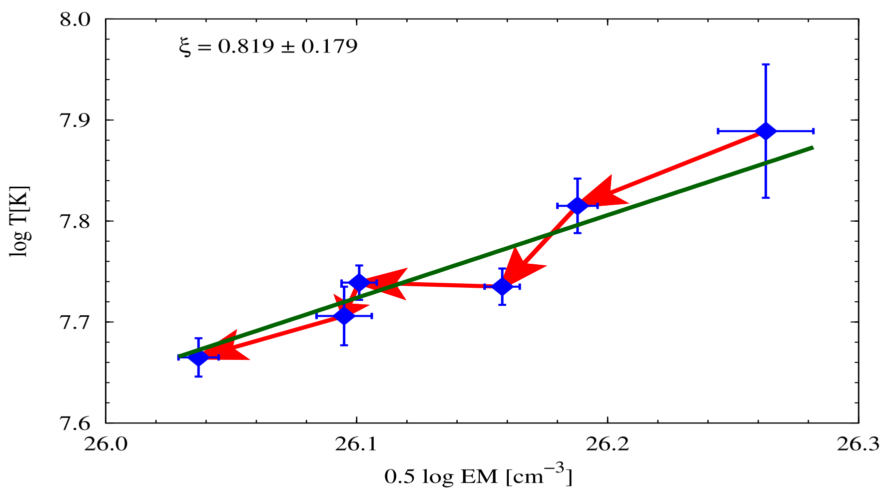

Figure 5.4: Evolution of flares FCC1 (left) and FCC2 (right) in log $\sqrt{\rm EM}$ – log T plane. The continuous line shows the best-fit during the decay phase of the flares with a slope ζ shown in the top left corner of each plot.

Table 5.5: Loop parameters derived for flares FCC1 and FCC2

Sl.	**Parameters**	**Flare F1**	**Flare F2**
1	$\tau_{\rm r,14-150}$ (s)	150 ± 12	146 ± 34
2	$\tau_{\rm d,14-150}$ (s)	283 ± 13	592 ± 114
3	$\tau_{\rm d,0.3-10}$ (s)	539 ± 4	1014 ± 17
4	$L_{\rm X,max}$ (10^{31} erg s^{-1})	17.3 ± 0.2	5.91 ± 0.06
5	$T_{\rm max}$ (10^6 K)	365 ± 33	170 ± 32
6	ζ	0.550 ± 0.047	0.819 ± 0.179
7	L (10^{10} cm)	1.2 ± 0.1	2.2 ± 0.6
8	p (10^5 dyn cm^{-2})	15 ± 5	0.8 ± 0.7
9	$n_{\rm e}$ (10^{12} cm^{-3})	15 ± 7	1.7 ± 1.7
10	V (10^{29} cm^3)	∼0.31	∼11.5
11	B (kG)	∼6.1	∼1.4
12	$E_{\rm H}$ (10^3 erg s^{-1} cm^{-3})	∼6.6	∼0.13
13	H (10^{32} erg s^{-1})	∼2.1	∼1.5
14	$E_{\rm X,tot}$ (10^{35} erg)	>1.4	>1.7
15	B_0 (kG)	>12	>2
16	$N_{\rm loops}$	∼1	∼3
17	$\theta(^\circ)$	∼90	–

1, 2: e-folding rise and decay times derived from the BAT light curve.
3: e-folding decay time derived from the XRT light curve.
4: luminosity at the flare peak in the XRT band.
5: the maximum temperature in the loop at the flare peak.
6: slope in the density-temperature diagram during the flare decay.
7: flaring loop length.
8: maximum loop pressure at the flare peak.
9: maximum electron density in the loop at the flare peak.
10: loop volume of the flaring region.
11: minimum magnetic field.
12: heating rate per unit volume at the flare peak.
13: total heating rate at the flare peak.
14: total radiated energy.
15: total magnetic field required to produce the flare.
16: the number of loops needed to fill the flare volume assuming loop aspect ratio of 0.1.
17: the astrocentric angle between observer and the flare location on the stellar disk.

5.6 Energetics

The derived loop lengths are much smaller than the pressure scale height[1] of the flaring plasma of CC Eri. Therefore, we can assume that the flaring loop is not far from a steady-state condition. We applied the RTV scaling laws (Rosner et al., 1978) to determine the maximum pressure (p) in the loop at the flare peak and found it to be $\sim 1.5 \times 10^6$ and $\sim 8 \times 10^4$ dyne cm^{-2} for the flares FCC1 and FCC2, respectively. The plasma density (n_e), the flaring volume (V), and the minimum magnetic field (B) to confine the flaring plasma were derived using equation 4.1.5.

The estimated values of n_e, V, and B during the flares FCC1 and FCC2 were 1.5×10^{13} and 1.7×10^{12} cm^{-3}, 3.1×10^{28} and 1.2×10^{30} cm^3, and $\sim$6.1 and $\sim$1.4 kG, respectively. Using the RTV scaling laws, we have also estimated the heating rate per unit volume ($E_H = \frac{dH}{dV dt} \simeq 10^5\ p^{7/6}\ L^{-5/6}$) at the peak of the flare as $\simeq 6.6 \times 10^3$ and $\simeq 1.3 \times 10^2$ erg cm^{-3} s^{-1} for the flares FCC1 and FCC2, respectively. The total heating rates ($\frac{dH}{dt} \simeq \frac{dH}{dV dt} \times V$) at the peak of the flares were derived to be $\sim 2.1 \times 10^{32}$ and $\sim 1.5 \times 10^{32}$ erg s^{-1} for the flares FCC1 and FCC2, which were, respectively, $\sim$1.2 and $\sim$2.5 times higher than the flare maximum luminosity. If we assume that the heating rate is constant throughout the rise and decay phases of the flare, the total energy radiated [$E_{\rm X,tot} > \frac{dH}{dt} \times (\tau_r + \tau_d)$] during the flares was derived to be $>1.4 \times 10^{35}$ erg for flare FCC1 and $>1.7 \times 10^{35}$ erg for flare FCC2. These values were $\sim$40 s and $\sim$47 s of bolometric energy output of the primary and $\sim$221 s and $\sim$264 s of bolometric energy output of the secondary for the flares FCC1 and FCC2, respectively.

5.7 Modeling of fluorescent Fe Kα emission

In the stellar context, the detected iron Kα line is generally attributed to a fluorescent process, where the fluorescing material is a neutral or low ionization state of photospheric iron (Fe I–Fe XII), which shines on the X-ray continuum emission arising from a loop-top source. Thus the detection of this line constraints the height of the flaring loop. The process involves photoionization of an inner K-shell electron and the de-excitation of an electron from a higher level at this energy. Thus the total photon flux above the Fe Kα ionization threshold of 7.11 keV is one of the

[1] The pressure scale height is defined as $h_{\rm p} = 2kT_{\rm max}/(\mu g)$, where μ is the average atomic weight and g is the surface gravity of the star. Considering both the stellar components, the derived values of $h_{\rm p}$ are $\geq 9.8 \times 10^{11}$ cm for flare FCC1 and $\geq 4.6 \times 10^{11}$ cm for flare FCC2.

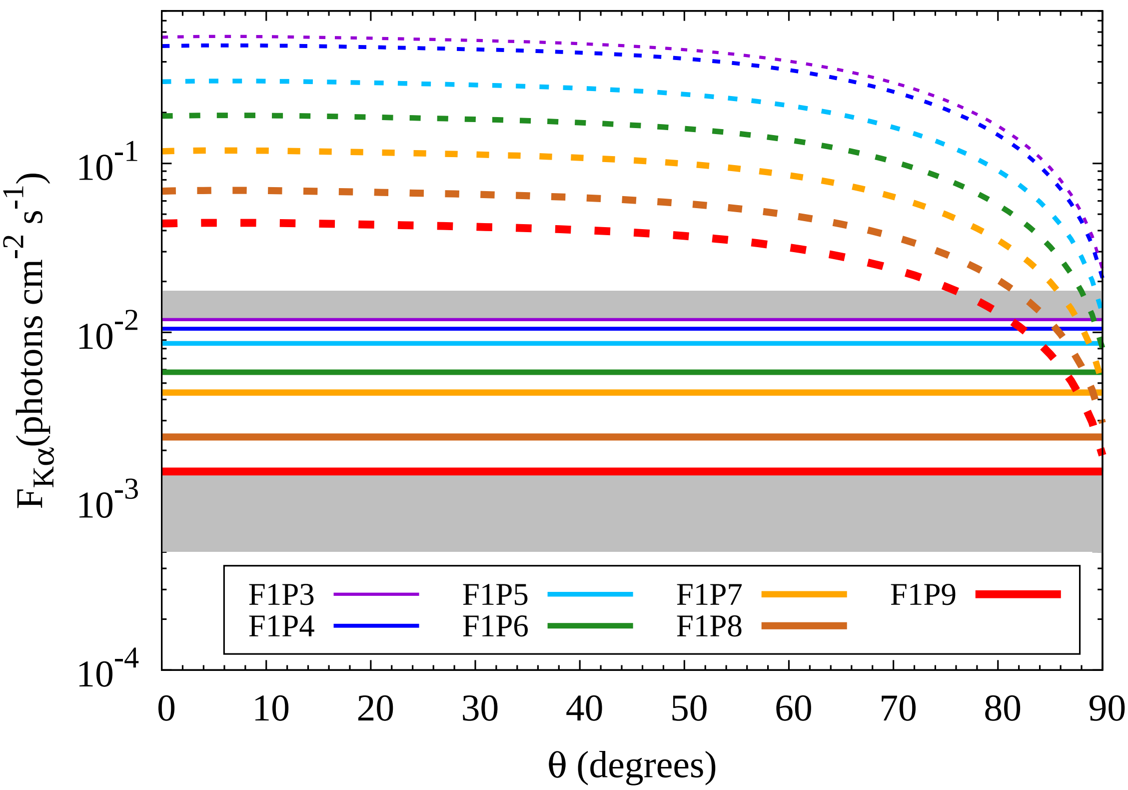

Figure 5.5: Modeling of 6.4 keV line flux for the seven time intervals during the decay of flare FCC1. The solid horizontal lines show the observed Fe Kα line fluxes of different time segments marked in the bottom of the plot. The dashed curves with similar thickness correspond to the modeled Fe Kα line flux variation with the astrocentric angle for the same time intervals. Thicker the lines correspond to the later time spans. The dark shaded regions indicate the upper and lower 68% confidence intervals of the first and last time segments, respectively.

main contributors to the observed flux in the Fe Kα line. For the solar flares, Bai (1979) derived a formula for the flux of Fe Kα photons received on the Earth, which was later extended to stellar context by Drake et al. (2008) and is given by

$$F_{K\alpha} = f(\theta)\Gamma(T,h)F_{7.11} \quad \text{photons cm}^{-2}\ \text{s}^{-1} \tag{5.3}$$

where $F_{7.11}$ is the total flux above 7.11 keV, $f(\theta)$ is a function that describes the angular dependence of the emitted flux on the astrocentric angle (defined as an angle subtended by the flare and the observer), and Γ is the fluorescent efficiency. We used the coefficients derived by Drake et al. (2008) to determine the functional dependence of $f(\theta)$ and Γ for different loop heights (see Tables 2 and 3 of Drake et al., 2008). We could only get enough statistics in both XRT and BAT spectra (required to estimate $F_{7.11}$) for the flare FCC1; therefore, we have done our analysis only for flare FCC1. The value of Γ was taken as 0.96 for a loop height of 0.1 R_* and a temperature of 100 MK, which are closest to the derived loop length and maximum temperature of the flare FCC1. Because photospheric iron abundances of CC Eri are not known, a default value of abundances of 3.16×10^{-5} was used in the calculations (see Drake et al., 2008). Since the flare FCC1 was only detected up to 50 keV (see § 5.1), in our analysis, we considered the upper limit of energy to be 50 keV. The model flux of the photon density spectrum above 7.11 keV was calculated by using best-fit APEC model parameters from the joint spectral fitting of XRT+BAT spectra in different time intervals for flare FCC1. Fig. 5.5 shows the modeled Fe Kα flux as a function of the astrocentric angle of a flare height of 0.1 R_* for different time segments. The corresponding observed flux is also shown by continuous lines of the same thickness. The modeled and observed Fe Kα line flux was found to overlap at an astrocentric angle of ∼90°.

5.8 Discussion

5.8.1 Temporal and spectral properties

Here we have presented a detailed study of two X-ray superflares observed on an active binary system CC Eri with the *Swift* satellite. These flares are remarkable in the large enhancement of peak luminosity in soft and hard X-ray energy bands. A total of eight flares have been detected in X-ray bands on CC Eri thus far. Out of the eight flares, two flares are the strongest flares in terms of energy released. The soft X-ray luminosity increased up to ∼400 and >3 times more than to that of the minimum observed values for the flares FCC1 and FCC2, respectively. The former is much larger than any of the previously reported flares on CC Eri observed with *MAXI* GCS (∼5–6 times more than quiescent; Suwa et al., 2011), *Chandra* (∼11 times more than quiescent; Nordon & Behar, 2007), *XMM-Newton* (∼2 times more than quiescent; Crespo-Chacón et al., 2007; Pandey & Singh, 2008), *ROSAT* (∼2 times more than quiescent; Pan & Jordan, 1995), and other flares observed with *EXOSAT* (Pallavicini et al., 1988), *Einstein* IPC (Caillault et al., 1988), and *HEAO1* (Tsikoudi, 1982). However, similar magnitude flares have been reported in other stars such as DG CVn (Fender et al., 2015; Osten et al., 2016), EV Lac (Favata et al., 2000; Osten et al., 2010), II Peg (Osten et al., 2007), UX Ari (Franciosini et al., 2001), AB Dor (Maggio et al., 2000), Algol (Favata & Schmitt, 1999), and EQ1839.6+8002 (Pan et al., 1997). Considering that the flare happened in the primary (K7.5 V), the peak X-ray luminosity of flare FCC1 and flare FCC2 were, respectively, found to be 48% and 16% of bolometric luminosity (L_{bol}); if the flare happened in the secondary (M3.5 V) star, the peak X-ray luminosity of flares FCC1 and FCC2 were 267% and 91% of L_{bol}, whereas the peak luminosity for flares FCC1 and FCC2 were found to be 41% and 14% of combined L_{bol}, respectively.

Both flares appear to be the shortest duration flares observed on CC Eri thus far. However, a weak flare with a similar duration was observed by the *XMM-Newton* satellite (Crespo-Chacón et al., 2007). The durations of all other previously observed flares on CC Eri were in the range of 9–13 ks. The durations of the superflares on CC Eri are also found to be smaller than other observed superflares, e.g. ∼3 ks for EV Lac (Osten et al., 2010), >10 ks for II Peg (Osten et al., 2007), ∼14 ks for AB Dor (Maggio et al., 2000), and ∼45 ks for Algol (Favata & Schmitt, 1999). The e-folding decay times of both X-ray flares are shorter in the hard spectral band than those in the softer band.

During the flares FCC1 and FCC2, the observed temperature reached a maximum value of ∼174 MK for flare FCC1 and ∼128 MK, respectively. These values of temperatures are quite high from previously observed maximum flare temperatures on CC Eri (Crespo-Chacón et al., 2007; Nordon & Behar, 2007; Pandey & Singh, 2008), but are of the similar order to those of other superflares detected on II Peg (≈300 MK; Osten et al., 2007), DG CVn (≈290 MK; Osten et al., 2016), EV Lac (≈150 MK and ≈142 MK; Favata et al., 2000; Osten et al., 2010), and AB Dor (≈114 MK; Maggio et al., 2000). The abundances during the flares FCC1 and FCC2 are found to enhance ∼9 and ∼2 times more than those of the minimum values observed. During other superflares, abundances were found to increase between two to three times more than that of the quiescent level (Favata et al., 2000; Favata & Schmitt, 1999; Maggio et al., 2000). However, in the case of the superflare observed with *Swift* in EV Lac, the abundances were found to remain constant throughout the flare. From Fig. 5.3, it is evident that the abundance peaks after the temperature and luminosity peaks, which is consistent with a current idea in the literature (see Reale, 2007). This could be due to the heating and evaporation of the chromospheric gas, which increases the metal abundances in the flaring loop. For both flares, the temperature was peaked before the EM did. A similar delay was also observed in many other solar and stellar flares (e.g. Favata et al., 2000; Favata & Schmitt, 1999; Pandey & Singh, 2008; Sylwester et al., 1993). The temperature increases due to beam driven plasma heating and later subsequent evaporation of the plasma into upper parts of the coronal loop that increases its density, and therefore EM ($\sim n_e^2$). Later coronal plasma cools down by thermal conduction and then via radiative losses (e.g. Cargill & Klimchuk, 2004).

5.8.2 Coronal loop properties

The derived loop lengths for the flares FCC1 and FCC2 are larger than previously observed flares by Crespo-Chacón et al. (2007) on CC Eri. The loop lengths are also in between the loop lengths derived for other G–K dwarfs, dMe stars, and RS CVn type binaries (e.g. Favata & Micela, 2003; Pandey & Singh, 2008, 2012). Instead of $\sim$3 times larger peak luminosity in flare FCC1 than that of the flare FCC2, the derived loop length for flare FCC2 is two times larger than that of flare FCC1, which might be interpreted as a result of an $\sim$1.4 times more sustained heating rate in the decay phase of flare FCC1 than that of flare FCC2. The heating rate during flare FCC1 is also found to be $\sim$49% of the bolometric luminosity of the CC Eri system, whereas during flare FCC2 the heating rate is only $\sim$35% of the combined bolometric luminosity. The derived heating rate is also found to be more than the maximum X-ray luminosity for both flares. This result is compatible with X-ray radiation being one of the major energy loss terms during the flares.

Present analysis allows us to make some relevant estimation of the magnetic field strength that would be required to accumulate the emitted energy and to keep the plasma confined in a stable magnetic loop configuration. Under the assumptions that the energy release is indeed of magnetic origin, the total non-potential magnetic field B_0 involved in a flare energy release within an active region of the star can be obtained from the relation given in equation 4.5. Assuming that the loop geometry does not change during the flare, B_0 is estimated to be >12 and >2 kG for the flares FCC1 and FCC2, respectively. Bopp & Evans (1973) also estimated a large magnetic field of 7 kG on CC Eri at photospheric level. We have used the loop volume in the derivation of B_0, but this may not imply that the magnetic field fills up the whole volume. Rather, our estimation of B_0 is based on the assumption that the energy is stored in the magnetic field configuration (e.g. a large group of spots) of the field strength of several kG with a volume comparable to one of the flaring loops.

5.8.3 Flare location and Fe Kα emission feature

Given that CC Eri is an active binary system, we can consider three possible scenarios of the flare origin: (i) energy release occurs due to magnetic reconnection between magnetic fields bridging two stars (see Graffagnino et al., 1995; Uchida & Sakurai, 1983), (ii) flares occurred on K-type primary star, and (iii) flares occurred on M-type secondary star. The binary separation of the CC Eri system of 1.4 $\times 10^{11}$ cm (Amado et al., 2000; Crespo-Chacón et al., 2007) is more than an order of the height of flaring loops for both flares. Therefore, it is more likely that the flares are attached to a corona of any one of the components of CC Eri. It is also very difficult to identify the component of the binaries on which the flares occurred.

One of the most interesting findings is the detection of Fe Kα emission line in the X-ray spectra of CC Eri during the flares, whose flux depends on the photospheric iron abundance, the height of the emitting source, and the astrocentric angle between the emitting source and observer(Bai, 1979; Drake et al., 2008). Recently, the Fe Kα emission line was also detected in several other cool active stars during large flares, such as HR 9024 (Testa et al., 2008) and II Peg (Ercolano et al., 2008), and has been well described by the fluorescence hypothesis. In most of the cases, the flaring loop length derived in this method was found to be consistent with the loop length derived from the hydrodynamic method. Using the loop length derived from the hydrodynamic model, the astrocentric angle between the flare and observer has been estimated as $\sim$90°. This shows that the region being illuminated by the flare, and thus fluorescing the photospheric iron, is located near the stellar limb.

5.9 Conclusions

In the present study, it has been found that the flares decay faster in the hard X-ray band than in the soft X-ray band. Both flares FCC1 and FCC2 are highly energetic with respective peak X-ray luminosities of $\sim 10^{32.2}$ and $\sim 10^{31.8}$ erg s^{-1} in 0.3–50 keV energy band, which are larger than any other flares previously observed on CC Eri. The time-resolved spectral analysis during the flares shows the variation in the coronal temperature, emission measure, and abundances. The elemental abundances are enhanced by a factor of $\sim$8 to the minimum observed in the post-flare phase for the flare FCC1. The observed peak temperatures in these two flares are found to be 174 MK and 128 MK. Using the hydrodynamic loop modeling, we derive loop lengths for both the flares as $1.2\pm0.1\times10^{10}$ cm and $2.2\pm0.6\times10^{10}$ cm, respectively. The Fe Kα emission at 6.4 keV is also detected in the X-ray spectra and we model the Kα emission feature as fluorescence from the hot flare source irradiating the photospheric iron. These superflares are the brightest, hottest, and shortest in duration observed thus far on CC Eri.

Chapter 6

A long duration flare from evolved RS CVn type eclipsing binary SZ Psc

In this chapter, we investigate a very long duration flaring event observed from *Swift* satellite from an RS CVn type eclipsing binary star SZ Psc. The system consists of a spotted, chromospherically active K1 subgiant and a much less luminous, inactive F8 star (Kharchenko et al., 2007), with an orbital period of about 3.9657 days (Eaton & Henry, 2007). The K1 subgiant is the more massive component and is filling 80–90% of its Roche lobe. The light variations in optical waveband on SZ Psc was found by several researcheres, such as Jakate et al. (1976), Catalano et al. (1978), Tumer & Kurutac (1979), Eaton et al. (1982), Tunca (1984), Antonopoulou et al. (1995), Lanza et al. (2001). The spot model was applied by Eaton & Hall (1979) to explain a distortion wave in optical light curves. Lanza et al. (2001) has studied Long-term starspot evolution, activity cycle and orbital period variation of SZ Psc. Whereas Kang et al. (2003) have studied chromospheric activity by analysing photometric data and have given light-curve/spot solutions. Doyle et al. (1994) observed flaring activity on SZ Psc in Ultraviolet waveband. They also found variation in Mg II strength, possibly phase dependent, and an apparent eclipse of a plage in Mg II. MAXI/GSC detection of a possible flare from SZ Psc was reported by Negoro et al. (2011).

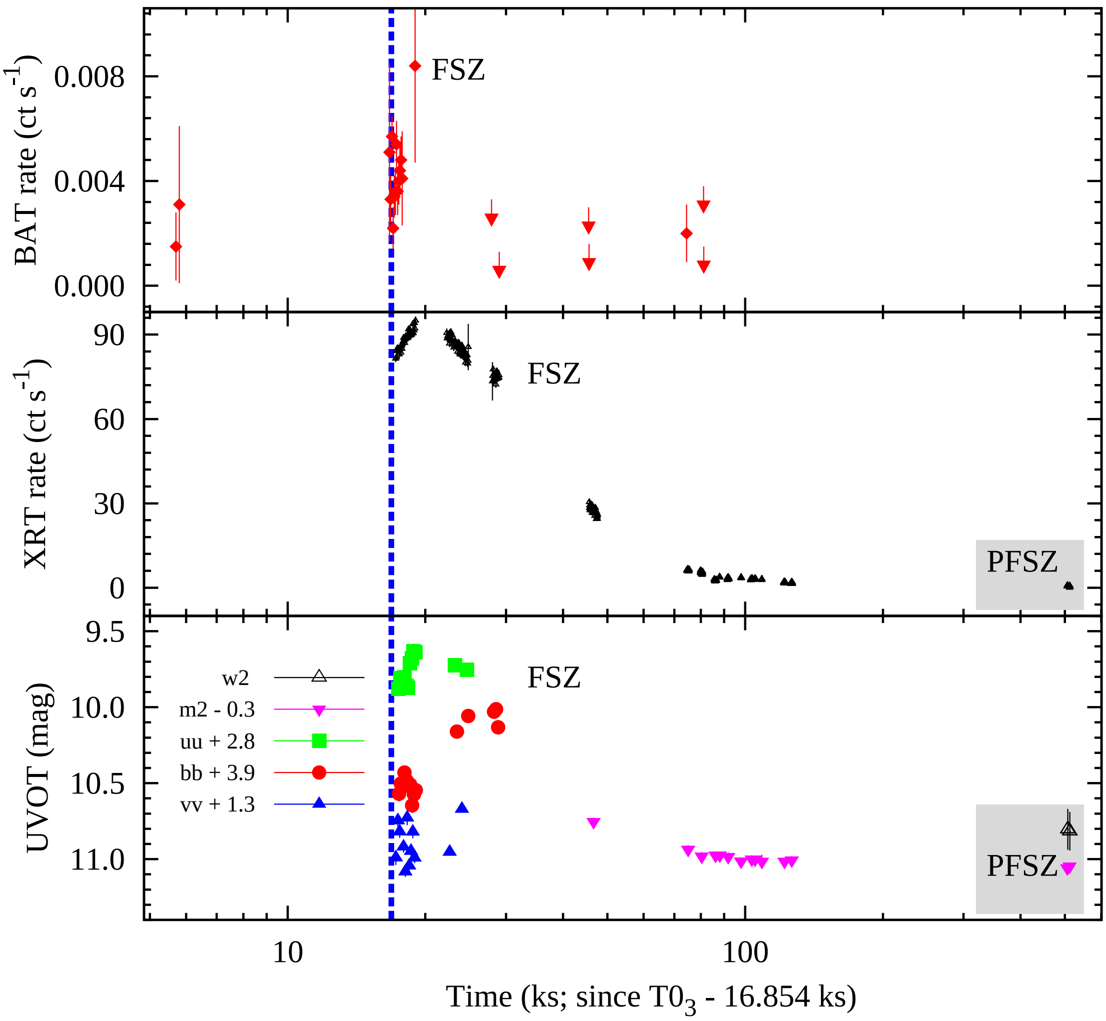

Figure 6.1: *Swift* BAT (top panel), XRT (middle panel), UVOT (bottom panel) observations show flare FSZ and the post-flare PFSZ.

6.1 X-ray light curves

Fig. 6.1 shows the X-ray light curves of SZ Psc obtained in 14–150 keV, 0.3–10 keV and five UVOT bands. The flare FSZ triggered *Swift*'s BAT on 2015 January 15 UT 09:08:42 (=$T0_3$) as an Automatic Target trigger on board (reported by D'Elia et al., 2015; Drake et al., 2015). SZ Psc entered in the BAT FOV around 100 s before the trigger interval. SZ Psc was also within the BAT FOV in the earlier orbits before $\sim$ 12 ks from the $T0_3$The BAT light curve shows variability during and after the trigger interval. The count rate initially appears to fall from an earlier peak, followed by an increase up to a count rate of $\sim$0.0084 counts s^{-1}.

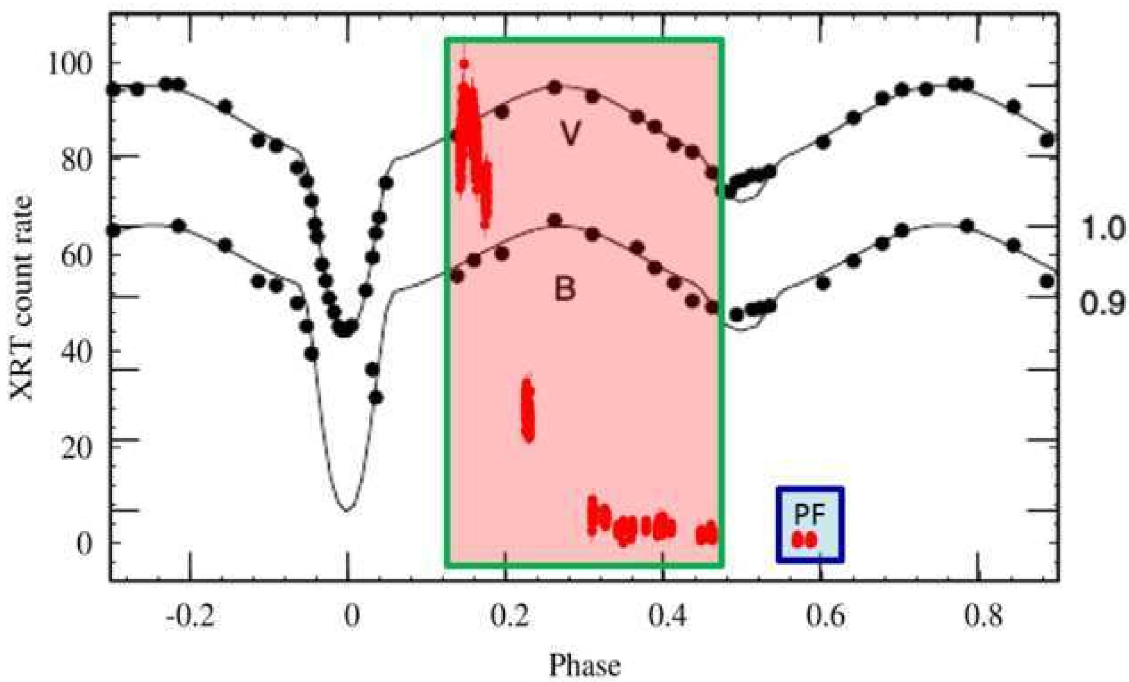

Figure 6.2: Phase folded X-ray light curve of SZ Psc overplotted with B and V band light curve.

The *Swift* XRT started to observe the flare FSZ from $T0_3$ + 380.5 s in WT mode, while the XRT count rate was ∼82.5 counts s^{-1}. The XRT count rate increased to ∼100 counts s^{-1} by the end of the initial observation at $T0_3$ + 2.2 ks, and then over the next 8 hours declined rapidly, dropping to ∼30 counts s^{-1}/s at $T0_3$ +30 ks. After a gap of ∼16 ks, the XRT observations for the period $T0_3$ + 58 ks to $T0_3$ + 92 ks shows much slower decay of the flare during which the count rate was decreased from ∼7 counts s^{-1} to 3 counts s^{-1}. After ∼109 ks of these observations, the soft X-ray flux of SZ Psc was decreased to 1.3 counts s^{-1}. The *Swift* returned to the field of view of SZ Psc after 5.67 days (or 0.49 Ms) from the trigger, where the XRT count rate dropped to a value of ∼0.5 counts s^{-1}. This region is marked as "PFSZ" in Fig. 6.1.

The *Swift* UVOT observations of the flare peak and early decay phases of SZ Psc were saturated by all three UV filters. However, the early rise phase was detected without saturation by the optical u, b and v filters, as shown in the lower panel of Fig. 6.1. This shows that, flare peaks earlier in the u band, then in the b and v band. This phenomenon is similar to the "Neupert Effect". Only in the $uvm2$ filter, the light curve is not saturated during the flare decay, and the light curve seems to follow the similar variation in the XRT energy band.

The duration for the flare FSZ is derived to be >70 ks, which is among the longest duration flares observed on SZ Psc, thus far. The flare duration is also very much larger than that of the flares derived in other BY Dra and RS CVn binaries (Pandey & Singh, 2008, 2012). The e-folding rise times (τ_r) and decay times (τ_d) of the flare FSZ in XRT band are derived using the equation 4.1 and found to be 12.5±0.4 and 19.9±0.1 ks, respectively. Both of these values are comparable or more than those of the observed flares in other G-K dwarfs, RS CVn binaries, and dMe stars (e.g. Osten & Brown, 1999; Pandey & Singh, 2008, 2012; Schmitt, 1994). Due to insufficient statistics for BAT data, and incompleteness of the flare in all the UV filters due to saturation or faintness, we could not derive the rise and decay time in other energy bands. Since SZ Psc is an eclipsing binary, we have also investigated if the flare is affected by the eclipse or not. We have phase folded the XRT light curve with a period of 3.96 days and according to the revised ephemeris from Eaton & Henry (2007). We have overplotted the X-ray light curve on the optical V and B band light curve derived by Kang et al. (2003), and shown Fig. 6.2. It is evident from the figure that the flare was observed out of eclipse from binary phase 0.18 to 0.4. The later phase of the flare was partially eclipsed. The post flaring region was very close to the secondary eclipse at binary phase 0.55 showing that the primary component of SZ Psc is relatively strong X-ray emitter.

6.2 X-ray Spectral Analysis

Both the BAT and XRT spectra during the flaring event were extract adopting the methods as given in Chapter 2. The detailed analysis of BAT spectra could not be done due to poor count statistics. Therefore, only XRT spectra were analysed to study the this long duration flare.

6.2.1 Post-Flare spectra

The spectra of post-flare phase were fitted single (1-T), double (2-T), and triple (3-T) temperature APEC model. The global abundances (Z) and interstellar HI column density (N_H) were left as free parameters. None of the plasma models (1-T, 2-T, or 3-T) were formally acceptable with solar photospheric abundances as large values of χ^2 were obtained. Only a 3-T plasma model with the sub-solar abundances was found to be acceptable with a reduced χ^2 value of 1.01 for 36 DOF. This shows that post-flare coronae of SZ Psc were well represented by three temperatures plasma. In

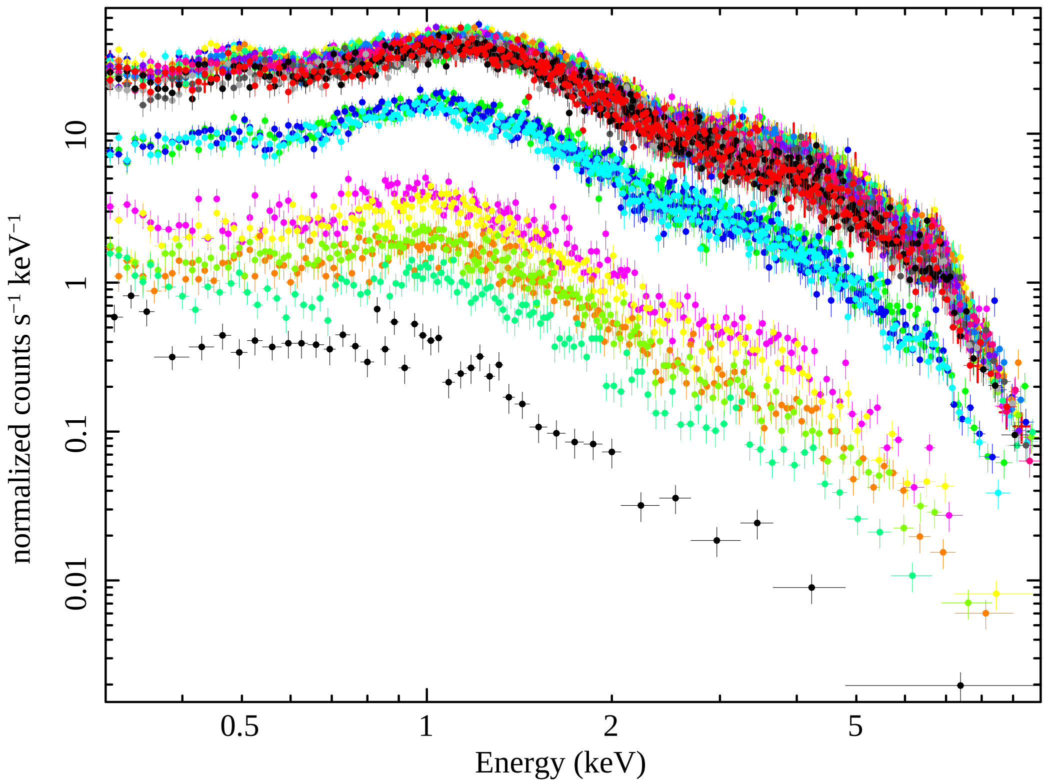

Figure 6.3: The time-resolved XRT spectra obtained in 0.3–10 keV. The black circle shows the spectra of the PFSZ phase. The rest spectra corresponds to the different parts of the flare rise and decay and the time-bins are as given in Table 6.1.

our analysis, N_H was a free parameter and the value was found to be less than the total galactic HI column density (Dickey & Lockman, 1990) towards the direction of SZ Psc. The three temperatures from the best-fit 3-T models were derived to be 0.027±0.009, $0.66^{+0.09}_{-0.06}$, and 7^{+12}_{-2} keV, respectively. The corresponding ratios of the emission measures were $EM_2/EM_1 = 2\times10^{-4}$ and $EM_3/EM_2 = 0.39$. The X-ray luminosity in 0.3–10.0 keV band during the post-flare region was derived to be $1.2\pm0.1\times10^{29}$ erg s^{-1}. The value of the luminosity is comparable or larger than the quiescent X-ray luminosities observed on other RS CVn stars (Pandey & Singh, 2012).

6.2.2 Flare spectra: Time-Resolved Spectroscopy

We have performed a detailed time-resolved analysis in order to investigate the evolution of spectral parameters during the flare FSZ in the soft X-rays. The flare was divided into twenty four time bins, so that each time bin contains sufficient and similar number of counts. The length of the time bins is variable, ranging from 210–

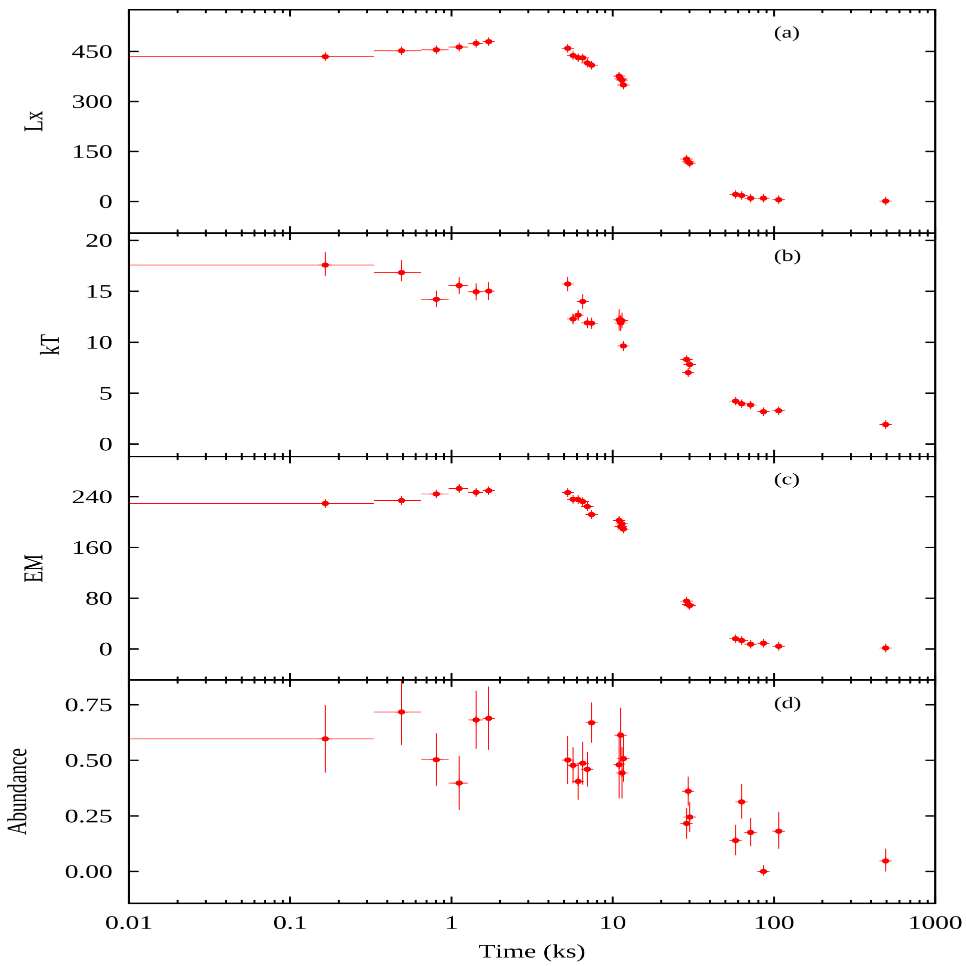

Figure 6.4: Evolution of XRT spectral parameters of SZ Psc during the flare. From top to bottom: (a) the X-ray luminosities are derived in 0.3–10 keV, (b) plasma temperature, (c) EM, and (d)abundance are shown. All the vertical bars shows 68% confidence interval, wheras horizontal bar shows the time interval for which the spectra were obtained.

10960 s. Larger time bins also contain large data gaps due to the earth occultation of satellite which also shows the decrement in the total counts. Table 6.1 gives the time intervals for which the X-ray spectra were accumulated and spectra for those time interval are shown in Fig. 6.3. In order to study the flare emission, we have performed 1-T, 2-T, and 3-T spectral fit of the data using the APEC model. A 1-T model gives the best-fit with the reduced χ^2 values as given in Table 6.1. Initially, in the spectral fitting N_H was a free parameter and found to be constant within a σ level of the quiescent state value. Therefore, it was fixed at a value of quiescent state in the next stage of spectral fitting. The time evolution of derived spectral

Table 6.1: XRT time-resolved spectral parameters during the flare from SZ Psc

Parts	**Time Interval** (s)	**kT** (keV)	**EM** (10^{54} cm^{-3})	$\mathbf{L_{x,[0.3-10]}}$ (10^{33} ergs^{-1})	**Z** ($Z_\odot$)	χ^2 **(DOF)**
P01	$T0_3$+380.5 : $T0_3$+710.5	$17.6^{+1.3}_{-1.1}$	$2.29^{+0.06}_{-0.05}$	$4.35^{+0.05}_{-0.05}$	$0.60^{+0.15}_{-0.15}$	1.082 (487)
P02	$T0_3$+710.5 : $T0_3$+1030.5	$16.8^{+1.2}_{-0.8}$	$2.34^{+0.06}_{-0.05}$	$4.52^{+0.03}_{-0.05}$	$0.72^{+0.15}_{-0.15}$	1.169 (484)
P03	$T0_3$+1030.5 : $T0_3$+1339.5	$14.2^{+0.8}_{-0.8}$	$2.44^{+0.05}_{-0.05}$	$4.55^{+0.06}_{-0.04}$	$0.50^{+0.12}_{-0.12}$	1.104 (475)
P04	$T0_3$+1339.5 : $T0_3$+1650.5	$15.6^{+0.8}_{-0.8}$	$2.53^{+0.05}_{-0.05}$	$4.63^{+0.05}_{-0.04}$	$0.40^{+0.12}_{-0.12}$	1.213 (478)
P05	$T0_3$+1650.5 : $T0_3$+1950.5	$14.9^{+0.8}_{-0.8}$	$2.47^{+0.05}_{-0.05}$	$4.74^{+0.06}_{-0.05}$	$0.68^{+0.13}_{-0.13}$	0.997 (480)
P06	$T0_3$+1950.5 : $T0_3$+2220.5	$15.0^{+0.9}_{-0.9}$	$2.49^{+0.06}_{-0.05}$	$4.79^{+0.05}_{-0.05}$	$0.69^{+0.14}_{-0.14}$	1.081 (459)
P07	$T0_3$+5440.5 : $T0_3$+5850.5	$15.7^{+0.7}_{-0.7}$	$2.46^{+0.04}_{-0.04}$	$4.59^{+0.02}_{-0.05}$	$0.50^{+0.11}_{-0.11}$	1.234 (536)
P08	$T0_3$+5850.5 : $T0_3$+6269.5	$12.3^{+0.5}_{-0.5}$	$2.36^{+0.04}_{-0.04}$	$4.38^{+0.04}_{-0.03}$	$0.48^{+0.08}_{-0.08}$	1.142 (529)
P09	$T0_3$+6269.5 : $T0_3$+6690.5	$12.7^{+0.5}_{-0.5}$	$2.36^{+0.04}_{-0.04}$	$4.31^{+0.03}_{-0.04}$	$0.40^{+0.08}_{-0.08}$	1.098 (525)
P10	$T0_3$+6690.5 : $T0_3$+7120.5	$14.0^{+0.7}_{-0.7}$	$2.32^{+0.04}_{-0.04}$	$4.31^{+0.03}_{-0.04}$	$0.49^{+0.10}_{-0.10}$	1.100 (528)
P11	$T0_3$+7120.5 : $T0_3$+7559.5	$11.9^{+0.5}_{-0.5}$	$2.24^{+0.03}_{-0.03}$	$4.16^{+0.03}_{-0.04}$	$0.46^{+0.08}_{-0.08}$	1.039 (522)
P12	$T0_3$+7559.5 : $T0_3$+7980.5	$11.9^{+0.5}_{-0.6}$	$2.11^{+0.03}_{-0.03}$	$4.09^{+0.03}_{-0.04}$	$0.67^{+0.09}_{-0.09}$	1.058 (522)
P13	$T0_3$+11220.5 : $T0_3$+11460.5	$15.2^{+1.0}_{-1.1}$	$2.02^{+0.05}_{-0.05}$	$3.76^{+0.05}_{-0.05}$	$0.48^{+0.15}_{-0.15}$	1.169 (385)
P14	$T0_3$+11460.5 : $T0_3$+11700.5	$11.9^{+0.8}_{-0.8}$	$1.92^{+0.04}_{-0.04}$	$3.68^{+0.03}_{-0.05}$	$0.61^{+0.12}_{-0.12}$	0.941 (387)
P15	$T0_3$+11700.5 : $T0_3$+11940.5	$12.1^{+0.8}_{-0.8}$	$1.97^{+0.04}_{-0.04}$	$3.64^{+0.06}_{-0.05}$	$0.44^{+0.12}_{-0.11}$	1.269 (382)
P16	$T0_3$+11940.5 : $T0_3$+12150.5	$9.6^{+0.5}_{-0.5}$	$1.89^{+0.04}_{-0.04}$	$3.49^{+0.05}_{-0.04}$	$0.51^{+0.11}_{-0.10}$	1.241 (363)
P17	$T0_3$+28789.5 : $T0_3$+29419.5	$8.3^{+0.3}_{-0.3}$	$0.75^{+0.01}_{-0.01}$	$1.27^{+0.01}_{-0.02}$	$0.22^{+0.07}_{-0.07}$	1.115 (376)
P18	$T0_3$+29419.5 : $T0_3$+30079.5	$7.0^{+0.3}_{-0.3}$	$0.70^{+0.01}_{-0.01}$	$1.19^{+0.01}_{-0.02}$	$0.36^{+0.07}_{-0.06}$	1.270 (363)
P19	$T0_3$+30079.5 : $T0_3$+30759.5	$7.8^{+0.3}_{-0.3}$	$0.68^{+0.01}_{-0.01}$	$1.15^{+0.02}_{-0.01}$	$0.24^{+0.07}_{-0.07}$	1.111 (372)
P20	$T0_3$+57685.5 : $T0_3$+58674.5	$4.2^{+0.2}_{-0.2}$	$0.162^{+0.004}_{-0.004}$	$0.215^{+0.004}_{-0.004}$	$0.14^{+0.07}_{-0.07}$	1.284 (203)
P21	$T0_3$+62964.5 : $T0_3$+63964.5	$4.0^{+0.2}_{-0.2}$	$0.132^{+0.004}_{-0.004}$	$0.182^{+0.005}_{-0.004}$	$0.31^{+0.08}_{-0.08}$	1.003 (177)
P22	$T0_3$+68742.5 : $T0_3$+75392.5	$3.8^{+0.2}_{-0.2}$	$0.076^{+0.002}_{-0.002}$	$0.098^{+0.002}_{-0.001}$	$0.18^{+0.06}_{-0.06}$	1.102 (196)
P23	$T0_3$+81037.5 : $T0_3$+91997.5	$3.2^{+0.1}_{-0.1}$	$0.091^{+0.001}_{-0.002}$	$0.098^{+0.002}_{-0.002}$	$0.00^{+0.03}_{-0.00}$	1.190 (200)
P24	$T0_3$+104574.5 : $T0_3$+110012.5	$3.3^{+0.2}_{-0.2}$	$0.043^{+0.002}_{-0.002}$	$0.052^{+0.001}_{-0.002}$	$0.18^{+0.09}_{-0.08}$	1.057 (118)
P25	$T0_3$+489136.5 : $T0_3$+495856.5	$1.9^{+0.2}_{-0.2}$	$0.014^{+0.001}_{-0.001}$	$0.012^{+0.001}_{-0.001}$	$0.05^{+0.06}_{-0.05}$	1.697 (40)

Notes. All the errors shown in this table are in 68% confidence interval.

parameters of the flare FSZ is shown in Fig. 6.4 and are given in Table 6.1. The abundances, temperature, and corresponding emission measure were found to vary during the flare FSZ. The peak values of abundances were derived to be 0.72±0.15 $Z_\odot$ which was ∼4 times more than that at the end of the flare. This value is also more than that of the other RS CVn type binaries as observed by Pandey & Singh (2012), indicating a higher amount of evaporation of the chromospheric plasma into the flaring loop.

The temperature was peaked at a value of 17.6±1.3 keV for the flare FSZ, which was ∼5.3 times more to that derived for end phase of the flare. The derived value of maximum temperature for the flare FSZ is quite high from previously observed maximum flare temperature on other RS CVn type binaries (Pandey & Singh, 2012), but this value is of the similar order to those of the superflares detected on CC Eri (Karmakar et al., 2017), EV Lac (≈150 MK and ≈142 MK; Favata et al., 2000; Osten et al., 2010), II Peg (≈300 MK; Osten et al., 2007), and AB Dor (≈114 MK; Maggio et al., 2000).

The EM followed the flare light curves and peaked at a value of 2.53±0.05 $\times 10^{54}$ cm^{-3} for the flare FSZ, which was ∼59 times more than the minimum value observed at the end of the flare. However, this value is within the range of earlier observed EM on RS CVn type stars (Pandey & Singh, 2012). The peak X-ray luminosity in 0.3–10 keV energy band during the flare was derived to be 4.79±0.05$\times 10^{33}$ erg s^{-1}, which was ∼92 times more luminous than that of the post flare phase. This value of the luminosity is larger than the earlier observed normal flares on late-type dwarfs and RS CVn binaries (Pandey & Singh, 2008, 2012). This is also one order greater than that of the observed superflares (see Favata et al., 2000; Karmakar et al., 2017; Maggio et al., 2000; Osten et al., 2007, 2010). However, the luminosity is found to be comparable with the large flares generally observed in PMS stars (Getman et al., 2008b). From Fig. 6.1, it is evident that the metal abundance and luminosity both found to vary along the flare light curves and they peak after the temperature peak, which is consistent with the idea of the hydrodynamic model (as discussed in detail in Chapter 5). This indicates the coherent plasma evolution and the heating causes the evaporation of the chromospheric gas and increase the metal abundances in the flaring loop.

6.3 Loop length of the flaring event

The loop length of the flare FSZ was determined using the hydrodynamic model as described in section 1.3.4.4, where $T_{\rm max}$ and $F(\zeta)$ are calibrated for spectral response of *Swift* XRT by Osten et al. (2010) and given in equations 5.2. As mentioned earlier, currently, for the stellar flares an evolution of density along the flare is not possible as one require time resolved high resolution X-ray spectra with good signal-to-noise ratio. Therefore, $\sqrt{EM}$ was chosen as a proxy of the density. Fig. 6.5 shows the path log $\sqrt{EM}$ versus log T for the flare FSZ. A linear fit to the data provided the slope ζ of 0.741 ± 0.014, indicating the presence of sustained heating during the decay phase of the flare FSZ. The maximum temperature at loop-apex was derived from the observed temperature using equation 5.1. The $T_{\rm max}$ was derived to be 567±48 MK. The loop length of the flare FSZ was derived to be 7.3±0.3$\times 10^{11}$ cm. The derived loop length is found to be similar to that of the other RS CVn binaries (see Pandey & Singh, 2012). Assuming a semi-circular geometry, the flaring loop height (L/π) was estimated to be 2.9 times of the stellar radius (R$_*$) of the primary component of SZ Psc. The derived parameters of the flaring loop are given in Table 6.2. The loop lengths are usually more than the loop lengths derived for other G–K dwarfs

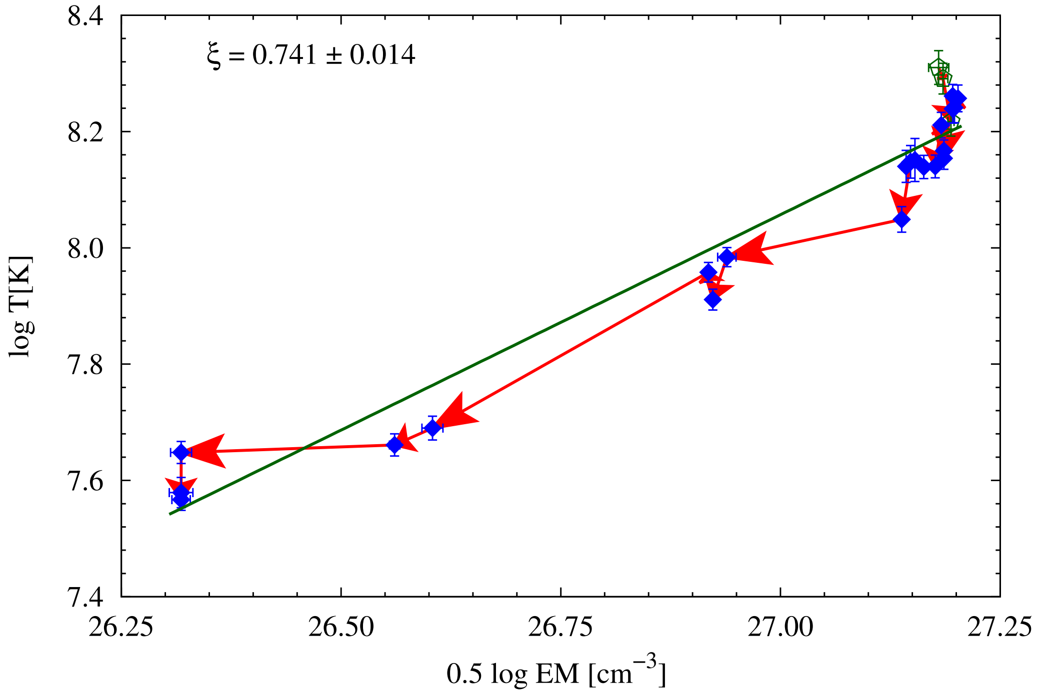

Figure 6.5: Evolution of the flare in log $\sqrt{\mathrm{EM}}$ – log T plane. The continuous line shows the best-fit during the decay phase of the flares with a slope ζ shown in top left corner.

and dMe (see Chapter 4 and 5, e.g. Favata & Micela, 2003; Pandey & Singh, 2008), but are in between for other RS CVn-type binaries (Pandey & Singh, 2012).

6.4 Properties of coronal loop

The primary component of SZ PSc is more active; therefore, can be safely assumed that the flare had happened in the primary. The peak X-ray luminosity of flare FSZ was then found to be 69% of bolometric luminosity (L_{bol}) of the primary, whereas the peak luminosity was found to be 58% of L_{bol} SZ Psc system. These values are larger than that of the earlier reported flares on RS CVn binaries (Pandey & Singh, 2012), however this is similar to that of the observed superflares (Favata et al., 2000; Karmakar et al., 2017; Maggio et al., 2000; Pan et al., 1997). The derived loop length of the flare FSZ was much smaller than the pressure scale height ($\geq 3.5 \times 10^{12}$ cm for primary); therefore, we can assume that the flaring loop to be not far from a steady state condition. We have applied the RTV scaling laws (Rosner et al., 1978) to determine the maximum pressure in the loop at the flare peak and

Table 6.2: Post loop modeling parameters

Parameters	Units	Flare FSZ
$\tau_{\rm R}$	(ks)	12.5 ± 0.4
$\tau_{\rm D}$	(ks)	19.9 ± 0.1
$L_{\rm X,max}$	(10^{33} erg s^{-1})	4.79 ± 0.05
ζ	–	0.741 ± 0.014
$T_{\rm max}$	(10^{8} K)	5.67 ± 0.48
L	(10^{11} cm)	7.3 ± 0.3
Loop-Height	(10^{11} cm)	2.4 ± 0.1
p	(10^{4} dyn cm^{-2})	9.1 ± 2.7
$n_{\rm e}$	(10^{11} cm^{-3})	5.8 ± 2.2
$V_{\rm F}$	(10^{30} cm^{3})	$\sim$7.6
B	(kG)	1.51 ± 0.23
$E_{\rm H}$	(erg s^{-1} cm^{-3})	$\sim$8
H	(10^{31} erg s^{-1})	$\sim$6.10
$E_{\rm X,tot}$	(10^{36} erg)	$>$1.98
$B_{\rm tot}$	(kG)	$>$2.98

The symbols has similar meaning as Table 5.5 of Chapter 5.

found to be $\sim$9.1$\times$10^{4} dyne cm^{-2} for the flare FSZ. We have derived the plasma density, the flaring volume, and the minimum magnetic field using equation 4.1.5. We have estimated the values of n_e, V and B for the flare FSZ as 5.8$\pm$2.2$\times$10^{11} cm^{-3}, 7.6$\times$10^{30} cm^{3}, and $\sim$1.5 kG, respectively. Using the scaling laws of Rosner et al. (1978), we have also estimated the heating rate per unit volume at the peak of the flare as $\simeq$8 erg cm^{-3} s^{-1}. The total heating rate ($\frac{dH}{dt} \simeq \frac{dH}{dV dt} \times V$) at the peak of the flare was derived to be $\sim$6.1$\times$10^{31} erg s^{-1}, which was $\sim$1.4 times more than the flare maximum X-ray luminosity. The heating rate during the flare FSZ was also found to be only $\sim$1% of the bolometric luminosity of the SZ Psc system. If the heating mechanism is responsible, the present flare are essentially due to some form of dissipation of magnetic energy. Assuming the constant heating rate throughout the decay phase of the flare, the total energy radiated during the flare was derived to be $\sim$29 s of bolometric energy output of the primary component of SZ Psc. This value is ten times larger than the normal flare on 47 Cas as discussed in Chapter 4, but less than both the superflares on CC Eri as discussed in Chapter 5. The magnetic field strength that would be required to accumulate the emitted energy and to keep the plasma confined in a stable magnetic loop configuration can be estimated under the assumptions that the energy release is indeed of magnetic origin. The total non-potential magnetic field B_0 involved in a flare energy release within an active region of the star can be estimated using the equation 4.5. The value of B_0 was estimated to be >2.98 kG for flare FSZ assuming the loop geometry does not change during the flare. This value is less than or comparable to that of the superflares observed on CC Eri as discussed in Chapter 5, but much greater than that of the normal flare as discussed in Chapter 4. However, this values are much larger than the derived magnetic fields on other RS CVn stars (Pandey & Singh, 2012).

6.5 Conclusions

In the present multi-band study of RS CVn type eclipsing binary, we have found that the flaring event is out of the eclipse. However, most of the flare parameters derived in this work are found to be at or beyond the extremum values, which makes this event very interesting. The peak X-ray luminosity was derived to be $\sim 10^{33.6}$ erg s^{-1} in 0.3–50 keV energy band, which are larger than any other flares previously observed on SZ PSc, and other RS CVn flares, thus far (to the best of our knowledge). The time-resolved spectral analysis during the flare shows the variation in the coronal temperature, EM, and abundances. Temperature shows earlier peak than EM and abundance. The peak elemental abundances are found to be $\sim 0.72 Z_\odot$, which is ~ 4 times than that of the minimum observed values at the end of the flare. The peak observed flare temperature was derived to be ~ 204 MK. Using the hydrodynamic loop modeling, we derive flaring loop lengths of $7.3 \pm 0.3 \times 10^{11}$ cm. The heating rate during the flare is found to be 1% of the bolometric luminosity of the SZ Psc system. The evolved RS CVn binary SZ Psc shows more magnetically active than the MS stars, discussed in earlier chapters, possibly due to their tidally locked binary nature and extended corona.

Chapter 7

Summary, Conclusion and Future Prospects

7.1 Summary

In this thesis, we have investigated the evolution of various magnetic activities on five late-type stars, which is expected to have a similar internal structure to that of the Sun. According to the current stellar magnetic dynamo theory, the magnetic field in these stars are generated in the outer convection zone due to the convective motion of the plasma, which is further amplified due to the strong shear at the tachocline. This magnetic dynamo theory is developed on the basis of the Sun, and it is now *state-of-the-art* and explains most of the observed phenomena at its best. However, the current observational evidences shows a range of magnetic activities which is not well explained by this dynamo theory. Therefore, it was very necessary to provide more observational evidences, which can constrain the present magnetic dynamo theory. In order to do that, in this thesis, we have set few objectives for our investigations (as discussed in §1.5). In the light of our objectives and the obtained results, the pointwise summary of this thesis is given below.

- A young, single, and MS UFR LO Peg is investigated in Chapter 3 with the aims to study the star-spot cycles, SDR, optical flares, evolution of star-spot distributions, and coronal activities. We have used a wealth of ∼24 yr multi-band data in our study. From the long-term V-band photometry, a rotational period of LO Peg is derived to be 0.4231 ± 0.0001 d. Using the seasonal variations on the rotational period, the SDR pattern is investigated, and shows a solar-like pattern of SDR. A cyclic pattern with period of ∼2.7 yr appears to be present in rotational period variation. During the observations, 20 optical flares are detected with a flare frequency of ∼1 flare per two days and with flare energy of $\sim 10^{31-34}$ erg. The surface coverage of cool spots is found to be in the range of ∼9–26 per cent. It appears that the high- and low-latitude spots are interchanging their positions. Quasi-simultaneous observations in X-ray, UV, and optical photometric bands show a signature of an excess of X-ray and UV activities in spotted regions. No correlation was found between the latitudinal position of spots and the flares.

- In Chapter 4, we moved to study the transient coronal magnetic activities on two active late-type MS stars. We have used *XMM-Newton* observations to investigate flare properties from a very active and poorly known stellar system 47 Cas and an fairly known system AB Dor. In case of 47 Cas, the luminosity at the peak of the flare was found to be $10^{30.55}$ erg s^{-1}, which is ∼ 2 times more than that at quiescent state. The quiescent state corona of 47 Cas was represented by two temperature plasma: 3.7 and 11.0 MK. The time-resolved X-ray spectroscopy of the flare showed the variable nature of the temperature, the emission measure, and the abundance. The maximum temperature during the flare was found to be 72.8 MK. We inferred the length of a flaring loop to be 3.3×10^{10} cm using a hydrodynamic loop model. Using the RGS spectra, the density during the flare was found to be 4.0×10^{10} cm^{-3}. Using ∼11 years *XMM-Newton* data, a flare morphology is studied in a young, main-sequence, ultra-fast rotator AB Dor. During the observations ∼140 X-ray flares were detected to be significant above the 3σ level. Flare frequency is derived to be ∼4 flares per rotation (or ∼2 flares per solar day). Based on the light curve morphology, we have classified the flares on AB Dor into five category namely typical, double, multiple, complex and slow-rise-top-flat flares. The rise and decay times of the flares are correlated with each other in the form of $\tau_d \propto \tau_r^{0.78\pm0.05}$, which is slight different from the theoretically obtained relation of $\tau_d \propto \tau_r^{0.5}$ with the assumption that the decay time equals to radiative cooling time.

- After the investigations on normal flares from MS stars, in Chapter 5, we moved to study two superflares detected on an active binary star CC Eri by the *Swift* observatory. These superflares are the brightest, hottest, and shortest in duration observed thus far on this star. It has been found that the flares decay faster in the hard X-ray band than in the soft X-ray band. Both flares are highly energetic with respective peak X-ray luminosities of $\sim 10^{32.2}$ and $\sim 10^{31.8}$ erg s^{-1} in 0.3–50 keV energy band, which are larger than any other flares previously observed on CC Eri. The time-resolved spectral analysis during the flares shows the variation in the coronal temperature, emission measure, and abundances. The elemental abundances are enhanced by a factor of ∼8 to the minimum observed in the post-flare phase of one of the flare. The observed peak temperatures in these two flares are found to be 174 MK and 128 MK. Using the hydrodynamic loop modeling, we derive loop lengths for both the flares as $1.2 \pm 0.1 \times 10^{10}$ cm and $2.2 \pm 0.6 \times 10^{10}$ cm. The Fe Kα emission at 6.4 keV is also detected in the X-ray spectra and we model the Kα emission feature as fluorescence from the hot flare source irradiating the photospheric iron.

- The study of Chapter 6 is quite interesting due to investigation of a large flaring activity on an evolved RS CVn type eclipsing binary system SZ Psc. This observations was also carried out by *Swift* observatory. The flare was simultaneously observed with BAT, XRT, and UVOT. The peak X-ray luminosity for flare in the 0.3–10 keV energy band was reached up to a value of $10^{33.6}$ erg s^{-1}. Spectral analysis indicates a presence of single temperature corona. The flare-temperature peaked at 204 MK which is one of the highest temperature observed on RS CVn type binaries. The abundances during the flare were subsolar and found to decrease during flare decay. Using hydrodynamic loop modeling, we derive loop-lengths of 7.3 $\times 10^{11}$ cm.

7.2 Conclusions

The magnetic activities of the late-type stars, investigated in this thesis, shows very interesting properties. Some of which supports the present existing dynamo theory, but few of them are against it. Both of them are very useful in order to constrain the existing theory. We have derived the surface coverage of LO Peg to be 9–26%. This value is quiet high comparing to the solar surface coverage of ∼0.5%. However, several other late-type stars also show this much of surface coverage (see Savanov, 2014, and references therin). We have also found flip-flop cycle which supports the earlier observations and the theory. A positive correlation between the absolute value of SDR and the stellar rotation period was predicted by dynamo models according to a power law. After the inclusion of LO Peg, the power law index is now modified to 1.4 ± 0.1 from the existing earlier value 1.4 ± 0.5 (Messina & Guinan, 2003). Both of this value contradicts with the theoretical power law index of >2. This suggests a consideration from the theoretical aspect is necessary.

A total of 164 flares including 20 optical flares and 144 X-ray flares are studied in this thesis. In general, the flares show an exponential increase in brightness followed by a gradual decay (see Hawley et al., 2014; Reale et al., 1997, and references therin). However, we have found all the X-ray flares does not show the same morphology (see Chapter 4 for more details). The presence of the multiple peaks might be due to several different flares at spatially different location on the stars, or they are from a single flare having multiple cascades. Further investigations from the aspect of spectral analysis may reveal the actual situation. We have also found some heighten emission pre- or post-flare apart from the main flares (as the 'U' part in case of the flare from 47 Cas; see Chapter 4), which is suspected to be due to micro-/nano-flares occurring in the stars.

Surprisingly, the derived loop-lengths for both the superflares of CC Eri, are found to be smaller than the derived loop-length of a normal flare observed in 47 Cas. The very large luminosity of the superflares than the normal flares could be due to the high density and high coronal magnetic field of the flaring loops of the CC Eri. From the earlier literature we found that CC Eri has a large surface magnetic field. But the transportation of such large amount of magnetic field from the stellar surface to the corona is still not very clear, and it is still a open question for the dynamo theoretician which is needed to be answered.

We have further investigated the flaring activities on an evolved RS CVn binary star. In this case, we found that the flaring loop-length are ∼100 times more than the loop-length of the normal stars. However, the derived loop length is found to be within the range of the RS CVn stars as derived by Pandey & Singh (2012). The density of the flaring loop was derived to be 10 times higher than the normal flares observed in 47 Cas, and 10–100 times lower than the superflares on CC Eri. However, magnetic field is found of the similar order for the superflare, which is also 10 times greater than the magnetic field observed on other RS CVn stars. The high magnetic activities in evolved RS CVn binaries could be due to their extended convection zone and tidal locking of binary components, which makes them rotate fast.

In a nutshell, we found that the magnetic activities in late-type stars change with time and the evolved stars show high level of magnetic activitiy than MS stars, *possibly due to their binarity and extended corona.*

7.3 Future perspectives

The research is nothing but to explore some *beautifully strange* and *strangely beautiful* ideas of the universe. We always becomes excited to expore the new problems and try to solve it drop-by-drop. In the journey of my PhD, while I found some new ideas to explore, still there are scopes in few areas which need to explore further, and I want proceed in those directions in recent future. My future plans are enumerated below.

1. Superflares on CC Eri, indicate the large magnetic fields at the coronal height, which is very exciting to investigate further. We have observed this object in multi-band with the latest indian facility *ASTROSAT* in 2016 October-March Cycle (PI: Karmakar). Just after completion of my PhD, I would like to analyse this new data from *ASTROSAT*.

2. The magnetic activity at fainter limit (fainter than 15 mag) of cool stars are not studied in detail thus far. Therefore, we would like to observe few low mass stars from the newly installed 3.6-m Devasthal Optical Telescope, ARIES, in order to study surface inhomogeneities and flares.

3. The inhomogeneity due to magnetic areas on the surface of the late-type stars produce a broad-band linear polarization (BLP). We have found that BLP is dependent on various magnetic activity parameters (Patel et al., 2013) for G–K dwarfs. Therefore, making use of AIMPOL mounted on 1.04-m ARIES ST, we would like to do similar study for evolved RS CVn binaries.

4. A detailed spectral analysis of 140 flares from AB Dor will be carried out in near future.

5. During my PhD, I have worked on an F-type star KIC 6791060 using the high cadence *Kepler* data, which is not included in this thesis. I would like to continue to work on this object, as well as like to start different project using the observations obtained from *Kepler*.

6. I like to continue the X-ray studies of late-type stars with *ASTROSAT*, *Swift*, *XMM-Newton*, *Chandra* NuStar, and other X-ray observatories.

References

Agrawal P. C., Rao A. R., Riegler G. R., 1986, MNRAS, 219, 777 9

Alekseev I. Y., 2003, Astronomy Reports, 47, 430 85, 87

Amado P. J., Doyle J. G., Byrne P. B., et al., 2000, A&A, 359, 159 119, 138

Anders E., Grevesse N., 1989, Geochim. Cosmochim. Acta, 53, 197 60, 95, 123

Antonopoulou E., Deliyannis J., Mitrou C. K., 1995, Information Bulletin on Variable Stars, 4262 141

Arnaud K. A., 1996, in Astronomical Data Analysis Software and Systems V, edited by G. H. Jacoby, J. Barnes, vol. 101 of Astronomical Society of the Pacific Conference Series, 17 59, 95

Aschwanden M. J., Stern R. A., Güdel M., 2008, ApJ, 672, 659 102

Ayres T. R., Osten R. A., Brown A., 2001, ApJ, 562, L83 95

Babcock H. W., 1961, ApJ, 133, 572 7

Bai T., 1979, Sol. Phys., 62, 113 26, 134, 138

Baliunas S., Soon W., 1995, ApJ, 450, 896 16

Baliunas S. L., Vaughan A. H., 1985, ARA&A, 23, 379 16

Barnes J. R., Collier Cameron A., Lister T. A., Pointer G. R., Still M. D., 2005, MNRAS, 356, 1501 65, 66, 70, 72, 80

Barthelmy S. D., Barbier L. M., Cummings J. R., et al., 2005, Space Sci. Rev., 120, 143 47, 57

Barthelmy S. D., Baumgartner W. H., Chester M. M., et al., 2012, GRB Coordinates Network, 12985 119

Benz A., ed., 2002, Plasma Astrophysics, second edition, vol. 279 of Astrophysics and Space Science Library 18

Berdyugina S. V., 2005, Living Reviews in Solar Physics, 2, 8 11

Berdyugina S. V., Pelt J., Tuominen I., 2002, A&A, 394, 505 72, 87

Berdyugina S. V., Usoskin I. G., 2003, A&A, 405, 1121 85

Bessell M. S., 1979, PASP, 91, 589 74

Bhatt H., Pandey J. C., Singh K. P., Sagar R., Kumar B., 2014, Journal of Astrophysics and Astronomy, 35, 39 25, 102

Bopp B. W., Evans D. S., 1973, MNRAS, 164, 343 29, 120, 137

Bopp B. W., Fekel Jr. F., 1977, AJ, 82, 490 29

Bopp B. W., Noah P., Klimke A., Hall D. S., Henry G. W., 1981, PASP, 93, 504 30

Brandenburg A., Subramanian K., 2005, Phys. Rep., 417, 1 8

Browning M. K., 2008, ApJ, 676, 1262 8

Browning M. K., Basri G., Marcy G. W., West A. A., Zhang J., 2010, AJ, 139, 504 8

Burrows D. N., Hill J. E., Nousek J. A., et al., 2005, Space Sci. Rev., 120, 165 47

Busko I. C., Quast G. R., Torres C. A. O., 1977, A&A, 60, L27 119

Caillault J.-P., Drake S., Florkowski D., 1988, AJ, 95, 887 119, 135

Candelaresi S., Hillier A., Maehara H., Brandenburg A., Shibata K., 2014, ApJ, 792, 67 79

Cargill P. J., Klimchuk J. A., 2004, ApJ, 605, 911 137

Carroll B. W., Ostlie D. A., 2006, An introduction to modern astrophysics and cosmology 7

Catalano S., Frisina A., Rodono M., Scaltriti F., 1978, Information Bulletin on Variable Stars, 1427 141

Catalano S., Lanzafame A., Pagano I., Rodono M., 1999, Mem. Soc. Astron. Italiana, 70, 463 14

Chabrier G., Küker M., 2006, A&A, 446, 1027 8

Charbonneau P., 2005, Living Reviews in Solar Physics, 2, 2 6, 8

Close L. M., Guirado J., Nielsen E., et al., 2005, in Protostars and Planets V Posters, vol. 1286, 8081 105

Close L. M., Thatte N., Nielsen E. L., Abuter R., Clarke F., Tecza M., 2007, ApJ, 665, 736 104, 105

Collier Cameron A., Donati J.-F., 2002a, MNRAS, 329, L23 16

Collier Cameron A., Donati J.-F., 2002b, MNRAS, 329, L23 69, 71, 72, 73

Collier Cameron A., Foing B. H., 1997, The Observatory, 117, 218 105

Covino S., Panzera M. R., Tagliaferri G., Pallavicini R., 2001, A&A, 371, 973 25, 102

Crespo-Chacón I., Micela G., Reale F., Caramazza M., López-Santiago J., Pillitteri I., 2007, A&A, 471, 929 95, 119, 124, 135, 136, 137, 138

Csorvási R., 2006, Publications of the Astronomy Department of the Eotvos Lorand University, 17, 95 65

Dal H. A., Sipahi E., Özdarcan O., 2012, PASA, 29, 54 77

Dal H. A., Taş G., 2003, Information Bulletin on Variable Stars, 5390 65

Das H. K., Menon S. M., Paranjpye A., Tandon S. N., 1999, Bulletin of the Astronomical Society of India, 27, 609 33

Davenport J. R. A., Hawley S. L., Hebb L., et al., 2014, ApJ, 797, 122 74, 77

D'Elia V., de Pasquale M., Evans P. A., et al., 2015, GRB Coordinates Network, 17303 142

Deng L. H., Li B., Xiang Y. Y., Dun G. T., 2016, AJ, 151, 2 2

Dere K. P., Landi E., Mason H. E., Monsignori Fossi B. C., Young P. R., 1997, A&AS, 125 99

Dhillon V. S., Privett G. J., Duffey K. P., 2001, Starlink User Note, 167 66

Dickey J. M., Lockman F. J., 1990, ARA&A, 28, 215 96, 123, 145

Donahue R. A., Dobson A. K., 1996, in Cool Stars, Stellar Systems, and the Sun, edited by R. Pallavicini, A. K. Dupree, vol. 109 of Astronomical Society of the Pacific Conference Series, 599 16, 73, 74

Donati J.-F., Mengel M., Carter B. D., Marsden S., Collier Cameron A., Wichmann R., 2000, MNRAS, 316, 699 16

Dorren J. D., Guinan E. F., 1990, ApJ, 348, 703 14

Doyle J. G., Mitrou C. K., Mathioudakis M., Antonopoulou E., 1994, A&A, 283, 522 141

Drake J. J., Ercolano B., Swartz D. A., 2008, ApJ, 678, 385 27, 134, 135, 138

Drake J. J., Laming J. M., Widing K. G., 1997, ApJ, 478, 403 62

Drake S. A., Osten R. A., Krimm H., De Pasquale M., Gehrels N., Barthelmy S., 2015, The Astronomer's Telegram, 6940 142

Drake S. A., Simon T., Linsky J. L., 1989, ApJS, 71, 905 11

Drake S. A., Simon T., Linsky J. L., 1992, ApJS, 82, 311 11

Durney B. R., De Young D. S., Roxburgh I. W., 1993, Sol. Phys., 145, 207 8

Eaton J. A., Hall D. S., 1979, ApJ, 227, 907 141

Eaton J. A., Henry G. W., 2007, PASP, 119, 259 141, 144

Eaton J. A., Scaltriti F., Cerruti-Sola M., et al., 1982, Ap&SS, 82, 289 141

Eibe M. T., Byrne P. B., Jeffries R. D., Gunn A. G., 1999, A&A, 341, 527 65

Elstner D., 2005, in The Magnetized Plasma in Galaxy Evolution, edited by K. T. Chyzy, K. Otmianowska-Mazur, M. Soida, R.-J. Dettmar, 117–124 85

Ercolano B., Drake J. J., Reale F., Testa P., Miller J. M., 2008, ApJ, 688, 1315 26, 138

Evans D. S., 1959, MNRAS, 119, 526 119

Evans P. A., Page K. L., Beardmore A. P., et al., 2008, The Astronomer's Telegram, 1787 119, 120, 124

Evren S., 1990, in NATO Advanced Science Institutes (ASI) Series C, vol. 319 of NATO Advanced Science Institutes (ASI) Series C, 561 14

Favata F., Micela G., 2003, Space Sci. Rev., 108, 577 137, 149

Favata F., Micela G., Reale F., 2001, A&A, 375, 485 25, 102

Favata F., Reale F., Micela G., Sciortino S., Maggio A., Matsumoto H., 2000, A&A, 353, 987 17, 21, 97, 135, 136, 147, 148, 149

Favata F., Schmitt J. H. M. M., 1999, A&A, 350, 900 17, 135, 136

Fender R., Stewart A., Macquart J. P., et al., 2015, Advancing Astrophysics with the Square Kilometre Array (AASKA14), 51 17, 135

Fleming T. A., Gioia I. M., Maccacaro T., 1989, ApJ, 340, 1011 9

Fleming T. A., Liebert J., Gioia I. M., Maccacaro T., 1988, ApJ, 331, 958 9

Fluri D. M., Berdyugina S. V., 2004, Sol. Phys., 224, 153 85

Foukal P., 1993, Sol. Phys., 148, 219 28

Foukal P., Lean J., 1986, ApJ, 302, 826 28

Franciosini E., Pallavicini R., Tagliaferri G., 2001, A&A, 375, 196 17, 135

Gabriel A. H., Jordan C., 1969, Nature, 221, 947 27, 98

García-Alvarez D., Drake J. J., Kashyap V. L., Lin L., Ball B., 2008, ApJ, 679, 1509 105

Garner H. L., Etzel P. B., 1998, in American Astronomical Society Meeting Abstracts #192, vol. 30 of Bulletin of the American Astronomical Society, 834 93

Gáspár A., Rieke G. H., Balog Z., 2013, ApJ, 768, 25 31, 119

Gehrels N., Chincarini G., Giommi P., et al., 2004, ApJ, 611, 1005 47

Getman K. V., Feigelson E. D., Broos P. S., Micela G., Garmire G. P., 2008a, ApJ, 688, 418 110

Getman K. V., Feigelson E. D., Micela G., Jardine M. M., Gregory S. G., Garmire G. P., 2008b, ApJ, 688, 437 94, 148

Godet O., Beardmore A. P., Abbey A. F., et al., 2009, A&A, 494, 775 60

Golovin A., Gálvez-Ortiz M. C., Hernán-Obispo M., et al., 2012, MNRAS, 421, 132 77, 79

Gondoin P., 2008, A&A, 478, 883 28

Graffagnino V. G., Wonnacott D., Schaeidt S., 1995, MNRAS, 275, 129 138

Gray D. F., Baliunas S. L., 1997, ApJ, 475, 303 73

Gray M. D., Bewley S. L., 2003, MNRAS, 344, 439 65

Güdel M., 1992, A&A, 264, L31 11

Güdel M., Audard M., Briggs K., et al., 2001, A&A, 365, L336 79, 105

Güdel M., Guinan E. F., Etzel P. B., Mewe R., Kaastra J. S., Skinner S. L., 1998, in Cool Stars, Stellar Systems, and the Sun, edited by R. A. Donahue, J. A. Bookbinder, vol. 154 of Astronomical Society of the Pacific Conference Series, 1247 93, 102

Güdel M., Linsky J. L., Brown A., Nagase F., 1999, ApJ, 511, 405 24

Güdel M., Schmitt J. H. M. M., Benz A. O., 1995, A&A, 293 93

Gudel M., Schmitt J. H. M. M., Bookbinder J. A., Fleming T. A., 1993, ApJ, 415, 236 11

Guinan E. F., Dorren J. D., 1992, in American Astronomical Society Meeting Abstracts, vol. 24 of Bulletin of the American Astronomical Society, 1205 14

Guirado J. C., Marcaide J. M., Martí-Vidal I., et al., 2011, A&A, 533, A106 31, 105

Guirado J. C., Reynolds J. E., Lestrade J.-F., et al., 1997, ApJ, 490, 835 104

Haisch B. M., 1983, in IAU Colloq. 71: Activity in Red-Dwarf Stars, edited by P. B. Byrne, M. Rodono, vol. 102 of Astrophysics and Space Science Library, 255–268 22, 25, 101

Hale G. E., 1908, ApJ, 28, 315 14

Hall D. S., 1976, in IAU Colloq. 29: Multiple Periodic Variable Stars, edited by W. S. Fitch, vol. 60 of Astrophysics and Space Science Library, 287 12, 29

Hall D. S., 1990, in NATO Advanced Science Institutes (ASI) Series C, vol. 319 of NATO Advanced Science Institutes (ASI) Series C, 95 14

Hall D. S., 1991, in IAU Colloq. 130: The Sun and Cool Stars. Activity, Magnetism, Dynamos, edited by I. Tuominen, D. Moss, G. Rüdiger, vol. 380 of Lecture Notes in Physics, Berlin Springer Verlag, 353 73

Hannah I. G., Christe S., Krucker S., Hurford G. J., Hudson H. S., Lin R. P., 2008, ApJ, 677, 704 2

Hawley S. L., Davenport J. R. A., Kowalski A. F., et al., 2014, ApJ, 797, 121 74, 77, 79, 156

Hawley S. L., Fisher G. H., Simon T., et al., 1995, ApJ, 453, 464 102

Henry G. W., Fekel F. C., Hall D. S., 1995, AJ, 110, 2926 14, 73

Horne J. H., Baliunas S. L., 1986, ApJ, 302, 757 66, 70

Howell S. B., Warnock III A., Mitchell K. J., 1988, AJ, 95, 247 42

Hunt-Walker N. M., Hilton E. J., Kowalski A. F., Hawley S. L., Matthews J. M., 2012, PASP, 124, 545 87

Hussain G. A. J., Jardine M., Donati J.-F., et al., 2007, MNRAS, 377, 1488 105

Ibanoglu C., 1990, in NATO Advanced Science Institutes (ASI) Series C, vol. 319 of NATO Advanced Science Institutes (ASI) Series C, 515 14

Isobe H., Yokoyama T., Shimojo M., et al., 2002, ApJ, 566, 528 117

Jakate S., Bakos G. A., Fernie J. D., Heard J. F., 1976, AJ, 81, 250 141

Jansen F., Lumb D., Altieri B., et al., 2001, A&A, 365, L1 44, 56

Järvinen S. P., Berdyugina S. V., Strassmeier K. G., 2005a, A&A, 440, 735 13, 85

Järvinen S. P., Berdyugina S. V., Tuominen I., Cutispoto G., Bos M., 2005b, A&A, 432, 657 14, 69, 87

Jeffries R. D., Byrne P. B., Doyle J. G., Anders G. J., James D. J., Lanzafame A. C., 1994, MNRAS, 270, 153 33, 37, 38, 65

Jeffries R. D., Jewell S. J., 1993, MNRAS, 264, 106 65

Jetsu L., Pelt J., Tuominen I., Nations H., 1991, in IAU Colloq. 130: The Sun and Cool Stars. Activity, Magnetism, Dynamos, edited by I. Tuominen, D. Moss, G. Rüdiger, vol. 380 of Lecture Notes in Physics, Berlin Springer Verlag, 381 85

Kane S. R., Hurley K., McTiernan J. M., Sommer M., Boer M., Niel M., 1995, ApJ, 446, L47 2

Kane S. R., McTiernan J. M., Hurley K., 2005, A&A, 433, 1133 2

Kang Y. W., Lee W.-B., Kim H.-i., Oh K.-D., 2003, MNRAS, 344, 1227 141, 144

Karmakar S., Pandey J. C., Airapetian V. S., Misra K., 2017, ApJ, 840, 102 119, 147, 148, 149

Karmakar S., Pandey J. C., Savanov I. S., et al., 2016, MNRAS, 459, 3112 65

Karoff C., Campante T. L., Ballot J., et al., 2013, ApJ, 767, 34 29

Kharchenko N. V., Scholz R.-D., Piskunov A. E., Roeser S., Schilbach E., 2007, VizieR Online Data Catalog, 3254 141

Kitchatinov L. L., Rüdiger G., 1999, A&A, 344, 911 73, 74

Kopp R. A., Pneuman G. W., 1976, Sol. Phys., 50, 85 20

Kopp R. A., Poletto G., 1984, Mem. Soc. Astron. Italiana, 55, 737 24

Korhonen H., Berdyugina S. V., Tuominen I., 2002, A&A, 390, 179 85

Korhonen H., Elstner D., 2005, A&A, 440, 1161 85

Kosovichev A. G., Fedorova A. V., 1991, Soviet Ast., 35, 507 4

Kron G. E., 1947, PASP, 59, 261 12, 13

Kron G. E., 1950, Leaflet of the Astronomical Society of the Pacific, 6, 52 13

Kuerster M., Schmitt J. H. M. M., Cutispoto G., Dennerl K., 1997a, A&A, 320, 831 95

Kuerster M., Schmitt J. H. M. M., Cutispoto G., Dennerl K., 1997b, A&A, 320, 831 105

Kurucz R. L., 1992, in The Stellar Populations of Galaxies, edited by B. Barbuy, A. Renzini, vol. 149 of IAU Symposium, 225 80

Lalitha S., Fuhrmeister B., Wolter U., Schmitt J. H. M. M., Engels D., Wieringa M. H., 2013, A&A, 560, A69 77, 105

Landi E., Young P. R., Dere K. P., Del Zanna G., Mason H. E., 2013, ApJ, 763, 86 99

Landstreet J. D., 1992, A&A Rev., 4, 35 6

Lang K. R., 2009, The Sun From Space, Springer-Verlag xxxix, 21

Lanza A. F., Rodonò M., Mazzola L., Messina S., 2001, A&A, 376, 1011 141

Lanza A. F., Rodono M., Rosner R., 1998, MNRAS, 296, 893 14

Larmor J., 1919, in 87th Meeting of Report of the British Association for the Advancement of Science, London, 159–160‘ 6

Leighton R. B., 1964, ApJ, 140, 1547 7

Lister T. A., Collier Cameron A., Bartus J., 1999, MNRAS, 307, 685 65

Llama J., Jardine M., Mackay D. H., Fares R., 2012, MNRAS, 422, L72 28

López-Santiago J., Crespo-Chacón I., Micela G., Reale F., 2010, ApJ, 712, 78 31

Lurie J. C., Davenport J. R. A., Hawley S. L., et al., 2015, ApJ, 800, 95 74, 79

Maggio A., Pallavicini R., Reale F., Tagliaferri G., 2000, A&A, 356, 627 17, 97, 135, 136, 147, 148, 149

Masuda S., Kosugi T., Hara H., Sakao T., Shibata K., Tsuneta S., 1995, PASJ, 47, 677 20

Masuda S., Kosugi T., Hara H., Tsuneta S., Ogawara Y., 1994, Nature, 371, 495 20

Mathioudakis M., Mullan D. J., 1999, A&A, 342, 524 95

Messina S., Guinan E. F., 2003, A&A, 409, 1017 14, 69, 72, 73, 74, 156

Mitra-Kraev U., Harra L. K., 2005, in 13th Cambridge Workshop on Cool Stars, Stellar Systems and the Sun, edited by F. Favata, G. A. J. Hussain, B. Battrick, vol. 560 of ESA Special Publication, 821 24

Montes D., López-Santiago J., Gálvez M. C., Fernández-Figueroa M. J., De Castro E., Cornide M., 2001, MNRAS, 328, 45 65

Moretti A., Campana S., Mineo T., et al., 2005, in UV, X-Ray, and Gamma-Ray Space Instrumentation for Astronomy XIV, edited by O. H. W. Siegmund, vol. 5898 of Proc. SPIE, 360–368 60, 61

Morrison R., McCammon D., 1983, ApJ, 270, 119 60, 95

Mullan D. J., Mathioudakis M., Bloomfield D. S., Christian D. J., 2006, ApJS, 164, 173 22

Murdin P., 2001, Encyclopedia of astronomy and astrophysics xxxix, 19

Negoro H., Usui R., Yamazaki K., et al., 2011, The Astronomer's Telegram, 3737 141

Ness J.-U., Schmitt J. H. M. M., Audard M., Güdel M., Mewe R., 2003, A&A, 407, 347 xxxix, 26, 93, 98

Nordon R., Behar E., 2007, A&A, 464, 309 135, 136

Nordon R., Behar E., 2008, A&A, 482, 639 93, 97, 98, 119

Oláh K., Kolláth Z., Granzer T., et al., 2009, A&A, 501, 703 13

Osten R. A., Brown A., 1999, ApJ, 515, 746 144

Osten R. A., Brown A., Wood B. E., Brady P., 2002, ApJS, 138, 99 119

Osten R. A., Drake S., Tueller J., et al., 2007, ApJ, 654, 1052 17, 135, 136, 147, 148

Osten R. A., Godet O., Drake S., et al., 2010, ApJ, 721, 785 17, 130, 131, 135, 136, 147, 148

Osten R. A., Kowalski A., Drake S. A., et al., 2016, ApJ, 832, 174 135, 136

Osten R. A., Kowalski A., Sahu K., Hawley S. L., 2012, ApJ, 754, 4 74

Pakull M. W., 1981, A&A, 104, 33 105

Pallavicini R., Golub L., Rosner R., Vaiana G. S., Ayres T., Linsky J. L., 1981, ApJ, 248, 279 8

Pallavicini R., Monsignori-Fossi B. C., Landini M., Schmitt J. H. M. M., 1988, A&A, 191, 109 119, 135

Pallavicini R., Tagliaferri G., Stella L., 1990, A&A, 228, 403 9, 18, 25, 94

Pan H. C., Jordan C., 1995, MNRAS, 272, 11 119, 135

Pan H. C., Jordan C., Makishima K., Stern R. A., Hayashida K., Inda-Koide M., 1997, MNRAS, 285, 735 135, 149

Pandey J. C., 2006, Optical studies of X-ray peculiar chromosphereically active stars, Ph.D. thesis, Aryabhatta Research Institute of Observational Sciences, Nainital, India 11

Pandey J. C., Karmakar S., 2015, AJ, 149, 47 93

Pandey J. C., Medhi B. J., Sagar R., Pandey A. K., 2009, MNRAS, 396, 1004 37, 38, 65

Pandey J. C., Singh K. P., 2008, MNRAS, 387, 1627 79, 94, 95, 97, 103, 119, 124, 125, 126, 135, 136, 137, 144, 148, 149

Pandey J. C., Singh K. P., 2012, MNRAS, 419, 1219 94, 97, 137, 144, 145, 147, 148, 149, 151, 156

Pandey J. C., Singh K. P., Drake S. A., Sagar R., 2005, AJ, 130, 1231 37, 38, 65, 80

Pandey J. C., Srivastava A. K., 2009, ApJ, 697, L153 24, 95

Parker E. N., 1955, ApJ, 122, 293 6

Parks J. R., White R. J., Schaefer G. H., Monnier J. D., Henry G. W., 2011, in 16th Cambridge Workshop on Cool Stars, Stellar Systems, and the Sun, edited by C. Johns-Krull, M. K. Browning, A. A. West, vol. 448 of Astronomical Society of the Pacific Conference Series, 1217 13

Parmar A. N., Culhane J. L., Rapley C. G., et al., 1984, ApJ, 279, 866 26

Patel M. K., Pandey J. C., Savanov I. S., Prasad V., Srivastava D. C., 2013, MNRAS, 430, 2154 85, 87, 157

Patkos L., 1981, Astrophys. Lett., 22, 1 77

Perryman M. A. C., 1997, in Hipparcos - Venice '97, edited by R. M. Bonnet, E. Høg, P. L. Bernacca, L. Emiliani, A. Blaauw, C. Turon, J. Kovalevsky, L. Lindegren, H. Hassan, M. Bouffard, B. Strim, D. Heger, M. A. C. Perryman, L. Woltjer, vol. 402 of ESA Special Publication, 1–4 79

Perryman M. A. C., Lindegren L., Kovalevsky J., et al., 1997, A&A, 323, L49 34

Petschek H. E., 1964, NASA Special Publication, 50, 425 117

Pettersen B. R., Hawley S. L., Fisher G. H., 1992, Sol. Phys., 142, 197 28

Phillips K. J. H., 1992, Guide to the sun 2

Phillips K. J. H., Feldman U., Landi E., 2008, Ultraviolet and X-ray Spectroscopy of the Solar Atmosphere, Cambridge University Press 5

Pi Q.-f., Zhang L.-Y., Li Z.-m., Zhang X.-l., 2014, AJ, 147, 50 77, 79

Piluso N., Lanza A. F., Pagano I., Lanzafame A. C., Donati J.-F., 2008, MNRAS, 387, 237 65, 70, 71, 72, 73, 80, 87

Pojmanski G., 2002, Acta Astron., 52, 397 34, 37

Poletto G., Pallavicini R., Kopp R. A., 1988, A&A, 201, 93 24, 25

Pollacco D. L., Skillen I., Collier Cameron A., et al., 2006, PASP, 118, 1407 34, 38

Porquet D., Mewe R., Dubau J., Raassen A. J. J., Kaastra J. S., 2001, A&A, 376, 1113 27, 98

Pradhan A. K., Shull J. M., 1981, ApJ, 249, 821 27

Press W. H., Rybicki G. B., 1989, ApJ, 338, 277 66

Priest E., 2000, Sun and Solar-terrestrial Physics 2

Priest E. R., 1984, Solar magneto-hydrodynamics 5

Qian S.-B., Zhang J., Zhu L.-Y., et al., 2012, MNRAS, 423, 3646 79

Randich S., 2000, in Stellar Clusters and Associations: Convection, Rotation, and Dynamos, edited by R. Pallavicini, G. Micela, S. Sciortino, vol. 198 of Astronomical Society of the Pacific Conference Series, 401 9

Reale F., 2007, A&A, 471, 271 23, 24, 101, 136

Reale F., Betta R., Peres G., Serio S., McTiernan J., 1997, A&A, 325, 782 23, 25, 102, 130, 156

Reale F., Güdel M., Peres G., Audard M., 2004, A&A, 416, 733 21, 22, 101

Reale F., Serio S., Peres G., 1993, Mem. Soc. Astron. Italiana, 64, 555 23

Reiners A., Basri G., 2009, A&A, 496, 787 4

Reiners A., Schmitt J. H. M. M., 2002, A&A, 384, 155 16

Rodono M., 1981, in Photometric and Spectroscopic Binary Systems, edited by E. B. Carling, Z. Kopal, 285 14

Rodonò M., 2000, RS Canum Venaticorum 14

Roettenbacher R. M., Monnier J. D., Harmon R. O., Barclay T., Still M., 2013, ApJ, 767, 60 13, 87

Romano P., Campana S., Chincarini G., et al., 2006, A&A, 456, 917 49

Roming P., Gronwall C., Breeveld A., Poole T. S., Blustin A., Boyd P., 2005a, GRB Coordinates Network, 4309 56

Roming P. W. A., Kennedy T. E., Mason K. O., et al., 2005b, Space Sci. Rev., 120, 95 47

Rosner R., Tucker W. H., Vaiana G. S., 1978, ApJ, 220, 643 23, 103, 133, 149, 150

Rucinski S. M., 1998, AJ, 115, 1135 30

Rüdiger G., von Rekowski B., Donahue R. A., Baliunas S. L., 1998, ApJ, 494, 691 74

Sakamoto T., Donato D., Gehrels N., Okajima T., Ukwatta T. N., 2009, in American Institute of Physics Conference Series, edited by C. Meegan, C. Kouveliotou, N. Gehrels, vol. 1133 of American Institute of Physics Conference Series, 244–246 33

Sakurai T., 1981, Sol. Phys., 69, 343 10

Sanz-Forcada J., Maggio A., Micela G., 2003, A&A, 408, 1087 105

Savanov I. S., 2014, Astronomy Reports, 58, 478 85, 87, 155

Savanov I. S., Dmitrienko E. S., 2011, Astronomy Reports, 55, 437 80

Savanov I. S., Strassmeier K. G., 2008, Astronomische Nachrichten, 329, 364 13, 80

Scargle J. D., 1982, ApJ, 263, 835 66

Schaefer B. E., King J. R., Deliyannis C. P., 2000, ApJ, 529, 1026 17

Schmidt J., Salo H., Spahn F., Petzschmann O., 1999, in AAS/Division for Planetary Sciences Meeting Abstracts #31, vol. 31 of AAS/Division for Planetary Sciences Meeting Abstracts, 44.07 21

Schmitt D., 1994, in Advances in Solar Physics, edited by G. Belvedere, M. Rodono, G. M. Simnett, vol. 432 of Lecture Notes in Physics, Berlin Springer Verlag, 61–72 144

Schrijver C. J., 1991, in Reviews in Modern Astronomy, edited by G. Klare, vol. 4 of Reviews in Modern Astronomy, 18–42 6

Schwabe M., 1844, Astronomische Nachrichten, 21, 233 14

Schwarzschild K., 1906, Nachrichten von der Königlichen Gesellschaft der Wissenschaften zu Göttingen. Math.-phys. Klasse, 195, p. 41-53, 195, 41 4

Serio S., Reale F., Jakimiec J., Sylwester B., Sylwester J., 1991, A&A, 241, 197 23

Shibata K., Yokoyama T., 1999, ApJ, 526, L49 24

Shibata K., Yokoyama T., 2002, ApJ, 577, 422 24, 25, 102

Shibayama T., Maehara H., Notsu S., et al., 2013, ApJS, 209, 5 17, 74

Sinvhal S. D., Kandpal C. D., Mahra H. S., Joshi S. C., Srivastava J. B., 1972, in Optical astronomy with moderate size telescopes, Symposium held at Centre of Advanced STudy in Astronomy, Osmania Univ., Hyderabad, p. 20 - 34 = Uttar Pradesh State Obs., Naini Tal, Repr. No. 64, vol. 64, 20–34 33

Slee O. B., Budding E., Carter B. D., Mengel M. W., Waite I., Donati J.-F., 2004, PASA, 21, 72 119

Smith R. K., Brickhouse N. S., Liedahl D. A., Raymond J. C., 2001, ApJ, 556, L91 62, 89, 95, 122

Srivastava A. K., Lalitha S., Pandey J. C., 2013, ApJ, 778, L28 102

Steenbeck M., Krause F., Rädler K.-H., 1966, Zeitschrift Naturforschung Teil A, 21, 369 6

Stelzer B., Burwitz V., Audard M., et al., 2002, A&A, 392, 585 97

Stetson P. B., 1990, PASP, 102, 932 41

Strassmeier K. G., 2009, A&A Rev., 17, 251 12, 105

Strassmeier K. G., Bartus J., 2000, A&A, 354, 537 80

Suwa F., Asada M., Sugizaki M., et al., 2011, The Astronomer's Telegram, 3837 119, 135

Sylwester B., Sylwester J., Serio S., Reale F., Bentley R. D., Fludra A., 1993, A&A, 267, 586 23, 97, 136

Taş G., 2011, Astronomische Nachrichten, 332, 57 33, 37, 38, 65, 72

Tandberg-Hanssen E., 1967, Solar activity 12

Telleschi A., Güdel M., Briggs K., Audard M., Ness J.-U., Skinner S. L., 2005, ApJ, 622, 653 93, 97, 98

Testa P., Drake J. J., Ercolano B., et al., 2008, ApJ, 675, L97 26, 138

Tsikoudi V., 1982, ApJ, 262, 263 119, 135

Tsuneta S., Hara H., Shimizu T., et al., 1992, PASJ, 44, L63 20

Tumer O., Kurutac M., 1979, Information Bulletin on Variable Stars, 1547 141

Tunca Z., 1984, Ap&SS, 105, 23 141

Uchida Y., Sakurai T., 1983, in IAU Colloq. 71: Activity in Red-Dwarf Stars, edited by P. B. Byrne, M. Rodono, vol. 102 of Astrophysics and Space Science Library, 629–632 138

van den Oord G. H. J., Mewe R., 1989, A&A, 213, 245 25

Vernazza J. E., Avrett E. H., Loeser R., 1981, ApJS, 45, 635 5

Vilhu O., 1984, A&A, 133, 117 9

Vilhu O., Linsky J. L., 1987, PASP, 99, 1071 105

Vilhu O., Rucinski S. M., 1983, A&A, 127, 5 9

Vilhu O., Tsuru T., Collier Cameron A., et al., 1993, A&A, 278, 467 95, 105

Vilhu O., Walter F. M., 1987, ApJ, 321, 958 9

Vogt S. S., Penrod G. D., 1983a, PASP, 95, 565 16

Vogt S. S., Penrod G. D., 1983b, in IAU Colloq. 71: Activity in Red-Dwarf Stars, edited by P. B. Byrne, M. Rodono, vol. 102 of Astrophysics and Space Science Library, 379–385 13

Walker G., Matthews J., Kuschnig R., et al., 2003, PASP, 115, 1023 28

Wiegelmann T., 2008, Journal of Geophysical Research (Space Physics), 113, A03S02 10

Willson R. C., Hudson H. S., 1988, Nature, 332, 810 28

Wilson R., 1978, A Study of Early Type Emission Line Stars, IUE Proposal 16

Woltjer L., 1958, Proceedings of the National Academy of Science, 44, 489 10

Wu S. T., de Jager C., Dennis B. R., et al., 1986, in NASA Conference Publication, vol. 2439 of NASA Conference Publication 103

Zacharias N., Monet D. G., Levine S. E., Urban S. E., Gaume R., Wycoff G. L., 2005, VizieR Online Data Catalog, 1297 43

Zarro D. M., Dennis B. R., Slater G. L., 1992, ApJ, 391, 865 26

Zeilik M., Elston R., Henson G., 1982, Information Bulletin on Variable Stars, 2200 77

Zhang R.-X., Zhai D.-S., Zhang X.-B., Zhang J.-T., Li Q.-S., 1990, Information Bulletin on Variable Stars, 3456 77

Zuckerman B., Song I., 2004, ARA&A, 42, 685 31

Zuckerman B., Song I., Bessell M. S., 2004, ApJ, 613, L65 65

SCHOOL OF STUDIES IN PHYSICS AND ASTROPHYSICS
PT. RAVISHANKAR SHUKLA UNIVERSITY,
RAIPUR - 492010 , CHHATTISGARH (INDIA)

Dr. Nameeta Brahme
M. Phil, Ph. D.
Professor & Head

Phone : (M) 96913-18995
: (O) (0771) 2262864
Email : namitabrahme@gmail.com

Ref. :...3027......

List of Publications

Date :...13-07-2017

Refereed Journal

To be Submitted

1. A Very Long and Hot X-ray flare on an RS CVn type eclipsing binary SZ Psc.
Karmakar, Subhajeet; Pandey, Jeewan C., 2017, Monthly Notices of the Royal Astronomical Society, to be submitted [IF = 4.961]
2. XMM Newton observations of AB Dor : X-ray flares.
Karmakar, Subhajeet & Pandey, Jeewan C., 2017, Astrophysical Journal Suplimentary Series, in preperation [IF = 11.257]

Published

3. X-ray Superflares on CC Eri.
Karmakar, Subhajeet; Pandey, Jeewan C.; Airapetian, V. S.; Misra, K, 2017, Astrophysical Journal, 840, 102 [IF = 5.909]
4. LO Peg: surface differential rotation, flares, and spot-topographic evolution.
Karmakar, Subhajeet; Pandey, Jeewan C.; Savanov, I. S.; Taş, G.; Pandey, S. B.; Dmitrienko, E. S.; Joshi; S. Misra, K; Sakamoto, T.; Gehrels, N.; Okajima, T., 2016, Monthly Notices of the Royal Astronomical Society, 459, 3112 [IF = 4.952]
5. Broad-band linear polarization in late-type active dwarfs.
Patel, Manoj K.; Pandey, Jeewan C.; Karmakar, Subhajeet; Srivastava, D. C.; Savanov, Igor S., 2016, Monthly Notices of the Royal Astronomical Society, 457, 3178 [IF = 4.952]
6. Photometric Observations of LO Peg in 2014-2015.
Savanov, I. S. et al. 2016, Acta Astronomica, 66, 381 [IF = 2.000]
7. An X-Ray Flare from 47 Cas.
Pandey, Jeewan C.; Karmakar, Subhajeet, 2015, Astronomical Journal, 149, 47 [IF = 4.617]
8. Phase-resolved XMM-Newton and Swift Observations of WR 25.
Pandey, Jeewan C.; Pandey, S. B.; Karmakar, Subhajeet, 2014, Astrophysical Journal, 788, 84 [IF = 5.993]

Nameeta
13/07/2017

Chairman
Departmental Research Committee
SoS in Physics & Astrophysics
Pt. Ravishankar Shukla University, Raipur

CHAIRMAN,
Deptt. Research Committee
SOS in Physics & Astrophysics,
Pt. R.S. University, RAIPUR (CG)

Monthly Notices of the ROYAL ASTRONOMICAL SOCIETY

MNRAS **459,** 3112–3129 (2016) doi:10.1093/mnras/stw855
Advance Access publication 2016 April 15

LO Peg: surface differential rotation, flares, and spot-topographic evolution

Subhajeet Karmakar,[1★] J. C. Pandey,[1★] I. S. Savanov,[2★] G. Taş,[3] S. B. Pandey,[1] K. Misra,[1] S. Joshi,[1] E. S. Dmitrienko,[4] T. Sakamoto,[5] N. Gehrels[6] and T. Okajima[6]

[1]*Aryabhatta Research Institute of observational sciencES (ARIES), Manora Peak, Nainital 263002, India*
[2]*Institute of Astronomy, Russian Academy of Sciences, ul. Pyatniskaya 48, Moscow 119017, Russia*
[3]*Astronomy and Space Sciences Department, Science Faculty, Ege University, İzmir 35100, Turkey*
[4]*Sternberg Astronomical Institute, Moscow State University, Universiteskii pr 13, Moscow 119992, Russia*
[5]*Department of Physics and Mathematics, Aoyama Gakuin University 5-10-1 Fuchinobe, Chuo-ku Sagamihara-shi Kanagawa 252-5258, Japan*
[6]*NASA Goddard Space Flight Center Greenbelt, MD 20771, USA*

Accepted 2016 April 11. Received 2016 April 11; in original form 2015 September 12

ABSTRACT

Using the wealth of ∼24 yr multiband data, we present an in-depth study of the star-spot cycles, surface differential rotations (SDR), optical flares, evolution of star-spot distributions, and coronal activities on the surface of young, single, main-sequence, ultrafast rotator LO Peg. From the long-term *V*-band photometry, we derive rotational period of LO Peg to be 0.4231 ± 0.0001 d. Using the seasonal variations on the rotational period, the SDR pattern is investigated, and shows a solar-like pattern of SDR. A cyclic pattern with period of ∼2.7 yr appears to be present in rotational period variation. During the observations, 20 optical flares are detected with a flare frequency of ∼1 flare per two days and with flare energy of $\sim 10^{31-34}$ erg. The surface coverage of cool spots is found to be in the range of ∼9–26 per cent. It appears that the high- and low-latitude spots are interchanging their positions. Quasi-simultaneous observations in X-ray, UV, and optical photometric bands show a signature of an excess of X-ray and UV activities in spotted regions.

Key words: stars: activity – stars: flare – stars: imaging – stars: individual: (LO Peg) – stars: late-type – starspots.

1 INTRODUCTION

Stars with spectral type from late-F to early-K have a convective envelope above a radiative interior with an interface where strong shear leads to amplification of magnetic fields. Observations of these stars provide good constraints on present theoretical dynamo models, which are developed on the basis of the Sun. The solar activity cycle is believed to be generated through dynamo mechanism operating either in the convection zone or in the stably stratified layer beneath it. Stars with a similar internal structure to that of the Sun are also expected to show the solar-type dynamo operation. The strong dynamo in solar-type stars leads to rich variety of magnetic activities such as surface inhomogeneities due to the presence of dark spots, short- and long-term variations in spot cycles, and flares.

Dark spots move across the stellar disc due to the stellar rotation and thus modulate the total brightness with the rotational period of the star which in turn allows us to derive the stellar rotational period. The spots on the stellar surface have been imaged by using a variety of techniques like Doppler imaging (Vogt & Penrod 1983) and interferometric technique (Parks et al. 2011). However, high-resolution spectroscopic observations with a high-signal-to-noise ratio and a good phase coverage as required for Doppler imaging are limited. Further, the Doppler imaging technique can only be applied for fast-rotating stars with low inclination, whereas, the interferometric technique can be used for nearby stars of large angular size. The vast majority of spotted stars cannot be imaged with either of these techniques. Therefore, long-term traditional photometric observations are important to understand the active region evolution and the stellar activity cycles (e.g. Järvinen, Berdyugina & Strassmeier 2005b; Oláh et al. 2009; Roettenbacher et al. 2013). Since a light curve represents a one-dimensional time series, the resulting stellar image contains information mostly in the direction of rotation, i.e. in the longitude, rather than spot size and locations in the latitude (Savanov & Strassmeier 2008). Although the projection effects and limb darkening allow the inversion technique to recover more structures than is obvious at first glance. The surface differential rotations (SDR) in these stars can be determined by measuring the rotational period of stars with spots. Several authors

★ E-mail: subhajeet09@gmail.com, subhajeet@aries.res.in (SK); jeewan@aries.res.in (JCP); igs231@mail.ru (ISS)

in the past have studied SDR in solar-type stars using long-term photometry (e.g. Baliunas & Vaughan 1985; Hall 1991; Walker et al. 2007; Reinhold, Reiners & Basri 2013; Reinhold & Arlt 2015). Since spots cover a limited range of latitudes on the stellar surface; therefore, amplitudes of SDR derived with this method give the lower limits. The season-to-season variations of the rotational period as measured from spectrophotometric (Donahue & Dobson 1996) or broad-band photometric observations can be termed as a proxy of stellar butterfly diagram. In analogy with the Sun, such diagrams are interpreted in terms of migration of activity centres towards latitudes with different angular velocities. Another consequence of stellar magnetic activities are flares, which are the result of reconnection of magnetic field lines at coronal height. Flares are explosions on the stellar surface releasing huge amount of the magnetic energy stored near star-spots in the outer atmosphere of stars (e.g. Gershberg 2005; Benz & Güdel 2010; Shibata & Magara 2011). Observationally flares are detected over all frequencies of the electro-magnetic spectrum. The average flare duration is 10^{2-4} s (Kuijpers 1989). The total energy released during a flare (in all wavelengths) is 10^{34-36} erg, i.e. 10^{2-4} times more powerful than the solar analogue (Byrne & McKay 1989).

In this paper, we have investigated an active, young, single, main-sequence, K5–8 type ultrafast rotator (UFR) LO Peg. LO Peg has been an interesting object to study over the last two decades. From photometric observations, Barnes et al. (2005) derived a rotational period of 0.423 23 d. A presence of strong flaring activity was also identified by Jeffries et al. (1994) and Eibe et al. (1999) from H α and He I D3 observations. Taş (2011) found evidence of flares in the optical band. Doppler imaging of LO Peg showed evidence of high polar activities (Lister, Collier Cameron & Bartus 1999; Barnes et al. 2005; Piluso et al. 2008). Several photometric, polarimetric, and X-ray studies were also carried out by Dal & Taş (2003), Pandey et al. (2005), Pandey et al. (2009), Csorvási (2006), and Taş (2011). The above results encouraged us to collect all available data and analyse them with the aim to establish whether the star exhibits active longitudes and cyclic behaviour in spot patterns and overall spot activity.

The paper is organized as follows: in Section 2 we provide details on observational data sets and discuss the data analysis techniques. In Section 3, we present our analysis and results on light curves, SDR, flaring activity, surface inhomogeneity, and coronal activities. Finally, we discuss all the results in the light of present understanding in Section 4 and a brief summary of our results is given in Section 5.

2 OBSERVATIONS AND DATA REDUCTION

2.1 Optical data

We observed LO Peg on 30 nights between 2009 October 25 and 2013 December 18 in Johnson U, B, V, and R photometric bands with the 2-m IUCAA Girawali Observatory (IGO; see Das et al. 1999), 1.04-m ARIES Sampurnanand Telescope (ST; see Sinvhal et al. 1972), and 0.36-m Goddard Robotic Telescope (GRT; see Sakamoto et al. 2009). The exposure time was between 5 and 60 s depending on the seeing condition, filter, and telescope used. Several bias and twilight flat frames were taken in each observing night. Bias subtraction, flat-fielding, and aperture photometry were performed using the standard tasks in IRAF.[1] In order to get the standard magnitude of the program star, differential photometry had been adopted, assuming that the errors introduced due to colour differences between comparison and program stars are very much small. We have chosen TYC 2188-1288-1 and TYC 2188-700-1 as the comparison and check stars, respectively. The differences in the measured U, B, V, and R magnitudes of comparison and check stars did not show any secular trend during our observations. The nightly means of standard deviations of these differences were 0.009, 0.008, 0.008, and 0.007 mag in U, B, V, and R bands, respectively. This indicates that both the comparison and check stars were constant during the observing run. The standard magnitudes of comparison and check stars were taken from Naval Observatory Merged Astrometric Dataset (NOMAD) Catalogue (Zacharias et al. 2004). The derived photometric uncertainties for program star, check star, and comparison star were propagated to get the final photometric uncertainty of LO Peg.

We have compiled various other available data sets in U, B, V, and R band from literature (Jeffries et al. 1994; Pandey et al. 2005, 2009; Taş 2011) and from archives to supplement our data sets. The archival data were taken from *Hipparcos*[2] (Perryman et al. 1997), All Sky Automated Survey[3] (ASAS; Pojmanski 2002), and Super Wide Angle Search for Planets[4] (SuperWASP; Pollacco et al. 2006) observations. The log of optical observations is listed in Table 1. *Hipparcos* observations spanned over ∼3 yr from 1989 November 27 to 1992 December 15. The *Hipparcos* magnitude ($V_{\rm H}$) was converted to Johnson V magnitude by using the relation $V = V_{\rm H} - (V - I)_c$, where $(V - I)_c$ is the catalogue value corresponding to the colour $(V - I)$. With a $(V - I)$ colour of 1.288 mag for G-M dwarfs, we get the $(V - I)_c$ value of LO Peg to be 0.124 mag. ASAS survey was done in V band and has a much longer observing span of ∼7 yr (2003 April 26–2009 October 1). In the ASAS observations, we have used only ‘A’ and ‘B’ grade data within 1 arcsec of the star LO Peg. ASAS photometry provides five sets of magnitudes corresponding to five aperture values varying in size from 2 to 6 pixels in diameter. For bright objects, Pojmanski (2002) suggested that these magnitudes corresponding to the largest aperture (diameter 6 pixels) are useful. Therefore, we took magnitudes corresponding to the largest aperture for further analysis. SuperWASP observations of LO Peg during 2004 May 3 to 2006 June were unfiltered which were not useful for our study (see Pollacco et al. 2006). A broad-band filter with a pass-band from 400 to 700 nm (known as SuperWASP V band) was installed on 2006 June. In our analysis, we make use of the data taken from 2006 June, onwards. Since the SuperWASP data were taken in a broader band than the Johnson V band; it is necessary to convert SuperWASP band magnitude ($V_{\rm W}$) to Johnson V magnitude. Fortunately, the Landolt standard field TPHE with seven standard stars was observed by SuperWASP. Fig. 1 shows the plot between V and $V_{\rm W}$ of Landolt standard stars, where the continuous line shows the best-fitting straight line. We derived the relation between V and $V_{\rm W}$ as $V = V_{\rm W} - 0.09$, and converted the $V_{\rm W}$ magnitude into V. Further, we have restricted our analysis within magnitude error less than or equal to 0.04 mag both in ASAS and SuperWASP data. Including present observations along with the data compiled from literature and archive, LO Peg was observed for ∼24.1 yr from 1989 to 2013.

[1] http://iraf.net

[2] http://heasarc.gsfc.nasa.gov/W3Browse/all/hipparcos.html

[3] http://www.astrouw.edu.pl/asas/?page=main

[4] http://exoplanetarchive.ipac.caltech.edu/applications/TblSearch/tblSearch.html?app=ExoSearch&config=superwasptimeseries

Table 1. Log of optical observations of LO Peg.

Observatories	Start HJD (2400000+)	End HJD (2400000+)	Number of exposures *U* band	*B* band	*V* band	*R* band	Ref
ARIES ST	55130.118	56645.365	5	67	72	5	P
GRT	55766.811	55775.771	–	4	9	3	P
IGO	55130.100	55135.130	–	10	30	–	P
Archive							
Hipparcos	47857.501	48972.277	–	–	136[a]	–	a
ASAS	52755.911	55092.673	–	–	259	–	b
SuperWASP	53128.655	54410.482	–	–	8047[a]		c
Literature							
JKT	48874.519	48883.592	25	25	25	25	d
ARIES ST	52181.167	54421.047	–	90	119	–	e
EUO	52851.445	55071.521	5566	5566	5566	5566	f

Notes. P – Present study; a – *Hipparcos* archive ; b – ASAS archive; c – SuperWASP archive
d – Jeffries et al. (1994); e – Pandey et al. (2005, 2009); f – Taş (2011).
[a] *Hipparcos* and SuperWASP data were converted to corresponding *V*-band magnitude.

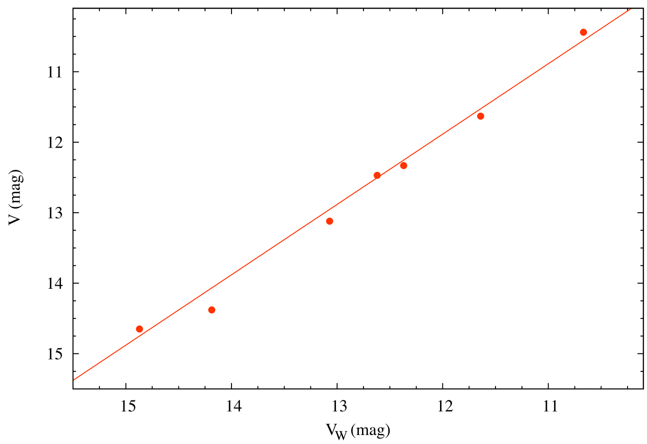

Figure 1. The relation between SuperWASP magnitude (V_W) and Johnson V-magnitude (V) of Landolt standard stars (TPHE field). Error bars shown in both axes are less than the size of the symbol. Continuous line shows the best-fitting straight line. We derived the relation between V and V_W as $V = V_W - 0.09$.

2.2 X-ray and UV data

LO Peg was observed in 17 epochs with *Swift* satellite (P.I. Pandey, ID: 0123720201) from 2008 April 30 to 2012 July 2. The observations were made in soft X-ray band (0.3–10.0 keV) with X-Ray Telescope (XRT; Burrows et al. 2005) in conjunction with UV/Optical Telescope (UVOT; Gehrels et al. 2004) in UV bands (170–650 nm). The offset of the observations lies between 1.11 and 4.35 arcmin. The XRT exposure time of LO Peg ranges from 0.3 to 5.0 ks. X-ray light curves and spectra of LO Peg were extracted from on-source counts obtained from a circular region of 36 arcsec on the sky centred on the X-ray peaks. Whereas, the background was extracted from an annular region having an inner circle of 75 arcsec and outer circle of 400 arcsec co-axially centred on the X-ray peaks. The X-ray light curves and spectra for the source and background were extracted using the XSELECT package. In order to see the long-term X-ray variation, we converted *ROSAT* Position Sensitive Proportional Counter (PSPC) count rate (Pandey et al. 2005) to *Swift* XRT count rate with multiple component models of WEBPIMMS (see Section 3.5 for further details). Simultaneous observations of LO Peg with *Swift* UVOT were carried out in *uvw*2 (192.8 nm), *uvm*2 (224.6 nm), and *uvw*1 (260.0 nm) filters (Roming et al. 2005) with exposure times between 0.02 and 3.06 ks. UV light curves were extracted using the UVOTMAGHIST task.

3 ANALYSIS AND RESULTS

3.1 Optical light curves and period analysis

Fig. 2 shows the multiwavelength light curves of LO Peg where bottom four panels indicate the optical U, B, V, and R photometric bands. The optical light curves display high amplitude both in short-term and long-term flux variations. The most populous V-band data was analysed for the periodicity using Scargle–Press period search method (Scargle 1982; Horne & Baliunas 1986; Press & Rybicki 1989) available in the UK Starlink PERIOD package (version-5.0-2; see Dhillon, Privett & Duffey 2001). Top panel of Fig. 3(a) shows the power spectra obtained from Scargle periodogram. We have also calculated the False Alarm Probability (FAP) for any peak frequency using the method given by Horne & Baliunas (1986). The significance level of 99.9 per cent is shown by continuous horizontal line in the Fig. 3. Large and almost periodic gaps in the data set led to further complications in the power spectrum. True frequencies of the source were further modulated by the irregular infrequent sampling defined by window function of the data. In order to resolve this problem, we have computed window function with the same time sampling and photometric errors of the actual light curve, but contains only a constant magnitude as the average magnitude of the data (9.250 mag). We have repeated the process with many realization of noise, where we have generated 1000 random numbers within 3σ range of the mean value and taking these value as a constant we computed each periodogram. The resulting periodograms were averaged and shown in bottom panel of Fig. 3.

In Scargle power spectra the peak marked as ‘S’ corresponds to the rotational period of 0.422 923 ± 0.000 005 d, where the uncertainty in period was derived using the method given by Horne & Baliunas (1986). The uncertainty in the derived period was very small (<1 s) due to the long base line of unevenly sample data. Further, there was a large gap in the data. Therefore, we derived the rotational period and corresponding error by averaging the seasonal rotational periods (see Section 3.2). The value of mean seasonal rotation period was found to be 0.4231 ± 0.0001 d. Two other smaller peaks at periods of ∼0.212 d and ∼0.846 d were identified in the power spectra as the harmonic and sub-harmonic, respectively. The

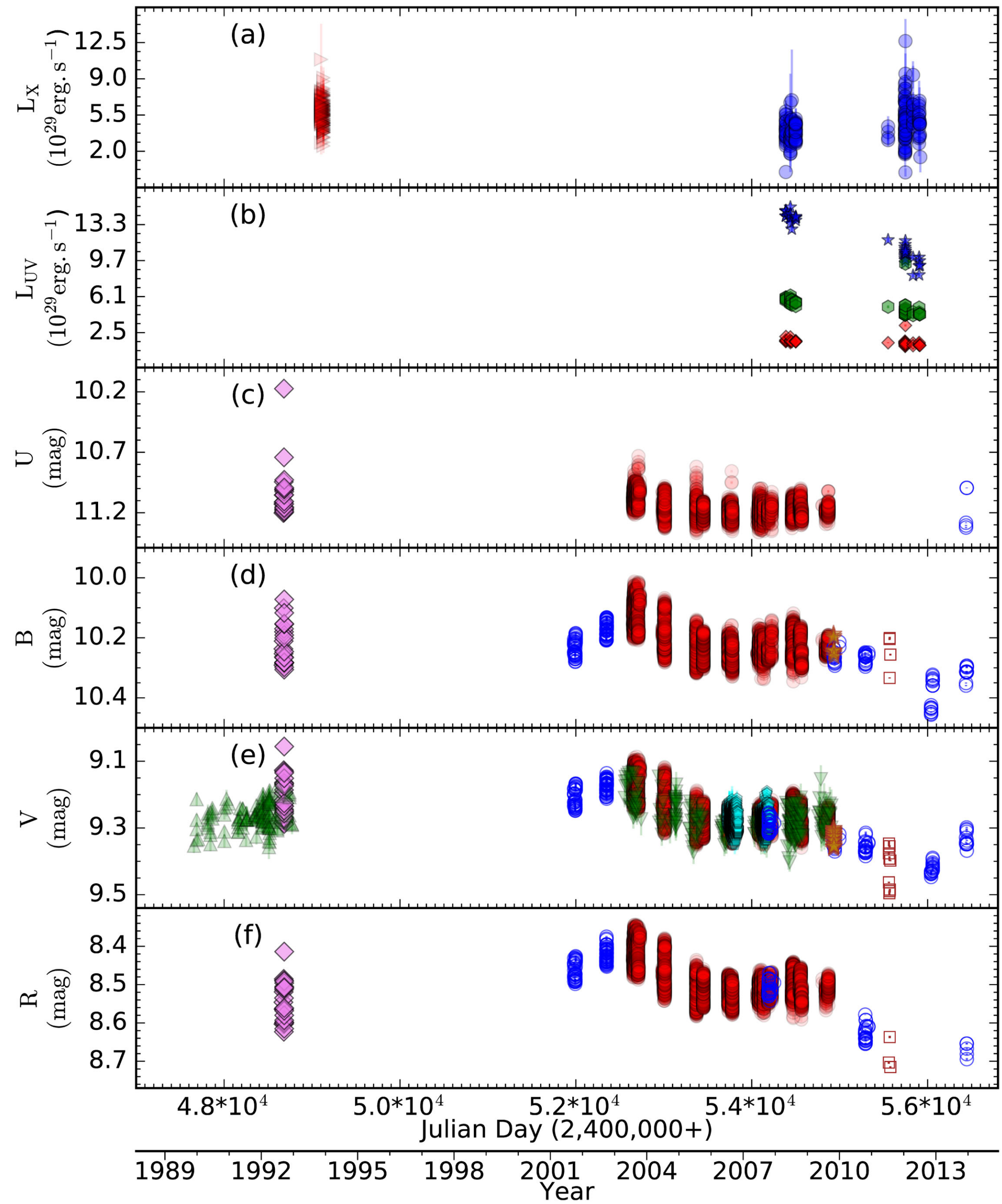

Figure 2. Multiband light curve of LO Peg. From top to bottom – (a) the X-ray light curves obtained from *Swift* XRT (solid circle) and *ROSAT* PSPC (solid right triangle) instruments. (b) The UV light curve obtained from *Swift* UVOT in three different *UV*-filters: *uvw*2 (solid hexagon), *uvm*2 (solid diamond), and *uvw*1 (solid star). (c–f) The next four panels shows optical light curves obtained in *U*, *B*, *V*, and *R* bands, respectively. Observations were taken from ARIES (open circle), IGO (solid star), GRT (open square), EUO (solid circle), and JKT (solid diamond) telescopes and archival data were obtained from *Hipparcos* satellite (solid triangle), SuperWASP (solid pentagon), and ASAS (solid reverse triangle).

former may indicate the existence of two active regions over the surface of LO Peg, whereas the later appears due to repeated occurrence of the same spot at multiple of its period. In order to search for the long-term periodicity, we have zoomed the lower frequency range of Fig. 3(a) and shown in Fig. 3(b). Several peaks were found above the 99.9 per cent confidence level, these peaks are marked by L*i*, where $i = 1$ to 11. However, many of the peaks were found under window function (see shaded region of Fig. 3b). Peaks corresponding to the periods L3 and L4 did not fall under the window function. Further, we have folded the data in each period and found periodic modulation only for periods 5.98 and 2.2 yr corresponding to L2 and L3. To avoid the modulation due to its rotation, we have made one point of every five-rotation period (∼2 d). Further, the light curve evolved over a long time; therefore, for folding the data on the long periods, we have split the light curves for different time segments such that each segment has a length of minimum to those long periods. The top and bottom panels of Fig 4 show the folded light curves on periods 5.98 and 2.2 yr for different time segments, respectively. For the period 5.98 yr, we found only three time segments of ∼6 yr. For 2.2 yr period, we could make only four time segments of each

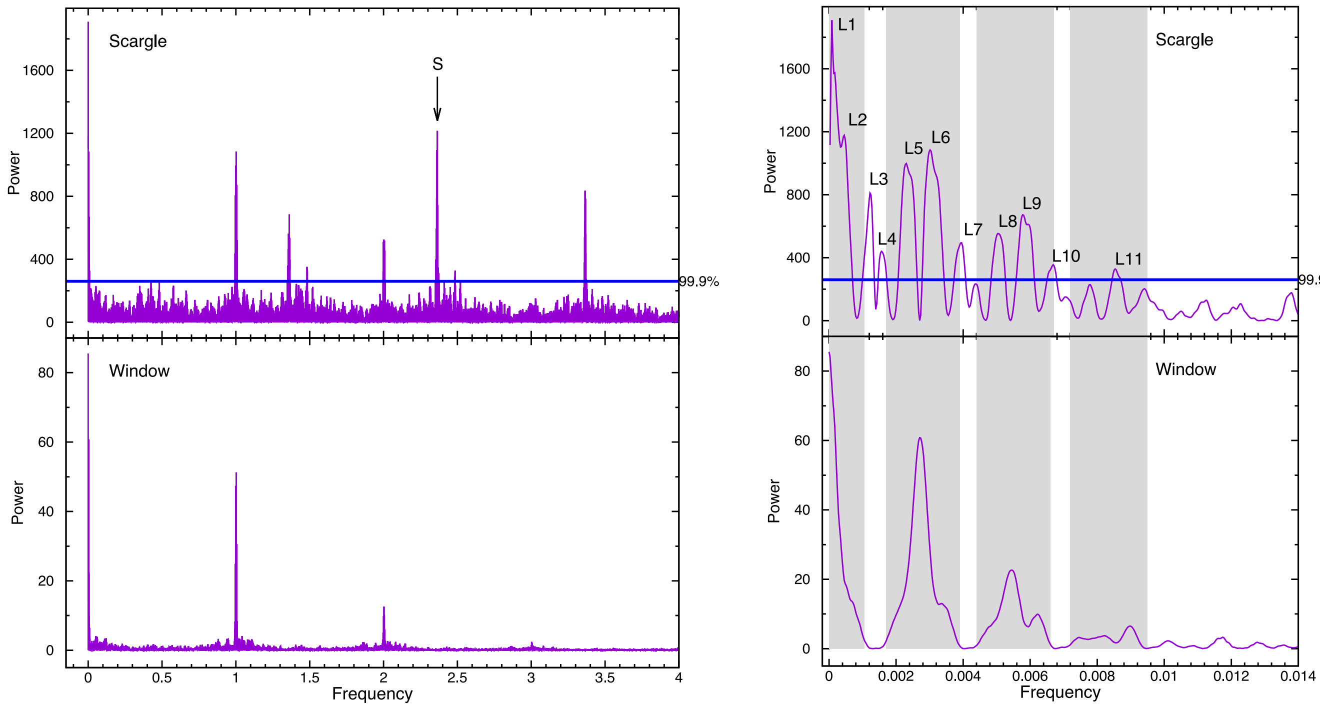

Figure 3. (a) Scargle–Press periodogram obtained from *V*-band data (top) along with the calculated window function (bottom). The significance level of 99.9 per cent is shown by continuous horizontal line. The peak marked as 'S' corresponds to the stellar rotation period. (b) The low-frequency region is zoomed to show the long-term periods, the shaded regions show the frequency domain ascribed to window function. Long-term peaks are marked by 'L1–L11' (see the text for detailed description).

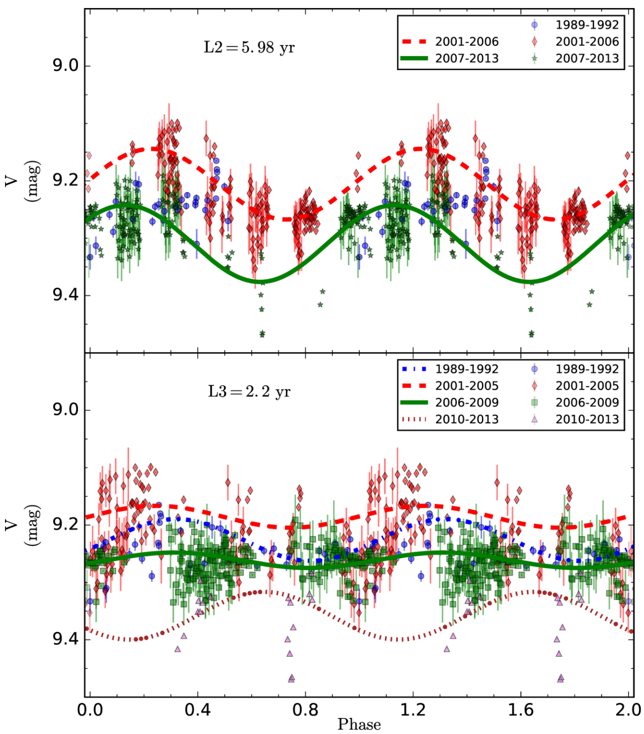

Figure 4. Folded light curve of LO Peg in *V* band with periods of 5.98 yr (top) and 2.2 yr (bottom). The best-fitting sinusoids are shown by dashed, dotted, dash–dotted, and continuous lines for different time-intervals marked at the top-right corner of each panel. We could not fit the time-interval of 1989–1992 in top panel due to partial phase coverage of data points.

3–4 yr. Further, we have fitted sinusoids in the phase-folded light curves for each interval. In the top panel of Fig. 4, the best-fitting sinusoids are shown by dashed and continuous curves for the time interval 2001–2006 and 2007–2013, respectively. Sinusoid was not fitted to the time interval of 1989–1992 due to the partial phase coverage. The long-term evolution of the activity seems to present. Similar behaviour of the light curve was also seen while fitting sinusoid to the phase-folded light curves on 2.2 yr in the bottom panel of Fig. 4.

3.2 Surface differential rotation

The visibility of photospheric star-spots is modulated by stellar rotation which causes quasi-periodic brightness variations on timescales of the order of the rotational period. The modulation period indicates the angular velocity of the latitude at which starspot activity is predominantly centred. Since the circumpolar spots will not affect the rotational modulation, with an inclination angle (i) of $45\overset{\circ}{.}0 \pm 2\overset{\circ}{.}5$ on LO Peg (Barnes et al. 2005; Piluso et al. 2008), any modulation observed on stellar surface would be only due to the spot groups present within a latitude of $\pm 45^{\circ}$ from the stellar equator. Similar to the solar case, the year to year variations of the rotational period can be described as the migration of stellar activity centres towards latitudes possessing different angular velocity. This migration is caused by the internal radial shear, which is assumed to be coupled with observed latitudinal shear (e.g. in $\alpha - \Omega$ dynamo model).

In order to search for any change in the rotational period, we have determined photometric period of each observing season separately. We have chosen the observing seasons to derive the period due to the fact that the brightness of star in each season

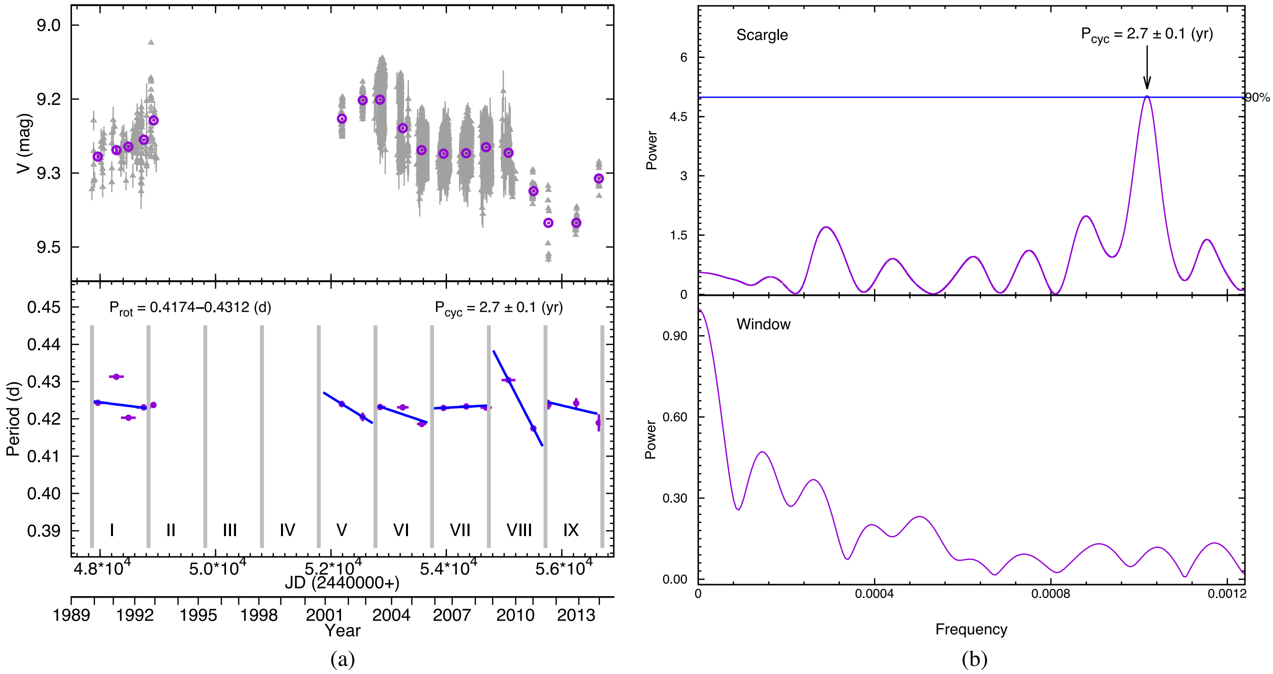

Figure 5. Top panel of (a) shows the *V*-band light curve (solid triangles) along with the mean magnitude of each season (open circles). Solid circles in bottom panel of (a) shows the derived rotational periods in each season. The Scargle–Press periodogram of these seasonal periods along with calculated window function shown in top and bottom panel of (b), respectively, with 90 per cent significance level marked with blue horizontal lines. The highest peak above 90 per cent significance level indicates the cyclic period of 2.7 ± 0.1 yr. In bottom panel of (a) each period of 2.7 ± 0.1 yr is indicated with the vertical lines. The straight lines in each cycle show a linear fit to data during the cycle. The rotation period monotonically decreases along most the star-spot cycles showing a solar-like behaviour.

Table 2. Parameters derived from SDR analysis.

Cycle[a]	Start HJD (2400000+)	END HJD (2400000+)	MEAN HJD (2400000+)	N_0	V_{avg} (mag)	P_{sr} (d)	FAP
I	47857.500	48066.063	47961.782	19	9.268 ± 0.004	0.4243 ± 0.0003	0.05
	48113.175	48368.850	48282.378	13	9.255 ± 0.005	0.4313 ± 0.0005	0.12
	48368.850	48624.525	48490.262	30	9.248 ± 0.003	0.4203 ± 0.0002	0.03
	48624.525	48880.200	48756.841	73	9.233 ± 0.002	0.4231 ± 0.0001	3.28e-08
II	48880.200	48972.277	48926.410	25	9.194 ± 0.002	0.4237 ± 0.0004	2.31e-03
V	52181.166	52198.126	52189.646	37	9.1909 ± 0.001	0.4240 ± 0.0009	1.25e-06
	52546.207	52551.254	52548.731	50	9.154 ± 0.001	0.421 ± 0.001	1.99e-07
VI	52755.911	52942.538	52849.224	894	9.1522 ± 0.0003	0.42319 ± 0.00002	2.45e-165
	53142.922	53344.523	53243.722	574	9.2100 ± 0.0005	0.42308 ± 0.00005	6.20e-105
	53487.918	53650.354	53569.136	889	9.2546 ± 0.0003	0.41864 ± 0.00004	1.14e-144
VII	53853.920	54044.457	53949.188	4792	9.2617 ± 0.0002	0.42295 ± 0.00001	∼0
	54227.896	54454.050	54340.973	4700	9.2610 ± 0.0002	0.42331 ± 0.00001	∼0
	54590.916	54785.517	54688.216	1061	9.2487 ± 0.0004	0.42305 ± 0.00002	3.37e-177
VIII	54954.917	55196.045	55075.481	386	9.2603 ± 0.0008	0.4304 ± 0.0001	1.48e-09
	55489.158	55526.101	55507.630	23	9.338 ± 0.001	0.417 ± 0.001	0.05
IX	55758.817	55775.770	55767.294	9	9.402 ± 0.003	0.424 ± 0.001	0.22
	56239.143	56257.173	56248.158	20	9.402 ± 0.001	0.424 ± 0.001	0.01
	56636.357	56645.364	56640.861	12	9.312 ± 0.001	0.419 ± 0.002	0.05

Notes. [a]Detected star-spot cycles of 2.7 ± 0.1 yr (shown in bottom panel of Fig. 5a). N_0 is the number of data points during each season, V_{avg} is the average *V*-band magnitude in each season, P_{sr} is the seasonal rotational period, and FAP is false alarm probability.

showed regular modulation which could be attributed to rotation of a stationary spot pattern of the star. Smaller time interval and hence smaller baseline introduces large uncertainty in determination of photometric period, whereas larger time intervals shows a significant change in shape of the light curve. In case of the sparse data obtained from *Hipparcos* satellite, the interval were chosen similar to the maximum data length of 0.7 yr obtained from ground-based observations. In this way we could obtain 18 seasonal light curves, and average values of each seasonal light curve are shown in the top panel of Fig. 5 along with the time sequence of *V*-band magnitudes of LO Peg. Each seasonal data were analysed using the Scargle–Press period search method. The uncertainty in photometric period and FAP were calculated following the method of Horne & Baliunas (1986). In the bottom panel of Fig. 5(a), we plot the seasonal values of the measured rotational periods (P_{sr}) and the results are summarized in Table 2. These modulation periods correspond to

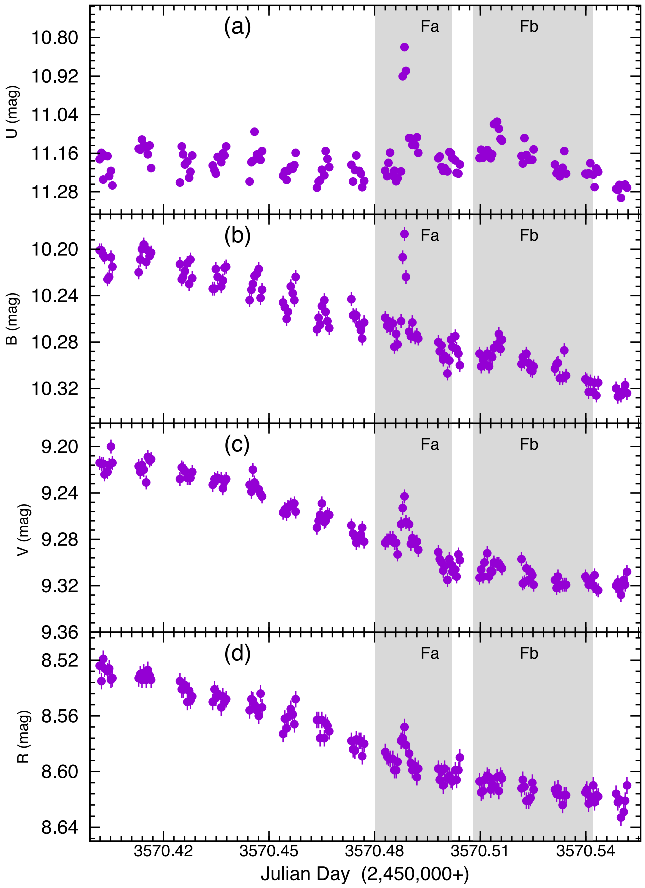

Figure 6. Two consecutive representative flares (shaded regions) on LO Peg simultaneously observed in *U* (a), *B* (b), *V* (c), and *R* (d) optical bands. The first flare shows activity level in all four optical bands. Whereas the second flare is detected only in shorter wavelengths (*U* and *B* bands).

the angular velocity of the latitudes at which non-circumpolar spot groups are present. Fig. 5(b) shows the Scargle power spectra of the measured seasonal rotational periods. Within the Nyquist frequency of 0.001 24, we found maximum peak in the Scargle–Press periodogram is above 90 per cent significance level and has an periodicity of 2.7 ± 0.1 yr. This period is well within 3σ level of the identified periodicity of brightness variation (see Section 3.1). In ∼24 yr of observations nine cycles of 2.7 yr period can be made, where we have detected six full cycles and one incomplete cycle (II). We found that the rotational period tends to decrease steadily during an 'cycle' of ∼2.7 yr, and jumping back to a higher value at the beginning of a new cycle. The abrupt changes in period of cycle-I may be a result of the sparse data set obtained from *Hipparcos* satellite. However, in cycle-VII, we did not see any noticeable change in the rotational period.

3.3 Flare analysis

Flares in LO Peg were searched using *U*, *B*, *V*, and *R* data. For this analysis, we have converted the magnitude into flux using the zero-points given in Bessell (1979). Fig. 6 shows two consecutive representative flares observed simultaneously in all four optical bands. The first flare was detected in all four bands while next flare was not detected in longer wavelengths (*V* and *R* band). Thus, a flare detected in one band is not necessarily detected in each of the optical bands. Due to the sparse data, we have not followed the usual flare detection methods as described in Osten et al. (2012), Hawley et al. (2014), and Shibayama et al. (2013). We have chosen different epochs such that, each epoch contains a continuous single night observation with at least 16 data points and minimum observing span of ∼1 h. A total of 501 epochs were found using the most populous *V*-band data, among which only 82 epochs have simultaneous observations with other three optical bands.

The light curve of each epoch was first detrended to remove the rotational modulation by fitting a sinusoidal function. The local mean flux ($F_{\rm lm}$) and standard deviation ($\sigma_{\rm ql}$) of the flux were then computed at each time-sampled data set. To avoid misdetection of short stellar brightness enhancement as a flare, candidate flares were flagged as excursions of two or more consecutive data points above 2.5$\sigma_{\rm ql}$ from $F_{\rm lm}$ (see Davenport et al. 2014; Hawley et al. 2014; Lurie et al. 2015) with at least one of those points being $\geq 3\sigma_{\rm ql}$ above $F_{\rm lm}$ in any of the optical band. Once the flare was detected using the above criteria, the flare segment was removed to calculate the exact value of $\sigma_{\rm ql}$, where most of the flares were identified above the 3$\sigma_{\rm ql}$ from the quiescent state. This derived value of $\sigma_{\rm ql}$ was not used for further flare identification. Finally, each flare candidate, in each photometric band was inspected manually to confirm it as real flares. In this way, we have detected 20 optical flares. Flare nomenclatures were given as 'F*i*', where $i = 1, 2, 3,..., 20$; denotes the chronological order of the detected flares. Flare parameters of all the detected flares are listed in Table 3.

Fig. 7 shows flares detected in *V* band, where top panels of each plot show *V*-band magnitude variation during flares along with the fitted sinusoidal function and bottom panels show the detrended light curve with best-fitted exponential function. Most of the flares of LO Peg show usual fast rise (impulsive phase) followed by a slower exponential decay (gradual phase). The e-folding rise (τ_r) and decay times (τ_d) have been derived from the least-squares fit of the exponential function in the form of $F(t) = A_{\rm pk} e^{(t_{\rm pk}-t)/\tau} + F_{\rm lm}$ from flare-start to flare-peak, and from flare-peak to flare-end, respectively. In the fitting procedure $A_{\rm pk}(= F_{\rm pk} - F_{\rm lm})$, $F_{\rm lm}$ and $t_{\rm pk}$ were fixed parameters. Here, $F_{\rm pk}$ is flux at flare peak at time $t_{\rm pk}$. For the flare F13, the peak was not observed, therefore, the parameters A and $t_{\rm pk}$ were also kept as free parameters in exponential fitting. In order to get a meaningful fit, we restricted our analysis to those flares which contain more than two data points in rise/decay phase. The fitted values of τ_r and τ_d are given in columns 10 and 11 of Table 3. The values of τ_r were found to be in the range of 0.3–14 min with a median value of 2.5 min. Whereas, values of τ_d were derived in the range of 0.4–22 min, with a median of 3.3 min. Most of the time τ_d was found to be more than τ_r.

The amplitude of a flare is defined as

$$A = \frac{A_{\rm pk}}{F_{\rm lm}} = \left(\frac{F_{\rm pk} - F_{\rm lm}}{F_{\rm lm}}\right). \qquad (1)$$

The amplitude of the flare is thus measured relative to the current state of the underlying star, including effects from star-spots, and represents the excess emission above the local mean flux. The highest amplitude of 1.02 was found in the long-lasting flare F13, while smallest amplitude of 0.016 was found for a small duration flare indicating that long-lasting flares are more powerful than small duration flares. The duration (Dn) of a flare is defined as the difference between the start time (the point in time when the flare flux starts to deviate from the local mean flux) and the end time (when the flare flux returns to the local mean flux). The start and end times for each flare were obtained by manual inspection. Flare durations are found within a range of 12–202 min with a median value of 47 min. Flare

Table 3. Parameters obtained from flare analysis.

Sl No.	Flare name	Filter	t_{st}[a] (HJD) (2400000+)	Dn[b] (min)	t_{pk}[c] (HJD) (2400000+)	F_{lm}[d]	$\left(\frac{A_{pk}}{\sigma_{ql}}\right)$[e]	A[f] (frac)	τ_r[g] (min)	τ_d[h] (min)	Energy[i] (10^{32} erg)
1	F1	*U*	52857.437	26	52857.445	3.67	3.61	0.133	–	10.5 ± 2.6	> 2.31
2		*B*	52857.437	26	52857.445	11.26	3.37	0.026	–	21.9 ± 5.0	> 2.81
3	F2	*U*	53206.468	12	53206.513	3.50	3.03	0.062	3.0 ± 1.2	2.9 ± 1.2	0.57
4		*B*	53206.465	12	53206.511	11.11	2.61	0.016	$\sim$0.4	$\sim$0.7	0.09
5	F3	*U*	53570.317	29	53570.323	3.54	9.50	0.269	3.9 ± 1.4	4.8 ± 1.4	3.25
6		*B*	53570.318	26	53570.322	11.03	6.11	0.048	1.4 ± 0.4	1.0 ± 0.4	0.49
7	F4	*U*	53570.331	42	53570.344	3.45	6.78	0.200	6.9 ± 2.7	$\sim$1.3	2.38
8		*B*	53570.331	42	53570.341	11.04	5.21	0.040	4.9 ± 1.7	2.0 ± 1.0	1.29
9	F5	*U*	53570.359	72	53570.384	3.40	8.42	0.256	13.8 ± 2.2	$\sim$0.7	5.56
10		*B*	53570.354	72	53570.376	10.99	4.72	0.036	9.8 ± 2.5	9.2 ± 2.0	3.37
11		*V*	53570.354	68	53570.368	25.80	4.48	0.027	0.3 ± 0.1	5.5 ± 1.9	1.80
12		*R*	53570.353	63	53570.366	24.46	6.01	0.031	2.0 ± 0.6	7.9 ± 1.3	3.40
13	F6	*U*	53570.482	32	53570.488	3.22	14.55	0.454	1.0 ± 0.1	2.3 ± 0.3	2.18
14		*B*	53570.481	23	53570.488	10.22	10.54	0.090	1.3 ± 0.3	1.2 ± 0.1	0.99
15		*V*	53570.482	22	53570.488	23.96	6.52	0.040	1.3 ± 0.3	1.6 ± 0.4	1.26
16		*R*	53570.482	20	53570.488	23.00	4.68	0.024	1.3 ± 0.6	1.0 ± 0.4	0.58
17	F7	*U*	53570.500	71	53570.515	3.17	6.18	0.196	8.6 ± 1.3	18.7 ± 1.6	7.37
18		*B*	53570.508	49	53570.515	9.93	3.10	0.027	2.3 ± 0.9	15.0 ± 2.3	2.06
19	F8	*U*	53971.346	52	53971.359	3.47	10.79	0.302	1.7 ± 0.3	1.2 ± 0.3	1.34
20		*B*	53971.339	52	53971.359	10.77	6.10	0.048	2.5 ± 0.9	4.2 ± 0.7	1.55
21		*V*	53971.347	49	53971.359	25.17	3.43	0.023	2.6 ± 1.6	5.0 ± 1.4	1.98
22		*R*	53971.346	49	53971.358	24.07	2.56	0.015	–	5.5 ± 2.2	> 0.87
23	F9	*V*	54003.386	33	54003.396	24.48	7.44	0.045	4.5 ± 1.4	5.8 ± 1.6	5.16
24	F10	*V*	54324.568	58	54324.579	23.98	12.97	0.047	–	12.1 ± 1.7	> 6.22
25	F11	*V*	54330.631	25	54330.639	24.58	4.34	0.027	–	$\sim$1.0	> 0.32
26	F12	*V*	54347.557	66	54347.572	24.95	24.25	0.062	5.0 ± 1.0	20.7 ± 3.3	14.63
27	F13	*V*	54372.403	202	54372.466	24.04	231.62	1.023	11.2 ± 0.7	22.0 ± 1.3	153.61
28	F14	*U*	54390.293	50	54390.305	3.28	5.56	0.127	3.2 ± 0.7	2.6 ± 0.9	1.10
29		*B*	54390.290	50	54390.307	10.27	8.15	0.041	5.8 ± 0.7	–	> 1.09
30		*V*	54390.293	49	54390.307	24.05	4.19	0.026	6.5 ± 1.4	–	> 1.83
31		*R*	54390.294	48	54390.306	23.15	3.28	0.018	1.9 ± 0.9	0.9 ± 0.6	0.54
32	F15	*U*	54657.392	22	54657.401	3.27	5.36	0.161	–	2.3 ± 1.0	> 0.54
33	F16	*U*	54657.503	46	54657.516	3.23	4.15	0.115	$\sim$3.2	5.8 ± 1.3	1.48
34		*B*	54657.504	43	54657.517	10.27	3.45	0.028	7.3 ± 2.3	3.6 ± 1.0	1.42
35	F17	*U*	54747.324	33	54747.336	3.56	3.87	0.067	–	1.0 ± 0.4	> 0.11
36	F18	*U*	55070.300	26	55070.307	3.53	4.92	0.097	$\sim$2.0	2.6 ± 1.3	0.71
37		*B*	55070.298	26	55070.308	10.77	3.14	0.017	$\sim$2.6	$\sim$0.4	0.26
38	F19	*U*	55071.261	72	55071.289	3.25	3.04	0.077	11.2 ± 4.5	9.1 ± 2.9	2.26
39	F20	*U*	55071.335	57	55071.350	3.29	3.13	0.078	$\sim$4.2	7.8 ± 2.5	1.40
40		*B*	55071.337	56	55071.349	10.52	5.68	0.040	$\sim$0.9	3.7 ± 1.4	0.87
41		*V*	55071.337	55	55071.350	24.60	3.17	0.022	11.1 ± 2.2	–	>2.73
42		*R*	55071.338	52	55071.349	23.73	3.59	0.021	9.4 ± 2.6	–	>2.09

Notes. [a]Flare start time; [b]Flare duration; [c]Flare peak time; [d]Local mean flux (F_{lm}) in unit 10^{-11} erg s^{-1} cm^{-2}; [e]measure of maximum flux increase during flare from quiescent level in multiple of σ_{ql}; [f]Amplitude of the flare; [g, h]e-folding rise and decay time of flare; [i]Flare energy.

start time, flare peak time, flare durations, and flare amplitudes are given in fourth, sixth, fifth, and ninth column of Table 3.

The flare energy is computed using the area under the flare light curve i.e. the integrated excess flux ($F_e(t)$) released during the flare as

$$E_{flare} = 4\pi d^2 \int F_e(t)\,dt \tag{2}$$

With a distance (d) of 25.1 pc for LO Peg (Perryman et al. 1997), the derived values of energy in different filters for all detected flares are given in column 12 of Table 3. The flare energies are found in between 9×10^{30} erg and 1.54×10^{34} erg. The most energetic flare is the longest flare. Since the total energy released by the flare must be smaller than (or equal to) the magnetic energy stored around the star-spots (i.e. $E_{flare} \leq E_{mag}$), the minimum magnetic field can be estimated during the flare as $E_{mag} \propto B^2 l^3$. Assuming the loop-length of typical flares on G-K stars are of the order of 10^{10} cm (see Güdel et al. 2001; Pandey & Singh 2008). The minimum magnetic field in the observed flares are estimated to be 0.1–3.5 kG.

3.4 Surface imaging with light-curve inversion technique

In order to determine locations of spots on the stellar surface, we have performed inversion of the phased light curves into

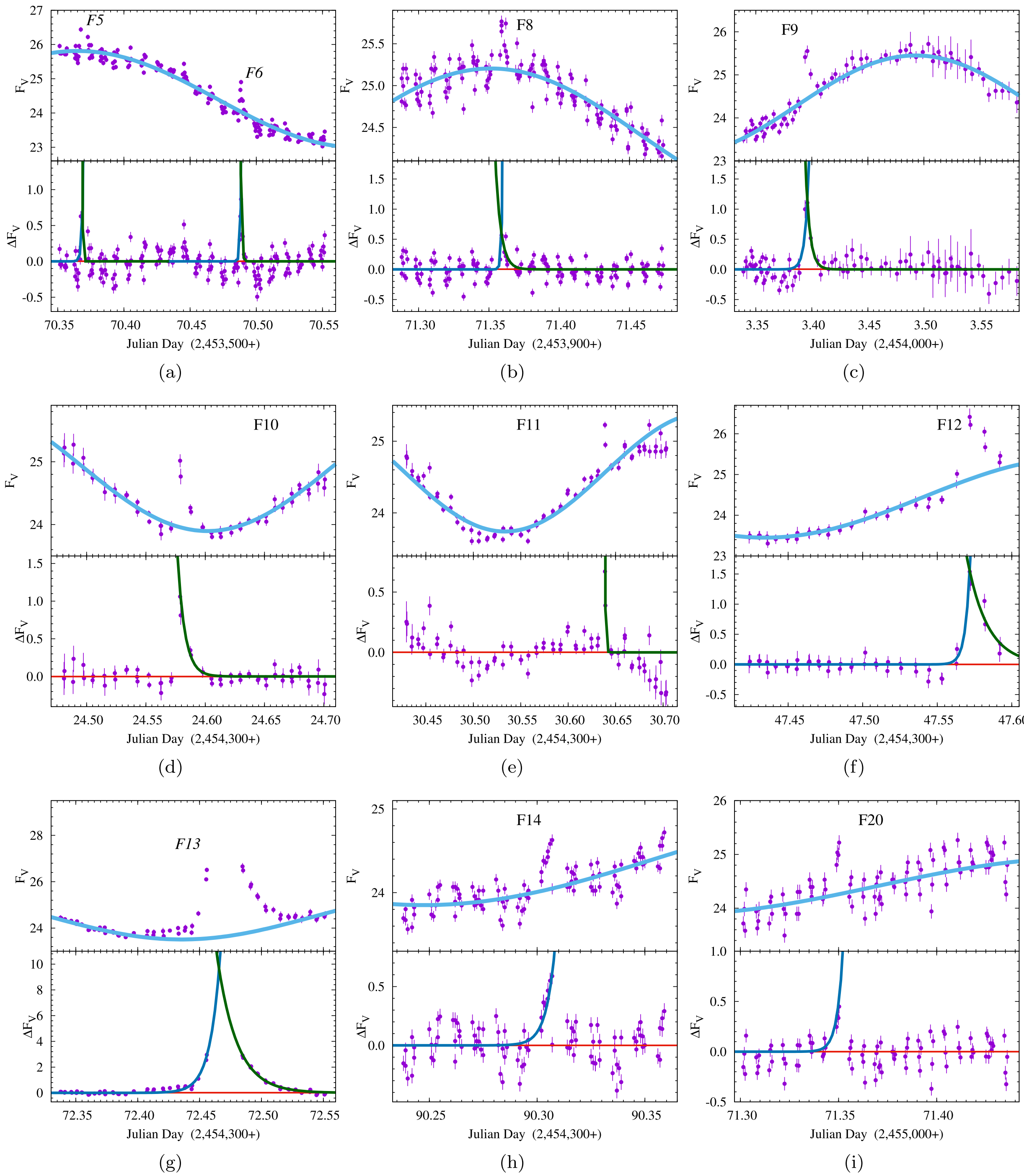

Figure 7. Light curves of all detected *V*-band flares on LO Peg. Top panel of each plot shows the light curve along with best-fitted sinusoid. The bottom panel shows the detrended light curve along with best-fitted exponential functions fitted to flare rise and/or flare decay.

stellar images using the light-curve inversion code (IPH; see Savanov & Strassmeier 2008; Savanov & Dmitrienko 2011). The model assumes that, due to the low spatial resolution, the local intensity of the stellar surface always has a contribution from the photosphere (I_P) and from cool spots (I_S) weighted by the fraction of the surface covered by spots, i.e. the spot-filling factor f by the following relation: $I = f \times I_P + (1 - f) \times I_S$; with $0 < f < 1$. The inversion of a light curve results in a distribution of the spot-filling factor (f) over the visible stellar surface. Although this approach is less informative than the Doppler imaging technique (see Strassmeier & Bartus 2000; Barnes et al. 2005; Piluso et al. 2008); however, analysis of long time series of photometric observations allows us to recover longitudinal spot patterns and study of their long-term evolution.

We could make 47 time intervals by manual inspection such that each interval had a sufficient number of data points and had no noticeable changes in their shape. Individual light curves were analysed using the IPH code. Several sets of time interval contain a large number of observations within it (e.g. set 33 includes 1007

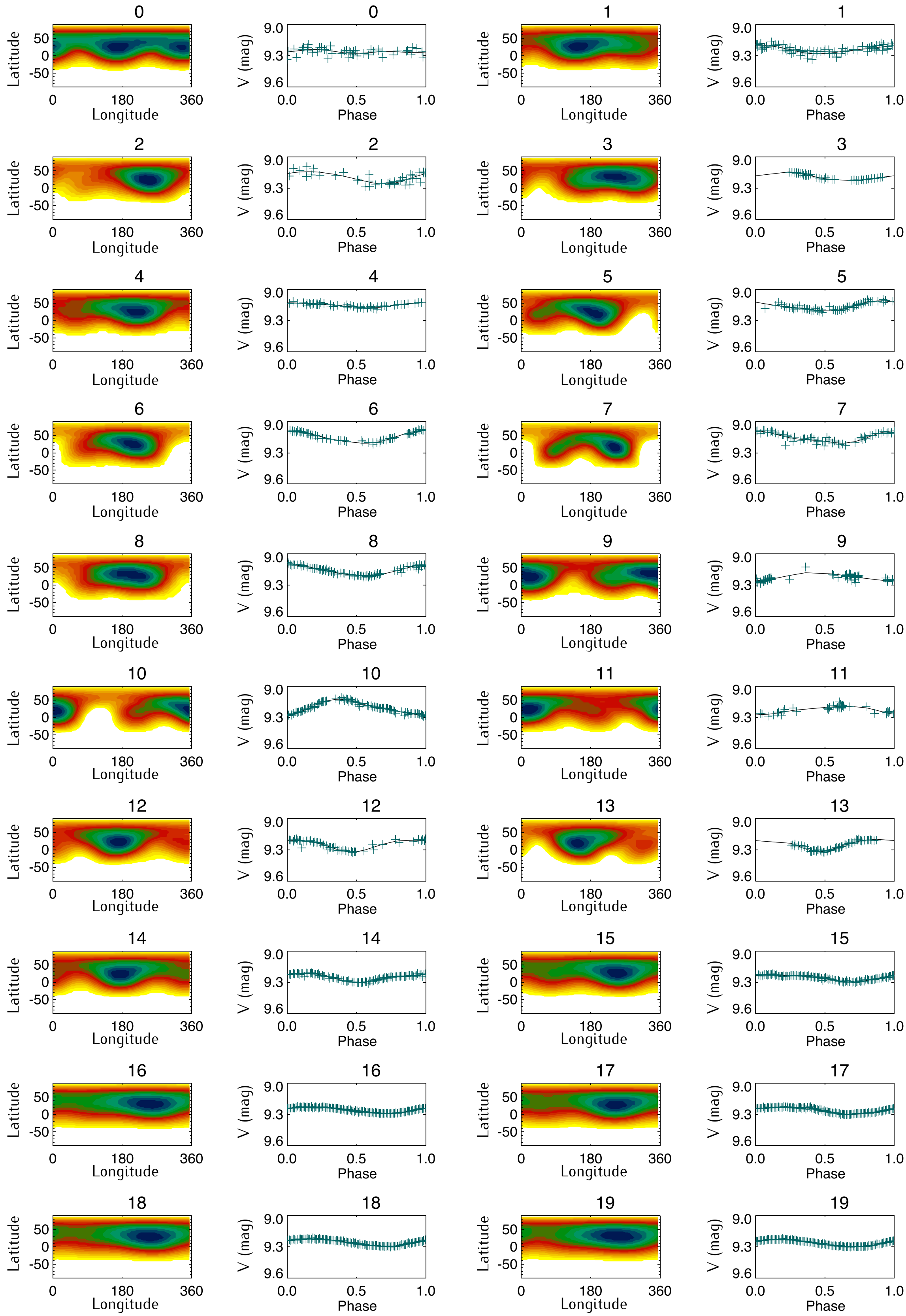

Figure 8. The surface temperature inhomogeneity maps of LO Peg for 47 epochs are shown in left-hand panels (first and third columns). The surface maps are presented on the same scale, with darker regions corresponding to higher spot-filling factors. Right-hand panels (second and fourth columns) show the light curves folded on each epoch. Observed and calculated *V*-band light curves are presented by crosses and continuous lines, respectively.

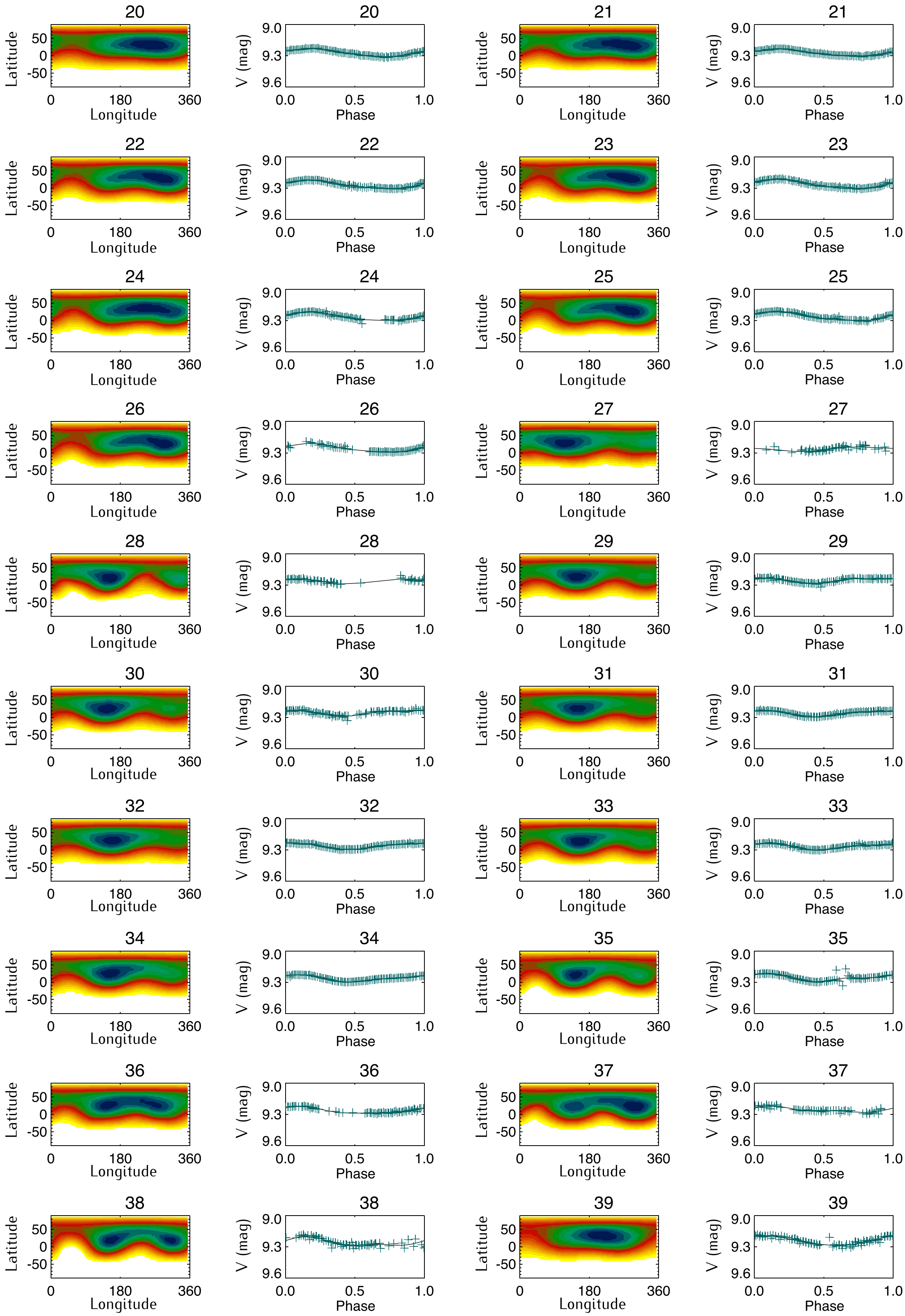

Figure 8. (continued).

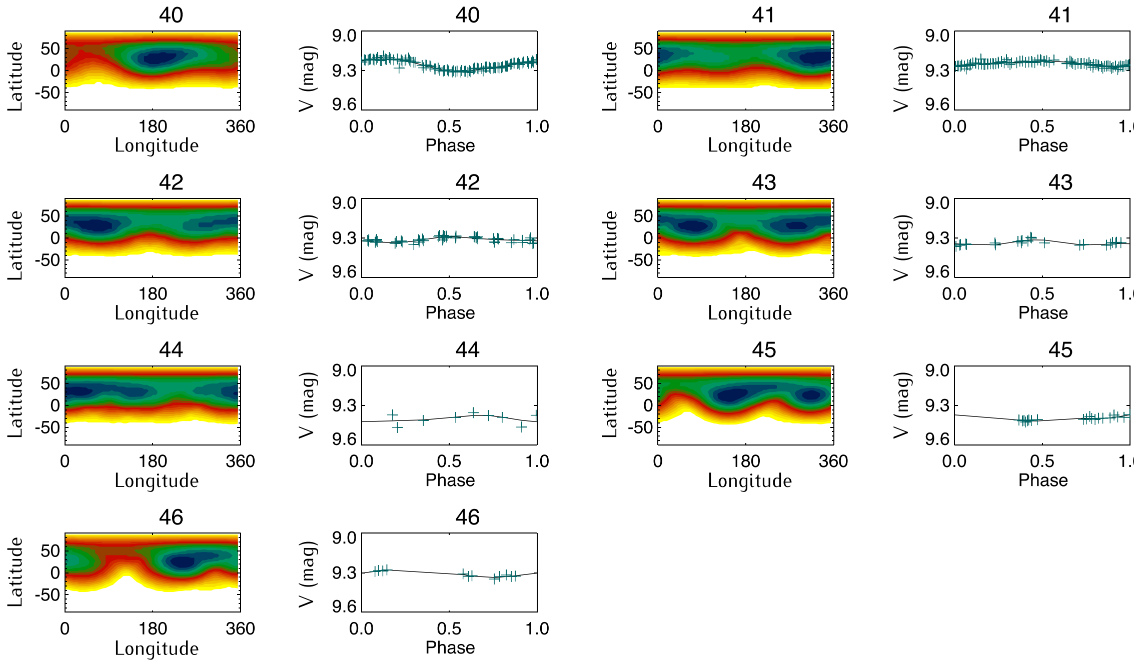

Figure 8. (continued).

measurement), in those cases we divided the time axis of the phase diagram into 100 bins and averaged the measurements. In our modelling, the surface of the star was divided into a grid of 6° × 6° pixels (unit areas), and the values of *f* were determined for each grid pixel. We adopt the photospheric temperature of LO Peg to be ∼4500 K (see Pandey et al. 2005) and the spot temperature to be 750 K lower than the photospheric temperature (Piluso et al. 2008; Savanov & Dmitrienko 2011). The stellar astrophysical input includes a set of photometric fluxes calculated from atmospheric model by Kurucz (1992) as a function of temperature and gravity. For LO Peg, the '*i*' was precisely determined with the analysis of a very extensive set of high-resolution spectra (see Barnes et al. 2005; Piluso et al. 2008), therefore, in our reconstruction of the temperature inhomogeneity maps we safely fixed the inclination angle at 45°. Various test cases were performed to recover the artificial maps and include data errors and different input parameter errors which demonstrate the robustness of our solution to various false parameters.

Fig. 8 shows the reconstructed temperature inhomogeneity maps of LO Peg, which reveal that the spots have a tendency to concentrate at two longitudes corresponding to two active regions on the stellar surface. The difference between two active longitudes was found to be inconstant. The uncertainty in the positions of the active longitudes on the stellar surface was on average of about 6° (or 0.02 in phase). The derived stellar parameters active longitude regions (ψ_1, ψ_2), spottedness (Sp), and *V*-band amplitudes ($A_{\rm LI}$) corresponding to each surface brightness map shown in Fig. 8 are plotted with HJD in Fig. 9. The filled and open circles in Fig. 9(b) show high and low active regions, respectively. The derived parameters are also given in Table 4. First three surface maps were created with the sparse data of *Hipparcos* satellite, and to create good-quality maps, data of ∼2, ∼0.5, and ∼0.5 yr were used. We get a signature of presence of two equal spot groups ∼170° apart in first two years (1989 to 1991), whereas the presence of single spot group was indicated with the surface map of the third year (1992). From 2001 to 2013 with ground-based observations and archival data, it became possible to create at least one surface map per year. Using high-cadence data of SuperWASP in 2006 and 2007, we created 12 surface maps (Set-15 to Set-26) in three months of 2006 (July 27th to November 4th) and 10 surface maps (Set-27 to Set-36) in three months of 2007 (July 24th to December 19th). This enables us to make a detailed study on the surface structure of LO Peg. It appears that LO Peg consists only one spot group during the observations of 2006 August (Set-16 to Set-21). In 2006 September, migration from single spotted surface to double spotted surface was clearly noticeable (Set-22 to Set-26). Both spots are separated by <115°. Two spot groups were also observed during 2007, but the separations of two spot groups were >125°. It was also noticed that the active regions changed their position from 2006 to 2007, which indicates a flip-flop cycle of ∼1 yr (see shaded regions on the Fig. 9b). Similar phenomena were also noticed during the year 2004 and 2005 with an approximately same period. But due to uncertainty on the position of the spot groups, it was not possible to say whether the flip-flop cyclic behaviour continues in later years.

The total area of the visible stellar surface covered by spots, known as spottedness (Sp), varies within a range of 8.8–25.7 per cent (see Fig. 9c), with a median value of 16.3 per cent. From the year 2001 to 2005, it was found to decrease until its minimum in 2003 August, and then return to its median value in 2005. It remained constant for ∼4 yr at this value, and then increased to reach its maximum. Further the spottedness of the star has returned to its median value again. The time interval of returning to its median value was approximately same as 4 yr. As seen in Fig. 9(d), the amplitude of the brightness varies within a range 0.06–0.19 mag, with a median value of 0.12 mag.

3.5 Coronal and chromospheric features

The background subtracted X-ray light curves of LO Peg as observed with *Swift* XRT and *ROSAT* PSPC instruments are shown in the top panel of Fig. 2. The temporal binning of the X-ray light curves are 100 s. XRT light curves were obtained in energy band 0.3–10.0 keV, whereas *ROSAT* light curves were obtained in an

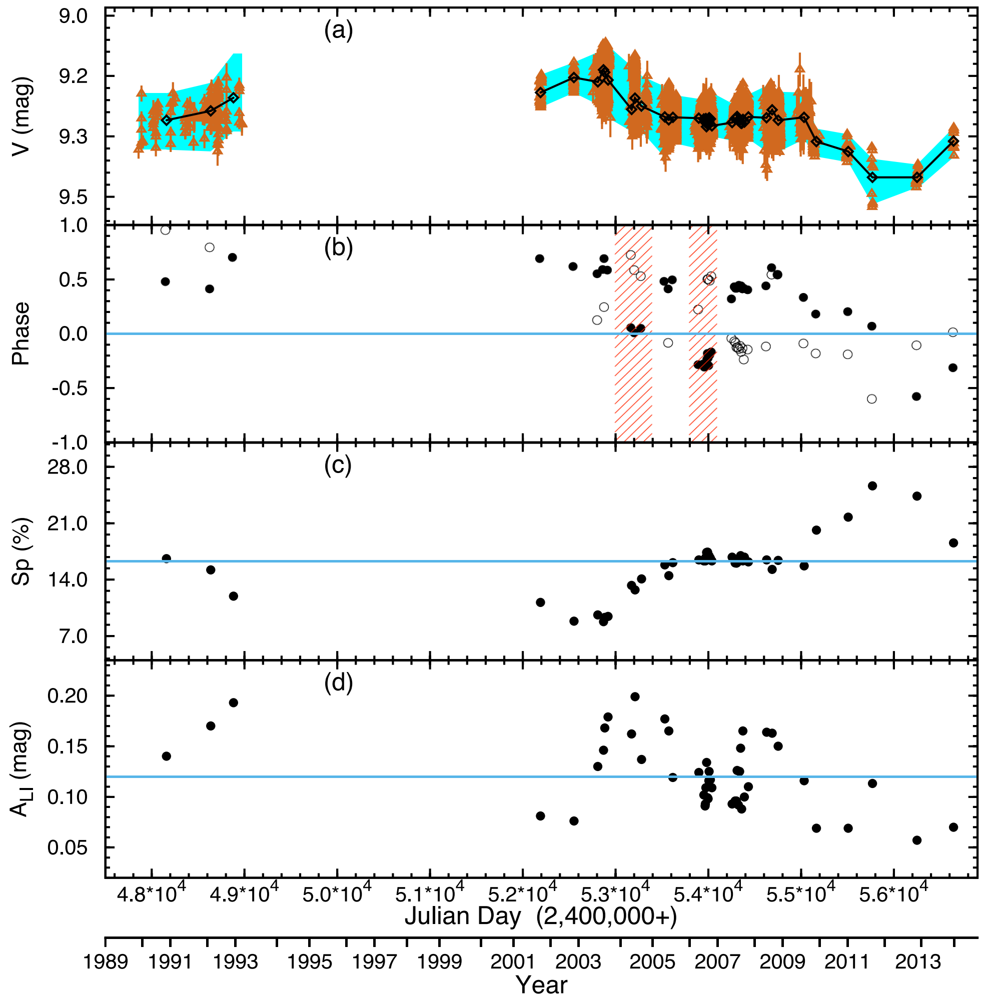

Figure 9. Parameters of LO Peg derived from modelling. From top to bottom – (a) *V*-band light curve of LO Peg (open triangles) plotted with mean magnitude of each epoch (open diamonds). The shaded regions show the errors in data points. (b) Phases/longitudes of spots recovered from light curve inversion. Filled and open circles show primary and secondary active longitudes, respectively. Vertical-shaded regions indicate the time intervals when the possible flip-flop events occur. (c) Recovered surface coverage of cool spots (per cent) on LO Peg. (d) The amplitude of brightness variations in unit of magnitude.

energy band 0.3–2.0 keV. *ROSAT* PSPC count rate were converted to *Swift* XRT count rate using WEBPIMMS[5], where we assumed two temperature components 0.27 and 1.08 keV and 0.2 solar abundances. To check for the variability, the significance of deviations from the mean count rate were measured using the standard χ^2-test. For our X-ray light curves, derived value of χ^2 is 664 which is very large in comparison to the 190 degrees of freedom ($\chi^2_\nu = 3.5$). This indicates that LO Peg is essentially variable in X-ray band.

On one occasion (ID: 00037810011), sudden enhancement of X-ray count rates was detected along with a simultaneous enhancement in UV count rates in each of the UV filters. This enhancement could be due to flaring activity, where flare peak count rates were $\sim$3 times higher than a quiescent level of 0.20 counts s^{-1}. The close inspection of the X-ray light curve shows the decay phase of the flare. We could not analyse this flare due to poor statistics. However, the flare duration was found to be 1.2 ks.

Fig. 10 shows the rotationally modulated X-ray, UV (uvm2 filter), and optical (*V* band) light curves. Observations of the year 2008 were used for rotational modulation, where we have removed the flaring feature from X-ray light curve. Optical and X-ray observations are $\sim$100 d apart. It appears that both X-ray and UV light curves were rotationally modulated. X-ray and UV light curves appear to be anti-correlated with *V*-band light curve. The Pearson correlation coefficients between X-ray and *V* band, and UV and *V*-band light curve were found to be −0.22 and −0.57, respectively.

The *Swift* XRT spectra of the star LO Peg, as shown in Fig. 11, were best fitted with two temperature (2T) astrophysical plasma model (APEC; Smith et al. 2001), with variable elemental abundances (Z). The interstellar hydrogen column density ($N_{\rm H}$) was left free to vary. Since all the parameters were found to be constant within a 1σ level, we determined the parameters from joint spectral fitting. The two temperatures and corresponding emission measures were 0.28 $\pm$ 0.04 keV and 1.03 $\pm$ 0.05 keV, and 3.1 $\pm$ 0.9 $\times$ 10^{52} cm^{-3} and 4.6 $\pm$ 0.6 $\times$ 10^{52} cm^{-3}, respectively. Global abundances were found to be 0.13 $\pm$ 0.02 solar unit ($Z_\odot$). The derived value of unabsorbed luminosity is given by $1.4^{+0.5}_{-0.4} \times 10^{29}$ erg s^{-1} cm^{-2}.

4 DISCUSSION

Using the long-term *V*-band photometry, we have obtained mean seasonal rotation period of 0.4231 $\pm$ 0.0001 d, which is very similar

[5] http://heasarc.nasa.gov/cgi-bin/Tools/w3pimms/w3pimms.pl

Table 4. Parameters derived from light-curve modelling.

Epoch	No. of points	HJD_{beg} (2400000+)	HJD_{end} (2400000+)	HJD_{middle} (2400000+)	V_{max} (mag)	V_{min} (mag)	V_{mean} (mag)	A_{LI} (mag)	Sp (per cent)	ψ_1 (°)	ψ_2 (°)	Note[a]
0	47	47857.50	48458.42	48157.96	9.193	9.333	9.260	0.140	16.6	172	342	e
1	74	48550.46	48717.97	48634.22	9.167	9.337	9.237	0.170	15.2	148	285	n
2	39	48788.25	48972.28	48880.26	9.094	9.287	9.204	0.193	11.9	252	–	n
3	37	52181.17	52198.13	52189.65	9.147	9.228	9.191	0.081	11.2	248	–	u
4	50	52546.21	52551.25	52548.73	9.116	9.192	9.154	0.076	8.8	222	–	n
5	232	52755.91	52860.68	52808.29	9.091	9.221	9.165	0.130	9.6	198	45	n
6	204	52863.39	52872.41	52867.90	9.071	9.217	9.135	0.146	8.8	212	–	n
7	168	52874.64	52890.55	52882.59	9.067	9.235	9.141	0.168	9.3	248	88	n
8	290	52893.59	52942.54	52918.07	9.075	9.254	9.160	0.179	9.4	210	–	n
9	74	53142.92	53199.49	53171.21	9.126	9.288	9.233	0.162	13.3	20	260	u
10	464	53203.42	53211.47	53207.44	9.098	9.297	9.205	0.199	12.7	3	210	n
11	36	53212.39	53344.52	53278.46	9.150	9.287	9.225	0.137	14.1	18	190	n
12	221	53487.92	53570.69	53529.30	9.176	9.353	9.252	0.177	15.8	173	–	n
13	242	53571.30	53574.69	53572.99	9.168	9.333	9.259	0.165	14.5	148	330	u
14	426	53584.66	53650.35	53617.51	9.197	9.316	9.253	0.119	16.1	178	–	n
15	746	53853.92	53938.68	53896.30	9.207	9.331	9.255	0.124	16.4	258	80	n
16	555	53943.57	53955.73	53949.65	9.200	9.302	9.257	0.102	16.3	260	–	n
17	315	53960.41	53963.44	53961.93	9.216	9.307	9.264	0.091	16.5	250	–	n
18	308	53966.46	53969.69	53968.08	9.210	9.303	9.258	0.093	16.3	253	–	n
19	638	53970.41	53973.68	53972.04	9.206	9.315	9.256	0.109	16.8	252	–	n
20	599	53975.40	53981.55	53978.48	9.194	9.328	9.276	0.134	17.4	260	–	n
21	504	53987.40	53994.62	53991.01	9.217	9.316	9.270	0.099	17.4	275	–	n
22	241	53995.36	53998.61	53996.98	9.212	9.310	9.258	0.098	17.1	295	180	n
23	286	54001.34	54005.59	54003.47	9.204	9.320	9.264	0.116	16.8	280	180	n
24	228	54006.39	54011.57	54008.98	9.206	9.331	9.254	0.125	16.9	255	–	n
25	242	54017.33	54023.38	54020.36	9.202	9.319	9.257	0.117	16.7	290	175	n
26	130	54029.40	54044.46	54036.93	9.191	9.300	9.274	0.109	16.3	300	190	n
27	181	54227.90	54281.78	54254.84	9.218	9.311	9.266	0.093	16.8	115	345	n
28	243	54283.77	54289.74	54286.75	9.207	9.303	9.256	0.096	16.1	155	335	u
29	266	54293.75	54305.73	54299.74	9.223	9.319	9.254	0.096	16.0	150	330	n
30	428	54306.49	54312.69	54309.59	9.204	9.330	9.251	0.126	16.1	150	315	n
31	686	54315.69	54328.70	54322.19	9.217	9.309	9.261	0.092	16.5	152	315	n
32	1007	54329.43	54340.68	54335.06	9.206	9.331	9.261	0.125	16.7	160	310	n
33	557	54343.59	54352.64	54348.12	9.179	9.327	9.267	0.148	17.0	155	320	n
34	546	54353.37	54364.53	54358.95	9.219	9.307	9.268	0.088	16.8	158	300	n
35	320	54368.37	54377.43	54372.90	9.169	9.334	9.258	0.165	16.3	148	312	n
36	333	54381.44	54394.27	54387.86	9.203	9.303	9.265	0.100	16.8	150	275	e
37	133	54405.31	54454.05	54429.68	9.196	9.306	9.252	0.110	16.2	145	308	n
38	224	54590.92	54661.78	54626.35	9.174	9.338	9.254	0.164	16.4	158	318	n
39	385	54663.77	54710.68	54687.22	9.169	9.332	9.234	0.163	15.3	218	–	n
40	452	54716.66	54785.52	54751.09	9.189	9.339	9.260	0.150	16.4	195	–	n
41	339	54954.92	55105.62	55030.27	9.191	9.307	9.253	0.116	15.7	120	328	n
42	47	55130.10	55196.05	55163.07	9.281	9.350	9.313	0.069	20.1	65	295	n
43	23	55489.16	55526.10	55507.63	9.295	9.364	9.338	0.069	21.8	73	292	u
44	9	55758.82	55775.77	55767.29	9.356	9.469	9.402	0.113	25.7	25	145	u
45	20	56239.14	56257.17	56248.16	9.370	9.427	9.402	0.057	24.3	153	322	u
46	12	56636.36	56645.36	56640.86	9.278	9.348	9.312	0.070	18.6	248	5	u

Notes. HJD_{beg}, HJD_{end}, and HJD_{middle} are start, end, and middle time of each epoch. V_{max}, V_{min}, and V_{mean} are maximum, minimum and mean magnitudes of LO Peg. A_{LI} is the amplitude of variability. Sp is the spottedness of the stellar surface. ψ_1 and ψ_2 are active longitudes.[a]e – size of both spots were approximately equal; n – size of both spots were different; u – uncertain results due to incomplete light curve.

to the previously determined period (Barnes et al. 2005). For the first time, we have studied long-term variations in LO Peg. A long-term periodicity with periods of ∼2.2 and ∼5.98 yr appears to present in the light curve. However, a long-term continuous monitoring is necessary to confirm any long-term periodicity. The first period is also found to be similar to the latitudinal spot migration period derived from SDR analysis, which could be similar to the 11 yr cycle of the solar butterfly diagram. This type of activity cycle was also observed in similar fast-rotating stars such as AB Dor (Collier Cameron & Donati 2002; Järvinen et al. 2005a) and LQ Hya (Messina & Guinan 2003). In the SDR analysis, the decrease in photometric periods within most of the cycles is reminiscent of the sunspot cyclic behaviour, where the latitude of spot-forming region moves towards the equator, i.e. towards progressively faster rotating latitudes along an activity cycle, and spot groups were present within ±45° latitude of LO Peg. This finding indicates that LO Peg has a solar-like SDR pattern. From spectroscopic analysis, Piluso et al. (2008) also detected the presence of such lower latitude spots. It is interesting to note that the slope of the rotational period on LO Peg varies and therefore SDR amplitude $\Delta P\,(= P_{max} - P_{min})$

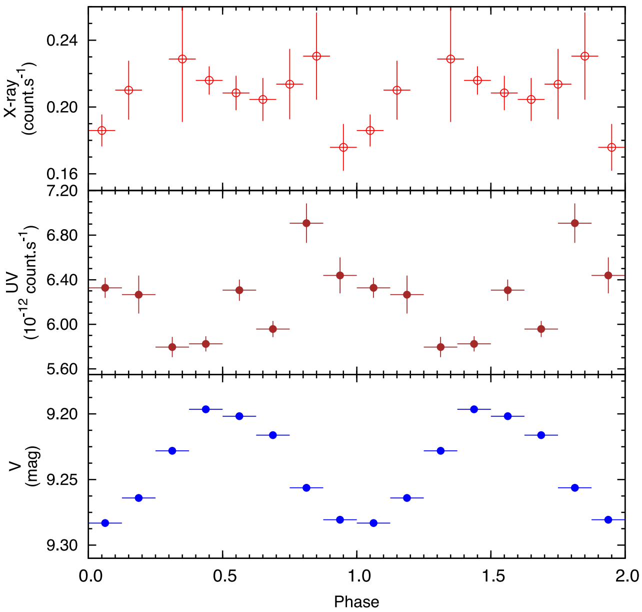

Figure 10. From top to bottom the X-ray, UV, and optical folded light curves are shown. Each folded light curve is binned at bin-size 0.1.

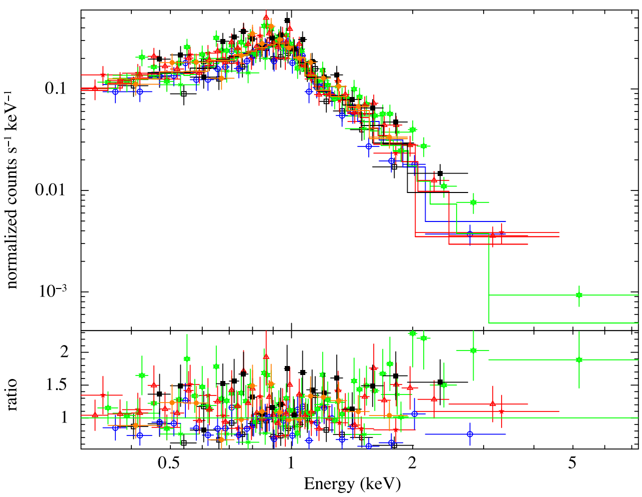

Figure 11. X-ray Spectra of LO Peg obtained from *Swift* XRT along with the best-fitting APEC 2T model (top panel). Different symbols denote different observation IDs. The bottom panel represents the ratio of the observed counts to the counts predicted by best-fitting model.

changes from cycle to cycle. Similar behaviour was also observed in AB Dor (Collier Cameron & Donati 2002), BE Cet, DX Leo, and LQ Hya (Messina & Guinan 2003). This resembles either a wave of excess rotation on a time-scale of the order of decades, or a variation of the width of the latitude band in which spots occur. LO Peg shows a change in rotation period from 0.431 33 to 0.417 43 d, which corresponds to ~3 km s^{-1} change in $v\sin i$, which is nearly 15 times more than AB Dor. We have estimated the differential rotation on LO Peg with $\Delta\Omega/\Omega$ ranging from 0.001–0.03, which is similar to that obtained by Barnes et al. (2005). AB Dor and LQ Hya having very similar spectral class and periodicity showed similar feature with the star LO Peg. Derived values of $\Delta\Omega/\Omega$ for AB Dor (Collier Cameron & Donati 2002) and LQ Hya (Berdyugina, Pelt & Tuominen 2002) are also similar to that for LO Peg. During more than two decades of observations only in 2003 September LO Peg was observed both photometrically (Taş 2011) and spectroscopically (Piluso et al. 2008). In our SDR analysis, the first point of cycle-VI corresponds to that time interval (see Table 2 and Fig. 5). This time interval being at the starting of the cycle indicates the period corresponds to higher latitude. Therefore, we expect presence of spots on higher latitude on the surface of LO Peg. Piluso et al. (2008) have also found star-spot concentration towards the polar region.

A positive correlation between the absolute value of SDR and the stellar rotation period was predicted by dynamo models according to a power law (Kitchatinov & Rüdiger 1999) i.e. $\Delta P \;\alpha\; P^n_{\rm rot}$; where ΔP is the SDR amplitude, $P_{\rm rot}$ is the rotational period and n is the power index. Kitchatinov & Rüdiger (1999) found that n varies with both rotation rate and with spectral type. This power-law dependence is confirmed by observational data (Hall 1991; Henry, Fekel & Hall 1995), although the observational and theoretical values of n differ (see Messina & Guinan 2003). Fig. 12 shows the plot between ΔP and $P_{\rm rot}$ of LO Peg with other 14 stars with known activity cycles and SDR (Donahue & Dobson 1996; Gray & Baliunas 1997; Collier Cameron & Donati 2002; Messina & Guinan 2003). We found LO Peg (solid diamond) follows the same trend with the nearest candidate AB Dor. Including LO Peg, we derive the relation $\Delta P \;\alpha\; P^{1.4\pm0.1}_{\rm rot}$, which is very similar to the relations derived from other observational evidences such as $n = 1.4 \pm 0.5$ (Messina & Guinan 2003), $n = 1.30$ (Donahue & Dobson 1996), and $n = 1.15$–1.30 (Rüdiger et al. 1998). This indicates the disagreement between the observational ($n = 1.1$–1.4) and the theoretical ($n > 2$) values of power-law index (Kitchatinov & Rüdiger 1999).

Present surface imaging indicates that, in most of the cases the spots on LO Peg were concentrated in two groups separated by less than 180° along the longitude. Indication of the flip-flop effect in LO Peg is quite similar to that observed by Korhonen, Berdyugina & Tuominen (2002) and Järvinen et al. (2005b). The flip-flop phenomenon has been noticed for the first time by Jetsu et al. (1991) in the giant star FK Com. Later it was found to be cyclic in RS CVn and FK Com-type stars, as well as in some young solar analogues (e.g. Korhonen et al. 2002). After its discovery in cool stars, the flip-flop phenomena have also been reported in the Sun (Berdyugina & Usoskin 2003). This phenomenon is well explained by the dynamo-based solution where a non-axisymmetric dynamo component, giving rise to two permanent active longitudes 180° apart, is needed together with an oscillating axisymmetric magnetic field (Elstner & Korhonen 2005; Korhonen & Elstner 2005). Fluri & Berdyugina (2004) suggest another possibility with a combination of stationary axisymmetric and varying non-axisymmetric components. It also appears that, the flip-flop cycle is approximately one-third of the latitudinal spot migration cycle.

Modelling of LO Peg reveals that the stellar surface is spotted up to 25.7 per cent, which is very similar to that found in K-type stars XX Tri (Savanov 2014), V1147 Tau (Patel et al. 2013), LQ Hya, and MS Ser (Alekseev 2003). We did not see any relation between spottedness and cyclic behaviour or the rotational period. However, from the year 2005 to 2009 spottedness variation is found to be almost constant (shown in third panel of Fig 9). At the same time duration, SDR analysis also indicates that the seasonal rotational period and hence the latitude of the spot groups also remains constant (see cycle-VII in second panel of Fig. 5). This suggests that the magnetic activities remains constant within that period of time. In all other cycles, the seasonal rotational period and hence latitudinal spot groups follows solar-like butterfly pattern with a ~2.7 yr period. Whereas, spottedness variation does not show any periodic modulation. The observations of Set-8 (2003

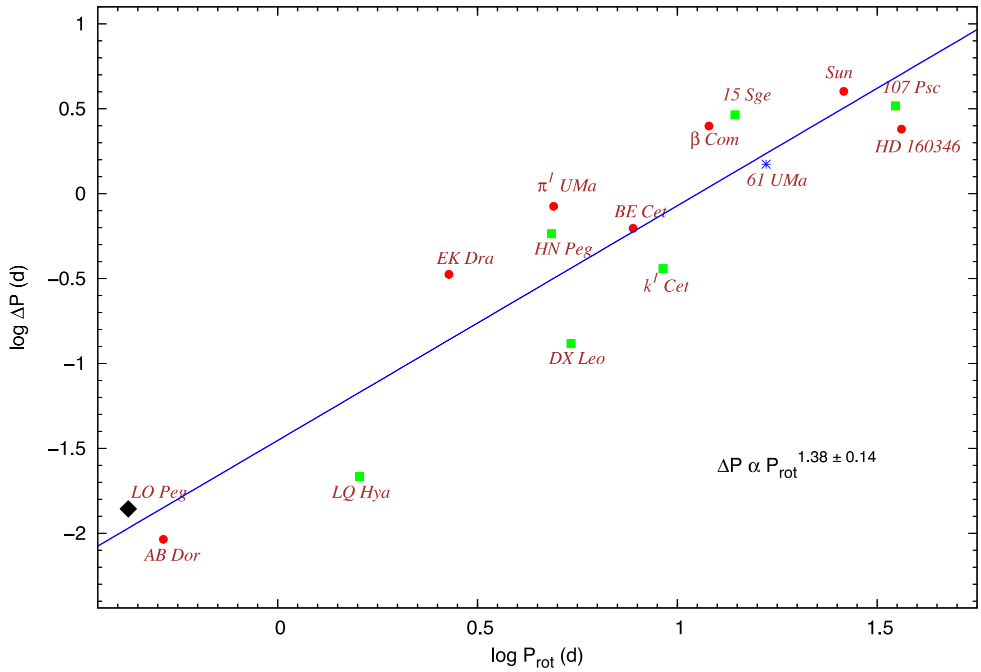

Figure 12. The log rotational period variations versus the mean rotational period of stars. Solid circle, solid squares, and asterisks denote the stars with solar, anti-solar and hybrid pattern. LO Peg is shown with solid diamond. The continuous line is a power-law fit to the whole sample.

September 11–October 30) are quasi-simultaneous with the spectroscopic observation of Piluso et al. (2008). During this period, our analysis shows single spot at phase 210°. Whereas Doppler imaging study of Piluso et al. (2008) shows a signature of low-latitude spot at phase ∼0.7. Correcting for the difference in ephemeris, we get the corresponding star-spot longitude to be ∼226°, which is almost similar to our derived value. The longer time span used in the generation of surface map may cause the difference between the two longitude positions. The brightness variability amplitudes of LO Peg were found to vary from 0.06 to 0.19 mag. This value is very similar to variability amplitude of other K-type stars such as V1147 Tau (Patel et al. 2013), LQ Hya (Berdyugina et al. 2002), AB Dor (Järvinen et al. 2005a), and MS Ser (Alekseev 2003). Savanov (2014) detected the variability amplitude up to 0.8 mag in late-type star ASAS 063656-0521.0.

In our multiband photometric study, we detected a total of 20 optical flares with a frequency of ∼1 flare per two days. There are very few detailed studies of optical flares on UFRs due to constraints in their detection limit, detection timing, and very less flare frequency. Recent studies on optical flares done with ground-based observatories on DV Psc (Pi et al. 2014) and CU Cnc (Qian et al. 2012) show flare frequency of ∼2 flares per day and ∼1 flare per day, respectively, which is similar to that for LO Peg. However, several other studies done with *Kepler* satellite (Hawley et al. 2014; Lurie et al. 2015) on M dwarfs reveal that flare frequency varies over a wide range of ∼1 flare per month to ∼10 flares per day. In our study, we have also detected an X-ray flare simultaneously observed with the UV-band. Derived value of X-ray flare frequency is ∼3 flares per day. This suggests that LO Peg shows more activity in X-rays than in optical bands. Multiwavelength simultaneous studies of another UFR AB Dor also shows a similar behaviour (Lalitha et al. 2013). This implies that the corona is more active in comparison to photosphere in these stars. Most of the flares are ∼1 hr long with a minimum and maximum flare duration of ∼12 min and ∼3.4 hr. Flare observed on SV Cam (Patkos 1981), XY UMa (Zeilik, Elston & Henson 1982), DK CVn (Dal, Sipahi & Özdarcan 2012), FR Cnc (Golovin et al. 2012), AB Dor (Lalitha et al. 2013), and DV Psc (Pi et al. 2014) studied in optical bands also lie in the same range. Several flares observed on M-dwarfs by Hawley et al. (2014) show similar feature but with a flare duration of ∼2 min. The derived flare amplitudes on LO Peg were found to be higher in shorter wavelengths than that in longer wavelengths (see two representative flares in Fig. 6). Similar feature was also found in multiwavelength studies of the flare on FR Cnc (Golovin et al. 2012). Although most of the flares occurred on LO Peg show the usual fast rise and slow decay, there were a few flares that show the reverse phenomena. This was also previously observed on K-type star V711 Tau (Zhang et al. 1990), which may be the result of complex flaring activity at the rise phase of the flare which could not be resolved due to instrumental limitations. Davenport et al. (2014) show the existence of complex flares with high-cadence *Kepler* data which can be explained by a superposition of multiple flares. Flare energies derived for LO Peg lies in the range of $\sim 10^{31-34}$ erg. 17 out of 20 flares having energy less than 10^{33} erg, signifies more energetic flares are less in number. With *Kepler* data, Hawley et al. (2014) also detected most of the flares on M dwarf GJ 1243 having energy of the order of 10^{31} erg. One flare (F13) is found to have total energy more than 10^{34} erg, therefore, this flare can be classified as a Superflare (see Candelaresi et al. 2014). The derived energy of this flare was ∼10.5 times more than the next largest flare and 668 times more than the weakest flare observed on LO Peg. During the flare F13, the *V*-band magnitude increases up to 0.42 mag, similar enhancement in *V*-band mag also noticed in FR Cnc (Golovin et al. 2012). We inspected the list of flares for further evidence of a correlation between flare timing and orientation of the dominant spot group. The phase minima as a function of flare phase is plotted in Fig. 13(a), where we did not find any correlation. This finding is also consistent with the flare study of Hunt-Walker et al. (2012) and Roettenbacher et al. (2013). From this result, we conclude that most of the flares on LO Peg may not originate in the strongest spot group, but rather come from

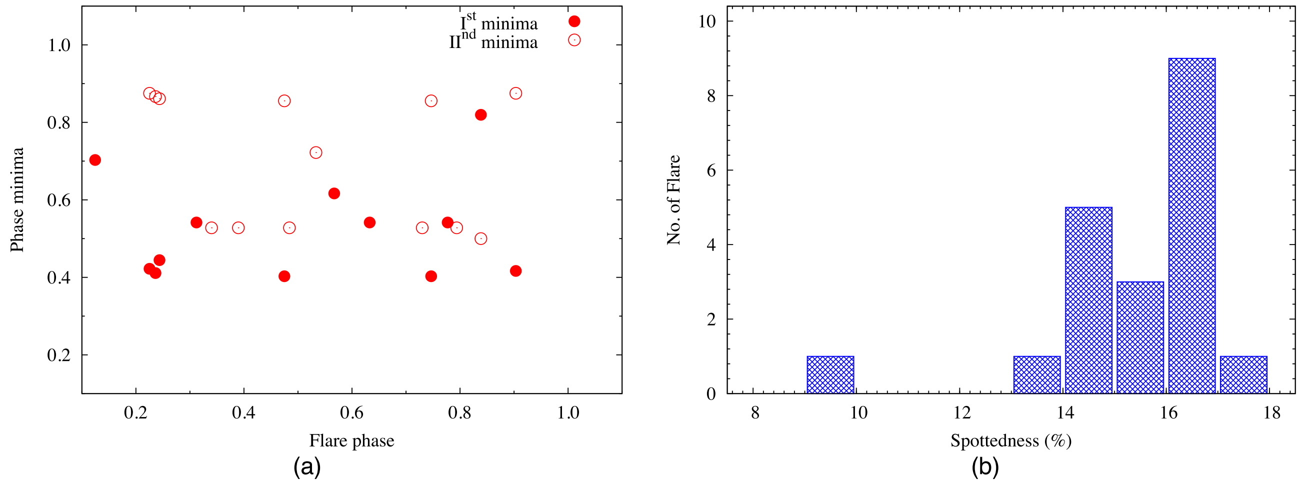

Figure 13. (a) Phase minima is plotted as a function of flare peak phase. (b) Observed distribution of detected flares with stellar spottedness.

small spot structures or polar spots. In order to check whether the spottedness on the stellar surface is related to occurrence rate of flare, we plotted the distribution of detected flares in each percentage binning of spottedness shown in Fig. 13(b). Most of the flares detected on LO Peg are found to occur within a spottedness range of 13–18 per cent, with a highest number of nine flares occurred at a spottedness range of 16–17 per cent.

The coronal parameters derived in this study are very similar to that derived by Pandey et al. (2005) using *ROSAT* data. The corona of LO Peg consists of two temperature, which is similar to few UFRs such as Speedy Mic, YY Gem, and HK Aqr (Singh et al. 1999), whereas it differs from other UFRs such as AB Dor, HD 283572, and EK Dra (Güdel et al. 2001; Scelsi et al. 2005), which consists of three temperature corona. From the present analysis, light curve in X-ray and UV band were found to be anti-correlated with optical *V* band. This feature was also noticed in similar type of stars such as HR 1099, σ Gem, V1147 Tau, and AB Dor (Agrawal & Vaidya 1988; Lalitha et al. 2013; Patel et al. 2013) which indicates the presence of high chromospheric and coronal activity in the spotted region.

5 SUMMARY

In this study, with ~24 yr long photometric observations from different worldwide telescopes, and X-ray and UV observations obtained with *Swift* satellite, we have investigated the properties of a UFR LO Peg. The results of this study are summarized as below.

(i) The rotational period of LO Peg steadily decreases along the activity cycle, jumping back to higher values at the beginning of the next cycle with a cycle of 2.7 ± 0.1 yr, indicating a solar-like SDR pattern on LO Peg.

(ii) We have detected 20 optical flares, where the most energetic flare has energy of $10^{34.2}$ erg whereas the least energetic flare has energy of $10^{30.9}$ erg with flare duration range of 12–202 min.

(iii) Our inversion of phased light curves show the surface coverage of cool spots are in the range of ~9–26 per cent. Evidence of flip-flop cycle of ~1 yr is also found.

(iv) Corona of LO Peg consist of two temperatures of ~3 MK and ~12 MK. Quasi-simultaneous observations in X-ray, UV, and optical *UBVR* bands show a signature of high X-ray and UV activities in the direction of spotted regions.

ACKNOWLEDGEMENTS

We thank the referee for his/her comments and suggestions that helped to considerably improve the manuscript. This research has been done under the Indo–Russian DST-RFBR project reference INT/RUS/RFBR/P-167 (for India) and Grant RFBR Ind_a 14-02-92694 (for Russia). SJ acknowledges the grant received under the Indo–Russian DST-RFBR project reference INT/RUS/RFBR/P-118. We acknowledge NASA Exoplanet Archive, All Sky Automated Survey archive, *Hipparcos* archive, *Swift* archive, and different telescope facilities we used to carry out our research.

REFERENCES

Agrawal P. C., Vaidya J., 1988, MNRAS, 235, 239
Alekseev I. Y., 2003, Astron. Rep., 47, 430
Baliunas S. L., Vaughan A. H., 1985, ARA&A, 23, 379
Barnes J. R., Collier Cameron A., Lister T. A., Pointer G. R., Still M. D., 2005, MNRAS, 356, 1501
Benz A. O., Güdel M., 2010, ARA&A, 48, 241
Berdyugina S. V., Usoskin I. G., 2003, A&A, 405, 1121
Berdyugina S. V., Pelt J., Tuominen I., 2002, A&A, 394, 505
Bessell M. S., 1979, PASP, 91, 589
Burrows D. N. et al., 2005, Space Sci. Rev., 120, 165
Byrne P. B., McKay D., 1989, A&A, 223, 241
Candelaresi S., Hillier A., Maehara H., Brandenburg A., Shibata K., 2014, ApJ, 792, 67
Collier Cameron A., Donati J.-F., 2002, MNRAS, 329, L23
Csorvási R., 2006, in Forgács-Dajka E., ed., Proc. 4th Workshop of Young Researchers in Astronomy & Astrophysics, Vol. 17, Photometry of LO Pegasi in B, V, R colors. Eotvos Lorand University, Budapest, p. 95
Dal H. A., Taş G., 2003, Inf. Bull. Var. Stars, 5390, 1
Dal H. A., Sipahi E., Özdarcan O., 2012, PASA, 29, 54
Das H. K., Menon S. M., Paranjpye A., Tandon S. N., 1999, Bull. Astron. Soc. India, 27, 609
Davenport J. R. A. et al., 2014, ApJ, 797, 122
Dhillon V. S., Privett G. J., Duffey K. P., 2001, PERIOD – A Time-Series Analysis Package. Starlink User Note, 167
Donahue R. A., Dobson A. K., 1996, in Pallavicini R., Dupree A. K., eds, ASP Conf. Ser. Vol. 109, Cool Stars, Stellar Systems, and the Sun. Astron. Soc. Pac., San Francisco, p. 599
Eibe M. T., Byrne P. B., Jeffries R. D., Gunn A. G., 1999, A&A, 341, 527
Elstner D., Korhonen H., 2005, Astron. Nachr., 326, 278
Fluri D. M., Berdyugina S. V., 2004, Sol. Phys., 224, 153

Gehrels N. et al., 2004, ApJ, 611, 1005
Gershberg R. E., 2005, Solar-Type Activity in Main-Sequence Stars. Springer-Verlag, Berlin
Golovin A. et al., 2012, MNRAS, 421, 132
Gray D. F., Baliunas S. L., 1997, ApJ, 475, 303
Güdel M. et al., 2001, A&A, 365, L336
Hall D. S., 1991, in Tuominen I., Moss D., Rüdiger G., eds, Lecture Notes in Physics, Vol. 380, IAU Colloq. 130: The Sun and Cool Stars. Activity, Magnetism, Dynamos. Springer-Verlag, Berlin, p. 353
Hawley S. L., Davenport J. R. A., Kowalski A. F., Wisniewski J. P., Hebb L., Deitrick R., Hilton E. J., 2014, ApJ, 797, 121
Henry G. W., Fekel F. C., Hall D. S., 1995, AJ, 110, 2926
Horne J. H., Baliunas S. L., 1986, ApJ, 302, 757
Hunt-Walker N. M., Hilton E. J., Kowalski A. F., Hawley S. L., Matthews J. M., 2012, PASP, 124, 545
Järvinen S. P., Berdyugina S. V., Tuominen I., Cutispoto G., Bos M., 2005a, A&A, 432, 657
Järvinen S. P., Berdyugina S. V., Strassmeier K. G., 2005b, A&A, 440, 735
Jeffries R. D., Byrne P. B., Doyle J. G., Anders G. J., James D. J., Lanzafame A. C., 1994, MNRAS, 270, 153
Jetsu L., Pelt J., Tuominen I., Nations H., 1991, in Tuominen I., Moss D., Rüdiger G., eds, Lecture Notes in Physics, Vol. 380, IAU Colloq. 130: The Sun and Cool Stars. Activity, Magnetism, Dynamos. Springer-Verlag, Berlin, p. 381
Kitchatinov L. L., Rüdiger G., 1999, A&A, 344, 911
Korhonen H., Elstner D., 2005, A&A, 440, 1161
Korhonen H., Berdyugina S. V., Tuominen I., 2002, A&A, 390, 179
Kuijpers J., 1989, Sol. Phys., 121, 163
Kurucz R. L., 1992, in Barbuy B., Renzini A., eds, Proc. IAU Symp. 149, The Stellar Populations of Galaxies. Kluwer, Dordrecht, p. 225
Lalitha S., Fuhrmeister B., Wolter U., Schmitt J. H. M. M., Engels D., Wieringa M. H., 2013, A&A, 560, A69
Lister T. A., Collier Cameron A., Bartus J., 1999, MNRAS, 307, 685
Lurie J. C., Davenport J. R. A., Hawley S. L., Wilkinson T. D., Wisniewski J. P., Kowalski A. F., Hebb L., 2015, ApJ, 800, 95
Messina S., Guinan E. F., 2003, A&A, 409, 1017
Oláh K. et al., 2009, A&A, 501, 703
Osten R. A., Kowalski A., Sahu K., Hawley S. L., 2012, ApJ, 754, 4
Pandey J. C., Singh K. P., 2008, MNRAS, 387, 1627
Pandey J. C., Singh K. P., Drake S. A., Sagar R., 2005, AJ, 130, 1231
Pandey J. C., Medhi B. J., Sagar R., Pandey A. K., 2009, MNRAS, 396, 1004
Parks J. R., White R. J., Schaefer G. H., Monnier J. D., Henry G. W., 2011, in Johns-Krull C., Browning M. K., West A. A., eds, ASP Conf. Ser. Vol. 448, 16th Cambridge Workshop on Cool Stars, Stellar Systems, and the Sun. Astron. Soc. Pac., San Francisco, p. 1217
Patel M. K., Pandey J. C., Savanov I. S., Prasad V., Srivastava D. C., 2013, MNRAS, 430, 2154
Patkos L., 1981, Astrophys. Lett., 22, 1
Perryman M. A. C. et al., 1997, A&A, 23, L49
Pi Q.-f., Zhang L.-Y., Li Z.-m., Zhang X.-l., 2014, AJ, 147, 50
Piluso N., Lanza A. F., Pagano I., Lanzafame A. C., Donati J.-F., 2008, MNRAS, 387, 237
Pojmanski G., 2002, Acta Astron., 52, 397
Pollacco D. L. et al., 2006, PASP, 118, 1407
Press W. H., Rybicki G. B., 1989, ApJ, 338, 277
Qian S.-B. et al., 2012, MNRAS, 423, 3646
Reinhold T., Arlt R., 2015, A&A, 576, A15
Reinhold T., Reiners A., Basri G., 2013, A&A, 560, A4
Roettenbacher R. M., Monnier J. D., Harmon R. O., Barclay T., Still M., 2013, ApJ, 767, 60
Roming P. W. A. et al., 2005, Space Sci. Rev., 120, 95
Rüdiger G., von Rekowski B., Donahue R. A., Baliunas S. L., 1998, ApJ, 494, 691
Sakamoto T., Donato D., Gehrels N., Okajima T., Ukwatta T. N., 2009, in Meegan C., Kouveliotou C., Gehrels N., eds, AIP Conf. Ser. Vol. 1133, GAMMA-RAY BURST: Sixth Huntsville Symposium. Am. Inst. Phys., New York, p. 244
Savanov I. S., 2014, Astron. Rep., 58, 478
Savanov I. S., Dmitrienko E. S., 2011, Astron. Rep., 55, 437
Savanov I. S., Strassmeier K. G., 2008, Astron. Nachr.', 329, 364
Scargle J. D., 1982, ApJ, 263, 835
Scelsi L., Maggio A., Peres G., Pallavicini R., 2005, A&A, 432, 671
Shibata K., Magara T., 2011, Living Rev. Sol. Phys., 8, 6
Shibayama T. et al., 2013, ApJS, 209, 5
Singh K. P., Drake S. A., Gotthelf E. V., White N. E., 1999, ApJ, 512, 874
Sinvhal S. D., Kandpal C. D., Mahra H. S., Joshi S. C., Srivastava J. B., 1972, in Optical astronomy with moderate size telescopes. p. 20
Smith R. K., Brickhouse N. S., Liedahl D. A., Raymond J. C., 2001, ApJ, 556, L91
Strassmeier K. G., Bartus J., 2000, A&A, 354, 537
Taş G., 2011, Astron. Nachr., 332, 57
Vogt S. S., Penrod G. D., 1983, PASP, 95, 565
Walker G. A. H. et al., 2007, ApJ, 659, 1611
Zacharias N., Monet D. G., Levine S. E., Urban S. E., Gaume R., Wycoff G. L., 2004, BAAS, 36, 1418
Zeilik M., Elston R., Henson G., 1982, Inf. Bull. Var. Stars 2200, 1
Zhang R.-X., Zhai D.-S., Zhang X.-B., Zhang J.-T., Li Q.-S., 1990, Inf. Bull. Var. Stars, 3456, 1

This paper has been typeset from a TEX/LATEX file prepared by the author.

The Astrophysical Journal, 840:102 (12pp), 2017 May 10 https://doi.org/10.3847/1538-4357/aa6cb0

X-Ray Superflares on CC Eri

Subhajeet Karmakar[1,2], J. C. Pandey[1], V. S. Airapetian[3], and Kuntal Misra[1]
[1] Aryabhatta Research Institute of observational sciencES (ARIES), Nainital 263002, India; subhajeet@aries.res.in
[2] Pt. Ravishankar Shukla University, Raipur 492010, India
[3] NASA Goddard Space Flight Center, 8800 Greenbelt Road, Greenbelt, Maryland 20771, USA
Received 2016 August 4; revised 2017 April 5; accepted 2017 April 9; published 2017 May 12

Abstract

We present an in-depth study of two superflares (F1 and F2) detected on an active binary star CC Eridani by the *Swift* observatory. These superflares triggered the Burst Alert Telescope (BAT) in the hard X-ray band on 2008 October 16 and 2012 February 24. The rise phases of both the flares were observed only with BAT, whereas the decay phases were observed simultaneously with the X-ray Telescope. It has been found that the flares decay faster in the hard X-ray band than in the soft X-ray band. Both flares F1 and F2 are highly energetic with respective peak X-ray luminosities of $\sim 10^{32.2}$ and $\sim 10^{31.8}$ erg s^{-1} in 0.3–50 keV energy band, which are larger than any other flares previously observed on CC Eri. The time-resolved spectral analysis during the flares shows the variation in the coronal temperature, emission measure, and abundances. The elemental abundances are enhanced by a factor of ~ 8 to the minimum observed in the post-flare phase for the flare F1. The observed peak temperatures in these two flares are found to be 174 and 128 MK. Using the hydrodynamic loop modeling, we derive loop lengths for both the flares as $1.2 \pm 0.1 \times 10^{10}$ cm and $2.2 \pm 0.6 \times 10^{10}$ cm, respectively. The Fe Kα emission at 6.4 keV is also detected in the X-ray spectra and we model the Kα emission feature as fluorescence from the hot flare source irradiating the photospheric iron. These superflares are the brightest, hottest, and shortest in duration observed thus far on CC Eri.

Key words: stars: activity – stars: coronae – stars: flare – stars: individual (CC Eridani) – stars: low-mass – stars: magnetic field

1. Introduction

Flares on the Sun and solar-type stars are generally interpreted as a rapid and transient release of magnetic energy in coronal layers driven by reconnection processes, associated with electromagnetic radiation from radio waves to γ-rays. As a consequence, the charge particles are accelerated and gyrate downward along the magnetic field lines, producing synchrotron radio emission, whereas these electron and proton beams collide with the denser material of the chromosphere and emit in hard X-rays (>20 keV). Simultaneous heating of plasma up to tens of MK evaporates the material from the chromospheric footpoints, which in turn increases the density on newly formed coronal loops emitting at extreme UV and X-rays. Since the non-flaring coronal emission only contains the information about an optically thin, multi-temperature, and possibly multi-density plasma in coronal equilibrium; therefore, it is very important to understand the dynamic behavior of the corona flaring events. Extreme flaring events are even more useful to understand the extent to which the dynamic behavior can vary within the stellar environments.

The typical total energy of solar flares ranges from 10^{29-32} erg, whereas the flares on normal solar-type stars, having a total energy range of 10^{33-38} erg, are generally termed as "superflares" (Schaefer et al. 2000; Shibayama et al. 2013). In the past, X-ray superflares have been observed and analyzed in the late-type stars Algol (Favata & Schmitt 1999), AB Dor (Maggio et al. 2000), EV Lac (Favata et al. 2000; Osten et al. 2010), UX Ari (Franciosini et al. 2001), II Peg (Osten et al. 2007), and DG CVn (Fender et al. 2015). Recent observations of X-ray superflares reveal an important aspect of the detection of iron Kα fluorescence emission during flaring events (Ercolano et al. 2008; Testa et al. 2008). Previously, this iron Kα fluorescence emission line was detected on the solar flares (Parmar et al. 1984; Zarro et al. 1992). The X-ray emissions during the solar and stellar flares interact with the photospheric layers and become reprocessed through scattering and photoionization. These processes also produce characteristic fluorescent emission from astrophysically abundant species.

In this paper, we describe two superflares serendipitously observed by the *Swift* observatory on an active spectroscopic binary star CC Eri. This binary consists of a K7.5Ve primary and M3.5Ve secondary (Amado et al. 2000), and is located at a distance of ~ 11.5 pc. With a mass ratio ≈ 2 (Evans 1959), the system is tidally locked and the primary component is one of the fastest rotating K dwarfs in the solar vicinity with a rotation period of 1.56 day. Demircan et al. (2006) estimated the age of the CC Eri system to be 9.16 Gyr. The chromospheric emission was found to vary in anti-phase with its optical continuum, suggesting the association of active emission regions with starspots (Busko et al. 1977; Amado et al. 2000). The polarization of the quiescent radio emission was found to be 10%–20% (Osten et al. 2002; Slee et al. 2004), which implies the presence of a large-scale magnetic field. The first X-ray detection was done with *HEAO1* showing X-ray luminosity (L_X) of $10^{29.6}$ erg s^{-1} in the 2–20 keV energy band (Tsikoudi 1982). Later several X-ray observations were made with other satellites such as *Einstein* IPC (Caillault et al. 1988) and *EXOSAT* (Pallavicini et al. 1988). Using *XMM-Newton* observations, the quiescent state coronae of CC Eri were well described by two-temperature plasma models (~ 3 and ~ 10 MK) with a luminosity of $\sim 10^{29}$ erg s^{-1} in 0.3–10 keV energy band (Pandey & Singh 2008). CC Eri has a record of frequent flaring activity observed across a wide range of the electromagnetic spectrum. The first ever X-ray flare on CC Eri was detected with the *ROSAT* satellite (Pan & Jordan 1995). Later several X-ray flares were detected with *XMM-Newton* (Crespo-Chacón et al. 2007; Pandey & Singh 2008), *Chandra* (Nordon & Behar 2007), *Swift* (Evans et al. 2008; Barthelmy et al. 2012), and *MAXI* GCS (Suwa et al. 2011). Among the previously observed flares, the largest one was observed with *Chandra*, having a peak X-ray flux that is $\sim$11 times more than that of the quiescent value. Superflares from CC Eri are expected to be driven by strong surface magnetic fields as estimated by Bopp & Evans (1973).

The paper is organized as follows. Observations and the data reduction procedure are discussed in Section 2. Analysis and results from X-ray timing and spectral analysis along with the time-resolved spectroscopy, loop modeling, and Fe Kα modeling are discussed in Section 3. Finally, in Section 4, we discuss our results and present conclusions.

2. Observations and Data Reduction

2.1. BAT Data

The flare F1 triggered *Swift*'s Burst Alert Telescope (BAT; Barthelmy et al. 2005) on 2008 October 16 UT 11:22:52 ($=T0_1$) during a preplanned spacecraft slew. The flare F2 was detected as an Automatic Target triggered on board on 2012 February 24 UT 19:05:44 ($=T0_2$). We have used BAT pipeline software within FTOOLS[4] version 6.20 with the latest CALDB version "BAT (20090130)" to correct the energy from the efficient but slightly non-linear on board energy assignment. BAT light curves were extracted using the task BATBINEVT. For the spectral data reported here, the mask-weighted spectra in the 14–50 keV band were produced using BATMASKWTEVT and BATBINEVT tasks with an energy bin of 80 channels. The BAT ray tracing columns in spectral files were updated using the BATUPDATEPHAKW task, whereas the systematic error vector was applied to the spectra from the calibration database using the BATPHASYSERR task. The BAT detector response matrix was computed using the BATDRMGEN task. The sky images in two broad energy bins were created using BATBINEVT and BATFFTIMAGE, and flux at the source position was found using BATCELLDETECT, after removing a fit to the diffuse background and the contribution of bright sources in the field of view. The spectral analysis of all the BAT spectra was done using the X-ray spectral fitting package (XSPEC; version 12.9.0n; Arnaud 1996). All the errors associated with the fitting of the BAT spectra were calculated for a confidence interval of 68% ($\Delta\chi^2 = 1$).

2.2. X-Ray Telescope (XRT) Data

Flaring events F1 and F2 were observed by the X-ray telescope (XRT; Burrows et al. 2005) from $T0_1$+147.2 and $T0_2$+397.5 s, respectively. The XRT observes in the energy range of 0.3–10 keV using CCD detectors, with the energy resolution of $\approx$140 eV at the Fe K (6 keV) region as measured at launch time. In order to produce the cleaned and calibrated event files, all the data were reduced using the *Swift* XRTPIPELINE task (version 0.13.2) and calibration files from the latest CALDB version "XRT (20160609)" release.[5] The cleaned event lists generated with this pipeline are free from the effects of hot pixels and the bright Earth. In the case of flare F1, due to the large XRT count rate, the initial data recording was in Windowed Timing (WT) mode; whereas from $T0_1 + 11.7$ s until the end of the observation ($T0_1 + 31.1$ s), data were taken in Photon Counting (PC) mode. The flare F2 was observed only in WT mode after $T0_2$ for 1.2 ks. From the cleaned event list, images, light curves, and spectra for each observation were obtained with the XSELECT (version 2.4d) package. We have used only grade 0–2 events in WT mode and grade 0–12 events in PC mode to optimize the effective area and hence the number of collected counts. Taking into account the point-spread function correction (PSF; Moretti et al. 2005) as well as the exposure map correction, the ancillary response files for the WT and PC modes were produced using the task XRTMKARF. In order to perform the spectral analysis, we have used the latest response matrix files (Godet et al. 2009), i.e., SWXWT0TO2S6_20010101V015.RMF for the flare F1 and SWXWT0TO2S6_20110101V015.RMF the flare F2 in WT mode and SWXPC0TO12S6_20010101V014.RMF for flare F1 in PC mode. All XRT spectra were binned to contain more than 20 counts bin^{-1}. The spectral analysis of all the XRT spectra was carried out in an energy range of 0.3–10 keV using XSPEC. All the errors of XRT spectral fitting were estimated with a 68% confidence interval ($\Delta\chi^2 = 1$), equivalent to $\pm 1\sigma$. In our analysis, the solar photospheric abundances ($Z_\odot$) were adopted from Anders & Grevesse (1989), whereas, to model $N_{\rm H}$, we used the cross-sections obtained by Morrison & McCammon (1983).

While extracting the light curve and spectra, we took great care in order to correct the data for the effect of pile-up in both WT and PC modes. At high observed count rates in WT mode (several hundred counts s^{-1}) and PC mode (above 2 counts s^{-1}), the effects of pile-up are observed as an apparent loss of flux, particularly from the center of the PSF and a migration from 0–12 grades to higher grades and energies at high count rates. To account for this effect, the source region of WT data were extracted in a rectangular 40×20 pixel region (40 pixels long along the image strip and 20 pixels wide; 1 pixel = $2\overset{''}{.}36$) with a region of increasing size (0×20–20×20 pixels) excluded from its center, whereas the background region was extracted as 40×20 pixel region in the fainter end of the image strip. We produced a sample of grade ratio distribution using background-subtracted source event lists created in each region. The grade ratio distribution for the grade 0 event is defined as the ratio of the grade 0 event over the sum of grade 0–2 events per energy bin in the 0.3–10 keV energy range. Comparing the grade ratio distribution with that obtained using non-piled-up WT data, in order to estimate the number of pixels to exclude, we find that an exclusion of the innermost 5 pixels for F1 and 3 pixels for F2 were necessary when all the WT data are used. In order to carry out a more robust analysis for pile-up corrections, we also fit the spectra with an absorbed power law. The hydrogen column density $N_{\rm H}$ was fixed to the values that were obtained from the fit of the non-piled-up spectrum (exclusion of innermost 20 pixels was assumed to be unaffected by piled-up). This gives similar results of exclusion of the innermost pixels within its 1σ value. In PC mode, since the pile-up affects the center of the source radial PSF, we fit the wings of the source radial PSF profile with the XRT PSF model (a King function; see Moretti et al. 2005) excluding 15 pixels from the center and then extrapolated to the inner region. The PSF profile of the innermost 4 pixels was found to deviate from

[4] The mission-specific data analysis procedures are provided in FTOOLS software package; a full description of the procedures mentioned here can be found at https://heasarc.gsfc.nasa.gov/docs/software/ftools/ftools_menu.html.
[5] See http://heasarc.gsfc.nasa.gov/docs/heasarc/caldb/swift/.

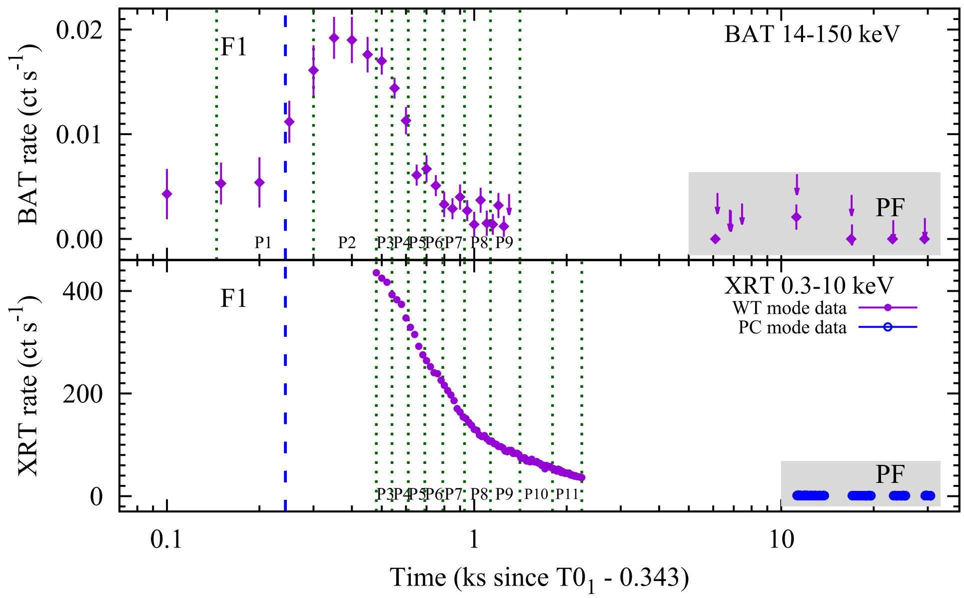

(a) Observations in 2008 shows flare F1 with a post-flare (PF) region

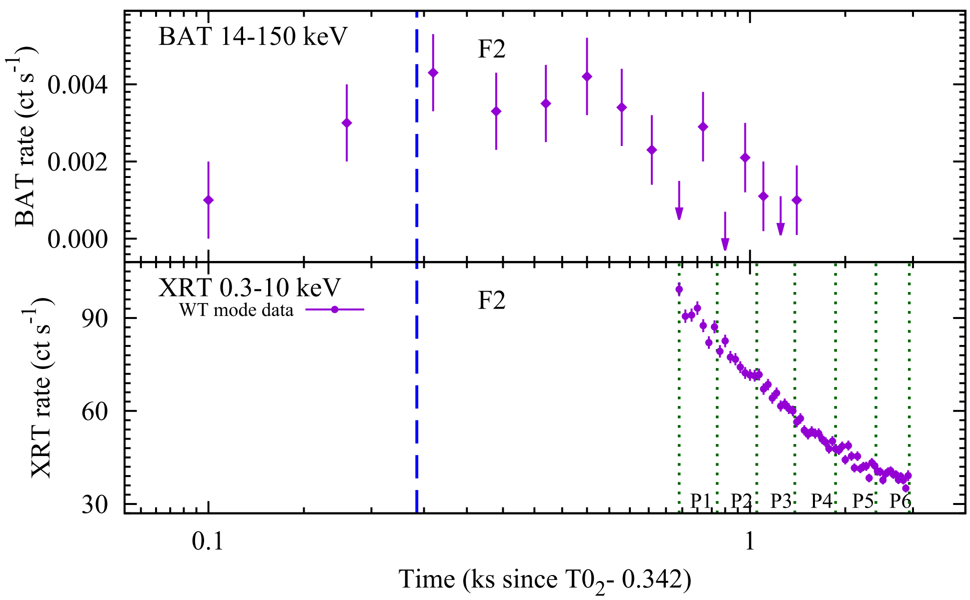

(b) Observations in 2012 shows flare F2

Figure 1. X-ray light curves of the flares (a) F1 and (b) F2 of CC Eri. Temporal binning for BAT light curves is 50 and 80 s for flares F1 and F2, respectively, whereas the binning for XRT light curves is 10 s for both flares. Dashed vertical lines indicate the trigger time, whereas dotted vertical lines show the time intervals for which time-resolved spectroscopy was performed. The time intervals are represented by P_i, where i = 1–11 for F1 and 1–6 for F2.

the King function, the exclusion of which enables us to mitigate the effects of pile-up from PC mode data.

3. Results and Analysis

3.1. X-Ray Light Curves

X-ray light curves of CC Eri obtained in 0.3–10 keV and 14–150 keV energy bands are shown in Figure 1. The BAT observation in 2008, which began at $T0_1$–243 s, shows a rise in intensity up to $T0_1$+100 s, where it reached a peak intensity with a count rate of 0.024 ± 0.005 counts s^{-1}, which is ∼24 times higher than the minimum observed count rate. A sharp decrease in intensity up to nearly $T0_1$+450 s was observed followed by a shallower decay until the end of the BAT observations at ∼$T0_1$+950 s. The XRT count rate of flare F1 was already declining as it entered the XRT field of view at $T0_1$+142 s. The peak XRT count rate for the pile-up corrected data was found to be 437 ± 7 counts s^{-1}, which was ∼100 counts s^{-1} lower than the previously reported count rate (Evans et al. 2008). Flare F1 survived the entire WT mode of observation of 1.8 ks, after that the observation was switched over in PC mode where count rates were found to be constant and marked as "PF" in Figure 1(a). The BAT observation of flare F2, which began at $T0_2$–240 s, shows a rise in intensity and peaked around $T0_2$, followed by a decline in intensity until the end of the BAT observation. The peak BAT count rate for flare F2 was found to be ∼0.004 counts s^{-1}, which was ∼4 times more than the minimum count rate observed. The flare

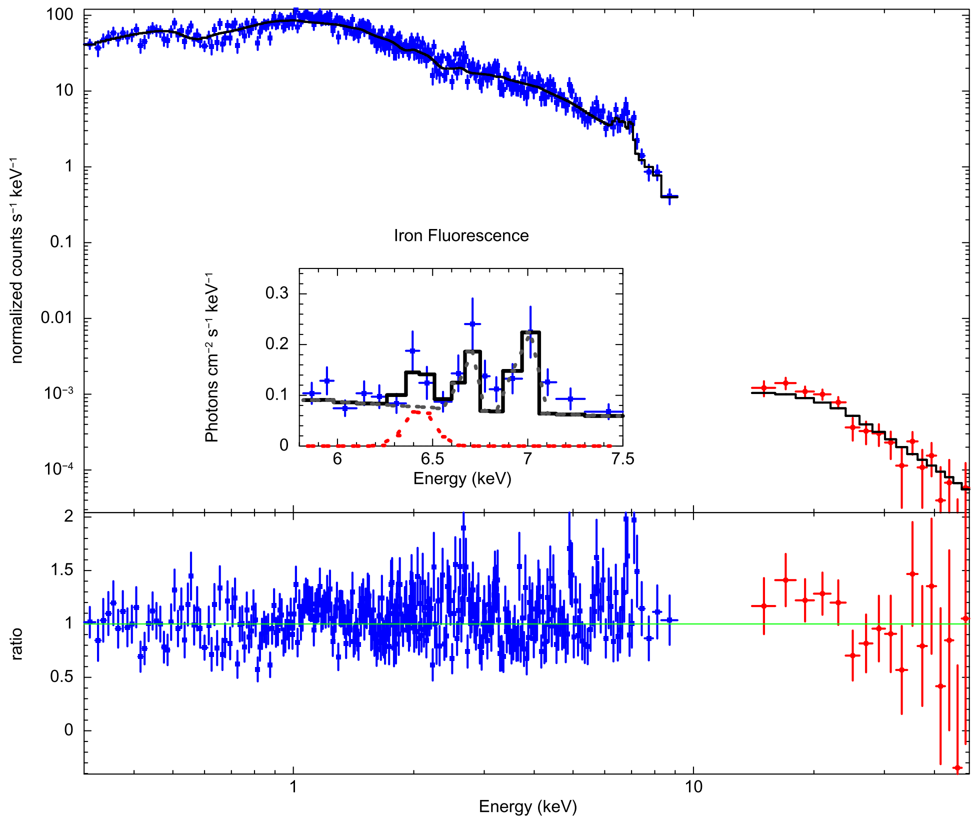

Figure 2. Combined XRT and BAT spectra near the peak phase of flare F1 (i.e., part P3) are shown as representative spectra. In the top panel, the XRT and BAT spectra are shown with solid squares and solid circles, respectively, whereas the best-fit APEC 3-T model is over-plotted with a continuous line. The bottom panel plots the ratio between data and model. The inset of the top panel shows a close-up view of the Fe Kα complex, where the 6.4 keV emission line is fitted with a Gaussian. The contribution of APEC component and the Gaussian component is shown by dashed lines.

"F2" was also already declining when it entered in the XRT field of view with a pile-up corrected peak count rate of 99 $\pm$ 2 counts s^{-1}. The XRT count rates at the peak of the flares F1 and F2 were found to be 474 and 108 times more than the minimum observed count rates, respectively. The durations of the flares were more than 2.2 for F1 and 1.8 ks for F2. The e-folding rise times (τ_r) of the flares F1 and F2 derived from BAT data were found to be 150 ± 12 and 146 ± 34 s, respectively; whereas e-folding decay times (τ_d) with BAT and XRT data were found to be 283 ± 13 and 539 ± 4 s for flare F1 and 592 ± 114 and 1014 ± 17 s for flare F2, respectively. This indicates a faster decay in the hard X-ray band than in the soft X-ray. Both flaring events were clearly identified in the energy band of 14–50 keV, but they were barely detectable above 50 keV.

3.2. BAT Spectral Analysis

Spectral parameters during the flares evolve with time as flare emission rises, reaches its peak, and later decays similarly to the X-ray light curve. Therefore, in order to trace the spectral change, we have divided the BAT light curve of the flare F1 into nine time segments and extracted the spectra of each segment, whereas we could not divide the flare F2 into any further segments due to poor statistics. The combined BAT and XRT spectra near the peak phase of the flare F1 (i.e. part P3) of CC Eri are shown in Figure 2. The dotted vertical lines in the top panel of Figure 1(a) indicate the time intervals during which BAT spectra were accumulated. In this section, we analyze those time segments where only the BAT observations were available, i.e., the first two time segments for flare F1 (P1 and P2), and only one for flare F2. The hard X-ray spectra were best-fitted using single temperature Astrophysical Plasma Emission Code (APEC; see Smith et al. 2001) as implemented for collisionally ionized plasma. The addition of another thermal or non-thermal component does not improve the fit-statistics. Since the standard APEC model included in the XSPEC distribution only considers emission up to photon energies of 50 keV; therefore, we restricted our analysis in 14–50 keV energy band. The abundances in this analysis were fixed to the mean abundances derived from XRT spectral fitting (see Section 3.3) given in a multiple of the solar values of Anders & Grevesse (1989). The galactic H I column density ($N_{\rm H}$) in the direction of CC Eri is calculated according to the survey of Dickey & Lockman (1990) and kept fixed at the value of 2.5×10^{20} cm^{-2}. The unabsorbed X-ray fluxes were calculated using the CFLUX model. The variation in hard X-ray luminosity ($L_{\rm X,[14-50]}$), plasma temperature (kT), emission measure (EM), and abundances (Z) derived from the BAT spectra are illustrated in Figure 3 and given in Table 4. The peak plasma temperatures were derived to be >14.4 keV and ∼11 keV for flares F1 and F2, whereas peak $L_{x,[14-50]}$ were derived to be $1.2 \pm 0.1 \times 10^{32}$ and $1.1 \pm 0.1 \times 10^{31}$ erg s^{-1}.

3.3. XRT Spectral Analysis

Time-resolved spectral analysis was also performed for the XRT data of both flares. The WT mode data for flares F1 and F2 were divided into nine and six time bins, respectively, so that each time bin contains sufficient and a similar number of

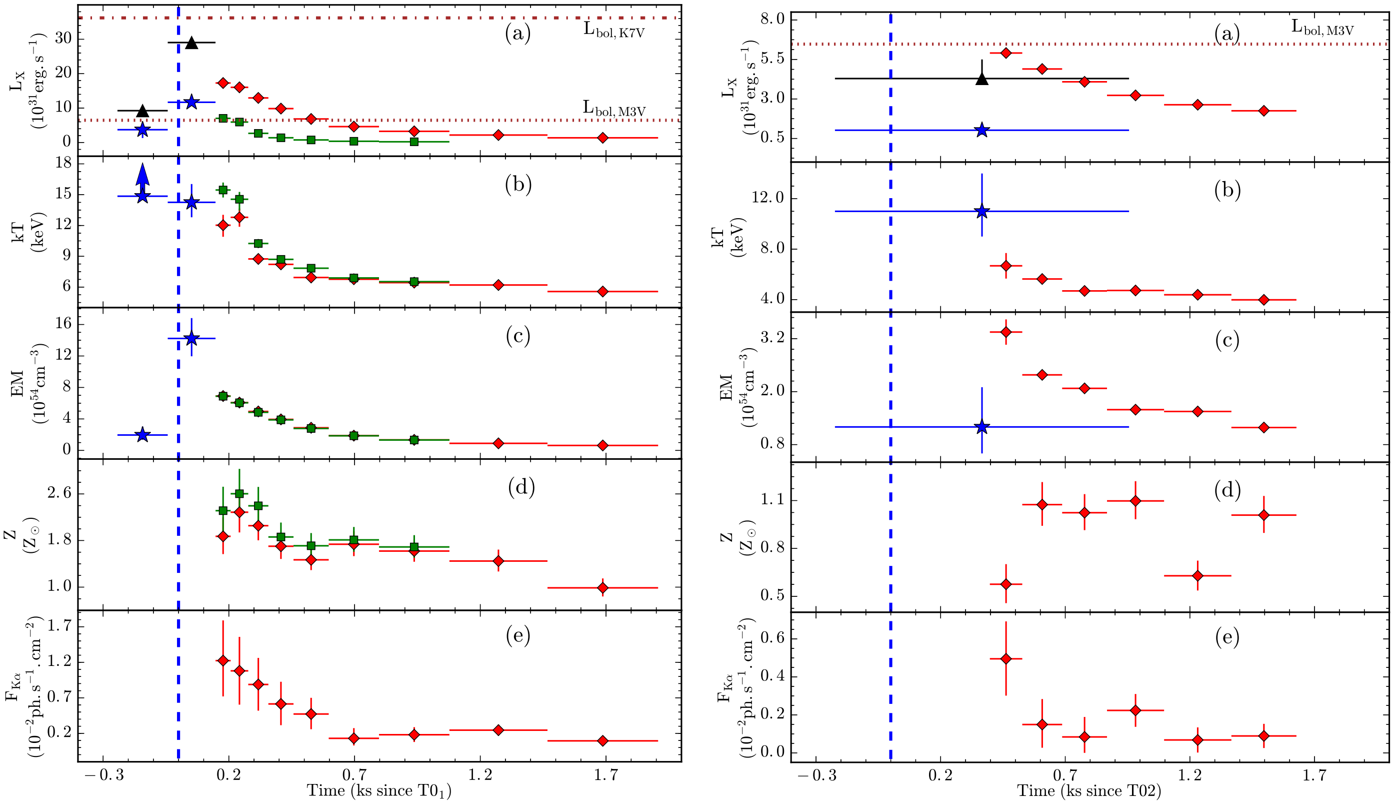

(i) Flare F1 (ii) Flare F2

Figure 3. Evolution of spectral parameters of CC Eri during the flares F1 (i) and F2 (ii). Parameters derived with the XRT, BAT, and XRT+BAT spectral fitting in all the panels are represented by the solid diamonds, solid stars, and solid squares, respectively. In the top panel (a), the X-ray luminosities are derived in 0.3–10 keV (solid diamond) and 14–50 keV (solid star and solid squares) energy bands. For the first two segments, BAT luminosity derived in the 14–50 keV energy band is extrapolated to the 0.3–10 keV energy band (solid triangles). The dashed–dotted and dotted horizontal lines correspond to bolometric luminosity of the primary and secondary components of CC Eri, respectively. Panels (b)–(e) display the variations of plasma temperature, EM, abundance, and Fe Kα line flux, respectively. The dashed vertical line indicates the trigger time of the flares F1 and F2. Horizontal bars give the time range over which spectra were extracted; vertical bars show a 68% confidence interval of the parameters.

counts. The length of time bins is variable, ranging from 60–440 s for the flare F1 and 130–261 s for the flare F2. The dotted vertical lines in the bottom panel of Figures 1(a) and (b) show the time intervals for which the XRT spectra were accumulated. The first seven time segments of XRT data were common with BAT data for the flare F1.

3.3.1. *Post-flare Phase of the Flaring Event F1*

The coronal parameters of the PF phase were derived by the fitting single (1-T), two (2-T), and three (3-T) temperatures APEC model. The global abundances (Z) and interstellar H I column density (N_H) were left as free parameters. None of the plasma models (1-T, 2-T, or 3-T) with solar abundances ($Z_\odot$) were formally acceptable because large values of χ^2 were obtained. The 2-T plasma model with sub-solar abundances was found to have a significantly better fit than the 1-T model with reduced χ^2 (χ^2_ν) of 1.56 for 120 degrees of freedom (dof). Adding one more plasma component improves the fit significantly with $\chi^2_\nu = 1.08$ for 118 dof. The F-test applied to the χ^2 resulting from the fits with APEC 2-T and 3-T models showed that the 3-T model was more significant with an F-statistics of 27.7 with a null hypothesis probability of 1.4×10^{-10}. The addition of one more thermal component did not show any further improvement in the χ^2_ν; therefore, we assume that the post-flare coronae of CC Eri were well represented by three temperature plasma. Table 1 summarizes the best-fit values of the 2-T and 3-T plasma models of various parameters along with their χ^2_ν value. The first two temperatures in the 3-T model were derived as 0.25 ± 0.02 and 0.94 ± 0.03 keV. These two temperatures are consistent to that derived by Crespo-Chacón et al. (2007) and Pandey & Singh (2008) for quiescent coronae

Table 1
Spectral Parameters Derived for the Post-flare Emission of CC Eri from *Swift* XRT PC mode Spectra during the Time Interval "PF" as Shown in Figure 1 Using APEC 2-T and APEC 3-T Models

Parameters	2T	3T
N_H (10^{20} atoms cm^{-2})	$0.9^{+0.8}_{-0.8}$	$2.8^{+1.1}_{-1.1}$
kT_1 (keV)	$0.83^{+0.02}_{-0.02}$	$0.25^{+0.02}_{-0.02}$
EM_1 (10^{52} cm^{-3})	$3.4^{+0.6}_{-0.6}$	$1.4^{+0.4}_{-0.4}$
kT_2 (keV)	$3.9^{+2.4}_{-0.9}$	$0.94^{+0.03}_{-0.03}$
EM_2 (10^{52} cm^{-3})	$0.8^{+0.2}_{-0.2}$	$1.7^{+0.4}_{-0.4}$
kT_3 (keV)	...	$3.4^{+0.7}_{-0.6}$
EM_3 (10^{52} cm^{-3})	...	$0.9^{+0.2}_{-0.1}$
Z ($Z_\odot$)	$0.13^{+0.03}_{-0.02}$	$0.29^{+0.09}_{-0.05}$
$L_{X,[0.3-10]}$ (10^{29} erg s^{-1})	$3.88^{+0.06}_{-0.06}$	$4.33^{+0.07}_{-0.07}$
χ^2_ν(dof)	1.56 (120)	1.08 (118)

Note. N_H, kT, and EM are the galactic H I column density, plasma temperature, and emission measures, respectively. Z is global metallic abundances and $L_{X,[0.3-10]}$ is the derived luminosity in the XRT band.

Table 2
X-Ray Spectral Parameters of CC Eri during the Flare F1 Derived from the XRT Time-resolved Spectra

Parts	Time Interval	kT_3	EM_3	Z	Fe Kα			$L_{x,[0.3-10]}$	χ^2_ν (dof)	P
					E (keV)	EW (keV)	$F_{K\alpha}$ (10^{-2} ph cm^{-2} s^{-1})			
	(s)	(keV)	(10^{54} cm^{-3})	($Z_\odot$)				(10^{31} erg s^{-1})		(%)
P3	$T0_1+137:T0_1+197$	$11.6^{+1.0}_{-1.1}$	$6.9^{+0.3}_{-0.3}$	$1.9^{+0.3}_{-0.3}$	$6.37^{+0.06}_{-0.08}$	132^{+64}_{-67}	$1.2^{+0.6}_{-0.5}$	$17.3^{+0.2}_{-0.2}$	1.179 (303)	89.3
P4	$T0_1+197:T0_1+267$	$12.3^{+0.9}_{-0.9}$	$6.1^{+0.3}_{-0.3}$	$2.3^{+0.4}_{-0.4}$	$6.38^{+0.07}_{-0.07}$	124^{+46}_{-66}	$1.1^{+0.5}_{-0.5}$	$16.0^{+0.2}_{-0.2}$	1.119 (312)	88.5
P5	$T0_1+267:T0_1+347$	$8.3^{+0.5}_{-0.3}$	$5.0^{+0.2}_{-0.2}$	$2.1^{+0.3}_{-0.3}$	$6.21^{+0.05}_{-0.05}$	173^{+90}_{-73}	$0.9^{+0.4}_{-0.4}$	$13.0^{+0.1}_{-0.1}$	0.951 (303)	93.9
P6	$T0_1+347:T0_1+447$	$7.7^{+0.4}_{-0.4}$	$3.9^{+0.2}_{-0.2}$	$1.7^{+0.2}_{-0.2}$	$6.34^{+0.06}_{-0.05}$	132^{+80}_{-77}	$0.6^{+0.3}_{-0.3}$	$9.9^{+0.1}_{-0.1}$	1.149 (292)	78.9
P7	$T0_1+447:T0_1+587$	$6.5^{+0.2}_{-0.2}$	$2.9^{+0.1}_{-0.1}$	$1.5^{+0.2}_{-0.2}$	$6.41^{+0.06}_{-0.07}$	77^{+92}_{-37}	$0.4^{+0.2}_{-0.2}$	$6.85^{+0.07}_{-0.07}$	1.238 (288)	80.3
P8	$T0_1+587:T0_1+787$	$6.3^{+0.2}_{-0.2}$	$1.88^{+0.08}_{-0.08}$	$1.7^{+0.2}_{-0.2}$	6.39	23^{+25}_{-23}	<0.24	$4.62^{+0.05}_{-0.05}$	1.134 (282)	48.6
P9	$T0_1+787:T0_1+1067$	$6.0^{+0.2}_{-0.2}$	$1.34^{+0.05}_{-0.05}$	$1.6^{+0.2}_{-0.2}$	$6.38^{+0.08}_{-0.10}$	77^{+68}_{-48}	$0.2^{+0.1}_{-0.1}$	$3.26^{+0.03}_{-0.03}$	1.273 (276)	55.1
P10	$T0_1+1067:T0_1+1457$	$5.8^{+0.3}_{-0.3}$	$0.90^{+0.04}_{-0.04}$	$1.5^{+0.2}_{-0.2}$	$6.40^{+0.05}_{-0.05}$	118^{+131}_{-24}	$0.22^{+0.08}_{-0.08}$	$2.18^{+0.02}_{-0.02}$	1.179 (266)	96.4
P11	$T0_1+1457:T0_1+1897$	$5.1^{+0.2}_{-0.3}$	$0.63^{+0.03}_{-0.03}$	$1.0^{+0.2}_{-0.2}$	6.41	68^{+55}_{-52}	$0.06^{+0.05}_{-0.05}$	$1.37^{+0.02}_{-0.02}$	1.043 (220)	77.4

Note. kT_3, EM_3, and Z are the "effective" plasma temperature, emission measures, and abundances during different time intervals of flare decay, respectively. E is the Gaussian peak around 6.4 keV, EW is the equivalent width, $F_{K\alpha}$ is the Kα line flux, $L_{X,[0.3-10]}$ is the derived luminosity in XRT band, and P is the F-test probability, which indicates how much of an addition of the Gaussian line at 6.4 keV is significant, i.e., the emission line is not a result of random fluctuation of the data points. All the errors shown in this table are in the 68% confidence interval.

of CC Eri using *XMM-Newton* data. This indicates that the post-flaring region has not yet returned to the quiescent level and has a third thermal component of $3.4^{+0.7}_{-0.6}$ keV. With the preliminary analysis of the same data, Evans et al. (2008) also suspected that the post-flare region was not a quiescent state. The X-ray luminosity in the 0.3–10.0 keV band during the post-flare region was derived to be $4.33 \pm 0.07 \times 10^{29}$ erg s^{-1}, which was $\sim$5 times higher than the previously determined quiescent state luminosity in the same energy band by Pandey & Singh (2008) using *XMM-Newton*.

3.3.2. The Flaring Event F1

A 3-T plasma model was found to be acceptable in each segment of flaring event F1. The first two temperatures, corresponding EMs, and N_H were found to be constant within a 1σ level. The average values of all the segments of the first two temperatures were 0.3 ± 0.1 and 1.1 ± 0.2 keV, respectively. These two temperatures were very similar to that of the first two temperatures of the PF phase. Therefore, for the further spectral fitting of flare-segments of the flare F1, we fixed the first two temperatures to the average values. The free parameters were temperature and corresponding normalization of the third component along with the abundances. The time evolution of derived spectral parameters of flare F1 is shown in Figure 3(a) and are given in Table 2. The abundance, temperature, and corresponding EM were found to vary during the flare. The peak values of abundances were derived to be 2.3 ± 0.4 $Z_\odot$, which was $\sim$8 times more than the post-flaring region and $\sim$13 times more than that of the quiescent value of CC Eri (Pandey & Singh 2008). The derived peak flare temperature of 12.3 ± 0.9 keV was $\sim$3.6 times more than the third thermal component observed in the PF phase. The EM followed the flare light curve and peaked at a value of $6.9 \pm 0.3 \times 10^{54}$ cm^{-3}, which was $\sim$766 times more than the minimum value observed at the post-flare region. The peak X-ray luminosity in 0.3–10 keV energy band during flare F1 was derived to be $10^{32.2}$ erg s^{-1}, which was $\sim$400 times more luminous than that of the post-flare regions, whereas $\sim$1922 times more luminous than that of the quiescent state of CC Eri derived by Pandey & Singh (2008). The amount of soft X-ray luminosity during the time segments when only BAT data were collected were estimated by extrapolating the 14–50 keV luminosity derived from the best-fit APEC model of the BAT data using WEBPIMMS[6] and is shown by solid triangles in the top panels of Figure 3(i).

3.3.3. The Flaring Event F2

For the flaring event F2, no pre-/post-flare or quiescent states were observed; therefore, a time-resolved spectroscopy was done by fitting 1-T, 2-T, and 3-T plasma models. A 2-T plasma model was found suitable for each flare segment as the minimum value of χ^2_ν was obtained. Initially, in the spectral fitting N_H was a free parameter and was constant within a 1σ level; therefore, in the next stage of spectral fitting, we fixed N_H to its average value. The derived spectral parameters are given in Tables 3. Both the temperatures and the corresponding EM along with the global abundances were found to be variable during the flare. In order to compare the plasma properties of the flare represented by two-temperature components, the total EM and temperature were calculated as $EM = (EM_1 + EM_2)$ and $T = (EM_1.T_1 + EM_2.T_2)/EM$. The time evolution of spectral parameters along with the X-ray luminosity in 0.3–10 keV energy band for the flare F2 are shown in Figure 3(ii). The abundances were varied from 0.5 to 1.1 $Z_\odot$. The flare temperature (weighted sum) and total EM were peaked at 6.7 ± 1.0 keV and $3.3 \pm 0.3 \times 10^{54}$ cm^{-3}, respectively. These values are two to three times higher than the respective minimum observed values. At the end of the flare, the X-ray luminosity was found to be 38% of its maximum value of $10^{31.8}$ erg s^{-1}.

3.3.4. The Emission Line at 6.4 keV

In the spectral fitting of XRT spectra with the 3-T APEC model for F1 and the 2-T APEC model for F2, significant positive residuals redward of the prominent Fe K complex at $\approx$6.7 keV were detected. This excess emission occurs at the expected position of the 6.4 keV Fe fluorescent line, which is not included in the APEC line list. To determine whether indeed such emission is present in the XRT spectrum, we have fitted

[6] https://heasarc.gsfc.nasa.gov/cgi-bin/Tools/w3pimms/w3pimms.pl

Table 3
Time-resolved Spectral Parameters of CC Eri during the Flare F2 Derived from the XRT Spectra

Parts	Time Interval	kT_1	kT_2	EM_1	EM_2	Z	Fe Kα			$L_{x,[0.3-10]}$	χ^2_ν (dof)	P
							E	EW	$F_{K\alpha}$ (10^{-2}			
	(s)	(keV)	(keV)	(10^{54} cm^{-3})	(10^{54} cm^{-3})	($Z_\odot$)	(keV)	(keV)	ph cm^{-2} s^{-1})	(10^{31} erg s^{-1})		(%)
P1	$T0_2+397:T0_2+527$	$1.63^{+0.05}_{-0.07}$	$8.7^{+1.8}_{-1.0}$	$1.0^{+0.3}_{-0.2}$	$2.4^{+0.1}_{-0.1}$	$0.54^{+0.13}_{-0.12}$	$6.46^{+0.05}_{-0.05}$	181^{+108}_{-75}	$0.50^{+0.20}_{-0.19}$	$5.91^{+0.06}_{-0.06}$	1.298 (288)	92.2
P2	$T0_2+527:T0_2+687$	$1.25^{+0.04}_{-0.06}$	$6.0^{+0.4}_{-0.4}$	$0.20^{+0.05}_{-0.04}$	$2.18^{+0.07}_{-0.07}$	$1.03^{+0.14}_{-0.13}$	$6.28^{+0.13}_{-0.11}$	101^{+42}_{-83}	$0.15^{+0.13}_{-0.12}$	$4.90^{+0.05}_{-0.05}$	1.205 (289)	46.2
P3	$T0_2+687:T0_2+867$	$1.05^{+0.02}_{-0.03}$	$4.9^{+0.2}_{-0.2}$	$0.13^{+0.02}_{-0.02}$	$1.94^{+0.06}_{-0.06}$	$0.98^{+0.12}_{-0.11}$	6.35	47^{+56}_{-47}	$0.08^{+0.11}_{-0.08}$	$4.09^{+0.04}_{-0.04}$	1.164 (285)	91.6
P4	$T0_2+867:T0_2+1096$	$1.02^{+0.03}_{-0.03}$	$4.9^{+0.2}_{-0.2}$	$0.09^{+0.01}_{-0.01}$	$1.50^{+0.05}_{-0.05}$	$1.06^{+0.12}_{-0.11}$	$6.19^{+0.06}_{-0.06}$	244^{+76}_{-106}	$0.22^{+0.09}_{-0.09}$	$3.23^{+0.03}_{-0.03}$	0.968 (283)	96.7
P5	$T0_2+1096:T0_2+1366$	$1.25^{+0.05}_{-0.07}$	$4.9^{+0.4}_{-0.3}$	$0.21^{+0.07}_{-0.05}$	$1.34^{+0.05}_{-0.05}$	$0.59^{+0.09}_{-0.19}$	6.24	94^{+83}_{-80}	$0.07^{+0.07}_{-0.07}$	$2.63^{+0.02}_{-0.03}$	1.134 (277)	66.4
P6	$T0_2+1366:T0_2+1627$	$1.04^{+0.02}_{-0.03}$	$4.2^{+0.2}_{-0.2}$	$0.08^{+0.01}_{-0.01}$	$1.11^{+0.04}_{-0.04}$	$0.97^{+0.12}_{-0.11}$	$6.25^{+0.13}_{-0.13}$	162^{+112}_{-114}	$0.09^{+0.06}_{-0.06}$	$2.25^{+0.02}_{-0.02}$	0.925 (253)	65.2

Note. Parameters have similar meanings as in Tables 1 and 2.

Table 4
Time-resolved Spectral Parameters of the BAT and XRT+BAT Spectra of the Flares F1 and F2

Flare	Parts	Time Interval (s)	kT (keV)	EM (10^{54} cm^{-3})	Z ($Z_\odot$)	$F_{7.11-50}$ (10^{-2} ph cm^{-2} s^{-1})	$L_{x,[14-50]}$ (10^{31} erg s^{-1})	χ^2_ν (dof)
F1	P1[a]	$T0_1$–243:$T0_1$–43	>14.4	$2.0^{+1.1}_{-0.6}$	1.64[b]	…	$3.7^{+0.6}_{-0.6}$	0.893 (15)
	P2[a]	$T0_1$–43:$T0_1$+137	14^{+2}_{-1}	$14.2^{+2.6}_{-2.3}$	1.64[b]	…	$11.7^{+1.0}_{-1.1}$	0.581 (15)
	P3	$T0_1$+137:$T0_1$+197	$15.0^{+0.7}_{-0.7}$	$6.9^{+0.3}_{-0.3}$	$2.3^{+0.4}_{-0.4}$	$37.3^{+0.4}_{-0.4}$	$7.02^{+0.07}_{-0.07}$	1.193 (322)
	P4	$T0_1$+197:$T0_1$+267	$14.1^{+0.7}_{-1.1}$	$6.1^{+0.3}_{-0.3}$	$2.6^{+0.4}_{-0.4}$	$33.1^{+0.3}_{-0.3}$	$5.95^{+0.06}_{-0.06}$	1.104 (331)
	P5	$T0_1$+267:$T0_1$+347	$9.80^{+0.4}_{-0.4}$	$4.8^{+0.2}_{-0.2}$	$2.4^{+0.3}_{-0.3}$	$20.3^{+0.2}_{-0.2}$	$2.67^{+0.03}_{-0.03}$	0.978 (322)
	P6	$T0_1$+347:$T0_1$+447	$8.25^{+0.3}_{-0.3}$	$3.9^{+0.2}_{-0.2}$	$1.9^{+0.3}_{-0.2}$	$12.7^{+0.1}_{-0.1}$	$1.38^{+0.01}_{-0.01}$	1.173 (311)
	P7	$T0_1$+447:$T0_1$+587	$7.39^{+0.4}_{-0.4}$	$2.8^{+0.1}_{-0.1}$	$1.7^{+0.2}_{-0.2}$	$7.88^{+0.08}_{-0.08}$	$0.752^{+0.008}_{-0.008}$	1.256 (307)
	P8	$T0_1$+587:$T0_1$+787	$6.44^{+0.2}_{-0.2}$	$1.86^{+0.07}_{-0.07}$	$1.8^{+0.2}_{-0.2}$	$4.58^{+0.05}_{-0.05}$	$0.364^{+0.004}_{-0.004}$	1.134 (300)
	P9	$T0_1$+787:$T0_1$+957	$6.08^{+0.2}_{-0.2}$	$1.33^{+0.05}_{-0.05}$	$1.7^{+0.2}_{-0.2}$	$2.94^{+0.03}_{-0.03}$	$0.217^{+0.002}_{-0.002}$	1.247 (295)
F2[a]	…	$T0_2$–242:$T0_2$+938	11^{+3}_{-2}	$1.2^{+0.9}_{-0.6}$	1.00[b]	…	$1.1^{+0.1}_{-0.1}$	0.683 (15)

Notes. kT, EM, and Z are the "effective" plasma temperature, emission measures, and abundances during different time intervals of flare decay, respectively. $F_{7.11-50}$ is the flux derived in the 7.11–50 keV energy band. $L_{X,[14-50]}$ is the luminosity derived in the 14–50 keV energy band. All the errors shown in this table are in the 68% confidence interval.

[a] In these time segments, only BAT spectra were available and best-fitted with the single temperature APEC model, whereas in other segments, XRT+BAT spectra were fitted with three temperature APEC with the first two temperatures fixed to the quiescent value.

[b] The abundances were kept fixed at the average abundance derived from XRT spectral fitting.

again the spectra with an additional Gaussian line component along with the best-fit plasma model. Initially, keeping free the width of the Gaussian line (σ), it converges to a very large value than the actual line width. Therefore, in order to get a best fit, we fixed the σ in every value from 10–200 eV with an increment of 10 eV. In this analysis, we have used the σ corresponding to the minimum χ^2_ν value, ranging from 40–80 eV for a different time segment of the flare. The line centroid (E) and the normalization along with the temperature, abundances, and EM were left free to vary. The best-fit parameters are given in Tables 2 and 3, for the flares F1 and F2, respectively. In each segment, the best-fit line energy agrees with the Fe fluorescent feature at $E \sim 6.4$ keV (see the sixth column of Table 2 and eighth column of Table 3). We applied the F-test to the χ^2 resulting from the fits with and without an additional Gaussian line, which shows the significance of the Fe Kα feature with a probability of the line not being a result of random fluctuation (see the last column of Tables 2 and 3). The derived Fe Kα line flux shows variability and follows the light curve and peaked at a value of $1.2^{+0.6}_{-0.5} \times 10^{-2}$ photons s^{-1}cm^{-2} for the flare F1 and $5.0^{+2.0}_{-1.9} \times 10^{-3}$ photons s^{-1} cm^{-2} for the flare F2, which is ~20 and ~7 times more than the minimum observed Fe Kα flux, respectively. The equivalent width (EW) was found to be in the range of 23–173 eV for the flare F1 and 47–244 eV for the flare F2.

3.4. XRT+BAT Spectral Analysis

Time-resolved spectroscopy for the flare F1 was also performed with the XRT+BAT data. Very poor statistics of the BAT spectra did not allow us a time-resolved spectral analysis of the XRT+BAT spectra for the flare F2. A similar approach, as applied for the XRT spectral fitting was also applied for the XRT+BAT spectral fitting. For the flare F1, we choose seven time bins (P3–P9) similar to the spectral fitting of only-XRT data as described in the previous section (see Figure 1). Since galactic H I column density was not found to be variable during only-XRT spectral analysis; therefore, we fixed N_H to its average value. The global abundances, temperature, and corresponding EMs of the third component were free parameters in the spectral fitting. The derived parameters are given in Table 4 and the variations of the spectral parameters are shown in Figure 3. The peak temperature derived in this spectral fitting was found to be 15.0 ± 0.7 keV, which is higher than the highest temperature derived from XRT spectral analysis. The EM was found to have similar values as those derived from XRT spectral fitting, whereas the peak abundance was found to be ~1.1 times higher than that derived from XRT data.

3.5. Hydrodynamic Modeling of Flare Decay

Although stellar flares cannot be spatially resolved, it is possible to infer the physical size and structure of flares from the flare loop models. A time-dependent one-dimensional hydrodynamic model developed by Reale et al. (1997) to analyze the stellar flares assumes that the energy release occurs inside closed magnetic coronal structures, which confine the flaring plasma. The heat pulse is assumed to be released at the beginning of the flare at the apex of the flaring loop, and the thermodynamic cooling timescales the length of the flaring loop. Since the flaring plasma is also subjected to further prolonged heating, which extends into the decay phase of the flare, the actual flare decay time determined from the flare light curve would be longer than usual thermodynamic cooling time. In the case of spatially resolved solar flares, Sylwester et al. (1993) showed that the slope (ζ) in the density-temperature plane of the flare decay path provides diagnostics of sustained heating. Using hydrodynamic simulations of semi-circular flaring loops with constant cross-sections, and including the effect of the heating in the decay, Reale et al. (1997) derived an empirical formula of loop length as

$$L = \frac{\tau_d \sqrt{T_{\max}}}{1.85 \times 10^{-4} F(\zeta)} \qquad F(\zeta) \geqslant 1, \tag{1}$$

where L is the loop length in centimeters, $T_{\max}$ is the maximum temperature (K) of the loop apex, and $F(\zeta)$ is a non-dimensional factor that provides a quantitative diagnostic of the ratio between the observed decay time (τ_d) to the thermodynamic cooling time ($\tau_{\rm th}$). The actual functional form of the parameter $F(\zeta)$ depends on the bandpass and spectral response of the instruments. For *Swift* XRT observations, the $F(\zeta)$ was calibrated by Osten et al. (2010) as

$$\frac{\tau_{\rm d}}{\tau_{\rm th}} = F(\zeta) = \frac{1.81}{\zeta - 0.1} + 0.67 \qquad 0.4 < \zeta \lesssim 1.9. \quad (2)$$

This limits the applicability of this model, because it assumes a flare process as a sequence of quasi-static states for the loop, in which the heating timescale ($\tau_{\rm H}$) is very long in order to mask the loop's intrinsic decay ($\tau_{\rm H} \gg \tau_{\rm th}$) in the lower end, and a freely decaying loop with no heating ($\tau_{\rm H} = 0$) on the upper end. For stellar observations, no density determination is normally available; therefore, we used the quantity $\sqrt{\rm EM}$ as a proxy of the density assuming the geometry of the flaring loop during the decay. Figure 4 shows the path log $\sqrt{\rm EM}$ versus log T for flares F1 and F2. A linear fit to the data provided the value of ζ as 0.550 ± 0.047 for flare F1 and 0.819 ± 0.179 for flare F2. This indicates the presence of sustained heating during the decay phase of both flares.

The relationship between $T_{\rm max}$ and observed peak temperature ($T_{\rm obs}$) was also calibrated for *Swift* XRT by Osten et al. (2010) as $T_{\rm max} = 0.0261 \times T_{\rm obs}^{1.244}$, where both temperatures are in K. For flares F1 and F2, $T_{\rm max}$ was calculated to be 365 ± 33 and 170 ± 32 MK, respectively. The flaring loop length was derived as $1.2 \pm 0.1 \times 10^{10}$ cm for flare F1 and $2.2 \pm 0.6 \times 10^{10}$ cm for flare F2. Assuming a semi-circular geometry, the flaring loop height (L/π) was estimated to be 0.1 and 0.2 times the stellar radius ($R_\star$) of the primary component of CC Eri of the flares F1 and F2. The loop parameters for both the flares are given in Table 5.

3.6. Energetics

The derived loop lengths are much smaller than the pressure scale height[7] of the flaring plasma of CC Eri. Therefore, we can assume that the flaring loop is not far from a steady-state condition. We applied the RTV scaling laws (Rosner et al. 1978) to determine the maximum pressure (p) in the loop at the flare peak and found it to be $\sim 1.5 \times 10^6$ and $\sim 8 \times 10^4$ dyne cm^{-2} for the flares F1 and F2, respectively. The plasma density (n_e), the flaring volume (V), and the minimum magnetic field (B) to confine the flaring plasma were derived as

$$n_e = \frac{p}{2\,k\,T_{\rm max}}\ {\rm cm^{-3}}; \quad V = \frac{\rm EM}{n_e^2}\ {\rm cm^3};$$
$$B = \sqrt{8\pi\,p}\ \ {\rm G}. \quad (3)$$

The estimated values of n_e, V, and B during the flares F1 and F2 were 1.5×10^{13} and 1.7×10^{12} cm^{-3}, 3.1×10^{28} and 1.2×10^{30} cm^3, and ∼6.1 and ∼1.4 kG, respectively. Using the RTV scaling laws, we have also estimated the heating rate per unit volume ($E_H = \frac{dH}{dVdt} \simeq 10^5\, p^{7/6}\, L^{-5/6}$) at the peak of the flare as $\simeq 6.6 \times 10^3$ and $\simeq 1.3 \times 10^2$ erg cm^{-3} s^{-1} for the flares F1 and F2, respectively. The total heating rates ($\frac{dH}{dt} \simeq \frac{dH}{dV\,dt} \times V$) at the peak of the flares were derived to be $\sim 2.1 \times 10^{32}$ and $\sim 1.5 \times 10^{32}$ erg s^{-1} for the flares F1 and F2, which were, respectively, ∼1.2 and ∼2.5 times higher than the flare maximum luminosity. If we assume that the heating rate is constant throughout the rise and decay phases of the flare, the total energy radiated [$E_{\rm X,tot} > \frac{dH}{dt} \times (\tau_r + \tau_d)$] during the flares was derived to be $>1.4 \times 10^{35}$ erg for flare F1 and $>1.7 \times 10^{35}$ erg for flare F2. These values were ∼40 s and ∼47 s of bolometric energy output of the primary and ∼221 s and ∼264 s of bolometric energy output of the secondary for the flares F1 and F2, respectively.

[7] The pressure scale height is defined as $h_{\rm p} = 2kT_{\rm max}/(\mu g)$, where μ is the average atomic weight and g is the surface gravity of the star. Considering both the stellar components, the derived values of $h_{\rm p}$ are $\geqslant 9.8 \times 10^{11}$ cm for flare F1 and $\geqslant 4.6 \times 10^{11}$ cm for flare F2.

Table 5
Loop Parameters Derived for Flares F1 and F2

Sl.	Parameters	Flare F1	Flare F2
1	$\tau_{\rm r,14-150}$ (s)	150 ± 12	146 ± 34
2	$\tau_{\rm d,14-150}$ (s)	283 ± 13	592 ± 114
3	$\tau_{\rm d,0.3-10}$ (s)	539 ± 4	1014 ± 17
4	$L_{\rm X,max}$ (10^{31} erg s^{-1})	17.3 ± 0.2	5.91 ± 0.06
5	$T_{\rm max}$ (10^6 K)	365 ± 33	170 ± 32
6	ζ	0.550 ± 0.047	0.819 ± 0.179
7	L (10^{10} cm)	1.2 ± 0.1	2.2 ± 0.6
8	p (10^5 dyn cm^{-2})	15 ± 5	0.8 ± 0.7
9	$n_{\rm e}$ (10^{12} cm^{-3})	15 ± 7	1.7 ± 1.7
10	V (10^{29} cm^3)	∼0.31	∼11.5
11	B (kG)	∼6.1	∼1.4
12	$E_{\rm H}$ (10^3 erg s^{-1} cm^{-3})	∼6.6	∼0.13
13	H (10^{32} erg s^{-1})	∼2.1	∼1.5
14	$E_{\rm X,tot}$ (10^{35} erg)	>1.4	>1.7
15	B_0 (kG)	>12	>2
16	$N_{\rm loops}$	∼1	∼3
17	θ (°)	∼90	…

Note. 1, 2: e-folding rise and decay times derived from the BAT light curve. 3: e-folding decay time derived from the XRT light curve. 4: luminosity at the flare peak in the XRT band. 5: the maximum temperature in the loop at the flare peak. 6: slope in the density-temperature diagram during the flare decay. 7: flaring loop length. 8: maximum loop pressure at the flare peak. 9: maximum electron density in the loop at the flare peak. 10: loop volume of the flaring region. 11: minimum magnetic field. 12: heating rate per unit volume at the flare peak. 13: total heating rate at the flare peak. 14: total radiated energy. 15: total magnetic field required to produce the flare. 16: the number of loops needed to fill the flare volume assuming a loop aspect ratio of 0.1. 17: the astrocentric angle between observer and the flare location on the stellar disk. (See the text for a detailed description).

3.7. Modeling of Fluorescent Fe Kα Emission

In the stellar context, the detected iron Kα line is generally attributed to a fluorescent process, where the fluorescing material is a neutral or low ionization state of photospheric iron (Fe I–Fe XII), which shines on the X-ray continuum emission arising from a loop-top source. Thus the detection of this line constraints the height of the flaring loop. The process involves photoionization of an inner K-shell electron and the de-excitation of an electron from a higher level at this energy. Thus the total photon flux above the Fe Kα ionization threshold of 7.11 keV is one of the main contributors to the observed flux in the Fe Kα line. For the solar flares, Bai (1979b) derived a formula for the flux of Fe Kα photons received on the Earth,

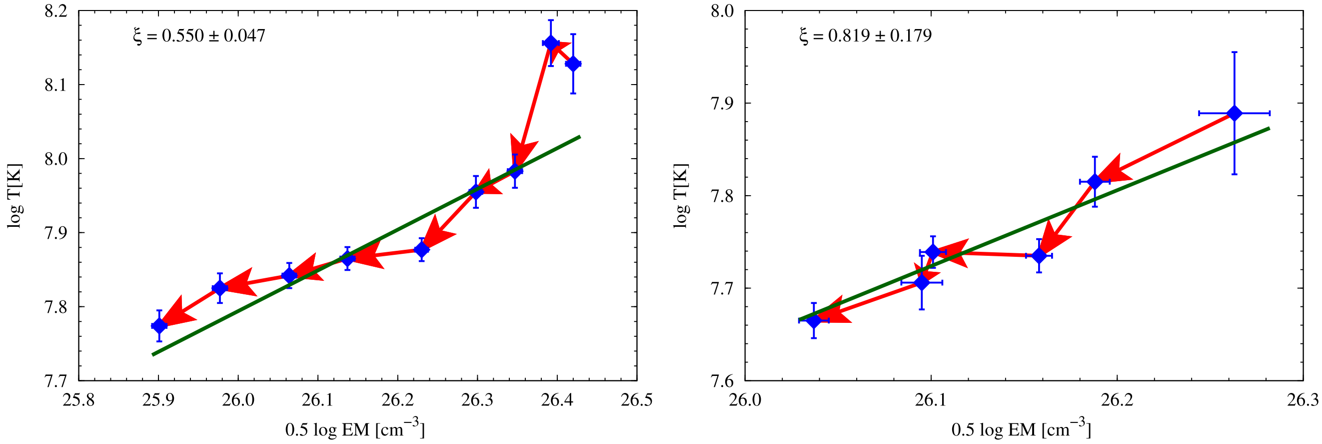

Figure 4. Evolution of flares F1 (left) and F2 (right) in the log $\sqrt{\mathrm{EM}}$ − log T plane. The continuous line shows the best-fit during the decay phase of the flares with a slope ζ shown in the top left corner of each plot.

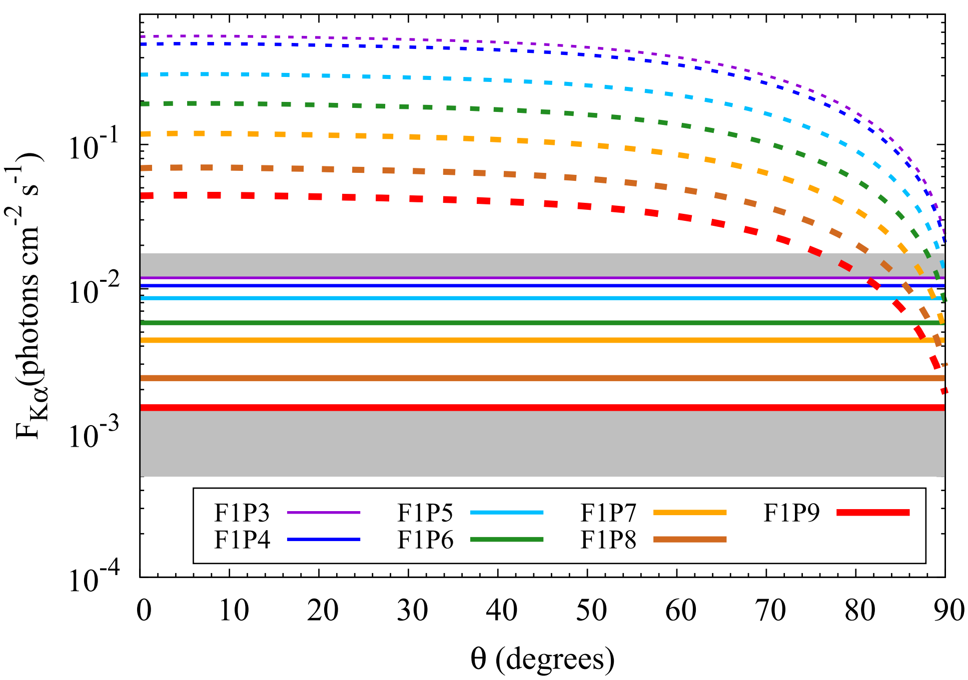

Figure 5. Modeling of 6.4 keV line flux for the seven time intervals during the decay of flare F1. The solid horizontal lines show the observed Fe Kα line fluxes of different time segments marked in the bottom of the plot. The dashed curves with similar thickness correspond to the modeled Fe Kα line flux variation with the astrocentric angle for the same time intervals. Thicker lines correspond to the later time spans. The dark shaded regions indicate the upper and lower 68% confidence intervals of the first and last time segments, respectively.

which was later extended to stellar context by Drake et al. (2008) and is given by

$$F_{K\alpha} = f(\theta)\Gamma(T, h)F_{7.11} \quad \text{photons} \quad \text{cm}^{-2}\,\text{s}^{-1} \qquad (4)$$

where $F_{7.11}$ is the total flux above 7.11 keV, $f(\theta)$ is a function that describes the angular dependence of the emitted flux on the astrocentric angle (defined as an angle subtended by the flare and the observer), and Γ is the fluorescent efficiency. We used the coefficients derived by Drake et al. (2008) to determine the functional dependence of $f(\theta)$ and Γ for different loop heights (see Tables 2 and 3 of Drake et al. 2008). We could only get enough statistics in both XRT and BAT spectra (required to estimate $F_{7.11}$) for the flare F1; therefore, we have done our analysis only for flare F1. The value of Γ was taken as 0.96 for a loop height of 0.1 $R_\star$ and a temperature of 100 MK, which are closest to the derived loop length and maximum temperature of the flare F1. Because photospheric iron abundances of CC Eri are not known, a default value of abundances of 3.16×10^{-5} was used in the calculations (see Drake et al. 2008). Since the flare F1 was only detected up to 50 keV (see Section 3.1), in our analysis, we considered the upper limit of energy to be 50 keV. The model flux of the photon density spectrum above 7.11 keV was calculated by using best-fit APEC model parameters from the joint spectral fitting of XRT+BAT spectra in different time intervals for flare F1. Figure 5 shows the modeled Fe Kα flux as a function of the astrocentric angle of a flare height of 0.1 $R_\star$ for different time segments. The corresponding observed flux is also shown by continuous lines of the same thickness. The modeled and observed Fe Kα line flux was found to overlap at an astrocentric angle of $\sim 90°$.

4. Discussion and Conclusions

4.1. Temporal and Spectral Properties

In this paper, we have presented a detailed study of two X-ray superflares observed on an active binary system CC Eri with the *Swift* satellite. These flares are remarkable in the large enhancement of peak luminosity in soft and hard X-ray energy bands. A total of eight flares have been detected in X-ray bands on CC Eri thus far. Out of the eight flares, two flares are the strongest flares in terms of energy released. The soft X-ray luminosity increased up to ~ 400 and >3 times more than to that of the minimum observed values for the flares F1 and F2, respectively. The former is much larger than any of the previously reported flares on CC Eri observed with *MAXI* GCS ($\sim$5–6 times more than quiescent; Suwa et al. 2011), *Chandra* ($\sim$11 times more than quiescent; Nordon & Behar 2007), *XMM-Newton* ($\sim$2 times more than quiescent; Crespo-Chacón et al. 2007; Pandey & Singh 2008), *ROSAT* ($\sim$2 times more than quiescent; Pan & Jordan 1995), and other flares observed with *EXOSAT* (Pallavicini et al. 1988), *Einstein* IPC (Caillault et al. 1988), and *HEAO1* (Tsikoudi 1982). However, similar magnitude flares have been reported in other stars such as DG CVn (Fender et al. 2015; Osten et al. 2016), EV Lac (Favata et al. 2000; Osten et al. 2010), II Peg (Osten et al. 2007), UX Ari (Franciosini et al. 2001), AB Dor (Maggio et al. 2000), Algol (Favata & Schmitt 1999), and EQ1839.6+8002 (Pan et al. 1997). Considering that the flare happened in the primary (K7.5 V), the peak X-ray luminosity of flare F1 and flare F2 were, respectively, found to be 48% and 16% of bolometric luminosity ($L_{\rm bol}$); if the flare happened in the secondary (M3.5 V) star, the peak X-ray luminosity of flares F1 and F2 were 267% and 91% of $L_{\rm bol}$, whereas the peak luminosity for flares F1 and F2 were found to be 41% and 14% of combined $L_{\rm bol}$, respectively.

Both flares appear to be the shortest duration flares observed on CC Eri thus far. However, a weak flare with a similar duration was observed by the *XMM-Newton* satellite (Crespo-Chacón et al. 2007). The durations of all other previously observed flares on CC Eri were in the range of 9–13 ks. The durations of the superflares on CC Eri are also found to be smaller than other observed superflares, e.g., $\sim$3 ks for EV Lac (Osten et al. 2010), $>$10 ks for II Peg (Osten et al. 2007), $\sim$14 ks for AB Dor (Maggio et al. 2000), and $\sim$45 ks for Algol (Favata & Schmitt 1999). The e-folding decay times of both X-ray flares are shorter in the hard spectral band than those in the softer band.

During the flares F1 and F2, the observed temperature reached a maximum value of $\sim$174 MK for flare F1 and $\sim$128 MK, respectively. These values of temperatures are quite high from previously observed maximum flare temperatures on CC Eri (Crespo-Chacón et al. 2007; Nordon & Behar 2007; Pandey & Singh 2008), but are of the similar order to those of other superflares detected on II Peg ($\approx$300 MK; Osten et al. 2007), DG CVn ($\approx$290 MK; Osten et al. 2016), EV Lac ($\approx$150 MK and $\approx$142 MK; Favata et al. 2000; Osten et al. 2010), and AB Dor ($\approx$114 MK; Maggio et al. 2000). The abundances during the flares F1 and F2 are found to enhance $\sim$9 and $\sim$2 times more than those of the minimum values observed. During other superflares, abundances were found to increase between two to three times more than that of the quiescent level (Favata & Schmitt 1999; Favata et al. 2000; Maggio et al. 2000). However, in the case of the superflare observed with *Swift* in EV Lac, the abundances were found to remain constant throughout the flare. From Figure 3, it is evident that the abundance peaks after the temperature and luminosity peaks, which is consistent with a current idea in the literature (see Reale 2007). This could be due to the heating and evaporation of the chromospheric gas, which increases the metal abundances in the flaring loop. For both flares, the temperature peaked before the EM did. A similar delay was also observed in many other solar and stellar flares (e.g., Sylwester et al. 1993; Favata & Schmitt 1999; Favata et al. 2000; Pandey & Singh 2008). The temperature increases due to beam driven plasma heating and later subsequent evaporation of the plasma into upper parts of the coronal loop that increases its density, and therefore EM ($\sim n_e^2$). Later coronal plasma cools down by thermal conduction and then via radiative losses (e.g., Cargill & Klimchuk 2004).

4.2. Coronal Loop Properties

The derived loop lengths for the flares F1 and F2 are larger than previously observed flares by Crespo-Chacón et al. (2007) on CC Eri. The loop lengths are also in between the loop lengths derived for other G–K dwarfs, dMe stars, and RS CVn type binaries (e.g., Favata & Micela 2003; Pandey & Singh 2008, 2012). Instead of $\sim$3 times larger peak luminosity in flare F1 than that of the flare F2, the derived loop length for flare F2 is two times larger than that of flare F1, which might be interpreted as a result of an $\sim$1.4 times more sustained heating rate in the decay phase of flare F1 than that of flare F2. The heating rate during flare F1 is also found to be $\sim$49% of the bolometric luminosity of the CC Eri system, whereas during flare F2 the heating rate is only $\sim$35% of the combined bolometric luminosity. The derived heating rate is also found to be more than the maximum X-ray luminosity for both flares. This result is compatible with X-ray radiation being one of the major energy loss terms during the flares.

Present analysis allows us to make some relevant estimation of the magnetic field strength that would be required to accumulate the emitted energy and to keep the plasma confined in a stable magnetic loop configuration. Under the assumptions that the energy release is indeed of magnetic origin, the total non-potential magnetic field B_0 involved in a flare energy release within an active region of the star can be obtained from the relation

$$E_{\rm X,tot} = \frac{(B_0^2 - B^2)}{8\pi} \times V. \quad (5)$$

Assuming that the loop geometry does not change during the flare, B_0 is estimated to be $>$12 and $>$2 kG for the flares F1 and F2, respectively. Bopp & Evans (1973) also estimated a large magnetic field of 7 kG on CC Eri at photospheric level. We have used the loop volume in the derivation of B_0, but this may not imply that the magnetic field fills up the whole volume. Rather, our estimation of B_0 is based on the assumption that the energy is stored in the magnetic field configuration (e.g., a large group of spots) of the field strength of several kG with a volume comparable to one of the flaring loops.

4.3. Flare Location and Fe Kα Emission Feature

Given that CC Eri is an active binary system, we can consider three possible scenarios of the flare origin: (i) energy release occurs due to magnetic reconnection between magnetic fields bridging two stars (see Uchida & Sakurai 1983; Graffagnino et al. 1995), (ii) flares occurred on K-type primary star, and (iii) flares occurred on M-type secondary star. The binary separation of the CC Eri system of 1.4×10^{11} cm (Amado et al. 2000; Crespo-Chacón et al. 2007) is more than an order of the height of flaring loops for both flares. Therefore, it is more likely that the flares are attached to a corona of any one of the components of CC Eri. It is also very difficult to identify the component of the binaries on which the flares occured.

One of the most interesting findings is the detection of Fe Kα emission line in the X-ray spectra of CC Eri during the flares, whose flux depends on the photospheric iron abundance, the height of the emitting source, and the astrocentric angle between the emitting source and observer (Bai 1979a; Drake et al. 2008). Recently, the Fe Kα emission line was also detected in several other cool active stars during large flares, such as HR 9024 (Testa et al. 2008) and II Peg (Ercolano et al. 2008), and has been well described by the fluorescence hypothesis. In most of the cases, the flaring loop length derived in this method was found to be consistent with the loop length derived from the hydrodynamic method. Using the loop length derived from the hydrodynamic model, the astrocentric angle between the flare and observer has been estimated as $\sim 90°$. This shows that the region being illuminated by the flare, and thus fluorescing the photospheric iron, is located near the stellar limb.

This work made use of data supplied by the UK Swift Science Data Centre at the University of Leicester. This research has made use of the XRT Data Analysis Software (XRTDAS) developed under the responsibility of the ASI Science Data Center (ASDC), Italy. We thank the anonymous referee for useful comments.

Facility: Swift (BAT, XRT).

References

Amado, P. J., Doyle, J. G., Byrne, P. B., et al. 2000, A&A, 359, 159
Anders, E., & Grevesse, N. 1989, GeCoA, 53, 197
Arnaud, K. A. 1996, in ASP Conf. Ser. 101, Astronomical Data Analysis Software and Systems V, ed. G. H. Jacoby & J. Barnes (San Francisco, CA: ASP), 17
Bai, T. 1979a, SoPh, 64, 417
Bai, T. 1979b, SoPh, 62, 113
Barthelmy, S. D., Barbier, L. M., Cummings, J. R., et al. 2005, SSRv, 120, 143
Barthelmy, S. D., Baumgartner, W. H., Chester, M. M., et al. 2012, GCN, 12985
Bopp, B. W., & Evans, D. S. 1973, MNRAS, 164, 343
Burrows, D. N., Hill, J. E., Nousek, J. A., et al. 2005, SSRv, 120, 165
Busko, I. C., Quast, G. R., & Torres, C. A. O. 1977, A&A, 60, L27
Caillault, J.-P., Drake, S., & Florkowski, D. 1988, AJ, 95, 887
Cargill, P. J., & Klimchuk, J. A. 2004, ApJ, 605, 911
Crespo-Chacón, I., Micela, G., Reale, F., et al. 2007, A&A, 471, 929
Demircan, O., Eker, Z., Karataş, Y., & Bilir, S. 2006, MNRAS, 366, 1511
Dickey, J. M., & Lockman, F. J. 1990, ARA&A, 28, 215
Drake, J. J., Ercolano, B., & Swartz, D. A. 2008, ApJ, 678, 385
Ercolano, B., Drake, J. J., Reale, F., Testa, P., & Miller, J. M. 2008, ApJ, 688, 1315
Evans, D. S. 1959, MNRAS, 119, 526
Evans, P. A., Page, K. L., Beardmore, A. P., et al. 2008, ATel, 1787
Favata, F., & Micela, G. 2003, SSRv, 108, 577
Favata, F., Reale, F., Micela, G., et al. 2000, A&A, 353, 987
Favata, F., & Schmitt, J. H. M. M. 1999, A&A, 350, 900
Fender, R. P., Anderson, G. E., Osten, R., et al. 2015, MNRAS, 446, L66
Franciosini, E., Pallavicini, R., & Tagliaferri, G. 2001, A&A, 375, 196
Godet, O., Beardmore, A. P., Abbey, A. F., et al. 2009, A&A, 494, 775
Graffagnino, V. G., Wonnacott, D., & Schaeidt, S. 1995, MNRAS, 275, 129
Maggio, A., Pallavicini, R., Reale, F., & Tagliaferri, G. 2000, A&A, 356, 627
Moretti, A., Campana, S., Mineo, T., et al. 2005, Proc. SPIE, 5898, 360
Morrison, R., & McCammon, D. 1983, ApJ, 270, 119
Nordon, R., & Behar, E. 2007, A&A, 464, 309
Osten, R. A., Brown, A., Wood, B. E., & Brady, P. 2002, ApJS, 138, 99
Osten, R. A., Drake, S., Tueller, J., et al. 2007, ApJ, 654, 1052
Osten, R. A., Godet, O., Drake, S., et al. 2010, ApJ, 721, 785
Osten, R. A., Kowalski, A., Drake, S. A., et al. 2016, ApJ, 832, 174
Pallavicini, R., Monsignori-Fossi, B. C., Landini, M., & Schmitt, J. H. M. M. 1988, A&A, 191, 109
Pan, H. C., & Jordan, C. 1995, MNRAS, 272, 11
Pan, H. C., Jordan, C., Makishima, K., et al. 1997, MNRAS, 285, 735
Pandey, J. C., & Singh, K. P. 2008, MNRAS, 387, 1627
Pandey, J. C., & Singh, K. P. 2012, MNRAS, 419, 1219
Parmar, A. N., Culhane, J. L., Rapley, C. G., et al. 1984, ApJ, 279, 866
Reale, F. 2007, A&A, 471, 271
Reale, F., Betta, R., Peres, G., Serio, S., & McTiernan, J. 1997, A&A, 325, 782
Rosner, R., Tucker, W. H., & Vaiana, G. S. 1978, ApJ, 220, 643
Schaefer, B. E., King, J. R., & Deliyannis, C. P. 2000, ApJ, 529, 1026
Shibayama, T., Maehara, H., Notsu, S., et al. 2013, ApJS, 209, 5
Slee, O. B., Budding, E., Carter, B. D., et al. 2004, PASA, 21, 72
Smith, R. K., Brickhouse, N. S., Liedahl, D. A., & Raymond, J. C. 2001, ApJL, 556, L91
Suwa, F., Asada, M., Sugizaki, M., et al. 2011, ATel, 3837
Sylwester, B., Sylwester, J., Serio, S., et al. 1993, A&A, 267, 586
Testa, P., Drake, J. J., Ercolano, B., et al. 2008, ApJL, 675, L97
Tsikoudi, V. 1982, ApJ, 262, 263
Uchida, Y., & Sakurai, T. 1983, ASSL, 102, 629
Zarro, D. M., Dennis, B. R., & Slater, G. L. 1992, ApJ, 391, 865